

Viscothermal acoustics using finite elements  
Analysis tools for engineers



*Ronald Kampinga*

# Viscothermal acoustics using finite elements

---

## Analysis tools for engineers

Ronald Kampinga

De promotiecommissie is als volgt samengesteld:

*Voorzitter en secretaris:*

Prof.dr. F. Eising                                 Universiteit Twente

*Promotor:*

Prof.dr.ir. A. de Boer                            Universiteit Twente

*Assistent Promotor:*

Dr.ir. Y.H. Wijnant                             Universiteit Twente

*Leden:*

Prof.dr. W. Lauriks                            Katholieke Universiteit Leuven

Prof.dr.ir. J.B. Jonker                         Universiteit Twente

Prof.dr.ir. H.W.M. Hoeijmakers             Universiteit Twente

Prof.dr.ir. D.J. Schipper                     Universiteit Twente

Ir. A.M. Lafort                                 Sonion Nederland B.V.

Viscothermal acoustics using finite elements — Analysis tools for  
engineers

Kampinga, Wim Ronald

PhD thesis, University of Twente, Enschede, The Netherlands

Subject headings: acoustics, viscothermal wave propagation,  
acousto-elasticity, finite elements

June 2010

ISBN 978-90-365-3050-7

URL <http://dx.doi.org/10.3990/1.9789036520507>

Copyright ©2010 by W.R. Kampinga, Enschede, The Netherlands

Printed by Ipskamp Drukkers

This research project was supported by Sonion Nederland B.V. in  
Amsterdam. This support is gratefully acknowledged.

VISCOTHERMAL ACOUSTICS USING FINITE ELEMENTS  
—  
ANALYSIS TOOLS FOR ENGINEERS

PROEFSCHRIFT

ter verkrijging van  
de graad van doctor aan de Universiteit Twente,  
op gezag van de rector magnificus,  
prof.dr. H. Brinksma,  
volgens besluit van het College voor Promoties  
in het openbaar te verdedigen  
op woensdag 23 juni 2010 om 16.45 uur

door

Wim Ronald Kampinga

geboren op 10 oktober 1978  
te Delfzijl

Dit proefschrift is goedgekeurd door de promotor

Prof.dr.ir. A. de Boer

en de assistent promotor

Dr.ir. Y.H. Wijnant

# Summary

Hearing aids contain miniature loudspeakers and microphones. Following the trend of miniaturization, hearing aids and the acoustic transducers inside become smaller and smaller. This presents new challenges for engineers who develop such transducers. Because of the small geometries, the viscothermal boundary layer effects cannot be neglected in their acoustic models. This thesis presents four numerical viscothermal acoustic models that can aid the engineer in the development of, for example, these miniature loudspeakers and microphones.

The ideal viscothermal acoustic model for a design environment would be computationally efficient, applicable for arbitrary geometries and usable in fluid structure interaction problems. These three aspects are satisfied to a different degree for each of the four presented models. The aspects of applicability for arbitrary geometries led to choosing the finite element method (FEM) as the numerical solution framework for the models. The software COMSOL is used to implement the presented viscothermal acoustic models. This has the added advantage that structural finite elements supplied by COMSOL can be used in fluid structure interaction problems.

The first of the presented models is a finite element implementation of the fully coupled viscothermal acoustic equations: the linear time harmonic Navier-Stokes equations. This general model requires a minimum of four field values in 3-D: three velocity components and the temperature. However, a mixed FEM formulation with the pressure as an additional field is used to ensure a good convergence rate. The drawback of this model is that it requires large computational resources, especially in 3-D.

Some authors label viscothermal acoustics as a ‘three wave theory’ with coupled viscous, thermal and acoustic waves. The viscous and thermal waves damp the acoustic waves. It is possible to make accurate models using the approximation that the acoustic wave does not influence the viscous and thermal waves. The other three of the four viscothermal acoustic models use this approximation. Two of these models are known in the literature. These models are computationally efficient, but have the disadvantage that they are not applicable for arbitrary geometries: one model is

for waveguides below the cut-off frequency and the other model is for geometries of which all characteristic lengths are much larger than the viscous and thermal boundary layer thicknesses. The third model is new and does not have this disadvantage. It can be used for arbitrary geometries and is computationally much more efficient than the fully coupled model.

The viscothermal acoustic models are validated by means of measurements, an analytic model and mutual comparisons. Besides the relatively simple examples that are used for the validation, a model of a hearing aid loudspeaker is presented. The model has a good correspondence to the measurements. Several parameter studies for this loudspeaker are presented.

Each of the the four presented viscothermal acoustic models has its own advantages, disadvantages and limitations. Together, they form a set of analysis tools for the engineer that can be used to develop small acoustic transducers, or efficiently solve many other viscothermal acoustic problems.

# Samenvatting

Hoorapparaten bevatten miniatuur luidsprekers en microfoons en worden steeds kleiner. Hierdoor moeten de akoestische componenten die erin zitten ook steeds kleiner worden. Dit stelt de ingenieurs die deze componenten ontwikkelen voor nieuwe uitdagingen. Vanwege de kleine geometrieën kunnen de viskeuze en thermische grenslaageffecten van de lucht niet worden verwaarloosd in de akoestische modellen die zij gebruiken. Dit proefschrift presenteert vier numerieke viskotherme akoestische modellen die de ingenieur kunnen ondersteunen bij het ontwikkelen van bijvoorbeeld deze kleine luidsprekers en microfoons.

Het ideale viskotherme akoestische model voor een ontwikkelomgeving is snel, toepasbaar voor willekeurige geometrieën en geschikt voor problemen waarin de akoestiek is gekoppeld aan een constructie. Deze drie aspecten worden in verschillende mate vervuld door elk van de vier viskotherme akoestische modellen. Het aspect van toepasbaarheid voor willekeurige geometrieën heeft geleid tot de keuze voor de eindige elementen methode (EEM) als de numerieke oplosmethode. Het computerprogramma COMSOL is gebruikt om de gepresenteerde viskotherme akoestische modellen te implementeren. Dit heeft als bijkomend voordeel dat de constructie in gekoppelde problemen met reeds in COMSOL aanwezige elementen kan worden gemodelleerd.

Het eerste van de gepresenteerde modellen is de eindige elementen formulering van de volledig gekoppelde viskotherme akoestische vergelijkingen: de lineaire tijd-harmonische Navier-Stokes vergelijkingen. Dit algemene model heeft minimaal vier velden nodig in 3-D: drie snelheidscomponenten en de temperatuur. Een gemixte EEM formulering met de druk als een extra veld is gebruikt om een goede convergentiesnelheid te verkrijgen. Dit model heeft een hoog geheugengebruik en een lange rekentijd als nadeel, vooral in 3-D.

Sommige auteurs bestempelen viskotherme akoestiek als een ‘drie golven theorie’, met gekoppelde viskeuze, thermische en akoestische golven. De viskeuze en thermische golven dempen de akoestische golven. Het is



mogelijk om nauwkeurige modellen te maken met de benadering dat de akoestische golven de viskeuze en thermische golven niet beïnvloeden. De overige drie van de vier viskotherme akoestische modellen gebruiken deze benadering. Twee hiervan zijn al bekend uit de literatuur. Deze modellen zijn efficiënt, maar hebben het nadeel dat ze niet voor willekeurige geometrieën toepasbaar zijn: één model is voor golfgeleiders onder de grensfrequentie en het andere model is voor geometrieën waarin alle karakteristieke lengtes veel groter zijn dan de viskeuze en thermische grenslaagdiktes. Het derde model is nieuw en heeft dit nadeel niet. Het kan gebruikt worden voor willekeurige geometrieën en heeft minder rekenkracht nodig dan het volledig gekoppelde model.

De vier viskotherme akoestische modellen zijn gevalideerd aan de hand van metingen, een analytisch model en onderlinge vergelijkingen. Naast de relatief eenvoudige voorbeelden die hiervoor gebruikt zijn, wordt een model van een hoorapparaatluidspreker gepresenteerd. Dit model komt goed overeen met de meetresultaten. Enkele parameterstudies voor de luidspreker worden gepresenteerd.

De vier viskotherme akoestische modellen hebben ieder hun eigen voordelen, nadelen en beperkingen. Ze vormen een verzameling analyse methodes voor de ingenieur die gebruikt kan worden om kleine akoestische componenten te ontwikkelen, of om vele andere viskotherme akoestische problemen efficiënt op te lossen.

# Dankwoord

Na vier en een half jaar is het promotieonderzoek afgerond met dit proefschrift als resultaat. Ik wil graag een aantal mensen bedanken voor hun bijdrage aan het onderzoek.

André, bedankt voor het vertrouwen in mij en het houden van het overzicht. Ysbrand, jouw eindeloze positiviteit is inspirerend. Ad, bedankt voor je begeleiding vanuit Sonion. Het is prettig samenwerken met iemand die zo snel tot de kern komt.

Maarten, Casper en Jeroen, bedankt voor uitvoeren van jullie afstudeeropdrachten in het kader van dit onderzoek. Jullie resultaten zijn waardevolle bijdragen geweest.

Debbie en Tanja bedankt voor het organiseren van alles wat er bij een promotie komt kijken: van de reizen naar conferenties tot de koffie en broodjes voor gasten.

Drie generaties AIO's, bedankt voor de gezelligheid en de goede werksfeer. Wandelen tijdens de lunch, bioscoopavondjes of gewoon wat ouwehoeren, ik heb er van genoten. Met name dank aan Marten: het was fijn om een 'sparring partner' te hebben die begreep waar ik precies mee bezig was.

Antoinette, je directe bijdrage aan het proefschrift is misschien klein, maar je indirecte bijdrage des te groter. Thuis is echt thuis na jouw 'ja' op Noah Beach. Dankjewel dat je er voor me bent.



# Contents

<b>Summary</b>	<b>v</b>
<b>Samenvatting</b>	<b>vii</b>
<b>Dankwoord</b>	<b>ix</b>
<b>Contents</b>	<b>xi</b>
<b>1 Introduction</b>	<b>1</b>
1.1 Problem definition . . . . .	1
1.1.1 Hearing aid receiver . . . . .	2
1.2 Introduction to viscothermal acoustics . . . . .	3
1.2.1 Time harmonic form and phasor notation . . . . .	4
1.2.2 Linear acoustic assumptions . . . . .	4
1.2.3 Isentropic acoustics . . . . .	5
1.2.4 Viscous and thermal effects . . . . .	6
1.2.5 Summary . . . . .	11
1.3 Introduction to finite element modeling . . . . .	12
1.3.1 From PDE to weak form . . . . .	12
1.3.2 Discretization of the weak form . . . . .	13
1.3.3 From discrete weak form to matrix equation . . . . .	14
1.3.4 Structural finite elements and fluid structure interaction . . . . .	16
1.3.5 Notation convention . . . . .	19
1.3.6 Summary . . . . .	19
1.4 Outline . . . . .	20
<b>2 The full linear Navier-Stokes model</b>	<b>23</b>
2.1 Governing equations . . . . .	23
2.1.1 Constitutive equations . . . . .	23
2.1.2 Balance laws . . . . .	26
2.1.3 Final set of equations . . . . .	29
2.1.4 Boundary conditions . . . . .	30
2.2 Finite element formulation . . . . .	31
2.2.1 Weak form . . . . .	32
2.2.2 Discretization . . . . .	33

2.3	Fluid structure interaction with the FLNS model . . . . .	40
2.4	Discussion . . . . .	41
<b>3</b>	<b>Approximate viscothermal acoustic models</b>	<b>43</b>
3.1	Common approximations . . . . .	44
3.1.1	Dimensionless equations and wave numbers . . . . .	45
3.1.2	Order of magnitude analyses . . . . .	46
3.1.3	Approximate viscothermal solutions . . . . .	48
3.1.4	Summary of the results in dimensional form . . . . .	51
3.2	The boundary layer impedance model . . . . .	52
3.2.1	Geometric constraints . . . . .	53
3.2.2	Viscous and thermal fields . . . . .	53
3.2.3	Acoustic pressure . . . . .	55
3.2.4	Fluid structure interaction with the BLI model . . . . .	57
3.2.5	BLI algorithm . . . . .	58
3.3	The low reduced frequency model . . . . .	58
3.3.1	Geometric constraints . . . . .	59
3.3.2	Viscous and thermal fields . . . . .	60
3.3.3	Acoustic pressure . . . . .	65
3.3.4	Fluid structure interaction with the LRF model . . . . .	68
3.3.5	LRF algorithm . . . . .	70
3.4	The sequential linear Navier-Stokes model . . . . .	71
3.4.1	Viscous and thermal fields . . . . .	71
3.4.2	Acoustic pressure . . . . .	72
3.4.3	Fluid structure interaction with the SLNS model . . . . .	74
3.4.4	SLNS algorithm . . . . .	74
3.5	Comparison of the models . . . . .	75
3.5.1	Summary: advantages and disadvantages per model . . . . .	75
3.5.2	Discussion: paradigms for the SLNS model . . . . .	77
<b>4</b>	<b>Validation and performance analyses</b>	<b>79</b>
4.1	Waveguides . . . . .	79
4.1.1	Frequency response of slit near resonance . . . . .	80
4.1.2	Convergence of the slit problem . . . . .	82
4.1.3	3-D cylindrical tube: element aspect ratio . . . . .	85
4.2	Impedance tube samples . . . . .	86
4.2.1	Impedance tube setup . . . . .	87
4.2.2	Jansen's sample . . . . .	88
4.2.3	Hannink's sample . . . . .	91
4.3	Condenser microphone . . . . .	95
4.3.1	Membrane model . . . . .	96
4.3.2	Results . . . . .	97
4.3.3	Microphone 2 . . . . .	99
4.4	On fluid structure interaction with the SLNS model . . . . .	102
4.5	Summary . . . . .	107
<b>5</b>	<b>Miniature loudspeaker</b>	<b>109</b>
5.1	Structure of the model . . . . .	109

5.2	Motor model . . . . .	111
5.2.1	Electro-magnetic coupling . . . . .	112
5.2.2	Magneto-mechanic coupling . . . . .	113
5.2.3	Mechanical model . . . . .	116
5.2.4	Complete motor model . . . . .	117
5.3	Finite element model . . . . .	117
5.3.1	Lumping the FEM model to a transmission matrix . . . . .	119
5.4	Coupler model . . . . .	120
5.4.1	Tube . . . . .	122
5.4.2	Volume . . . . .	122
5.4.3	Complete coupler . . . . .	123
5.5	Results of the complete receiver model . . . . .	123
5.6	Summary . . . . .	128
<b>6</b>	<b>Conclusions and discussion</b>	<b>129</b>
6.1	Conclusions . . . . .	129
6.2	Discussion . . . . .	131
6.2.1	Extending the models . . . . .	131
6.2.2	Improving the models . . . . .	132
	<b>Appendices</b>	<b>135</b>
A	Viscothermal fields for the LRF model: analytic solutions	137
B	Paper: Performance of Several Viscothermal Acoustic Finite Elements	139
C	Comsol script: FLNS microphone model	151
	<b>Nomenclature</b>	<b>155</b>
	<b>Bibliography</b>	<b>159</b>



# Introduction

Miniaturization is an ongoing trend in many products, to which hearing aids are no exception. Although the larger ‘behind the ear’ type is still the standard, the smallest types can fit in the ear canal. Clearly, the dimensions of the microphone and loudspeaker inside the hearing aid need to be reduced accordingly.

SONION is a company that manufactures and develops miniature microphones and loudspeakers for hearing aids. Accurate mathematical models are a valuable tool in the development process of these devices. The acoustic part of these models is not accurate if it is based on standard lossless acoustic theory: these devices are so small that viscothermal effects (heat conduction and viscous shear) have to be included. Therefore, the trend of miniaturization increases the need for viscothermal acoustic models.

This thesis is the final report of a PhD project that is a cooperation between the University of Twente and SONION. The title of this thesis is ‘Viscothermal acoustics using finite elements — Analysis tools for engineers’. The basic concepts of viscothermal acoustics and the finite element method are introduced after presenting the problem definition. This chapter ends with an outline of the thesis.

## 1.1 Problem definition

With hindsight, this thesis addresses the following problem: *How to make efficient viscothermal acoustic models for arbitrary geometries, including fluid structure interaction.* Because arbitrary geometries need to be modeled, numerical methods are a matter of course. Although the literature presents several viscothermal acoustic BEM models (see [20] and its references), FEM is used in this project such that the fluid structure interaction can be modeled in a straightforward manner using existing structural finite elements. The terms ‘efficient’ and ‘arbitrary geometries’ are rather incompatible: if certain geometric restrictions are accepted, the models can be



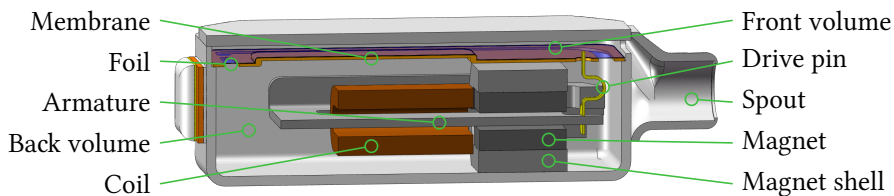
made more efficient. Therefore, this thesis also covers two of such models, which are recommended if applicable; see sections 3.2 and 3.3. Besides these existing models, two models that are applicable for arbitrary geometries are presented. The first of these models is a finite element formulation of the coupled linearized Navier-Stokes equations for viscothermal acoustics; see chapter 2. The second model is a more efficient alternative in which the full coupling is approximated as one-way coupling; see section 3.4.

As mentioned, SONION's goal is to create predictive models of their transducers, especially of their hearing aid loudspeakers (called receivers). Such a hearing aid receiver is introduced next, since it is useful to have a specific application in mind. Nevertheless, the finite element procedures developed in this thesis are general and can be applied to many acoustic problems, not just to hearing aid receivers.

### 1.1.1 Hearing aid receiver

The miniature loudspeaker that is used in hearing aids is called 'receiver' in the terminology that stems from telephony. Figure 1.1 shows a cross section of such a transducer. This type has a length of 8 mm, which is larger than average. The receiver contains a 'balanced armature' motor with an actuation principle that uses magnetic forces, instead of Lorenz forces that are commonly used in moving coil loudspeakers. The principle can be explained using the labeled parts in the figure. An armature is located between two equally poled permanent magnets that both attract it with an equal force; opposite magnetic poles face the armature. A current through the coil induces a magneto motive force in the armature. As a result, the tip of the armature, near the drive pin, is attracted more by one of the two permanent magnets and less by the other, depending on the direction of the current in the coil. The magnet shells close the magnetic loop to the armature (this is not clearly visible in figure 1.1). The armature bends and the drive pin transfers the movement of its tip to the membrane. Although in the figure the foil is drawn flat around the membrane, in the actual receiver it is formed as a gully to allow the membrane to move. Furthermore, the foil provides an airtight seal between the back volume and the front volume. Therefore the membrane movement compresses and rarefies the air in the back and front volume. The back volume is closed, but the front volume is connected to the spout, which can be connected to a tube that leads to the ear canal. Eventually, the compression in the front volume leads to a pressure that can be heard.

In the above description, four physical domains can be identified: electric, magnetic, mechanic and acoustic. Each of these domains presents its own difficulties and challenges, but this thesis focuses on the acoustic aspects. Because of the small size of the receiver, the dissipative viscothermal



**Figure 1.1:** Cross section of a hearing aid receiver. Its total length is 8 mm. The important parts are labeled.

effects, introduced later, cannot be neglected in the acoustic model. Furthermore, the geometry of the air domains in the receiver are relatively complicated, such that numerical models are beneficial. Analytic or semi-analytic models of the receiver may be created if simplified geometries are assumed, but this is a tedious process and the errors of simplifying the geometry are typically unknown. For this reason the focus of this project that started with a semi-analytic model of another receiver (see [40, 39, 11, 9]), shifted to finite element modeling. Chapter 5 presents a model of the receiver that uses one of the developed FEM methods.

## 1.2 Introduction to viscothermal acoustics

Viscothermal acoustics can be regarded as a special case of fluid dynamics, or as a generalized case of standard acoustics. Here, standard acoustics refers to lossless wave propagation, which is more clearly designated by the term *isentropic acoustics*. Chapter 2, which presents the governing equations, is written from a fluid dynamics point of view, while this introduction and chapter 3 focus on the differences between viscothermal acoustics and isentropic acoustics.

Readers who are interested in a historic perspective are encouraged to read Truesdell's 'History of classical mechanics' [69, 70], which covers many of the (fluid) mechanic, mathematic and thermodynamic contributions that are required for viscothermal acoustics. The history of the Navier-Stokes equations is presented in the PhD thesis of Inayat Hussain [34]. Kirchhoff was the first to combine the pieces of theory for viscothermal acoustics in his paper [47] published in 1868. The literature contains many (semi-)analytic solution methods of these equations that are inspired by this paper. Nijhof [55] elaborates on these methods. This thesis focuses on numerical finite element methods for these equations, starting with a direct implementation in chapter 2.

### 1.2.1 Time harmonic form and phasor notation

Before the basic properties of viscothermal acoustics are introduced, a few remarks should be made regarding the notation. The equations are formulated in the complex perturbation amplitudes, called phasors, which are commonly used in time harmonic acoustics with the Helmholtz equation. The time harmonic form is efficient because the PDES do not explicitly depend on time anymore. This comes at the relatively small cost of introducing complex valued fields. In problems with a single frequency, the relation for all fields is

$$\check{\phi} = \phi_0 + \Re\left(\phi e^{i\omega t}\right), \quad (1.1)$$

where the operator  $\Re$  takes the real value of its argument,  $\omega$  and  $t$  denote angular frequency and time,  $\check{\phi}$  is the time dependent total field value,  $\phi_0$  is the quiescent field value and  $\phi$  is the complex perturbation amplitude of the field also called phasor. The phasor represents both the magnitude  $|\phi|$  and the phase angle  $\angle\phi$  of the perturbation. The above relation holds for all fields, for example the pressure  $p$  in [Pa], the temperature  $T$  in [K] or the velocity  $\boldsymbol{v}$  in [m/s]. Notice that  $e^{i\omega t}$  is used in equation (1.1) and the remainder of this thesis, while  $e^{-i\omega t}$  is also widely used in the viscothermal acoustic literature.

Equation (1.1) provides a straightforward way to present the phasor notation. However, the models in this thesis are not only valid for single frequencies. The discrete Fourier transform may be used to decompose a more general problem into contributions at a limited number of frequencies. Next, a time harmonic problem can be solved for each of these frequencies. And last, the solution of the general problem can be expressed as the superposition of the solutions at the individual frequencies by using the inverse discrete Fourier transform.

### 1.2.2 Linear acoustic assumptions

The use of phasors is efficient for linear differential equations. However in general, the Navier-Stokes equations are nonlinear. The introduction of the Navier-Stokes equations is delayed until chapter 2, but the *linear acoustic assumptions* that eventually lead to the used time harmonic form are mentioned here. Equation (1.1) denotes a perturbation around a constant value. This perturbation should be relatively small in linear acoustics. The assumptions are:

1. Zero quiescent velocity:

$$\boldsymbol{v}_0 = 0. \quad (1.2)$$

2. The density, pressure, temperature, enthalpy and entropy perturbations are small compared to their quiescent values:

$$|\phi/\phi_0| \ll 1. \quad (1.3)$$

The exception is the velocity, which should be smaller than the speed of sound  $c_0$ :

$$|\mathbf{v}/c_0| \ll 1. \quad (1.4)$$

These assumptions are used in all models in this thesis. Applications in which non-linear effects are important require more general models.

### 1.2.3 Isentropic acoustics

Isentropic acoustics is conveniently introduced by two partial differential equations: the momentum equation (mass effects) and the continuity equation (stiffness effects):

$$i\omega\rho_0\mathbf{v} = -\nabla p \quad (\text{momentum}), \quad (1.5)$$

$$\rho_0\nabla\cdot\mathbf{v} = -i\omega\rho \quad (\text{continuity}), \quad (1.6)$$

where  $\mathbf{v}$ ,  $p$  and  $\rho$  denote the velocity, pressure and density perturbations,  $i$ ,  $\omega$  and  $\rho_0$  are imaginary unit, angular frequency and quiescent density, and the operators  $\nabla$  and  $\nabla\cdot$  are the gradient and the divergence. These equations are the *balance laws* of momentum and mass respectively. In addition to these, the *constitutive equations* are needed to relate the pressure to the density and to the temperature

$$\rho = \frac{p}{c_0^2}, \quad (1.7)$$

$$T = \frac{p}{\rho_0 C_p}, \quad (1.8)$$

for an isentropic ideal gas. Thus the relation between the temperature and the pressure is algebraic in isentropic acoustics. By contrast, a PDE is needed to describe this relation in viscothermal acoustics.

The momentum equation (1.5), continuity equation (1.6) and acoustic equation of state (1.7) can be combined, resulting in the acoustic Helmholtz equation

$$\Delta p + k_0^2 p = 0. \quad (1.9)$$

The symbol  $p$  denotes the complex valued amplitude of the pressure perturbation,  $\Delta$  is the Laplace operator and  $k_0$  is the (frequency dependent) acoustic wave number

$$k_0 \equiv \omega/c_0, \quad Z_0 \equiv \rho_0 c_0. \quad (1.10)$$

The characteristic impedance  $Z_0$  is another important acoustic parameter, which describes the ratio of the pressure over the velocity in the propagation direction for a plane wave. This can be easily verified in 1-D by using the momentum equation (1.5) and the plane wave solution  $p = e^{-ik_0x}$ .

The Helmholtz equation (1.9) can be solved if proper boundary conditions are prescribed; one at each boundary location. The possible boundary conditions are pressure, normal velocity and impedance (the ratio pressure/normal velocity). The 1-D Helmholtz equation can be solved analytically by scaling the rightward traveling wave  $e^{-ik_0x}$  and leftward traveling wave  $e^{ik_0x}$  to the boundary conditions. If convenient, the solutions  $\sin(k_0x)$  and  $\cos(k_0x)$  can be used instead of the exponentials to find a linear combination that satisfies the boundary conditions. Analytic solutions in 2-D and 3-D are only available for a few simple geometries with simple boundary conditions. All solutions of equation (1.9) describe lossless wave propagation. Although the boundary conditions can absorb and generate energy.

The isentropic acoustic momentum and continuity equations can be expressed with the wave number and the characteristic impedance as

$$\mathbf{v} = \frac{-\nabla p}{ik_0 Z_0} \quad (\text{momentum}), \quad (1.11)$$

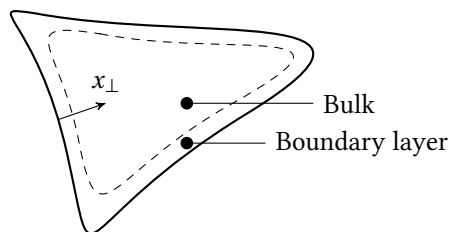
$$\nabla \cdot \mathbf{v} = \frac{-ik_0}{Z_0} p \quad (\text{continuity}). \quad (1.12)$$

The equations are presented in this form, because similar equations appear in the viscothermal acoustic models presented in Chapter 3. Unlike in isentropic acoustics, those models have a complex valued wave number and characteristic impedance.

#### 1.2.4 Viscous and thermal effects

The main concepts of viscothermal acoustics are introduced here. Viscothermal acoustics is more general than isentropic acoustics: it is more accurate especially for small geometries.

The acoustic domain can be divided into a boundary layer region and a bulk as shown in figure 1.2. The acoustics in the bulk can be accurately described as isentropic. In the boundary layer, however, the viscothermal effects are important and viscothermal acoustic models are needed to describe them. In problems with large geometries, the boundary layer effects can be neglected because the boundary layer regions are very small compared to the bulk, and the boundary layers do not change the pressure and pressure gradient much locally. By contrast, in problems with small geometries in which the boundary layers occupy a substantial part of the acoustic domain, the acoustic models typically need to account for the viscothermal effects to accurately describe the wave propagation.



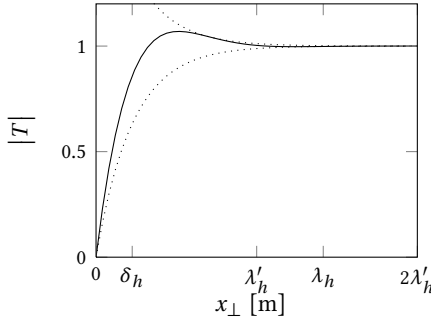
**Figure 1.2:** A geometry can be divided into two regions: the bulk and the boundary layer. The isentropic acoustic assumptions are accurate in the bulk, while viscothermal effects dominate in the boundary layer.

### Description of the viscous and thermal effects

The viscous effect is related to the viscosity of the acoustic medium (air). Viscosity resists velocity gradients by creating opposing forces. Imagine an acoustic shear velocity perturbation near a fixed wall, just in the bulk, which is described by equation (1.5). If the velocity of the air that is in contact with the wall is assumed to be zero, then the velocity varies from zero to the bulk value across the thin boundary layer. This results in high velocity gradients and proportionally high viscous forces. This viscous effect can be modeled by adding the appropriate terms to the momentum equation (1.5). These terms are not needed in the bulk, because there the velocity gradients and the resulting viscous forces are typically much smaller and can be neglected.

The thermal effect is related to the heat conductivity of air, which is proportional to the temperature gradient. It can be explained with a similar thought experiment. Now imagine an acoustic pressure perturbation near a wall, just inside the bulk. The isentropic acoustic model is accurate in the bulk and therefore the pressure perturbation causes a proportional temperature perturbation as equation (1.8) describes. Assume that the nearby wall and the air that is in contact with it remain at a constant temperature. Now the temperature *perturbation* varies across the thin boundary layer from zero to the bulk value. This large temperature gradient results in a harmonic heat flux to and from the wall. The thermal effect can be modeled by replacing equations (1.8) and (1.7) by alternatives that do account for heat conduction in the boundary layer. Heat flow is negligible in the bulk (away from walls), because the temperature gradients and the proportional heat flow are much smaller: regions of high and low pressure and temperature are typically half a wavelength apart.

The viscous forces and heat conduction are, in thermodynamic terminology, irreversible processes that damp the acoustic waves. This does not change the local pressure field much, the pressure and pressure gradients



$x_{\perp}$	Envelope of $ T $
$\delta_h$	$1 \pm e^{-1} = 1 \pm 0.368$
$\lambda'_h$	$1 \pm e^{-\sqrt{2}\pi} = 1 \pm 0.012$
$\lambda_h$	$1 \pm e^{-2\pi} = 1 \pm 0.002$

**Figure 1.3:** The boundary layer shape (—) and its envelope function (.....). The table shows the values of the envelope centered around unity for several distances from the boundary at  $x_{\perp} = 0$ . The envelope has values of approximately 1% of the jump at  $\lambda'_h$ , and 2‰ of the jump at  $\lambda_h$ .

remain smooth across the boundary layer despite the viscous and thermal effects, but the small local effects cumulate. In most cases, the viscous effects cause more damping than the thermal effects. This does not imply that the thermal effects are insignificant. Both contribute to the acoustic damping and do so at different locations: viscosity at locations with large shear velocity amplitudes near fixed walls and heat conduction at locations with large pressure amplitudes near isothermal walls.

### Boundary layer profiles

If a uniform pressure perturbation is present in the geometry of figure 1.2, then thermal boundary layers form along the isothermal walls as just described. The temperature distribution or ‘profile’ along the given coordinate  $x_{\perp}$  is plotted in figure 1.3. The distances  $\delta_h$ ,  $\lambda'_h$  and  $\lambda_h$  in the graph are different interpretations of the boundary layer thickness that are discussed later. Notice that the temperature does not increase monotonically from the wall to the bulk, but has a small ‘overshoot’ near  $\lambda'_h/2$ . In fact, the profile is a heavily damped sine around the bulk value (unity here) that oscillates within the exponential envelope function that is shown with dotted lines in the figure. The table in the figure lists the amplitude of the envelope at the marked locations.

The shear velocity profile (that occurs near no-slip walls with a non-zero velocity in the bulk) has an identical shape as the temperature profile in figure 1.3. The viscous and thermal profiles change if the boundary has a curvature, or if the geometry is so narrow that the bulk between two boundaries disappears. The thicknesses of the thermal and viscous boundary layers are not equal, but of the same order of magnitude and much smaller than the acoustic wavelength, as is shown next.

### Three wave numbers and length scales

Amongst other authors, Mechel [52] describes the Kirchhoff's viscothermal acoustic equations as a 'three wave theory': interaction of a viscous wave, a thermal wave and an acoustic wave.<sup>1</sup> This label may be confusing at first sight: while (isentropic) acoustics is clearly a wave and is described by the *wave equation* in time dependent models, the viscous and thermal effects certainly do not resemble a wave. In fact, these effects can be described by the *diffusion equation* in time dependent models. Still, the three wave paradigm is insightful, since both the wave equation and the diffusion equation simplify to the Helmholtz equation in time harmonic form. Therefore, they can be treated alike: isentropic acoustics is an undamped wave and the viscous and thermal effects are heavily damped waves. Moreover, the viscothermal effects add damping to the acoustic wave. In the limit of extremely narrow waveguides this damping is so profound that the acoustic wave equation becomes a diffusion equation itself. With that in mind it does not seem useful to discriminate between slightly damped and heavily damped waves, or between acoustics and viscous or thermal waves.

Each of the three waves has its own wave number and length scale. The acoustic  $k_0$ , viscous  $k_v$  and thermal  $k_h$  wave numbers are defined as

$$k_0 \equiv \omega/c_0, \quad k_v^2 \equiv -i\omega\rho_0/\mu, \quad k_h^2 \equiv -i\omega\rho_0 C_p/\kappa, \quad (1.13)$$

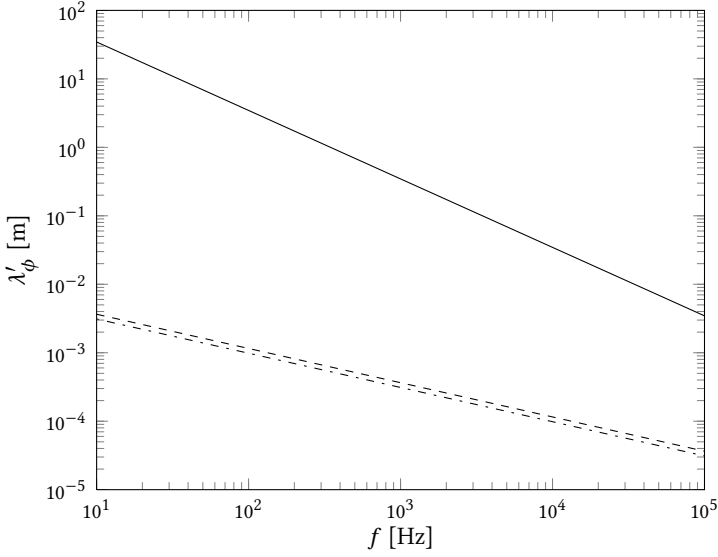
with  $\omega$ ,  $c_0$ ,  $\rho_0$ ,  $\mu$ ,  $C_p$ ,  $\kappa$  and  $i$  the angular frequency, speed of sound, quiescent density, dynamic viscosity, specific heat at constant pressure, heat conduction coefficient and imaginary unit respectively. The subscripts  $v$  and  $h$  are used to refer to 'viscous' and 'thermal' throughout this thesis. Notice that the squared viscous and thermal wave numbers are imaginary as is typical for the time harmonic form of the diffusion equation.<sup>2</sup> The wave number  $k_0$  characterizes the *isentropic acoustic wave*, which can be very different than the *viscothermal acoustic wave* if viscothermal effects are dominant. In some cases it is possible to define a (complex valued) viscothermal acoustic wave number; see chapter 3.

The three wave numbers represent three length scales. The length scale of the isentropic acoustic wave is defined as the wavelength  $\lambda_0$ , but there are several ways to define the length scale of the viscous and thermal waves. Similar definitions hold for both, therefore only the thermal wave is used as an example here. Three considered definitions are shown in figure 1.3:  $\delta_h$ ,  $\lambda'_h$  and  $\lambda_h$ . The symbol  $\lambda_h$  denotes the thermal wavelength which is the period of the damped sine: the thermal profile and its lower envelope

<sup>1</sup>The reference proposes a method to decouple the temperature wave.

<sup>2</sup>The viscous and thermal wave numbers themselves are complex valued, because  $\sqrt{-i} = (1-i)/\sqrt{2}$ .





**Figure 1.4:** The acoustic wavelength  $\lambda_0$  (—) and viscous and thermal boundary layer thicknesses  $\lambda'_v$  (· · ·) and  $\lambda'_h$  (- - -) versus the frequency, for air at typical conditions. The boundary layers are much thinner than the wavelength for all shown frequencies.

touch at  $x_\perp = 0$  and  $x_\perp = \lambda_h$ . Another definition for the thermal (and viscous) length scale is the the boundary layer thickness  $\delta_h$  as most commonly defined in the literature (conforming to [53, 58]). At this distance from the boundary, the magnitude of the temperature envelope is  $1 \pm e^{-1}$  times the bulk value. Although any definition of the boundary layer thickness is arbitrary,  $\delta_h$  seems too small for the boundary layer thickness and  $\lambda_h$  too large; see figure 1.3. An intermediate definition of the boundary layer thickness is used in this thesis denoted as  $\lambda'_h$ . At this value, the temperature perturbation magnitude is within 1% of the value of the bulk. The three different length scales are defined as

$$\delta_\phi \equiv \frac{-1}{\Im(k_\phi)}, \quad \lambda_\phi \equiv \frac{2\pi}{\Re(k_\phi)}, \quad \lambda'_\phi \equiv \frac{2\pi}{|k_\phi|}, \quad (1.14)$$

where  $\phi$  is either  $0$ ,  $v$  or  $h$ , and the operator  $\Im$  takes the imaginary part of its argument. Notice that  $\lambda'_0 = \lambda_0$ , because the isentropic acoustic wave number  $k_0$  is real valued. In short, each of the three waves has a wave number and a wavelength. The wavelengths of the viscous and thermal waves are related to their boundary layer thicknesses.

Figure 1.4 compares the length scales  $\lambda'_\phi$  of the viscous, thermal and acoustic waves for a large frequency range ( $f = \omega/(2\pi)$ ). Typical values

for air are used for the figure. Clearly, the viscous and thermal boundary layers have mutually comparable thicknesses that are much smaller than the acoustic wavelength at any plotted frequency. The ratio of the squared viscous and thermal wave number is known as the Prandtl number  $N_{Pr}$ :

$$\frac{k_h^2}{k_v^2} = N_{Pr} \equiv \frac{\mu C_p}{\kappa}, \quad (1.15)$$

which equals approximately 0.7 for air. Therefore, the thermal boundary layer is a factor  $1/\sqrt{0.7} \approx 1.2$  thicker than the viscous boundary layer; see figure 1.4.

Chapter 3 elaborates on the three-wave concept of viscothermal acoustics and presents an approximating framework that covers several efficient viscothermal acoustic models.

### 1.2.5 Summary

The following viscothermal acoustic concepts have been introduced:

- The time harmonic form of a linear PDE does not have time as an explicit variable, but uses complex perturbation amplitudes (phasors).
- Linear acoustic assumptions must be made to derive the acoustic and viscothermal equations from the non-linear Navier-Stokes equations.
- The momentum and continuity equations of isentropic (lossless) acoustics depend on two parameters: the wave number and the characteristic impedance. Some viscothermal acoustic models have complex valued equivalents of these parameters.
- The density and temperature are algebraically related to the pressure in isentropic acoustics, but not in viscothermal acoustics.
- A domain can be divided in a viscothermal boundary layer region and the isentropic bulk. Viscothermal effects are important in small domains for which the boundary layer thickness is significant.
- The viscous effect is viscous shear near no-slip walls and scales with the velocity amplitude.
- The thermal effect is heat conduction near isothermal walls and scales with the pressure amplitude.
- Viscous effects are often more important than thermal effects, although the thermal boundary layer is thicker. This does not mean that thermal effects can be neglected.
- Viscothermal acoustics is a coupled ‘three wave theory’ with an acoustic, a viscous and a thermal wave. Three wave numbers  $k_\phi$  and three corresponding length scales  $k'_\phi$  can be defined.
- Viscous and thermal boundary layers are much thinner than the wavelength in air at audible frequencies.



**Figure 1.5:** The finite element method, from PDE to FEM matrix equations.

## 1.3 Introduction to finite element modeling

The finite element method (FEM) is perhaps the most widely used method to numerically solve partial differential equations (PDEs). The method can solve PDEs for complicated geometries with unstructured grids. This makes it a very versatile tool for many problems. The literature on the finite element method is vast and an introduction to FEM may start in many different ways. The approach taken here is just one that briefly introduces the main concepts. However, many important parts of the theory are not mentioned and the reader is referred to an introductory book on the subject for these parts.

This introduction uses the Helmholtz equation as an example, because this equation appears several times in this thesis. A boundary value problem for this equation is

$$\Delta\phi + k^2\phi = f \quad \text{on } \Omega, \quad (1.16a)$$

$$\phi = g \quad \text{on } \partial\Omega_g, \quad (1.16b)$$

$$(\nabla\phi) \cdot \mathbf{n} = h \quad \text{on } \partial\Omega_h, \quad (1.16c)$$

where  $\Delta$  is the Laplace operator,  $\phi$  is the (complex valued) scalar field that is solved for,  $\Omega$  is the domain or geometry of the problem and  $k$  is the wave number which may be complex valued. The symbols  $f$ ,  $g$  and  $h$  contain the body sources/forces and the values prescribed at the locations  $\partial\Omega_g$  and  $\partial\Omega_h$  of the boundary. In this case, the subscript  $h$  in  $\partial\Omega_h$  does not refer to the thermal wave. On each location of the boundary  $\partial\Omega$  one of the two boundary conditions is prescribed, or  $\partial\Omega = \partial\Omega_g \cup \partial\Omega_h$ .

The finite element approximation of the above problem is obtained in three steps as shown in figure 1.5, which is inspired by the introduction in Hughes [31]. These steps are explained one by one.

### 1.3.1 From PDE to weak form

The weak form can be obtained from the PDE in two steps. First the PDE (1.16a) is multiplied by a weighing function and integrated over the domain:

$$\int_{\Omega} \phi_w [\Delta\phi + k^2\phi] \, d\Omega = \int_{\Omega} \phi_w f \, d\Omega, \quad (1.17)$$

where  $\phi_w$  is the weighing function (also called test function in the literature). The above equation is equivalent to the PDE if the equality holds for *all* weighing functions (that are integrable over  $\Omega$ ).

The second step in the derivation is to reduce the highest order of the derivatives as much as possible. This can be done with Green's theorem (also called Green's first identity), which is a combination of Gauss' divergence theorem and the divergence product rule:

$$\nabla \cdot (\alpha \boldsymbol{\beta}) = (\nabla \alpha) \cdot \boldsymbol{\beta} + \alpha (\nabla \cdot \boldsymbol{\beta}) \quad (\text{product rule}), \quad (1.18)$$

$$\int_{\Omega} \nabla \cdot (\alpha \boldsymbol{\beta}) \, d\Omega = \int_{\partial\Omega} (\alpha \boldsymbol{\beta}) \cdot \mathbf{n} \, d\partial\Omega \quad (\text{Gauss' theorem}), \quad (1.19)$$

$$\int_{\Omega} \alpha \nabla \cdot \boldsymbol{\beta} \, d\Omega = - \int_{\Omega} (\nabla \alpha) \cdot \boldsymbol{\beta} \, d\Omega + \int_{\partial\Omega} \alpha \boldsymbol{\beta} \cdot \mathbf{n} \, d\partial\Omega \quad (\text{Green's theorem}), \quad (1.20)$$

with  $\alpha$  a scalar field and  $\boldsymbol{\beta}$  a vector field. Green's theorem can be applied with  $\alpha = \phi_w$  and  $\boldsymbol{\beta} = \nabla \phi$  to the term that contains the Laplacian ( $\phi_w \Delta \phi = \alpha \nabla \cdot \boldsymbol{\beta}$ ). After application of Green's theorem, the weak form reads:

$$\int_{\Omega} [ -(\nabla \phi_w) \cdot (\nabla \phi) + k^2 \phi_w \phi ] \, d\Omega = \int_{\Omega} \phi_w f \, d\Omega - \int_{\partial\Omega} \phi_w (\nabla \phi) \cdot \mathbf{n} \, d\partial\Omega. \quad (1.21)$$

The weak form contains only first order spatial derivatives, both of the field that we want to solve and of the weighing functions. Therefore both  $\phi$  and  $\phi_w$  are required to have derivatives that are square integrable. These functions are typically continuous, but can have discontinuous spatial derivatives: these functions are  $\mathcal{C}^0$  continuous. The requirement for the solution of the original PDE (1.16a) is stronger: because it contains second order derivatives, the solution should be  $\mathcal{C}^1$  continuous. This explains the the name 'weak form'.

### 1.3.2 Discretization of the weak form

The solution, the boundary conditions and the weighing functions are approximated by a linear combination of a finite number of basis functions. This approximation reads

$$\phi \approx \phi^d + g^d, \quad (1.22a)$$

$$\phi_w \Rightarrow \phi_w^d, \quad (1.22b)$$

with  $g^d$  an approximation of the essential boundary conditions (1.16b),  $\phi_w^d$  a finite number of weighing functions and  $\phi^d$  an approximation of  $\phi - g^d$ ;  $\phi^d = 0$  on  $\partial\Omega_g$ . All finite dimensional approximations are indicated by the

superscript  $d$ . Moreover, the solution  $\phi^d$  uses the basis that is identical to the weighing functions  $\phi_w^d$ , as will be expressed later.

Substitution of the above weak approximations (1.22) into the weak form (1.21) yields

$$\int_{\Omega} \left[ -(\nabla \phi_w^d) \cdot (\nabla \phi^d) + k^2 \phi_w^d \phi^d \right] d\Omega = \int_{\Omega} \phi_w^d f d\Omega - \int_{\partial\Omega_h} \phi_w^d h d\partial\Omega - \int_{\Omega} \left[ -(\nabla \phi_w^d) \cdot (\nabla g^d) + k^2 \phi_w^d g^d \right] d\Omega. \quad (1.23)$$

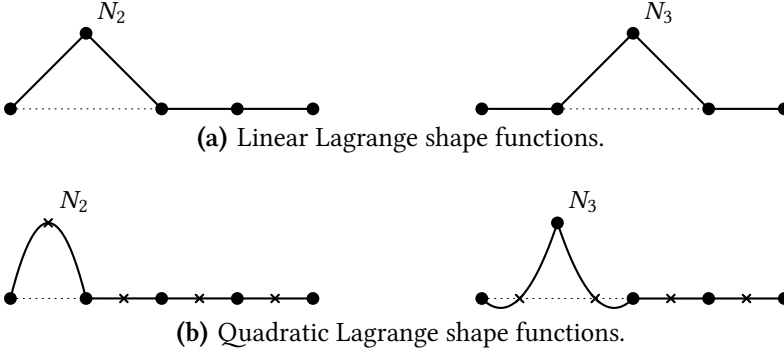
The boundary condition (1.16c) is substituted into the right-hand side boundary integral term. The region of integration of the boundary integral is changed to  $\partial\Omega_h$ , because there is no contribution at  $\partial\Omega_g$  where  $\phi_w^d = 0$ . Boundary conditions like these, which are included in the weak form itself, are called *natural boundary conditions*. By contrast, the boundary condition (1.16b) is enforced directly with the shape functions  $\phi^d$  and  $g^d$ . Notice that the left-hand side is similar to the integral that includes  $g^d$ . Such boundary conditions are called *essential boundary conditions*.

The right-hand side of the weak form (1.23) contains only known quantities, while in the left-hand side the solution  $\phi^d$  is unknown. This equation can be written as a matrix vector equation as is shown next.

### 1.3.3 From discrete weak form to matrix equation

The matrix equation that represents the weak form (1.23) depends on the choice of the basis of shape functions  $N_i$ . This basis is used to approximate the essential boundary conditions and the solution. The weighing functions are the basis functions themselves as presented soon. The finite element method uses a special shape function basis that is ‘nearly orthogonal’ to make the matrix sparse. The most widely used shape functions are the so-called Lagrangian shape functions; see figure 1.6 for linear and quadratic 1-D examples. Notice that for a given location of the nodes, the functions are completely defined by the order of the polynomial in the element and the requirement to be unity at a single node and zero at all other nodes. The same rules apply to higher dimensional Lagrangian shape functions.

It is convenient to renumber the shape functions to form two groups: one group contains only shape functions that are zero everywhere on the boundary with essential boundary conditions and one group with the remaining shape functions that are unity somewhere on this boundary. The first group has indices  $[1, 2, \dots, n]$  and the second group  $[n + 1, n + 2, \dots, m]$ . The approximations of the essential boundary conditions  $g^d$  and the solution



**Figure 1.6:** Lagrangian shape functions for a 1-D domain, with (●) element edge nodes and (×) internal nodes. All shape functions equal unity at one node and zero at all other nodes. Furthermore, they are smooth within the element, but have discontinuous derivatives at the element edges.

$\phi^d$ , and the shape functions  $\phi_w^d$  now read

$$g^d = \sum_{k=n+1}^m N_k g_k, \quad (1.24a)$$

$$\phi^d = \sum_{j=1}^n N_j \phi_j, \quad (1.24b)$$

$$\phi_w^d = N_i \quad \text{for } i = 1, 2, \dots, n. \quad (1.24c)$$

Different indices  $i, j, k$  are used to indicate to which approximation the shape belongs. The factors  $g_k$  are known beforehand and the goal is to find the scalars  $\phi_j$ , which define the FEM solution. Notice that the weighing functions are identical to the shape functions for the approximation of the unknown part of the solution  $\phi^d$ . This is known as the *Galerkin* method. More general finite element methods may use a different interpolation for the weighing functions.

Substitution of the approximation (1.24) into the weak form (1.23) results in the matrix equation

$$[\mathbf{K}] \vec{\phi} = \vec{f}. \quad (1.25)$$

The system matrix  $\mathbf{K}$  has the entries  $K_{ij}$  that are defined as

$$K_{ij} = \int_{\Omega} [ -(\nabla N_i) \cdot (\nabla N_j) + k^2 N_i N_j ] d\Omega. \quad (1.26)$$

Since the shape functions are zero in most elements, most entries of the matrix are zero:  $\mathbf{K}$  is sparse. The vector  $\vec{\phi}$  contains the unknown DOFs  $\phi_j$

of equation (1.24b). Thus the scalar field  $\phi^d$  is represented by a vector. The arrow over the variable indicates this construction. The system vector  $\vec{f}$  contains all knowns: body forces  $f$ , essential boundary conditions  $g$  (by means of  $g_j$ ) and natural boundary conditions  $h$ . Its entries are defined as

$$f_i = \int_{\Omega} N_i f \, d\Omega - \int_{\partial\Omega_h} N_i h \, d\partial\Omega - \sum_{k=n+1}^m g_k \int_{\Omega} [ -(\nabla N_i) \cdot (\nabla N_k) + k^2 N_i N_k ] \, d\Omega. \quad (1.27)$$

The above terms are usually calculated by integrating per element and then summing the contributions of all elements to get the integral over the complete domain. This integration can be a numerical approximation. Gaussian quadrature of an order that does not limit the order of convergence of the FEM method is typically used.

The solution is calculated by solving equation (1.25) to get  $\vec{\phi}$ . Solving requires a factorization of the system matrix  $\mathbf{K}$ . The computational time for this factorization depends on the number of DOFs and on the sparsity of the matrix. Therefore, 3-D problems are more costly to solve than 2-D problems, even if the total number of DOFs is equal. Furthermore, factorization of two systems with  $n$  DOFs is less costly than factorization of a single system with  $2n$  coupled DOFs.

### 1.3.4 Structural finite elements and fluid structure interaction

The viscothermal acoustic finite elements presented in this thesis can be coupled to structural finite elements. The general concept of fluid structure interaction modeling with finite elements is described here. The details that depend on the specific acoustic models are discussed in later chapters.

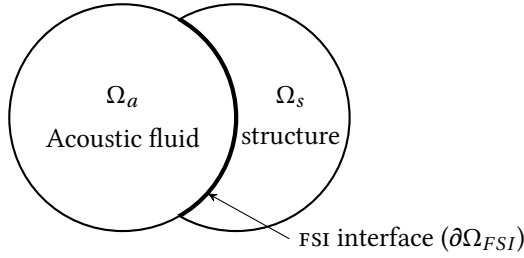
#### Structural finite elements

In the structural finite element literature, the distinction between a mass matrix  $\mathbf{M}_s$  and a stiffness matrix  $\mathbf{K}_s$  is often made, which is convenient in time dependent problems of the form

$$\frac{\partial^2}{\partial t^2} [\mathbf{M}_s] \vec{\mathbf{u}} + [\mathbf{K}_s] \vec{\mathbf{u}} = \vec{\mathbf{f}}_s, \quad (1.28)$$

where  $\vec{\mathbf{u}}$  denotes the time dependent displacement.

Since this thesis describes acoustics in time harmonic form, it is sensible to use a time harmonic structural formulation as well. This formulation can be obtained if the structure elements represent linear PDES, by replacing the differentiation to time with a multiplication by  $i\omega$ , and the time dependent



**Figure 1.7:** Fluid structure interaction, schematically. The acoustic fluid domain  $\Omega_a$  and the structure domain  $\Omega_s$  interact on the FSI interface. The structure domain can be a thin membrane, for example, but is shown as a solid here for clarity.

displacement  $\check{\mathbf{u}}$  with the complex valued phasor  $\mathbf{u}$ , and likewise for  $\check{\mathbf{f}}_s \rightarrow \mathbf{f}_s$ . The displacement  $\mathbf{u}$  and velocity  $\dot{\mathbf{u}}$  formulations now read

$$[\mathbf{K}_s - \omega^2 \mathbf{M}_s] \check{\mathbf{u}} = \check{\mathbf{f}}_s \quad (\text{displacement}), \quad (1.29)$$

$$[\mathbf{K}_s - \omega^2 \mathbf{M}_s] \check{\dot{\mathbf{u}}} = i\omega \check{\mathbf{f}}_s \quad (\text{velocity}). \quad (1.30)$$

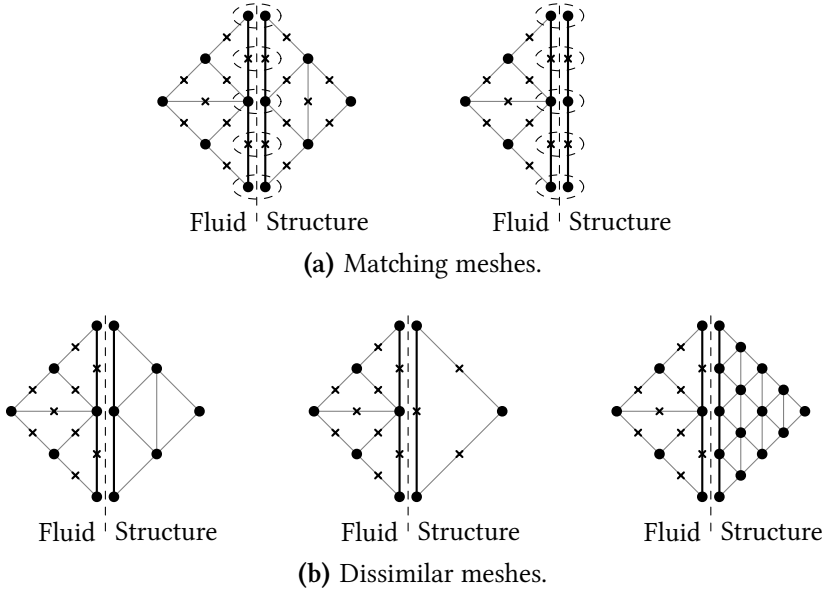
As usual, the system vector  $\check{\mathbf{f}}_s$  contains the known data: natural boundary conditions, essential boundary conditions and loads that are applied to the interior.

### Fluid structure interaction

The term fluid structure interaction (FSI) is descriptive: the fluid (air) and the structure influence each other. The interaction takes place at a surface that is shared by the two domains, see figure 1.7. The modeling starts with the weak forms of both the structure and the fluid. Next, the velocity of the fluid at  $\partial\Omega_{\text{FSI}}$  is prescribed as a function of the unknown structure DOFs. In the other direction, the load on the structure at  $\partial\Omega_{\text{FSI}}$  is prescribed as a function of the unknown fluid DOFs. Finally, the step from weak form to matrix equations can be followed, as presented in the beginning of this section. In general, the heat conduction in the structure can be coupled to the thermal effects in the air. However, this *thermal coupling* is typically neglected by assuming isothermal walls; see [12].

If an *essential* boundary condition is used in the coupling, a distinction between matching meshes and dissimilar meshes needs to be made; see figure 1.8. In matching meshes, the fluid and the structure have shape functions that are identical on the FSI interface. Therefore, the essential coupling boundary condition defines a one-to-one coupling between the fluid and the structure DOFs. In dissimilar meshes, a one-to-one coupling does





**Figure 1.8:** Matching meshes have identical shape functions on the FSI interface for the fluid and the structure. Therefore, matching meshes have one-to-one matching of the DOFs, which is an advantage in fluid structure interaction if it uses essential boundary conditions. Dissimilar meshes require a re-interpolation in that case.

not exist and a re-interpolation between the two domains is necessary. This thesis does not cover this topic. The distinction in matching and dissimilar meshes is only needed for essential boundary conditions, not if natural boundary conditions or body forces are prescribed. In those cases, the numerical integration in the assembly of the system matrix by default takes care of matching the prescribed data to the element to which it is prescribed, also if it depends on the DOFs of another domain.

Prescribed data usually appear in the system vector. However, the prescribed data are a function of the degrees of freedom of the other domain in the case of FSI. It can involve either an essential boundary condition, or a natural boundary condition or a body source. In any case, it contributes to the system matrix, because of the dependency on the degrees of freedom. The complete system matrix can be written as

$$\begin{bmatrix} \mathbf{S}_a & \mathbf{F}_{s \rightarrow a} \\ \mathbf{F}_{a \rightarrow s} & \mathbf{S}_s \end{bmatrix} \begin{Bmatrix} \vec{\phi} \\ \vec{u} \end{Bmatrix} = \begin{Bmatrix} \vec{f}_a \\ \vec{f}_s \end{Bmatrix}. \quad (1.31)$$

where  $\vec{\phi}$  contains the fluid DOFs,  $\vec{u}$  the structure displacement DOFs,  $\mathbf{S}_a$  is the acoustic part of the system matrix,  $\mathbf{S}_s = \mathbf{K}_s - \omega^2 \mathbf{M}_s$  is the structural part

of the system matrix,  $\mathbf{F}_{s \rightarrow a}$  represents the body forces and boundary conditions on the acoustics that depend on the structure, and  $\mathbf{F}_{a \rightarrow s}$  represents the body forces and boundary conditions on the structure that depend on the acoustics. The system vector still contains the explicitly prescribed body forces and boundary conditions on the acoustics  $\mathbf{f}_a$  and on the structure  $\mathbf{f}_s$ . A similar structure results from a formulation with velocity degrees of freedom for the structure:

$$\begin{bmatrix} \mathbf{S}_a & \frac{\mathbf{F}_{s \rightarrow a}}{i\omega} \\ i\omega \mathbf{F}_{a \rightarrow s} & \mathbf{S}_s \end{bmatrix} \begin{Bmatrix} \vec{\phi} \\ \vec{u} \end{Bmatrix} = \begin{Bmatrix} \vec{f}_a \\ i\omega \vec{f}_s \end{Bmatrix}. \quad (1.32)$$

The above equation and equation (1.31) describe the same problem, but one or the other may be preferred because it is better scaled, or because it results in a symmetric total system matrix.

This thesis studies viscothermal acoustics, that is the formulation of  $\mathbf{S}_a$ ,  $\mathbf{F}_{s \rightarrow a}$  and  $\vec{f}_a$  in equation (1.31). The remaining sub matrices and vectors depend on the specific formulation of the structural elements. In section 4.3, a microphone is modeled with a membrane as the structure. There, the weak form of the membrane and the corresponding coupling terms are presented explicitly.

### 1.3.5 Notation convention

Only weak forms before discretization are given in this thesis, like in equation (1.21). This information is sufficient to define the other steps from weak form to matrix equation if the type of shape functions are mentioned. In all cases the standard order of numerical integration is used in the assembly of the system matrix, unless mentioned otherwise.

All finite element results in this thesis are obtained with the finite element software COMSOL. This program accepts user defined weak formulations and takes care of the aforementioned approximations.

### 1.3.6 Summary

The following finite element method topics have been introduced:

- A weak form of a PDE is derived by multiplication with a test function and integration over the domain.
- Green's theorem is applied to reduce the order of the derivatives.
- Natural boundary conditions are included in the weak form itself (after application of Green's theorem) and essential boundary conditions must still be prescribed explicitly.

- The weak form is discretized by using a linear combination of shape functions to approximate the solution, the essential boundary conditions and the weighing functions.
- Lagrangian shape functions are unity on a single node and zero on all other nodes. Furthermore, the functions are continuous and defined by a polynomial in the element interiors, but have derivatives that are discontinuous over the element boundaries.
- The derivation of the system matrix from the discrete weak form is explained. Gaussian quadrature is typically used to calculate the integrals.
- The sparsity of the system matrix depends on the choice of shape functions.
- Structural finite elements are often defined in a time dependent form that can be easily reduced to a time harmonic form.
- Fluid structure interaction with the weak forms of the fluid and the structure results in a matrix equation that has the structure of equation (1.31).
- Matching meshes are advantageous if essential boundary conditions are used in fluid structure interaction.
- The computational costs depend both on the number of DOFs (matrix size) and on the couplings between these DOFs (matrix sparsity).

## 1.4 Outline

Several viscothermal acoustic finite element models are presented in this thesis. The theory is divided into two chapters. The other chapters are more applied in nature. The outline is as follows.

Chapter 2 presents the ‘full linear Navier-Stokes’ (FLNS) model. This is essentially a finite element formulation of the standard viscothermal acoustic equations [53, 58] since Kirchhoff’s publication [47]. The literature presents only a few comparable FEM formulations. The advantages of the formulation presented in this thesis are presented at the end of that chapter. Although one of these advantages is that it is relatively efficient, the major drawback of the FLNS model is still its high computational cost.

Chapter 3 presents several approximate viscothermal acoustic models, which are much less costly to solve than the FLNS model. This chapter introduces an approximating ‘three wave’ framework for viscothermal acoustics. The approximation is that one-way coupling between the viscous and thermal waves at one side and the acoustic wave at the other is used: the

viscous and thermal wave influence the acoustic wave, but are not influenced by it. Two interesting existing models from the literature are shown to fit this framework. However, these two models need to satisfy additional requirements that make their applicability limited to cases that fit these requirements. The first model is called boundary layer impedance (BLI) model. It models only the bulk and accounts for the viscothermal boundary layer effects by means of a dissipative boundary condition. It is valid if the bulk region is *not* small compared to the boundary layer region. The second model is the low reduced frequency (LRF) model. It is valid for waveguides that have a constant pressure over the cross section. This model lumps the viscothermal effects over the cross section, resulting in a very efficient problem of reduced dimensionality (1-D or 2-D). Besides these existing models, a new model is presented. This new model is called sequential linear Navier-Stokes (SLNS) model. The advantage over the existing models is that it does not impose any geometric requirements. This model has an efficiency between the costly FLNS model and the efficient BLI and LRF models.

Chapter 4 validates the four viscothermal acoustic models on several small problems. The models are compared to each other, to experimentally measured results and to an analytic model. Furthermore, the chapter demonstrates the efficiency and the limits of applicability of the models. The results confirm the theory and make it more concrete. The paper [43] contains additional validation tests and is reproduced in appendix B.

Chapter 5 presents an engineering application: a hearing aid loudspeaker is modeled. It shows how the FEM models can be used in a design environment. The focus is on the modeling of the acoustics, not on the other physical domains. Only the necessary parts are modeled with FEM. Where possible, more efficient lumped models are used. The chapter shows how the large FEM calculation can be lumped and coupled to the other efficient lumped parts of the model. This approach has the advantage that the influence of the parameters in the lumped parts of the model on the response of the loudspeaker can be studied without repeating the FEM calculations.

The conclusions of the thesis and a discussion on interesting possibilities for future research are presented in chapter 6.

Another thesis on viscothermal acoustics [55] written by colleague PhD candidate M.J.J. Nijhof appears in the same period as this thesis. The development of the finite element presented in chapter 2 can be regarded as a joint effort. Furthermore, the benchmark problem of section 4.2.3 also appears in Nijhof's thesis. Although these topics overlap, the two theses primarily complement each other. Nijhof's thesis focuses on the limits of (semi-)analytical modeling, contains more mathematical backgrounds and presents complete and general forms of several viscothermal acoustic models. This thesis focuses on finite element models and their efficiency, con-

tains fluid structure interaction and aims to present models that can be readily applied in a design environment.

Some readers may be less interested in the theory behind all models, but are looking for the best viscothermal acoustic model for a specific application. These readers can start reading in section 3.5 to select a model and then revert to the section that describes it.

# The full linear Navier-Stokes model

This chapter presents the most general model of viscothermal acoustics described in this thesis. It consists of the Navier-Stokes equations that are *linearized* for small acoustic perturbations. The other models, presented in the next chapter, are approximations of this model. All models are time harmonic. The governing equations are briefly introduced in section 2.1. Section 2.2 presents a finite element formulation of the full linear Navier-Stokes model, which is referred to with the abbreviation FLNS model in this thesis.

## 2.1 Governing equations

The Navier-Stokes equations describe fluid mechanics under the continuum assumption. These equations can be linearized under the assumption of small acoustic perturbations, presented in section 1.2.2. Subsequently, the equations are simplified to the time harmonic form, introduced in section 1.2.1. The result is a complex valued, coupled set of partial differential equations in which the degrees of freedom are complex perturbation amplitudes (phasors) of the field variables. Historically, the first use of these equations for viscothermal acoustics is attributed to Kirchhoff [47] in 1868. These equations form the basis for this thesis. More thorough discussions of the Navier-Stokes equations for acoustics can be found in Pierce [58] and Morse [53].

### 2.1.1 Constitutive equations

The material model for air used in this thesis is a Newton-Fourier ideal gas. This model is accurate for air under the linear acoustic assumptions; see for example [53, 58]. Most constitutive equations are given only in time harmonic form.

## Newtonian fluid

A Newtonian fluid model is used to express the stress tensor  $\sigma$  as a function of the velocity vector field  $\mathbf{v}$  and the pressure field  $p$ :

$$\sigma = \tau - p\mathbf{I}, \quad (2.1a)$$

$$\tau = \lambda(\nabla \cdot \mathbf{v})\mathbf{I} + 2\mu\epsilon, \quad (2.1b)$$

$$\epsilon = \frac{1}{2}(\nabla\mathbf{v} + (\nabla\mathbf{v})^T), \quad (2.1c)$$

where  $\tau$  is the viscous stress tensor in [Pa],  $\mathbf{I}$  is the identity tensor,  $\epsilon$  is the symmetric part of the velocity gradient (phasor) in [ $s^{-1}$ ], and  $\mu$  and  $\lambda$  are the dynamic viscosity and the second viscosity coefficients respectively, both in [Pas].

The bulk viscosity  $\eta$  (also called volume viscosity) is directly related to the dynamic viscosity and the second viscosity by the definition

$$\eta \equiv \frac{2}{3}\mu + \lambda. \quad (2.2)$$

This bulk viscosity quantifies the resistance to the rate of compression and rarefaction of a volume. The physical phenomenon behind the bulk viscosity is that the thermodynamic equilibrium is not instantaneously reached; see [53, 58]. According to Pierce [58], the bulk viscosity  $\eta$  equals zero for monatomic gases, and for air

$$\eta = 0.60\mu. \quad (2.3)$$

The second viscosity can be negative, but the bulk viscosity and the dynamic viscosity need to be larger than zero to ensure that their effects are dissipative:

$$\mu \geq 0, \quad \eta \geq 0. \quad (2.4)$$

In general, the viscosity coefficients depend on the state (especially the temperature) of the fluid. However, they are treated as constants in this thesis, which is accurate under the linear acoustic assumptions. Discussions on the bulk viscosity can be found in [27, 44].

## Fourier's law

The heat flow vector  $\mathbf{q}$  in [ $W/m^2$ ] can be expressed as a function of the temperature gradient by Fourier's law of heat conduction:

$$\mathbf{q} = -\kappa\nabla T, \quad (2.5)$$

where  $\kappa$  is the heat conduction coefficient with unit [ $W/(Km)$ ], which is also treated as a constant under the linear acoustic assumptions.

## Ideal gas

Finally, the assumptions of an ideal gas are made. Therefore the thermal and caloric equations of state of an ideal gas are used:

$$\frac{\rho}{\rho_0} = \frac{p}{p_0} - \frac{T}{T_0}, \quad (2.6)$$

$$H = C_p T, \quad (2.7)$$

where  $H$  is the specific enthalpy in [J/kg] and  $C_p$  is the specific heat at constant pressure in [J/(kgK)]. Notice that equation (2.6) is the linearized version of the well-known ideal gas law

$$\check{p} = \check{\rho} R_0 \check{T} \quad (\text{and: } p_0 = \rho_0 R_0 T_0), \quad (2.8)$$

with  $R_0$  the specific gas constant in [J/(kgK)]. The used notation is described in section 1.2.1.

Two useful expressions for the isentropic speed of sound  $c_0$ , in [m/s], are valid under the the ideal gas assumption:

$$c_0^2 = \gamma p_0 / \rho_0, \quad c_0^2 = \gamma R_0 T_0. \quad (2.9)$$

These expressions are related to each other through the ideal gas law. The symbol  $\gamma$  denotes the (dimensionless) ratio of specific heats

$$\gamma = C_p / C_v, \quad (2.10)$$

with  $C_v$  the specific heat at constant volume in [J/(kgK)]. For a monatomic gas  $\gamma = 5/3$ , see [21]; for air  $\gamma \approx 1.4$ . The last useful ideal gas relation is

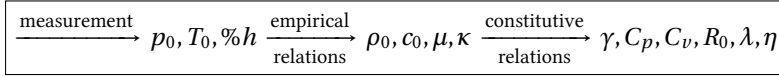
$$C_p = R_0 + C_v. \quad (2.11)$$

The above ideal gas relations are often applied throughout this thesis without explicitly referring to them. The Navier-Stokes equations can also be used in combination with constitutive equations of a liquid, instead of an ideal gas. Interested readers can find the equations for liquids in [34, 55].

## Empirical relations for air

In this section, twelve parameters of air have been introduced:  $p_0$ ,  $T_0$ ,  $\rho_0$ ,  $\mu$ ,  $\lambda$ ,  $\eta$ ,  $\kappa$ ,  $c_0$ ,  $\gamma$ ,  $R_0$ ,  $C_p$  and  $C_v$ . These parameters depend on the linearization point. For example, the viscosity depends on the temperature  $T_0$ . If a model is compared to an experiment, accurate values for each of these parameters are needed. However, it would be inconvenient to measure them all. Instead, a consistent set of coefficients can be obtained by using just three





**Figure 2.1:** Obtaining a consistent set of coefficients for Newton-Fourier ideal gases, using measurements, empirical relations and constitutive relations.

measurements (temperature, pressure and humidity) in combination with the above constitutive relations and a few additional empirical relations. Useful empirical relations can be found in Rasmussen [60] for example. His publication is aimed at air that is *not* approximated as an ideal gas, for slightly improved accuracy. Since the ideal gas assumption is used in this thesis, only a few of the results collected by Rasmussen are needed

The proposed process of obtaining a consistent set of coefficients for Newton-Fourier ideal gases is schematically shown in figure 2.1. The percentage of relative humidity  $\%h$  (only needed for the empirical relations), the quiescent pressure  $p_0$  and the quiescent temperature  $T_0$  are measured, which can be done with inexpensive equipment. Next, the empirical relations of Rasmussen [60] are used to obtain the dynamic viscosity  $\mu$ , the heat conduction coefficient  $\kappa$ , the speed of sound  $c_0$  and the density  $\rho_0$ . Last, the remaining variables can be calculated with relations for the viscosity coefficients (2.2) and (2.3), and the ideal gas relations (2.8), (2.9), (2.10) and (2.11). Using this approach, the viscothermal acoustic models for air only have three independent material parameters. Table 2.1 lists the consistent set of parameters that is used in this thesis.

### 2.1.2 Balance laws

While the constitutive equations describe the behavior of a material in mathematical form, the balance laws describe the general physical laws of conservation of mass, energy and momentum. The equations in this section are given both in the general non-linear form and in the linear time harmonic form, using the format

$$\text{general form} \quad \Rightarrow \quad \text{linear time harmonic form.}$$

Thus ‘ $\Rightarrow$ ’ implies linearization under the linear acoustic assumptions and subsequent conversion to the time harmonic form using complex valued amplitude variables (phasors).

In the general form, the material derivative or convective derivative  $\frac{D}{Dt}$  is used. This derivative is defined in an Eulerian (fixed) coordinate system

Parameter	Symbol	Value	Unit
Humidity	$\%h$	23	%
Quiescent temperature	$T_0$	294.3	K
Quiescent pressure	$p_0$	$1.015 \cdot 10^5$	Pa
Speed of sound	$c_0$	341.2	m/s
Quiescent density	$\rho_0$	1.225	kg/m <sup>3</sup>
Heat conduction	$\kappa$	$25.18 \cdot 10^{-3}$	W/(mK)
Dynamic viscosity	$\mu$	$18.29 \cdot 10^{-6}$	Pas
Bulk viscosity	$\eta$	$10.98 \cdot 10^{-6}$	Pas
Second viscosity	$\lambda$	$-1.22 \cdot 10^{-6}$	Pas
Ratio of specific heats	$\gamma$	1.406	1
Specific gas constant	$R_0$	281.4	J/(kgK)
Specific heat at constant pressure	$C_p$	975.3	J/(kgK)
Specific heat at constant volume	$C_v$	693.8	J/(kgK)

**Table 2.1:** A set of parameters that satisfies the Newton-Fourier ideal gas assumptions.

as

$$\frac{D\check{\phi}}{Dt} = \frac{\partial\check{\phi}}{\partial t} + \check{\mathbf{v}} \cdot \nabla\check{\phi} \quad \Rightarrow \quad i\omega\phi. \quad (2.12)$$

The linear approximation may be inaccurate at locations with near zero time derivative  $\partial\check{\phi}/\partial t$  or exceptionally high gradients  $\nabla\check{\phi}$ . These occur, for example, in standing wave fields and evanescent waves respectively (also in isentropic acoustics). However, these locations are usually very small compared to the total domain of interest. Therefore, Pierce [58] states that the solutions of the linear acoustic equations are not accurate near localized sources nor for propagation over large distances (accumulation of small errors). Despite these shortcomings, these simplifications are often made. It results in the isentropic acoustic wave or Helmholtz equation, which are widely used and accepted as the standard description of isentropic acoustics. Moreover, this linearization is also widely used in viscothermal acoustics. Nevertheless, phenomena that may be important in some cases are neglected; for example vortex shedding [5].

### Continuity equation

The mass balance or continuity equation states that the time rate of mass change within a volume is balanced with the nett mass flow over the boundary of that volume. In differential form, this equation reads

$$\frac{D\check{\rho}}{Dt} = -\check{\rho}\nabla \cdot \check{\mathbf{v}} \quad \Rightarrow \quad i\omega\rho = -\rho_0\nabla \cdot \mathbf{v}, \quad (2.13)$$

with  $\check{\rho}$ ,  $\rho_0$ ,  $\rho$ ,  $\check{\boldsymbol{v}}$  and  $\boldsymbol{v}$  the total density, quiescent density, density phasor, total velocity and velocity phasor respectively. The units of the density and velocity variables are  $[\text{kg}/\text{m}^3]$  and  $[\text{m}/\text{s}]$ .

### Momentum equation

The momentum equation states that the time rate of momentum change within a volume equals the nett sum of forces on the volume. In differential form, this vector equation reads

$$\check{\rho} \frac{D\check{\boldsymbol{v}}}{Dt} = \nabla \cdot \check{\boldsymbol{\sigma}} + \check{\boldsymbol{f}} \quad \Longrightarrow \quad i\omega\rho_0\boldsymbol{v} = \nabla \cdot \boldsymbol{\sigma} + \boldsymbol{f}, \quad (2.14)$$

with  $\check{\boldsymbol{\sigma}}$ ,  $\boldsymbol{\sigma}$ ,  $\check{\boldsymbol{f}}$ ,  $\boldsymbol{f}$  the total stress tensor, the stress tensor phasor, the total volumetric body force and the volumetric body force phasor. The units of the stress tensors and body forces are  $[\text{Pa}]$  and  $[\text{N}/\text{m}^3]$  respectively. Typically, the body forces equal zero. The stress tensor depends on the medium and is assumed to satisfy the constitutive equations of a Newtonian fluid, as presented in section 2.1.1.

### Entropy equation

The entropy equation relates time rate of specific entropy change within a volume to the nett sum of heat flow over the boundary and heat generation in the volume. This equation reads

$$\check{\rho}\check{T} \frac{D\check{s}}{Dt} = \check{\Phi} - \nabla \cdot \check{\boldsymbol{q}} + \check{Q} \quad \Longrightarrow \quad i\omega\rho_0 T_0 s = -\nabla \cdot \boldsymbol{q} + Q, \quad (2.15)$$

where  $\check{s}$ ,  $s$ ,  $\check{T}$ ,  $T_0$ ,  $T$ ,  $\check{\boldsymbol{q}}$ ,  $\boldsymbol{q}$ ,  $\check{Q}$  and  $Q$  are the total specific entropy, specific entropy phasor, total temperature, quiescent temperature, temperature phasor, total heat flow vector, heat flow vector phasor, total volumetric heat source and volumetric heat source phasor respectively. The units of specific entropy, temperature, heat flux and volumetric heat source are  $[\text{J}/(\text{Kkg})]$ ,  $[\text{K}]$ ,  $[\text{W}/\text{m}^2]$  and  $[\text{W}/\text{m}^3]$  respectively.

The heat flow  $\boldsymbol{q}$  is material dependent and can be described by Fourier's law as presented in section 2.1.1. The symbol  $\check{\Phi}$  denotes the viscous heating in  $[\text{W}/\text{m}^3]$  which is defined by  $\check{\Phi} = \check{\boldsymbol{\tau}}^T : \nabla \check{\boldsymbol{v}}$  in which  $\check{\boldsymbol{\tau}}$  is defined similarly as  $\boldsymbol{\tau}$  in equation (2.1b). Because  $\check{\Phi}$  is a small second order term under the linear acoustic assumptions, it can be neglected. Therefore, viscosity only enters the equations through the stress tensor in the momentum equation.

Notice that all terms in the entropy equation have the unit of rate of energy change per volume  $[\text{W}/\text{m}^3]$ . It is possible to rewrite the entropy equation to several equivalent energy equations, for example: total energy,

internal energy or entropy. The most convenient equation for the viscothermal acoustic model of an ideal gas is the enthalpy equation, because then the caloric equation of state (2.7) can be used. This enthalpy equation can be derived from the entropy equation by using the Gibbs relation presented below. The entropy equation is presented here because it demonstrates that entropy change equals zero if  $\check{\Phi}$ ,  $\check{\mathbf{q}}$  and  $\check{Q}$  equal zero. This requirement is satisfied if the heat conduction and the viscosity coefficients are zero  $\kappa = 0$ ,  $\mu = \nabla = 0$ , which conforms to the approximations of isentropic acoustics.

### Gibbs relation

Besides these conservation laws, the Gibbs relation is needed. This relation expresses the thermodynamic balance between entropy change, enthalpy change and pressure change, see for example [21]:

$$\check{\rho} \check{T} d\check{s} = \check{\rho} d\check{H} - d\check{p} \quad \Rightarrow \quad \rho_0 T_0 s = \rho_0 H - p. \quad (2.16)$$

Notice that the isentropic assumption  $s = 0$  in combination with the caloric equation of state (2.7) reduces the Gibbs relation to the isentropic equation of state (1.8).

### 2.1.3 Final set of equations

The balance laws are combined with the constitutive equations to a set in the chosen degrees of freedom, which are the velocity vector  $\mathbf{v}$ , the temperature  $T$  and the pressure  $p$ . The momentum equation, the entropy equation and the continuity equation can be written as

$$i\omega\rho_0\mathbf{v} - \nabla \cdot \boldsymbol{\sigma} = \mathbf{f}, \quad (2.17a)$$

$$i\omega\rho_0 C_p T + \nabla \cdot \mathbf{q} - i\omega p = Q, \quad (2.17b)$$

$$\nabla \cdot \mathbf{v} - i\omega \frac{T}{T_0} + i\omega \frac{p}{p_0} = 0. \quad (2.17c)$$

The divergence terms are also a function of the chosen degrees of freedom:

$$\nabla \cdot \boldsymbol{\sigma} = (\lambda + \mu)\nabla(\nabla \cdot \mathbf{v}) + \mu\Delta\mathbf{v} - \nabla p, \quad (2.18a)$$

$$\nabla \cdot \mathbf{q} = -\kappa\Delta T. \quad (2.18b)$$

This set of equations for viscothermal acoustics contains

- Momentum
  - Compressibility
  - Viscosity
  - Heat conduction
- } Acoustics
- ⇒ Viscous effects.
- ⇒ Thermal effects .

The assumptions that are made in its derivation include

- Linear acoustic assumptions; see section 1.2.2.
- Newton-Fourier ideal gas assumptions; see section 2.1.1.

Section 2.2 presents a finite element based on this set of equations. It is referred to as the full linear Navier-Stokes model, or abbreviated FLNS model.

### 2.1.4 Boundary conditions

The boundary conditions (BCs) are of great importance in viscothermal acoustics. Viscous and thermal boundary layers are *caused* by the prescribed BCs. In isentropic acoustics, only one BC for the pressure or its normal gradient (related to velocity) has to be given at each boundary location. By contrast, three additional BCs (in 3-D) need to be given in viscothermal acoustics; one thermal BC and two viscous BCs. The thermal BC is the temperature perturbation or the heat flux (proportional to the normal temperature gradient) and the two viscous BCs are the velocity or stress in the two directions tangential to the boundary (shear directions).

The *acoustic boundary conditions* for the FLNS model are

$$\mathbf{v} \cdot \mathbf{n} = g_a \quad (\text{normal velocity}), \quad (2.19a)$$

$$-(\boldsymbol{\sigma} \cdot \mathbf{n}) \cdot \mathbf{n} = h_a \quad (\text{normal stress} \approx \text{pressure}), \quad (2.19b)$$

where  $\mathbf{n}$  is the outward normal unit vector and  $g_a$  and  $h_a$  contain the prescribed values of the normal velocity and normal stress respectively. An impedance boundary condition can be prescribed as  $h_a = Z_a \mathbf{v} \cdot \mathbf{n}$ . One acoustic BC should be prescribed at each boundary location; either normal velocity, normal stress, or impedance.

The *thermal boundary conditions* of the FLNS model read

$$T = g_h \quad (\text{temperature}), \quad (2.20a)$$

$$\mathbf{q} \cdot \mathbf{n} = h_h \quad (\text{heat flux}), \quad (2.20b)$$

where,  $g_h$  and  $h_h$  contain the prescribed BC values. At each boundary location either the temperature or the heat flux should be prescribed.

Last, the *viscous boundary conditions* in the FLNS model can be prescribed as

$$\mathbf{v} \cdot \mathbf{t} = g_v \quad (\text{shear velocity}), \quad (2.21a)$$

$$-(\boldsymbol{\sigma} \cdot \mathbf{n}) \cdot \mathbf{t} = h_v \quad (\text{shear force}). \quad (2.21b)$$

Like above,  $g_v$  and  $h_v$  contain the prescribed BC values. In 3-D, there are two tangential directions, two tangential unit vectors  $\mathbf{t}$  and two viscous boundary conditions. At each boundary location one of the above BCs should be prescribed for each tangential direction.

Name	Symbol	Acoustic BC	Viscous BC	Thermal BC
Wall	$\partial\Omega_W$	$\mathbf{v} \cdot \mathbf{n} = 0$	$\mathbf{v} \cdot \mathbf{t} = 0$	$T = 0$
Unit velocity	$\partial\Omega_V$	$\mathbf{v} \cdot \mathbf{n} = 1$	$\mathbf{v} \cdot \mathbf{t} = 0$	$T = 0$
Symmetry	$\partial\Omega_S$	$\mathbf{v} \cdot \mathbf{n} = 0$	$(\boldsymbol{\sigma} \cdot \mathbf{n}) \cdot \mathbf{t} = 0$	$\mathbf{q} \cdot \mathbf{n} = 0$
Pressure release	$\partial\Omega_{P_0}$	$(\boldsymbol{\sigma} \cdot \mathbf{n}) \cdot \mathbf{n} = 0$	$(\boldsymbol{\sigma} \cdot \mathbf{n}) \cdot \mathbf{t} = 0$	$\mathbf{q} \cdot \mathbf{n} = 0$
Unit pressure	$\partial\Omega_P$	$(\boldsymbol{\sigma} \cdot \mathbf{n}) \cdot \mathbf{n} = 1$	$(\boldsymbol{\sigma} \cdot \mathbf{n}) \cdot \mathbf{t} = 0$	$\mathbf{q} \cdot \mathbf{n} = 0$

**Table 2.2:** A few standard boundary conditions. The viscous and thermal parts of these boundary conditions are all homogeneous.

Typically, homogeneous viscothermal boundary conditions  $\mathbf{v} \cdot \mathbf{t} = 0$  and  $T = 0$  are used at walls. However, in slightly rarefied gases, viscothermal impedance-like boundary conditions are more accurate; see Rathnam [61, 62]. These can be applied, like the acoustic impedance BC, as  $h_h = Z_h T$  and  $h_v = Z_v \mathbf{v} \cdot \mathbf{t}$ .

Viscous boundary layers are absent if  $(\boldsymbol{\sigma} \cdot \mathbf{n}) \cdot \mathbf{t} = 0$  and likewise, thermal boundary layers are absent if  $\mathbf{q} \cdot \mathbf{n} = 0$ . Solutions of problems with only these viscous and thermal boundary conditions are similar to the isentropic acoustic solutions.

It is convenient to specify a few standard boundary condition combinations that can be quickly referred to. For example, a *wall* can be defined as an isothermal zero velocity boundary. The most common boundary conditions are listed in table 2.2. Notice that the viscous and thermal boundary conditions are all homogeneous in the table. Non-homogeneous viscous or thermal boundary conditions are used in only few applications.

## 2.2 Finite element formulation

The set of PDES (2.17) is used to create a mixed finite element. The weak form and discretization are presented below. This particular finite element formulation results in a complex symmetric (not Hermitian) FEM system matrix. The element is implemented in the finite element software COMSOL [15], which contains solvers that benefit from the complex symmetry of the FEM matrix.

The distinction between essential boundary conditions and natural boundary conditions is important in FEM, as introduced in section 1.3. The boundary data  $g_a$ ,  $g_h$  and  $g_v$  in the equations above are prescribed as essential BCs;  $h_a$ ,  $h_h$  and  $h_v$  appear as natural BCs in the weak form derived next.

### 2.2.1 Weak form

The weak form of the set of equations (2.17) can be obtained by using the Galerkin approach. The equations in this set are multiplied by the weighing functions  $\mathbf{v}_w$ ,  $T_w$  and  $p_w$  respectively, and integrated over the domain  $\Omega$ . The entropy equation is divided by the quiescent temperature  $T_0$  to make the system complex symmetric. As usual in FEM, the second order derivatives (in the terms  $\nabla \cdot \boldsymbol{\sigma}$  and  $\nabla \cdot \mathbf{q}$ ) are reduced to first order by application of Green's theorem (1.20). This results in the anticipated natural boundary condition terms. The resulting weak form reads

$$a(\mathbf{v}_w, \mathbf{v}) - \langle \nabla \cdot \mathbf{v}_w, p \rangle = \langle \mathbf{v}_w, \mathbf{f} \rangle - \langle \mathbf{v}_w, \mathbf{h}_{av} \rangle_{\partial\Omega}, \quad (2.22a)$$

$$c(T_w, T) + \frac{i\omega}{T_0} \langle T_w, p \rangle = -\frac{1}{T_0} \langle T_w, Q \rangle + \frac{1}{T_0} \langle T_w, h_h \rangle_{\partial\Omega}, \quad (2.22b)$$

$$e(p_w, p) - \langle p_w, \nabla \cdot \mathbf{v} \rangle + \frac{i\omega}{T_0} \langle p_w, T \rangle = 0, \quad (2.22c)$$

where  $\mathbf{h}_{av} = -\boldsymbol{\sigma} \cdot \mathbf{n}$  denotes the vector that contains the values of the prescribed viscous and acoustic natural boundary conditions  $h_a$  and  $h_v$ . Furthermore,

$$a(\mathbf{v}_w, \mathbf{v}) = i\omega\rho_0 \langle \mathbf{v}_w, \mathbf{v} \rangle + 2\mu \langle \boldsymbol{\varepsilon}_w, \boldsymbol{\varepsilon} \rangle + \lambda \langle \nabla \cdot \mathbf{v}_w, \nabla \cdot \mathbf{v} \rangle, \quad (2.23a)$$

$$c(T_w, T) = -\frac{i\omega\rho_0 C_p}{T_0} \langle T_w, T \rangle - \frac{\kappa}{T_0} \langle \nabla T_w, \nabla T \rangle, \quad (2.23b)$$

$$e(p_w, p) = -\frac{i\omega}{p_0} \langle p_w, p \rangle, \quad (2.23c)$$

where  $\boldsymbol{\varepsilon}_w$  is defined like in equation (2.1c) for  $\boldsymbol{\varepsilon}$ , by replacing  $\mathbf{v}$  by  $\mathbf{v}_w$ . A brief notation of the Hermitian inner product is used in the above equations:

$$\langle \boldsymbol{\phi}_w, \boldsymbol{\phi} \rangle \equiv \int_{\Omega} \overline{\boldsymbol{\phi}_w} \cdot \boldsymbol{\phi} \, d\Omega, \quad \langle \boldsymbol{\phi}_w, \boldsymbol{\phi} \rangle_{\partial\Omega} \equiv \int_{\partial\Omega} \overline{\boldsymbol{\phi}_w} \cdot \boldsymbol{\phi} \, d\partial\Omega, \quad (2.24)$$

with dummy vector  $\boldsymbol{\phi}$ . In general, the inner product's subscript denotes the region of integration, but it is omitted if the region is the domain  $\Omega$ . The inner product is also defined for scalars and tensors for which the dot product is replaced by the scalar product and the double dot product respectively. The line over the variable denotes complex conjugation. Notice that this complex conjugation is only applied to the real valued weighing functions in the above weak form. Therefore, the conjugation does nothing in this weak form.

As usual in the Galerkin approach, the weighing functions and corresponding shape functions use the same basis. Still, the basis of  $p$  and  $p_w$

matrix	Weak term	vector	Weak term
$\mathbf{A}$	$a(\mathbf{v}_w, \mathbf{v})$	$\vec{\mathbf{v}}$	nodal $\mathbf{v}$ values
$\mathbf{B}, \mathbf{B}^T$	$\langle \nabla \cdot \mathbf{v}_w, p \rangle, \langle p_w, \nabla \cdot \mathbf{v} \rangle$	$\vec{T}$	nodal $T$ values
$\mathbf{C}$	$c(T_w, T)$	$\vec{p}$	nodal $p$ values
$\mathbf{D}, \mathbf{D}^T$	$\langle T_w, p \rangle, \langle p_w, T \rangle$	$\vec{\mathbf{f}}$	$\langle \mathbf{v}_w, \mathbf{f} \rangle, \langle \mathbf{v}_w, \mathbf{h}_{av} \rangle_{\partial\Omega}$
$\mathbf{E}$	$e(p_w, p)$	$\vec{Q}$	$\langle T_w, Q \rangle, \langle T_w, h_h \rangle_{\partial\Omega}$

**Table 2.3:** The sub-matrices and sub-vectors in the matrix equation (2.25) correspond to the weak form (2.22). The essential boundary conditions are not taken into account yet:  $g_a$  and  $h_v$  contribute to  $\vec{\mathbf{f}}$ , and  $g_h$  to  $\vec{Q}$ .

can be different than the basis of  $\mathbf{v}$  and  $\mathbf{v}_w$ , or  $T$  and  $T_w$ . For any choice, the ‘sesquilinear forms’  $a$ ,  $c$  and  $e$  lead to the complex symmetric sub-matrices  $\mathbf{A}$ ,  $\mathbf{C}$  and  $\mathbf{E}$  in the FEM system matrix

$$\begin{bmatrix} \mathbf{A} & 0 & \mathbf{B} \\ 0 & \mathbf{C} & \mathbf{D} \\ \mathbf{B}^T & \mathbf{D}^T & \mathbf{E} \end{bmatrix} \begin{Bmatrix} \vec{\mathbf{v}} \\ \vec{T} \\ \vec{p} \end{Bmatrix} = \begin{Bmatrix} \vec{\mathbf{f}} \\ \vec{Q} \\ 0 \end{Bmatrix}. \quad (2.25)$$

Table 2.3 shows the correspondence between this matrix equation and the weak form. The essential boundary conditions eventually also end up in  $\vec{\mathbf{f}}$  and  $\vec{Q}$ .

The complete system matrix is complex symmetric (not Hermitian). Not considered are the contributions which the natural boundary conditions and body forces at the right-hand sides in the weak form (2.22) may make on the system matrix if they are a function of the DOFs. However, these contributions are typically either zero, or symmetric.

## 2.2.2 Discretization

The weak form (2.22) is a mixed formulation: it contains both velocity and pressure degrees of freedom. It is possible to eliminate the pressure degree of freedom, but this may lead to an element that ‘locks’; see Malinen [51]. This locking phenomenon is related to the incompressibility of the medium. Clearly, an acoustic medium is compressible by definition, but not easily: compressing air requires much more force than shearing it. Therefore, an acoustic medium can be labeled ‘nearly incompressible’. Locking can be prevented with a mixed formulation, but a careful choice of the shape functions is essential.

Mixed formulations for the incompressible (Navier) Stokes flow are extensively studied in the literature. The theory focuses on the weak term

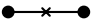
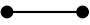
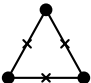
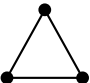
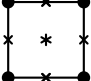


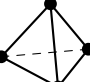

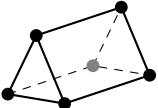

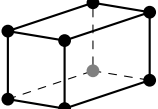


$\langle p_w, \nabla \cdot \mathbf{v} \rangle$ , which is also present in the weak form of viscothermal acoustics (2.22): it corresponds to  $\mathbf{B}^T$  in the system matrix (2.25). This term concerns only the velocity and pressure discretizations. Therefore, the temperature discretization is not considered yet. In the incompressible case, the weak continuity equation reads  $\langle p_w, \nabla \cdot \mathbf{v} \rangle = 0$ . It is important to enforce this continuity equation not too weakly and not too strongly. If it is enforced too weakly, the finite element has poor convergence. On the other hand, if the continuity equation is enforced too strongly, the element also suffers from poor convergence: most velocity DOFs are used to satisfy the continuity equation and only a few DOFs remain to approximate the momentum equation. In the extreme, all velocity DOFs are needed to satisfy the continuity equation, and the finite element locks. In nearly compressible media, the locking problem is alleviated, but only slightly [31].

The weighing of the equations can be manipulated in several ways, see for example Gunzburger [28] for a interesting overview. The only method considered here is the choice of the shape functions. The combination of pressure and velocity shape functions has to satisfy the so-called inf-sup condition, also known as the Babuška-Brezzi condition. Elements that satisfy this condition do not lock and do not suffer from spurious modes (another unwanted phenomenon in which the pressure does not converge). An overview of pairs of velocity and pressure shape functions that satisfy this condition for the Stokes equation can be found in many books and articles, for example [3, 26, 28]. The Stokes equations can be considered as one of the limits of the viscothermal acoustics. The other limit of viscothermal acoustics is isentropic acoustics for which Wang [71] used a comparable mixed form and identical pairs of shape functions. Here, these pairs of shape functions are used to discretize the weak form of viscothermal acoustics (2.22).

The convergence rates of several viscothermal acoustic finite elements with velocity and pressure shape function pairs that satisfy the inf-sup condition are studied in [43] on a 2-D thin gap problem. Good convergence rates are obtained with these elements. Furthermore, this reference shows the effect of the temperature shape function (the temperature is not present in the limit cases: the Stokes equation and isentropic acoustic equations). The best results were obtained with elements that have quadratic velocity and temperature shape functions, and linear pressure shape functions. This is in line with expectations, because the velocity and temperature profiles both tend to a quadratic shape for thin gaps. Moreover, the weak form contains first order derivatives of both the velocity and the temperature, and no pressure derivatives.

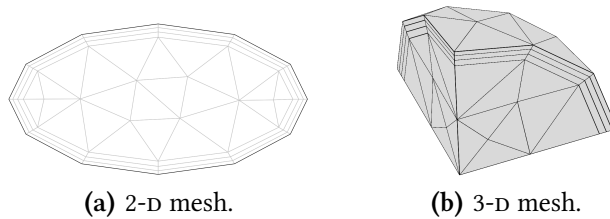
Of the elements that satisfy the inf-sup condition of the Stokes equation, the so-called Taylor-Hood elements are very versatile. A similar discretization for viscothermal acoustics has second order (that is (bi/tri-)quadratic)

Velocity and temperature shape functions		Element shape	Pressure shape functions	
Quadratic 3 nodes		Line		Linear 2 nodes
Quadratic 6 nodes		Triangle		Linear 3 nodes
Bi-quadratic 9 nodes		Quadrilateral		Bi-linear 4 nodes
Quadratic 10 nodes		Tetrahedron		Linear 4 nodes
Bi-quadratic 18 nodes		Prism		Bi-linear 6 nodes
Tri-quadratic 27 nodes		Brick		Tri-linear 8 nodes

**Table 2.4:** The Taylor-Hood-like elements with Lagrangian shape functions for several element shapes. The pressure is interpolated with first order shape functions, while second order shape functions are used for the temperature and the velocity components.

shape functions for the velocity and temperature and first order (that is (bi/tri-)linear) continuous pressure shape functions; see table 2.4. The advantage of the Taylor-Hood-like elements is that many element shapes are available and these element shapes can be easily combined in a single FEM model, for example in boundary layer meshes, see figure 2.2. Such meshes combine triangle and quadrilateral elements, for example, to provide an efficient discretization of the viscous and thermal boundary layers. Therefore, the Taylor-Hood-like elements are used for the full linear Navier-Stokes (FLNS) model throughout this thesis, unless mentioned otherwise.

Finite elements with pressure shape functions that are discontinuous over the element boundaries are an interesting alternative to the Taylor-Hood-like elements. The advantage of these elements is that these have more pressure degrees of freedom and that these DOFs can be eliminated at the element level [31]. Therefore, the global FEM system matrix contains only velocity and temperature DOFs and is relatively efficient to solve. For quadrilateral and brick element shapes, the combination of bi/tri-quadratic velocity shape functions and linear (not bi/tri-linear) discontinuous pressure



**Figure 2.2:** Boundary layer meshes: (a) 2-D mesh with triangle and quadrilateral elements, (b) 3-D mesh with tetrahedron and prism elements.

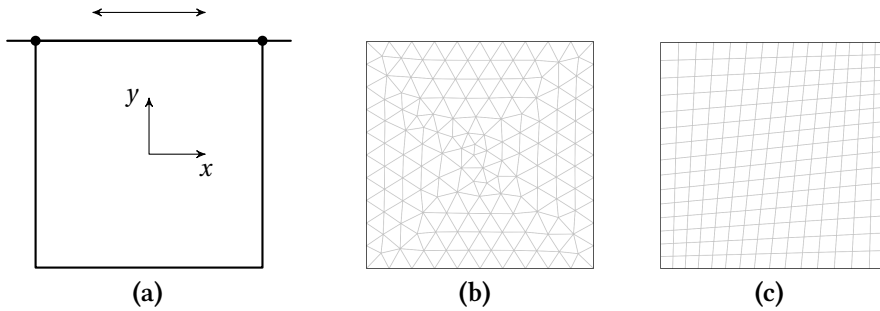
shape functions satisfies the inf-sup condition. A viscous acoustic mixed finite element (without thermal effects) that uses this discretization was presented by Cheng [14] in 2008. Unfortunately, COMSOL currently does not support linear discontinuous pressure shape functions on quadrilateral and brick shaped elements. It does support bi/tri-linear discontinuous shape functions on those elements, but these do not satisfy the inf-sup condition in combination with the mentioned velocity shape functions.

Another interesting discontinuous pressure element that satisfies the inf-sup condition is known as the Crouzeix-Raviart [18, 26] element for the incompressible Stokes equation. These elements have a triangular or tetrahedral shape and linear discontinuous pressure shape functions. The velocity shape functions are quadratic with added bubble functions. The convergence of the viscothermal acoustic Crouzeix-Raviart-like triangular finite element (with quadratic temperature shape functions) is also evaluated in [43]. The convergence is comparable to the Taylor-Hood-like elements in the studied case.

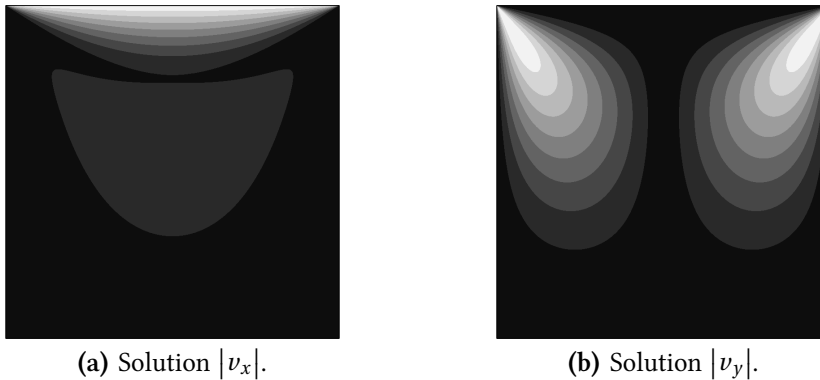
### Demonstration: lid-driven cavity flow

The necessity to make a proper choice of the shape functions in a mixed method, as discussed above, is best illustrated by a simple problem. The lid-driven cavity flow is a standard benchmark problem for the Stokes equation and is a useful demonstration for the viscothermal acoustic finite elements as well. The problem is shown in figure 2.3(a). Three fixed walls create a cavity of  $1 \times 1$  cm. The upper boundary is a lid that slides harmonically (at 1 Hz) over the cavity. The air in the cavity is moved by the velocity of the lid and the viscous friction. The prescribed boundary conditions are  $v_y = 0$  on every boundary,  $v_x = 0$  on the three walls,  $v_x = 1$  on the lid. At the two nodes where the lid meets the walls (indicated by a dot in figure 2.3(a))  $v_x = 0.5$ .

The problem is first solved with the Taylor-Hood-like elements on a fine mesh. This results in the velocity fields shown in figures 2.4(a) and 2.4(b).



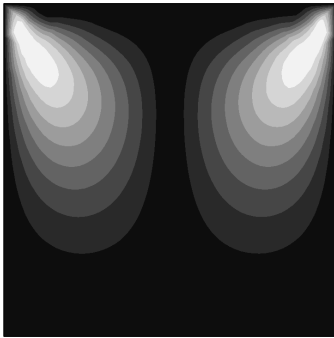
**Figure 2.3:** lid-driven cavity flow: a lid slides harmonically over a cavity. The viscous forces generate a shear velocity in the air in the cavity. (a) problem, (b) coarse triangular mesh, (c) coarse quadrilateral mesh.



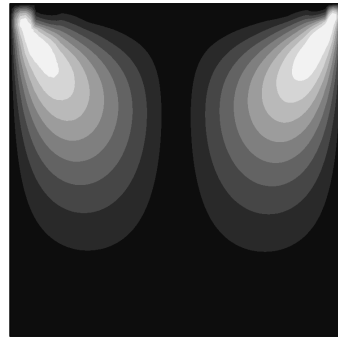
**Figure 2.4:** Reference solutions of the lid-driven cavity flow problem.

The pressure field has singularities at the corners between lid and wall. If the elements connected to both corner nodes are of equal size, the rest of the cavity has a pressure near zero. If these corner elements are not of equal size, the pressure perturbation has a non-zero value, because the interpolation of the essential boundary conditions results in a net inflow and outflow in such cases.

Next, the reference solution on the fine mesh is compared to solutions on coarse meshes for several finite element formulations. The used coarse meshes are shown in figures 2.3(b) and 2.3(c). The quadrilateral mesh is intentionally deformed slightly. The resulting velocity fields  $|v_y|$  from the Taylor-Hood-like viscothermal acoustic elements are shown in figures 2.5(a) and 2.5(b) for the triangle and quadrilateral meshes respectively. These results resemble the reference solution, as expected. Only near the corners, where the mesh is too coarse to represent the solution, do irregularities appear.

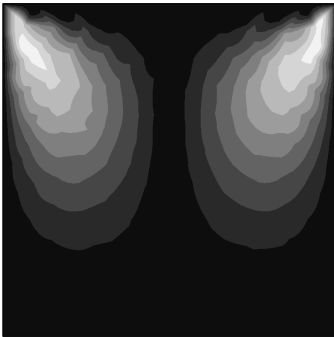


(a) Taylor Hood triangle.

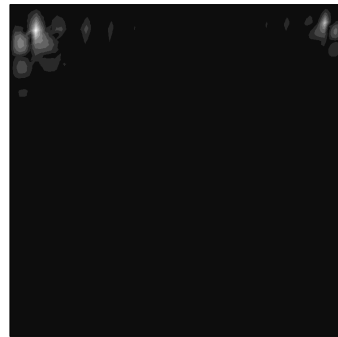


(b) Taylor Hood quadrilateral.

**Figure 2.5:** Solution  $|v_y|$  for the lid-driven cavity flow problem obtained with Taylor-Hood-like elements.

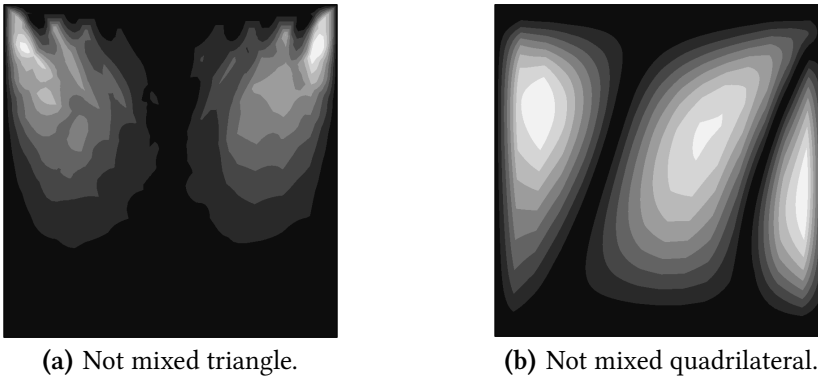


(a) All quadratic triangle.



(b) All quadratic quadrilateral.

**Figure 2.6:** Solution  $|v_y|$  for the lid-driven cavity flow problem obtained with elements that have second order shape functions for all DOFs, including the pressure.



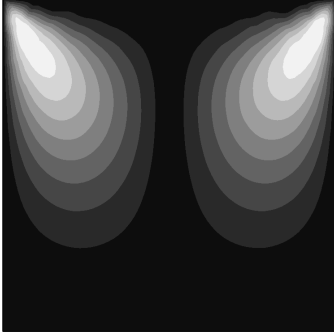
**Figure 2.7:** Solution  $|v_y|$  for the lid-driven cavity flow problem with a non-mixed formulation without pressure degree of freedom and second order shape functions for the temperature and velocity components.

If pressure degrees of freedom are added by using (bi-)quadratic shape functions instead of (bi-)linear shape functions, the results do not improve, but become worse. These results are plotted in figures 2.6(a) and 2.6(b). The solution of the quadrilateral mesh is useless and the solution of the triangular mesh still resembles the reference solution, but is poorer than the solution from the more efficient Taylor-Hood-like elements. The artifacts in this solution stem from enforcing the continuity equation too strongly.

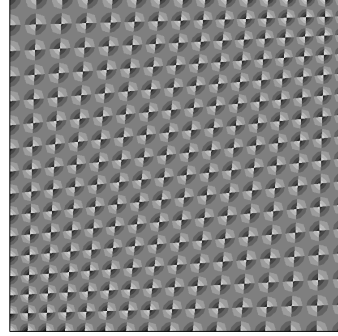
For a non-mixed formulation, the pressure degree of freedom can be eliminated from the weak formulation (2.22) by substitution of  $p_w = 0$  and  $p = T p_0 / T_0 - (\nabla \cdot \mathbf{v}) p_0 / (i\omega)$ . The resulting reduced weak form is discretized by (bi-)quadratic shape functions for the velocity components and the temperature. This finite element results in the solutions shown in figure 2.7(a) and 2.7(b). Again, the solution on the quadrilateral mesh is useless, although the result is deceptively smooth in this case. The solution on the triangle mesh roughly resembles the reference solution. However, it is much poorer than could be expected from the used mesh. If the mesh is refined, the solution improves. Joly [38, 36, 37] published good results obtained with similar non-mixed viscothermal acoustic finite elements. He used fine meshes that are created with *adaptive mesh refinement*.

Last, the results of two discontinuous pressure finite elements are evaluated. The solution of the Crouzeix-Raviart-like element, shown in figure 2.8(a), resembles the solution of the Taylor-Hood-like element. By contrast, the bi-quadratic velocity and temperature, bi-linear discontinuous pressure element (9/4-like element) shows a spurious mode in the pressure field, figure 2.8(b). Nevertheless, the velocity field is calculated accurately with this 9/4-like finite element (not shown). Unlike the more efficient 9/3

element (which uses a linear discontinuous pressure field), the 9/4 element does not satisfy the inf-sup condition. Therefore, problems like the spurious mode could have been expected.



(a) Crouzeix-Raviart triangle.



(b) Pressure of 9/4 quad element: spurious mode.

**Figure 2.8:** Solution for the lid-driven cavity flow problem: (a)  $|v_y|$  obtained with Crouzeix-Raviart-like elements; (b)  $|p|$  obtained with elements with bi-quadratic temperature and velocity components and bi-linear pressure.

The results of the lid-driven cavity flow problem confirm the theory of nearly incompressible problems. Mixed methods with velocity and pressure shape function pairs that satisfy the inf-sup condition in the limit cases of incompressible Stokes flow and isentropic acoustics can be used effectively for viscothermal acoustic finite elements as well.

## 2.3 Fluid structure interaction with the FLNS model

In the FLNS model presented in this chapter, three velocity components (in 3-D) and the temperature can be coupled to the structure. The structure may be described with displacement  $\mathbf{u}$  or velocity  $\dot{\mathbf{u}}$  degrees of freedom. The values at the fluid-structure interface  $\partial\Omega_{FSI}$  are prescribed as essential boundary conditions to the FLNS model

$$\begin{aligned} \mathbf{v} &= i\omega\mathbf{u}, \\ \mathbf{v} &= \dot{\mathbf{u}}, \end{aligned} \quad (\text{essential fluid BC at } \partial\Omega_{FSI}). \quad (2.26)$$

The implementation of this *essential* boundary condition is straightforward if the fluid and the structure use identical shape functions on the interface  $\partial\Omega_{FSI}$ ; recall figure 1.8. Since the velocity or displacement of the structure

is yet unknown, the boundary condition depends on the degrees of freedom. Therefore, the essential boundary condition does not appear in the system vector, but in the system matrix; in  $F_{s \rightarrow a}$  of equation (1.31) to be precise. The second coupling relation is the load of the fluid on the structure. This load is

$$\mathbf{f}_s = -\boldsymbol{\sigma} \cdot \mathbf{n} \quad (\text{structure load at } \partial\Omega_{FSI}), \quad (2.27)$$

with  $\mathbf{n}$  the unit vector normal to the boundary, away from the fluid domain, and  $\mathbf{f}_s$  the load on the structure in the global coordinate system. Because this load is yet unknown, it ends up in the system matrix in  $F_{a \rightarrow s}$  of equation (1.31).

If the structure does not have tangential displacement degrees of freedom (a membrane for example), there is clearly no fluid structure interaction in that direction. The tangential boundary conditions of the FLNS model should be explicitly prescribed in that case, and  $v_t = 0$  is typically used. Section 4.3 presents an example with membrane elements.

Heat conduction in the structure can also be coupled to the acoustics by using the temperature of the structure  $T_s$  as the essential boundary condition  $T = T_s$  for the fluid at the interface boundary. Furthermore, the heat flow  $\mathbf{q} \cdot \mathbf{n}$  is the thermal load on the structure in this case. Nevertheless, as already mentioned, isothermal  $T = 0$  boundary condition is typically used in the viscothermal acoustic models instead of a coupled formulation. This approximation is accurate, because the air can hardly heat the structure in most cases; see [12].

## 2.4 Discussion

This chapter has introduced the linear time harmonic Navier-Stokes equations for viscothermal acoustics. The study of these equations started in the literature with Kirchhoff's paper [47]. All analytic studies of these equations are limited to simple geometries. The viscothermal acoustic finite element formulation presented in this chapter offers a numerical alternative for more complicated geometries.

Comparable numerical viscothermal acoustic models are studied for BEM by, for example, Dokumaci [22, 23], Karra [45, 46] and Cutanda Henríquez [20]. Only the last of these references (from 2002) presents a BEM model with both viscous and thermal effects without using restrictive boundary layer approximations. Comparable viscothermal acoustic FEM models are presented by Malinen [51], Cheng [14] and Joly [38, 36, 37]. Malinen's publication is from 2004, the other references were published after the start of this PhD-project. Although the finite element of this chapter is



rather different from Malinen's element, his publication has been influential on its formulation. Malinen identified the viscothermal acoustic problem as nearly incompressible and used a mixed formulation to get a good convergence rate.

The finite element in this chapter has some advantages compared to Malinen's formulation. The velocity and temperature are discretized with quadratic shape functions which results in smaller errors in narrow geometries [43]. Malinen uses a mixed formulation with a dimensionless density, instead of the pressure, as the additional degree of freedom. The pressure is a smoother field and it does not rapidly change in the boundary layers, unlike the density field. Therefore it is better suited than the density to be discretized by the proposed Taylor-Hood-like shape functions. Malinen uses a different discretization. Moreover, Malinen's finite element does not have the preferred natural boundary condition terms and does not yield a complex symmetric FEM system matrix.

The finite element formulation of Cheng [14] does not include thermal effects. Like the finite element presented in this chapter, it uses a mixed formulation (albeit *displacement/pressure*). By contrast, the element of Joly [36, 37] does not use a mixed formulation. The convergence rate of this element is not studied in the mentioned references, but the result in figure 2.7(a) shows potential problems with it. Nevertheless, the results in his publication, calculated on a fine mesh obtained with adaptive mesh refinement, are good. The adaptive mesh refinement procedure presented by Joly is valuable to reduce the computational costs.

COMSOL has a template of viscothermal acoustic finite elements that is provided on request. This template uses a formulation that is very similar to the finite element presented in this chapter, although the two formulations are developed independently. The major advantage of the finite element of this thesis is that it results in complex symmetric FEM system matrices. This reduces the computational time and required memory; again see [43].

Validations of the FLNS FEM model on practical problems, including 3-D and FSI problems, are presented in chapter 4. First, approximate models that are faster to solve are presented.

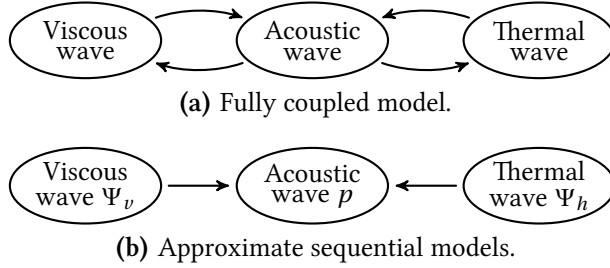
## Approximate viscothermal acoustic models

The full linearized Navier-Stokes model (FLNS) for viscothermal acoustics presented in the previous chapter requires large computational resources for solving in comparison with isentropic acoustic models. This becomes clear by counting the number of coupled fields: five for the FLNS model versus one (pressure or velocity potential) for isentropic acoustics.

In this chapter, three models are presented which can be solved with much lower computational costs than the FLNS model; sometimes even in the same order of magnitude as isentropic acoustic models. These models are an accurate approximation of the FLNS model. Figure 3.1 schematically shows the approximation: the fully coupled model is approximated as a sequential model. The viscous and thermal fields can be calculated without considering the acoustics. The approximation is accurate because of the difference between the viscothermal boundary layer thickness and the acoustic wavelength.

Two models in this chapter have been developed by other authors: the low reduced frequency model (LRF) and the boundary layer impedance model (BLI). The latter abbreviation is not used in the literature, but used here for brevity. The drawback of these models is their limited applicability: the LRF model is for layers and tubes below the cut-off frequency, and the BLI model is for geometries that are large compared to the viscothermal boundary layer thickness. In this thesis, a new approximate model is proposed, which does not require any geometrical constraints. It is called the sequential linearized Navier-Stokes model, SLNS. This model is more costly to solve than the LRF and BLI models, but much less costly than the FLNS model.

Another difference between the FLNS model and the approximate models concerns the boundary conditions. The *viscous and thermal boundary conditions* of the approximate models are assumed to be homogeneous. This includes no slip, no shear force, isothermal, adiabatic and impedance-like BCs.



**Figure 3.1:** Viscothermal acoustics is a three wave theory. These waves are fully coupled in the FLNS model of chapter 2 as in (a). By contrast, the models in this chapter are sequential approximations as in (b). The symbols  $\Psi_v$  and  $\Psi_h$  are used for the viscous and thermal fields in the approximate models.

Not included are, for example, non-zero shear velocities. Extensions to non-homogeneous viscothermal boundary conditions are possible, but require some modifications and extra calculations which are not dealt with in this thesis. The *acoustic boundary conditions* may still be non-homogeneous.

The derivation of the sequential framework which is common to the three approximate models is presented in section 3.1. Subsequently, the three approximate models are presented. The chapter ends with a comparison of the models in section 3.5. Chapter 4 validates the approximate models on several benchmark problems.

### 3.1 Common approximations

This section presents the order of magnitude analysis that is common to each of the three approximate models in this chapter. The analyses are expressions of the known properties of viscothermal acoustic solutions. The subsequent approximations in which small terms are neglected, are based on the differences between the acoustic wave number  $k_0$  versus the viscothermal wave numbers  $k_v$  and  $k_h$ . Recall the definition of the wave numbers from equation (1.13):

$$k_0 \equiv \omega/c_0, \quad k_v^2 \equiv -i\omega\rho_0/\mu, \quad k_h^2 \equiv -i\omega\rho_0 C_p/\kappa. \quad (3.1)$$

The governing viscothermal acoustic equations rewritten in dimensionless form to make the different orders of magnitude more apparent.

### 3.1.1 Dimensionless equations and wave numbers

The magnitude analyses are simplified by switching to the dimensionless variables, constants and gradient operator defined as

$$\begin{aligned} \tilde{\mathbf{v}} &\equiv \mathbf{v}/c_0, & \tilde{T} &\equiv T/T_0, & \tilde{p} &\equiv p/p_0, & \tilde{\rho} &\equiv \rho/\rho_0, \\ \tilde{k}_v &\equiv k_v/k_0, & \tilde{k}_h &\equiv k_h/k_0, & \tilde{\xi} &\equiv 1 + \lambda/\mu, & \tilde{\nabla} &\equiv k_0^{-1}\nabla. \end{aligned} \quad (3.2)$$

Other spatial derivatives are also made dimensionless with the wave number, like the gradient operator; for example: the dimensionless Laplacian is  $\tilde{\Delta} \equiv k_0^{-2}\Delta$ .

The set of linearized Navier-Stokes equations (2.17) rewritten in the above dimensionless variables reads

$$\tilde{\mathbf{v}} + \tilde{k}_v^{-2}\tilde{\xi}\tilde{\nabla}(\tilde{\nabla}\cdot\tilde{\mathbf{v}}) + \tilde{k}_v^{-2}\tilde{\Delta}\tilde{\mathbf{v}} = \frac{-\tilde{\nabla}\tilde{p}}{i\gamma}, \quad (3.3a)$$

$$\tilde{T} + \tilde{k}_h^{-2}\tilde{\Delta}\tilde{T} = \frac{\gamma-1}{\gamma}\tilde{p}, \quad (3.3b)$$

$$\tilde{\nabla}\cdot\tilde{\mathbf{v}} - i\tilde{T} + i\tilde{p} = 0. \quad (3.3c)$$

The source terms  $\mathbf{f}$  and  $Q$  are set to zero. Non-zero sources require the calculation of additional fields, which is not considered for simplicity. No approximations have been made in the derivation of this set of equations from the set (2.17). The values of  $\gamma$  and  $\tilde{\xi}$  are near unity for air.

The approximations in this chapter are based on two properties of the dimensionless wave numbers  $\tilde{k}_v$  and  $\tilde{k}_h$  defined in equation (3.2):

1. The viscous and thermal wave numbers have a positive real part of equal magnitude as the negative imaginary part (since  $\sqrt{-i} = (1-i)/\sqrt{2}$ ). This is typical for the time harmonic form of diffusion equations. Consequently, the viscous and thermal ‘waves’ are highly damped and form boundary layers.
2. The viscous and thermal boundary layer thicknesses are much smaller than the wavelength, expressed with the dimensionless wave numbers as

$$|\tilde{k}_v| \gg 1, \quad |\tilde{k}_h| \gg 1. \quad (3.4)$$

These relations are satisfied for air in the audible frequency band; recall figure 1.4.

### Definition of the orders of magnitude

Orders of magnitude based on equation (3.4) are defined in terms of the dimensionless wave numbers as

$$\mathcal{O}(\tilde{k}_\phi^{-2}) \ll \mathcal{O}(\tilde{k}_\phi^{-1}) \ll \mathcal{O}(1) \ll \mathcal{O}(\tilde{k}_\phi) \ll \mathcal{O}(\tilde{k}_\phi^2), \quad (3.5)$$

where the wave number  $\tilde{k}_\phi$  denotes either  $\tilde{k}_v$  or  $\tilde{k}_h$ , which are of equal order of magnitude for air. With respect to unity for example,  $\mathcal{O}(\tilde{k}_\phi^{-2})$  is called second order small and  $\mathcal{O}(\tilde{k}_\phi)$  is called first order large.

#### 3.1.2 Order of magnitude analyses

An acoustic domain can be subdivided in a boundary layer region in which the viscothermal effects dominate, and a bulk which can be accurately described as isentropic; this was introduced in figure 1.2. These two regions are treated separately, because viscothermal acoustic solutions and especially their spatial derivatives can have very different orders of magnitude in the boundary layer than in the bulk.

Evanescent waves are not considered in any of the order of magnitude analyses. Therefore, accuracy near sharp corners and point sources is likely to be poor. However, the linear acoustic equations are insufficient here anyway, as described in the discussion about the linearization of the Navier-Stokes equations in section 2.1.2. The resulting approximate viscothermal acoustic models are compared to the FLNS model in chapter 4 to verify whether disregarding these effects leads to significant errors.

#### Orders of magnitude in the bulk

The advantage of these dimensionless variables defined by equation (3.2) is that the temperature, pressure and velocity, and their dimensionless derivatives are of equal order of magnitude in the bulk for an acoustic plane wave. For acoustic fields that are not a plane wave, two groups can be identified: variables that are (nearly) in phase with the pressure, and variables that are (nearly) in phase with the pressure gradient. In each group, the variables are still of equal order of magnitude:

$$\begin{aligned} \tilde{T}, \tilde{\Delta}\tilde{T}, \tilde{\nabla} \cdot \tilde{\mathbf{v}} &= \mathcal{O}(\tilde{p}), \\ \tilde{\mathbf{v}}, \tilde{\Delta}\tilde{\mathbf{v}}, \tilde{\nabla}(\tilde{\nabla} \cdot \tilde{\mathbf{v}}) &= \mathcal{O}(\tilde{\nabla}\tilde{p}), \end{aligned} \quad (\text{bulk}). \quad (3.6a)$$

Finally a comparison of the pressure with the pressure gradient is needed. At all locations, except near nodes of either the pressure or the pressure gradient, these two are of comparable magnitude:

$$\mathcal{O}(\tilde{p}) = \mathcal{O}(\tilde{\nabla}\tilde{p}). \quad (3.6b)$$

This equation is invalid near locations where the pressure or pressure gradient vanishes, but the errors at these locations are neglected as mentioned above.

### Isentropic acoustic equations in the bulk

The reduction of the set of equations (3.3) to the isentropic equations is straightforward because only the two similarities (3.6a) have to be evaluated. All terms containing  $\tilde{k}_\phi^{-2}$  are second order small and can be neglected, resulting in

$$\tilde{\mathbf{v}} = \frac{-\tilde{\nabla}\tilde{p}}{i\gamma}, \quad \tilde{T} = \frac{\gamma-1}{\gamma}\tilde{p}, \quad \tilde{\nabla} \cdot \tilde{\mathbf{v}} - i\tilde{T} + i\tilde{p} = 0, \quad (\text{bulk}). \quad (3.7)$$

which are indeed the isentropic acoustic equations, see section 1.2.3, in dimensionless form. Substitution of the first two equations into the third equation for  $\tilde{\mathbf{v}}$  and  $\tilde{T}$  yields the dimensionless acoustic Helmholtz equation of the pressure:

$$\tilde{\Delta}\tilde{p} + \tilde{p} = 0 \quad (\text{bulk}). \quad (3.8)$$

The magnitude analysis presented next results in a reduced set of the viscothermal acoustic equations, which is valid not only in the bulk, but also in the boundary layer.

### Orders of magnitude in both boundary layer and bulk

The situation in the boundary layer is quite different than in the bulk, owing to the viscothermal effects caused by the isothermal and no slip boundary conditions. Within the thin boundary layer, the temperature and the (shear) velocity rapidly change from the value in the bulk to zero at the boundary. Therefore, temperature and velocity gradients are first order large: that is  $\tilde{k}_\phi$  times the variable itself. Furthermore, the Laplacians (second order derivatives) of these variables are known to be second order large. The pressure and the pressure gradient are the two variables that remain relatively smooth over the boundary layer and can be used to express the magnitudes of the other variables:

$$\begin{aligned} \tilde{T} &\leq \mathcal{O}(\tilde{p}), & \tilde{\mathbf{v}} &\leq \mathcal{O}(\tilde{\nabla}\tilde{p}), \\ \tilde{\nabla}\tilde{T} &\leq \mathcal{O}(\tilde{k}_h\tilde{\nabla}\tilde{p}), & \tilde{\nabla}\tilde{\mathbf{v}} &\leq \mathcal{O}(\tilde{k}_v\tilde{p}), & (\text{boundary layer and bulk}). & (3.9a) \\ \tilde{\Delta}\tilde{T} &\leq \mathcal{O}(\tilde{k}_h^2\tilde{p}), & \tilde{\Delta}\tilde{\mathbf{v}} &\leq \mathcal{O}(\tilde{k}_v^2\tilde{\nabla}\tilde{p}), \end{aligned}$$

The magnitudes of the terms in equation (3.6a) containing the divergence of the velocity can be evaluated using the continuity equation (3.3c):

$$\begin{aligned}\tilde{\nabla} \cdot \tilde{\mathbf{v}} &= \mathcal{O}(\tilde{p}), \\ \tilde{\nabla}(\tilde{\nabla} \cdot \tilde{\mathbf{v}}) &\leq \mathcal{O}(\tilde{k}_h \tilde{p}),\end{aligned}\quad (\text{boundary layer and bulk}). \quad (3.9b)$$

Like in the bulk, the pressure and pressure gradient are of comparable magnitude almost everywhere:

$$\mathcal{O}(\tilde{p}) = \mathcal{O}(\tilde{\nabla} \tilde{p}). \quad (3.9c)$$

### Governing equations in both boundary layer and bulk

Based on the above orders of magnitude, the set of equations (3.3) can be simplified. However, now only the term containing  $\tilde{\xi}$  is first order small (or smaller), and can be neglected with respect to the pressure gradient. The resulting set of equations is

$$\tilde{\mathbf{v}} + \tilde{k}_v^{-2} \tilde{\Delta} \tilde{\mathbf{v}} = \frac{-\tilde{\nabla} \tilde{p}}{i\gamma}, \quad (3.10a)$$

$$\tilde{T} + \tilde{k}_h^{-2} \tilde{\Delta} \tilde{T} = \frac{\gamma-1}{\gamma} \tilde{p}, \quad (3.10b)$$

$$\tilde{\nabla} \cdot \tilde{\mathbf{v}} - i\tilde{T} + i\tilde{p} = 0. \quad (3.10c)$$

This set contains all terms that are important in the boundary layer and in the bulk. It is the set of governing equations for this chapter. Notice that the set contains just three dimensionless parameters:  $\tilde{k}_v$ ,  $\tilde{k}_h$  and  $\gamma$ .

### 3.1.3 Approximate viscothermal solutions

The momentum equation (3.10a) and entropy equation (3.10b) both are inhomogeneous Helmholtz equations. These equations are solved approximately for unknown pressure fields in this subsection. The derivations of both solutions are essentially similar. Therefore, only the derivation of the temperature is presented in detail.

#### Approximate temperature solution

The temperature in entropy equation (3.10b) can be solved for homogeneous thermal boundary conditions and a yet *unknown* pressure field. Such solutions are generally expressed in integral form, involving Green's functions. However, in this particular case, the Green's function of the Helmholtz operator is very local, because of the large negative imaginary part of the wave

number  $\tilde{k}_h$ . Furthermore, the pressure field is relatively smooth because the acoustic wavelength is much larger than the boundary layer thicknesses; see equation (3.4). Therefore, an approximate yet accurate solution of the entropy equation (3.10b) can be written as the product

$$\tilde{T} = \Psi_h \frac{\gamma - 1}{\gamma} \tilde{p}. \quad (3.11)$$

In this solution,  $\Psi_h$  is a complex valued scalar field that accounts for the thermal boundary layer effects. In the bulk of the fluid this ‘thermal field’ equals unity and the solution becomes identical to the isentropic acoustic solution of equation (3.7). Based on the order of magnitude analysis (3.9), the thermal field  $\Psi_h$ , its gradient and its Laplacian satisfy

$$\Psi_h \leq \mathcal{O}(1), \quad \tilde{\nabla} \Psi_h \leq \mathcal{O}(\tilde{k}_h), \quad \tilde{\Delta} \Psi_h \leq \mathcal{O}(\tilde{k}_h^2). \quad (3.12)$$

The solution (3.11) can be verified by substituting it into the entropy equation (3.10b). This yields, after division by  $(\gamma - 1)/\gamma$ ,

$$[\Psi_h + \tilde{k}_h^{-2} \tilde{\Delta} \Psi_h] \tilde{p} + \tilde{k}_h^{-2} [\Psi_h \tilde{\Delta} \tilde{p} + 2(\tilde{\nabla} \Psi_h) \cdot (\tilde{\nabla} \tilde{p})] = \tilde{p}. \quad (3.13)$$

The second term in the above result is at least one order smaller than the first term, and can be neglected. This reduces the equation to

$$[\Psi_h + \tilde{k}_h^{-2} \tilde{\Delta} \Psi_h] \tilde{p} = \tilde{p}. \quad (3.14)$$

Therefore, equation (3.11) is an approximate solution of the entropy equation (3.10b) if  $\Psi_h$  satisfies the inhomogeneous PDE

$$\Psi_h + \tilde{k}_h^{-2} \tilde{\Delta} \Psi_h = 1. \quad (3.15)$$

Only homogeneous viscothermal boundary conditions are considered for the models in this chapter.<sup>1</sup> The boundary conditions for  $\Psi_h$  can be derived from these:

$$\tilde{T} = 0 \quad \Rightarrow \quad \Psi_h = 0 \quad (\text{isothermal BC}), \quad (3.16a)$$

$$\tilde{\nabla}_n \tilde{T} = 0 \quad \Rightarrow \quad \tilde{\nabla}_n \Psi_h = \frac{-\tilde{\nabla}_n \tilde{p}}{\tilde{p}} \Psi_h \quad (\text{adiabatic BC}), \quad (3.16b)$$

$$\Rightarrow \quad \tilde{\nabla}_n \Psi_h = 0 \quad (\text{approximate adiabatic BC}). \quad (3.16c)$$

The homogeneous impedance-like boundary condition and its approximation may be derived in a similar way.

---

<sup>1</sup>The acoustic boundary conditions (pressure and normal velocity) may be inhomogeneous



The adiabatic boundary condition requires knowledge of  $(\tilde{\nabla}_n \tilde{p})/\tilde{p}$  for an accurate prescription. Because this admittance is typically unknown, the approximate boundary condition is used instead. The approximation in this boundary condition is based on the magnitude analysis

$$\left| \frac{-\tilde{\nabla}_n \tilde{p}}{\tilde{p}} \Psi_h \right| = \mathcal{O}(1) \ll \mathcal{O}(\tilde{k}_h), \quad (3.17)$$

where the last term is the estimate of  $\tilde{\nabla} \Psi_h$  from equation (3.12).

### Approximate shear velocity solution

The velocity solution of the momentum equation (3.10a) is derived in a similar way as the temperature solution of the entropy equation presented above. However, the momentum equation is a vector equation. At this stage, only homogeneous boundary conditions (no-slip, no-force, or impedance-like) are considered. For this case, the approximate solution of the momentum equation (3.10a) is

$$\tilde{\mathbf{v}} = \frac{-\Psi_v \tilde{\nabla} \tilde{p}}{i\gamma}, \quad (3.18)$$

where  $\Psi_v$  is the complex valued *scalar* ‘viscous field’ that satisfies the inhomogeneous PDE

$$\Psi_v + \tilde{k}_v^{-2} \tilde{\Delta} \Psi_v = 1, \quad (3.19)$$

and the boundary conditions

$$\tilde{\mathbf{v}} = 0 \quad \Rightarrow \quad \Psi_v = 0 \quad (\text{no slip BC}), \quad (3.20a)$$

$$\tilde{\nabla}_n \tilde{\mathbf{v}} = 0 \quad \Rightarrow \quad \tilde{\nabla}_n \Psi_v = 0 \quad (\text{approximate no shear force BC}). \quad (3.20b)$$

The last boundary condition is an approximation, like the adiabatic boundary condition (3.16). The approximate homogeneous impedance-like boundary may be derived similarly. The solution (3.18) can be verified by substitution into the momentum equation (3.10a).

A homogeneous normal velocity boundary condition is assumed, but the models presented later can also be used with non-homogeneous normal velocities. Therefore the velocity solution (3.18) is accurate for the tangential (shear) velocity components, but not necessarily for the normal velocity component. Each of the models in the remainder of this section uses a slightly different approach for the normal velocity. Therefore, it is not discussed here, but separately for each model.

### Approximate continuity equation

The continuity equation (3.3c) can be simplified by substitution of the temperature solution (3.11):

$$\tilde{\nabla} \cdot \tilde{\mathbf{v}} + \frac{i\Psi'_h}{\gamma} \tilde{p} = 0, \quad (3.21)$$

in which  $\Psi'_h$  is the ‘modified thermal field’ defined as

$$\Psi'_h \equiv \gamma - (\gamma - 1)\Psi_h. \quad (3.22)$$

Furthermore, the dimensionless density is

$$\tilde{\rho} = \frac{\Psi'_h}{\gamma} \tilde{p}. \quad (3.23)$$

This relation follows from the ideal gas law (2.6) and the approximate solution of the temperature.

#### 3.1.4 Summary of the results in dimensional form

The dimensionless form was convenient for the magnitude analysis, but the dimensional form is more straightforward for building models. Therefore, the results that have been derived above are summarized here in dimensional form.

The viscous and thermal fields  $\Psi_\nu$  and  $\Psi_h$  remain dimensionless and satisfy the dimensional PDES equivalent to equations (3.19) and (3.15):

$$\Psi_\phi + k_\phi^{-2} \Delta \Psi_\phi = 1 \quad (3.24)$$

where  $\phi$  stands for  $\nu$  or  $h$ . The corresponding boundary conditions are

$$\Psi_\phi = 0 \quad (\text{no slip / isothermal BC}), \quad (3.25a)$$

$$\nabla_n \Psi_\phi = 0 \quad (\text{approximate no shear force / adiabatic BC}). \quad (3.25b)$$

The modified thermal field  $\Psi'_h$  also remains dimensionless:

$$\Psi'_h \equiv \gamma - (\gamma - 1)\Psi_h. \quad (3.26)$$

Realize that the three viscothermal fields  $\Psi_\nu$ ,  $\Psi_h$  and  $\Psi'_h$  all equal unity in the bulk and for isentropic acoustics.

The derived solutions for the velocity, temperature and density from equations (3.18), (3.11) and (3.23), are

$$\mathbf{v} = \frac{-\Psi_\nu \nabla p}{i k_0 Z_0}, \quad T = \frac{\Psi_h p}{\rho_0 C_p}, \quad \rho = \frac{\Psi'_h p}{c_0^2}. \quad (3.27)$$

The velocity solution is accurate for the shear components along the boundary. However, the velocity component perpendicular to the boundary needs to be revisited for non-homogeneous boundary conditions and accuracy. This is done separately for each approximate model in the following sections. The expression for  $\mathbf{v}$  closely resembles the isentropic acoustic momentum equation, or Euler equation, (1.11). Similarly, the expression for  $T$  and  $\rho$  resemble the isentropic acoustic constitutive equations (1.8) and (1.7). The isentropic relations indeed follow if  $\Psi_v$ ,  $\Psi_h$  and  $\Psi'_h$  all equal unity.

The pressure field still needs to be solved. This can be done with the continuity equation (3.21):

$$\nabla \cdot \mathbf{v} + \frac{ik_0}{Z_0} \Psi'_h p = 0, \quad (3.28)$$

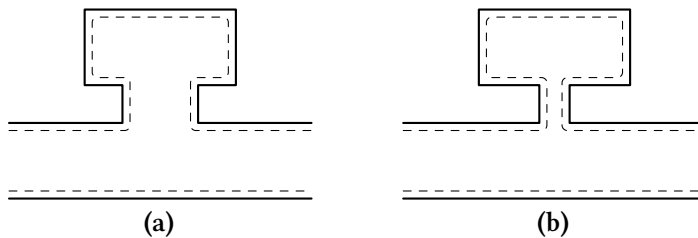
which resembles the isentropic acoustic continuity equation (1.6),

The following sections use the above results to build viscothermal acoustic models. The difference between these models is based on the way in which the viscothermal fields  $\Psi_v$  and  $\Psi_h$ , and the pressure field  $p$  are calculated. Furthermore, the models differ in how the acoustic normal velocity boundary condition (which may be non-homogeneous) is applied.

### 3.2 The boundary layer impedance model

The standard model of time harmonic isentropic acoustics is the Helmholtz equation. As mentioned, this model does not account for viscothermal effects and becomes inaccurate if the modeled geometry is not much larger than the viscothermal boundary layers. The model presented in this section was developed by Bossart [10] and can be regarded as a modification of the isentropic acoustic model. The concept is to include the viscothermal effects by an impedance boundary condition (BC). The model still becomes inaccurate if the viscothermal effects increase too much, but for many applications it is accurate. For brevity, this model is referred to as the BLI (boundary layer impedance) model, although this name is not used in Bossart's publication.

In 1948, Cremer [17] showed that the reflection of a harmonic plane wave from a plane boundary can be described by an impedance that depends on the viscothermal coefficients of the medium (air), and the wave's angle of incidence. His expression for the impedance is well known and can be found in, for example [12, 53, 58]. A few years later, Beatty [4] applied this impedance to calculate the viscothermal dissipation in higher order modes in waveguides. The BLI model can be regarded as a numerical method that uses Cremer's boundary impedance on arbitrary geometries. A key ingredient of the method is the estimation of the local angle of incidence.



**Figure 3.2:** The boundary layer in a tube with side resonator with two neck diameters. The BLI model can be used if the boundary layer is relatively small: (a) may be modeled accurately, (b) not.

In the brief derivation of the BLI model presented below, Bossart is followed and the results of the previous section are used. A more detailed derivation can be found in Bossart's original publication [10].

### 3.2.1 Geometric constraints

The boundary layer impedance model is not accurate for all geometries: the boundary layers in the geometry should be thin compared to all characteristic lengths of the geometry. This geometric constraint is rather paradoxical, because it guarantees accuracy for cases in which viscothermal effects may be neglected altogether. However, in practice, BLI models do yield better results than isentropic acoustic models in many cases, see section 4.2.3 for an example.

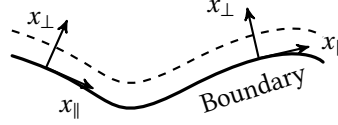
Figure 3.2 presents the geometric constraint graphically. In figure 3.2(a), the boundary layer is thin compared to the bulk everywhere, and the BLI model yields accurate results. However, in figure 3.2(b) neck of the resonator is thinner. In this case, the error in the flow in the neck is larger and the BLI model is inaccurate.

### 3.2.2 Viscous and thermal fields

Analytic expressions for the viscous and thermal fields  $\Psi_v$  and  $\Psi_h$  are used in the BLI model. For a plane wall, the PDE (3.24) has an exact solution that satisfies the no slip and isothermal boundary conditions ( $\Psi_\phi = 0$ ) at the wall, and the zero shear force and adiabatic boundary conditions ( $\nabla_n \Psi_\phi = 0$ ) in the bulk ( $x_\perp \gg \delta_\phi$ ):

$$\Psi_\phi = 1 - e^{-ik_\phi x_\perp}. \quad (3.29)$$

As before,  $\phi$  is a dummy variable that should be replaced by  $v$  or  $h$  for the viscous and the thermal field respectively. Furthermore,  $x_\perp$  is the coordinate that equals zero on the wall and increases in the direction normal to the



**Figure 3.3:** The coordinates, velocity and gradient can be decomposed in the directions perpendicular and parallel to the boundary, denoted by subscripts  $\perp$  and  $\parallel$  respectively. This decomposition is only needed in the boundary layer, not in the bulk.

plane wall, see figure 3.3. The above expression becomes inaccurate if the wall is curved, but fortunately, these errors are either small (smooth curve) or local (sharp corner). The expression clearly fails if boundary layers at opposite boundaries overlap, but this case violates the geometric constraints of the BLI model.

The shear velocity, temperature and density in the BLI model satisfy equation (3.27), with the above expression for the viscous and thermal fields. This equation is not accurate enough for the perpendicular velocity  $v_{\perp}$ , because it is the only means to account for the viscothermal effects in the BLI model. Therefore, Cremer's boundary impedance is used for the perpendicular velocity instead of equation (3.27).

### Normal velocity

An accurate expression of the velocity component perpendicular to the boundary is required in the BLI model. As shown below, this velocity is a function of the pressure and can be regarded as an impedance. The derivation starts with the divergence of the shear velocity from equation (3.27), which can be expressed in a form that seems awkward, but proves useful in the subsequent steps

$$\nabla_{\parallel} \cdot \mathbf{v}_{\parallel} = \frac{-\Psi_v \Delta_{\parallel} p}{ik_0 Z_0} = \frac{\Delta_{\perp} p + k_0^2 p - (\Psi_v - 1) \Delta_{\parallel} p}{ik_0 Z_0}. \quad (3.30)$$

The relation  $\nabla_{\parallel} \Psi_v = 0$  (exact for plane walls), and the acoustic Helmholtz equation (1.9) in the form  $\Delta_{\parallel} p = -k_0^2 p - \Delta_{\perp} p$  have been used. The subscripts  $\parallel$  and  $\perp$  are used for the parallel (shear) and perpendicular (normal) directions respectively; see figure 3.3.<sup>2</sup> Substitution of the above result into the continuity equation (3.28), yields

$$\nabla_{\perp} \cdot \mathbf{v}_{\perp} = \frac{\Delta_{\perp} p + (\Psi_v - 1) k_0^2 p + (\gamma - 1) (\Psi_h - 1) k_0^2 p}{-ik_0 Z_0}, \quad (3.31)$$

<sup>2</sup>Notice that  $v_n$  is only defined at the boundary, while  $v_{\perp}$  is also defined in the boundary layer; a similar difference holds for  $v_t$  and  $v_{\parallel}$ . Furthermore,  $v_n = -v_{\perp}$  at the boundary.

where  $\Delta_{\parallel} p = -k_{\parallel}^2 p$  is used. The coefficient  $k_{\parallel}$  can be thought of as a yet unknown acoustic wave number in the direction along the wall. This wave number is related to the angle of incidence  $\theta$ , see figure 3.4(a):

$$k_{\parallel}^2 / k_0^2 = \sin^2 \theta. \quad (3.32)$$

Notice that  $\nabla_{\perp} \cdot v_{\perp}$  in equation (3.31) is just  $\partial v_{\perp} / \partial x_{\perp}$ . Therefore, the velocity perpendicular to the boundary  $v_{\perp}$  results from integration of this equation over the interval  $x_{\perp} = [0, x_{\perp}]$ ; resulting in

$$v_{\perp} = \frac{-\nabla_{\perp} p}{i k_0 Z_0} - \left[ \frac{k_{\parallel}^2 k_0}{k_0^2 k_v} \Psi_v + (\gamma - 1) \frac{k_0}{k_h} \Psi_h \right] \frac{p}{Z_0}. \quad (3.33)$$

In the above result, the integration constant is already chosen such that the second term of this result equals zero at  $x_{\perp} = 0$ .

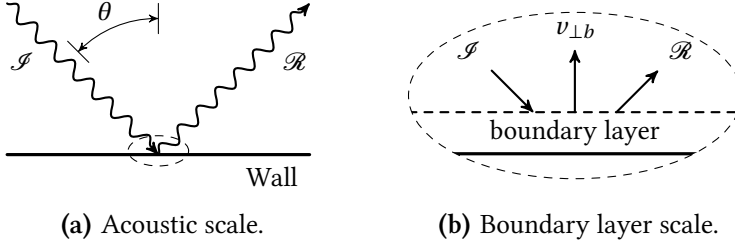
At the location just outside the boundary layer, the viscous and thermal fields  $\Psi_v$  and  $\Psi_h$  approximately equal unity. The perpendicular velocity evaluated at this location is

$$v_{\perp b} = \frac{-\nabla_{\perp} p}{i k_0 Z_0} - \left[ \frac{k_{\parallel}^2 k_0}{k_0^2 k_v} + (\gamma - 1) \frac{k_0}{k_h} \right] \frac{p}{Z_0}. \quad (3.34)$$

This velocity is applied *at* the wall in the BLI model. Figure 3.4(b) shows that this location is wrong:  $v_{\perp b}$  is valid at the dashed line, not at the solid line. However, this location is only slightly wrong compared to any characteristic length of the geometry, provided that the geometric constraints are satisfied. The first term in the above expression is the well-known isentropic acoustic pressure gradient from the Euler equation. This term vanishes at fixed walls. There, the second term, which contains the viscothermal effects, is more important. Bossart's method to determine the still unknown tangential wave number  $k_{\parallel}$  is presented later.

### 3.2.3 Acoustic pressure

Because the velocity between the boundary layer and the bulk is applied as a boundary condition at the wall, the entire domain in the BLI model can be modeled with the isentropic acoustic Helmholtz equation that is valid in the bulk; see figure 3.4(b). Bossart [10] demonstrated the BLI model for BEM. Nevertheless, his framework is directly applicable to FEM, as presented below.



**Figure 3.4:** Plane wall reflection of an harmonic plane wave, with incident wave  $\mathcal{I}$ , angle of incidence  $\theta$  and reflected wave  $\mathcal{R}$ . On the boundary layer scale, the pressure is nearly uniform. The perpendicular velocity just outside the boundary layer  $v_{\perp b}$  is shown.

### FEM for the pressure field

The weak form of the isentropic acoustic Helmholtz equation (1.9) is used in the BLI model and reads

$$k_0^2 \langle p_w, p \rangle - \langle \nabla p_w, \nabla p \rangle = i k_0 Z_0 \langle p_w, h_{\text{BLI}} \rangle_{\partial\Omega}. \quad (3.35)$$

The symbol  $h_{\text{BLI}}$  denotes the normal velocity, applied as a natural boundary condition (BC). This velocity satisfies  $h_{\text{BLI}} = -v_{\perp b}$  as expressed in equation (3.34). The pressure gradient term in this equation can be replaced by the wall's normal velocity  $v_{\text{wall}}$ , and the second term contains the significant viscothermal effects. The natural BC now reads

$$h_{\text{BLI}} = v_{\text{wall}} + \frac{p}{Z_0 \zeta_{\text{BLI}}}, \quad (3.36a)$$

where  $\zeta_{\text{BLI}}$  is the dimensionless impedance caused by the the viscothermal boundary layer effects:

$$\zeta_{\text{BLI}} = \left[ \frac{k_{\parallel}^2}{k_0^2} \frac{k_0}{k_v} + (\gamma - 1) \frac{k_0}{k_h} \right]^{-1}. \quad (3.36b)$$

Bossart's derivation [10] uses  $v_{\text{wall}} = 0$ , a fixed wall.

Alternatively, the usual isentropic acoustic boundary conditions can be prescribed (pressure, normal velocity or impedance).

### The tangential wave number

Because initially, the tangential wave number  $k_{\parallel}$  is unknown, the BLI model is first solved with an estimate of this parameter (Bossart suggests  $k_{\parallel}^2/k_0^2 =$

0.5). Subsequently, this initial pressure solution is used to update the tangential wave number with (recall  $k_{\parallel}^2 p = -\Delta_{\parallel} p$ )

$$\frac{k_{\parallel}^2}{k_0^2} = \min \left( \left| \frac{(\nabla \nabla p) : (\mathbf{t}_1 \mathbf{t}_1 + \mathbf{t}_2 \mathbf{t}_2)}{-k_0^2 p} \right|, 1 \right), \quad (3.37)$$

where  $\mathbf{t}_1$  and  $\mathbf{t}_2$  are the mutually perpendicular unit vectors tangential to the boundary surface. In 2-D there is only one tangential boundary vector and the other may be taken as zero. Equation (3.37) should be similar to equation (3.32) and yield a positive real valued result smaller or equal to unity. Therefore, the absolute value and threshold of unity are used. Bossart's publication [10] is unclear on the precise method for calculating  $k_{\parallel}$ . He may have used a slightly different method than equation (3.37).

Quadratic FEM shape functions are used for the pressure field  $p$  to permit the calculation of the tangential wave number (3.37). Linear shape functions cannot be used, because their second derivatives equal zero. Nevertheless, quadratic shape functions still give errors because of their  $\mathcal{C}^0$  continuity at the element boundaries.<sup>3</sup> A tangential wave number (or equivalently, a tangential Laplacian) also appears in the viscothermal acoustic BEM formulation of Cutanda Henríquez [20].

Once the updated wave number has been calculated from the initial pressure solution with equation (3.37), it can be used in the second and final calculation of the pressure field. Nijhof [55] proposes a BLI model that calculates the solution with a single pressure calculation. He uses an alternative boundary condition that contains the second order spatial derivative of the pressure.

### 3.2.4 Fluid structure interaction with the BLI model

Since the BLI model uses the isentropic acoustic Helmholtz equation, the fluid structure interaction with the BLI model is rather similar to fluid structure interaction with isentropic acoustics. Only the normal velocity and normal load (pressure) of the two domains are coupled. The temperature and shear velocities are not coupled, because non-homogeneous boundary conditions of these variables cannot be prescribed in the BLI model. The coupled normal velocity boundary condition on the fluid is

$$\begin{aligned} v_{wall} &= i\omega u_n, \\ v_{wall} &= \dot{u}_n, \end{aligned} \quad (\text{natural fluid BC at } \partial\Omega_{FSI}), \quad (3.38)$$

---

<sup>3</sup>Interesting research on smoother shape functions is done by, for example, Hughes [32]. This reference shows general advantages of NURBS (non-uniform rational B-splines) shape functions in FEM for the Helmholtz equation.



where  $v_{wall}$  is part of the natural boundary condition of equation (3.36). Since the normal velocity of the structure either  $\dot{u}_n$ , or  $i\omega u_n$  depends on the unknown structure DOFs, this boundary condition ends up in  $\mathbf{F}_{s \rightarrow a}$  in the system matrix of equation (1.31). The normal load on the structure, given as a vector in the global coordinates is

$$\mathbf{f}_s = p\mathbf{n} \quad (\text{structure load at } \partial\Omega_{FSI}), \quad (3.39)$$

with  $\mathbf{n}$  the unit vector normal to the boundary, away from the fluid domain. This coupling term forms  $\mathbf{F}_{a \rightarrow s}$  in the system matrix of equation (1.31).

### 3.2.5 BLI algorithm

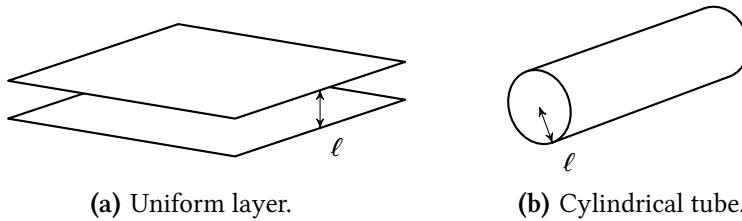
The calculations in the BLI model are given below, step-by-step

1. Calculate the initial solution of the pressure  $p$  with FEM, using the weak form (3.35), and the natural normal velocity BCs (3.36) or the essential pressure BCs. Use an estimate of  $k_{\parallel}^2/k_0^2 = 0.5$  (proposed by Bossart [10]) or a better guess in the normal velocity BCs. This step can include FSI.
2. Update the estimate of the tangential wave number  $k_{\parallel}$  with the solution from the previous step and equation (3.37).
3. Solve the FEM problem of the pressure for the second and final time, but now with the updated tangential wave number  $k_{\parallel}$  from the previous step in the normal velocity BC's. This step can include FSI.
4. If needed, calculate the temperature, density and velocity from the viscous, thermal and pressure fields, using equations (3.29), and (3.27). If an accurate expression for the perpendicular velocity in the boundary layer is required, use equation (3.33).

## 3.3 The low reduced frequency model

The Low Reduced Frequency (LRF) model describes viscothermal acoustics in tubes and layers (waveguides) that have a cross section smaller than the acoustic wavelength (below the cut-off frequency). The LRF model has two major assets. First, it covers the complete range from isentropic acoustics to linearized harmonic Reynolds flow [5], unlike the BLI model. Second, it is computationally efficient. The solving time is typically near that of 1-D or 2-D isentropic acoustic waveguide models. Analytic solutions can be derived for some cases.

According to Tijdeman, whose article [68] is a recommended introduction to the LRF model, the origin of the model is Zwikker and Kosten's



**Figure 3.5:** The uniform layer and cylindrical tube are prototypical geometries for the LRF model. Their characteristic length scales  $\ell$  are the thickness and radius respectively.

book [72] from 1949. Other recommended works on the LRF model are Belman's PhD thesis and journal papers [5, 6, 7]. Nijhof [55] presents the LRF model in a very general form. Many other authors have written articles on the subject, often without using the name 'LRF' coined by Tijedeman.

This section presents the basic form of the LRF model with a focus on two geometries: the uniform layer and the cylindrical tube; see figure 3.5.

### 3.3.1 Geometric constraints

A decomposition of the coordinates, gradients, velocity and momentum equation into the, mutually perpendicular, *propagation direction* and *cross section direction* is needed before the geometrical constraints can be stated. This decomposition of the geometry is listed in table 3.1 for the cylindrical tube and the uniform layer. The propagation directions are simply the directions in which wave propagation is assumed: the 2-D plane for layers or the 1-D axial direction for tubes. The cross section directions are perpendicular to the propagation directions: the 2-D directions on a circle surface for the cylindrical tube or the 1-D direction across the thickness for the layer. As shown later, the viscous and thermal fields depend only on the cross section coordinates, while the pressure field only depends on the propagation coordinates.

The geometric constraints for the LRF models especially concern the cross section geometry's size. A convenient measure of this size is the *hydraulic radius*,  $\ell$  in [m], defined as

$$\ell \equiv 2S_{cd}/P_{cd}, \quad (3.40)$$

with  $S_{cd}$  the cross section surface area and  $P_{cd}$  its perimeter. The hydraulic radii of the cylindrical tube and the uniform layer are the tube radius and the layer thickness respectively, as shown in figure 3.5. The advantage of

Symbol	Cylindrical tube	Uniform layer
$\Omega$	Volume $\Omega_{pd} \times \Omega_{cd}$	Volume $\Omega_{pd} \times \Omega_{cd}$
$\Omega_{pd}$	1-D axial line	2-D layer plane
$\Omega_{cd}$	2-D circle	1-D line
$\partial\Omega_{pd}$	Line endpoints	Layer edge
$\partial\Omega_{cd}$	Circle edge	Line endpoints

**Table 3.1:** Example of the domains and boundaries used in the LRF model. The subscripts  $pd$  and  $cd$  denote propagation direction and cross section direction respectively.

using the hydraulic radius as the length scale is that it makes all cross sections behave similarly in the isentropic acoustic limit (for large  $\ell$  or high  $\omega$ ); expressed later in equation (3.48).

The four assumptions, or requirements, that lead to the LRF model are

1. The viscous and thermal wave numbers must be much larger than the acoustic wave number; see equation (3.4).
2. The cross section must be much smaller than the acoustic wavelength:

$$k_0 \ell \ll 1. \quad (3.41)$$

The factor  $2\pi$  is omitted for simplicity.

3. The cross section should be uniform, or slowly varying, such that the cross section velocity components can be neglected.
4. The length of the geometry in the propagation direction should be large compared to the boundary layer thickness.

The first requirement is used throughout this chapter. The second requirement allows an approximation of the pressure as uniform over the cross section surface. The dimensionless variable  $k_0 \ell$  appearing in equation (3.41) is called the *reduced frequency*. Therefore, the name ‘low reduced frequency model’ is a statement of the second requirement. The third requirement is standard in acoustics for waveguides. It ensures that the velocity is mainly directed in the propagation directions. The fourth requirement is only necessary to make the viscothermal inlet effects negligible. The errors that result from violation of the third and fourth requirements may be easily compensated by acoustic end corrections in some cases. Therefore, some authors only mention the first two requirements.

### 3.3.2 Viscous and thermal fields

The derivation presented here is different from the derivation presented by Tijdeman [68]. This path is chosen to clearly show the differences and similarities with the sequential linear Navier-Stokes (SLNS) model. The original

derivation is briefly presented at the end of this subsection. The final result of both derivations is of course identical.

The viscous and thermal fields are in general based on the PDE (3.24). However, if the cross section geometry is uniform, the viscous and thermal fields do not vary along the propagation direction and may be calculated for just one cross section (neglecting effects at the waveguide ends).<sup>4</sup> Even if the waveguide cross section is slowly varying, the viscothermal fields may be calculated for each cross section independently. This can be stated in the PDE (3.24) by neglecting the derivatives in propagation direction:

$$\Psi_\phi + k_\phi^{-2} \Delta_{cd} \Psi_\phi = 1. \quad (3.42)$$

Recall that  $\phi$  is a dummy variable that should be replaced by  $h$  or  $v$  for the thermal field or viscous field respectively. Since the propagation direction is removed from this PDE, it can only satisfy boundary conditions on the cross section boundary  $\partial\Omega_{cd}$ . These boundary conditions are similar to equation (3.25):

$$\Psi_\phi = 0 \quad \text{at } \partial\Omega_{cd} \quad (\text{no slip / isothermal}), \quad (3.43)$$

$$\nabla_{n_{cd}} \Psi_\phi = 0 \quad \text{at } \partial\Omega_{cd} \quad (\text{no force / adiabatic}). \quad (3.44)$$

Recall that the Neumann boundary conditions are approximations, see equation (3.16). This approximation is very accurate under the LRF assumptions, because the pressure is nearly uniform over the cross section, or  $\nabla_n p \approx 0$ .

The above problem that defines the viscous and thermal fields can be solved analytically for all layer and some tube geometries. For the typically used no slip and isothermal boundary conditions, these solutions are

$$\Psi_\phi = 1 - \frac{\cos(k_\phi z)}{\cos(k_\phi \ell/2)} \quad \text{with } z = [-\ell/2, \ell/2] \quad (3.45a)$$

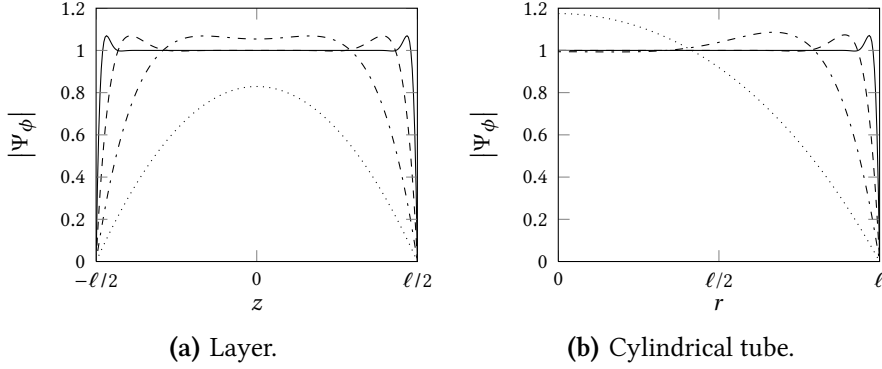
for layers using thickness coordinate  $z$ , and

$$\Psi_\phi = 1 - \frac{J_0(k_\phi r)}{J_0(k_\phi \ell)} \quad \text{with } r = [0, \ell] \quad (3.45b)$$

for cylindrical tubes with radial coordinate  $r$ . The symbol  $J$  denotes the Bessel function of the first kind.

For uniform waveguides (constant  $\ell$ ) the above solutions do not depend on the propagation coordinates. If the waveguide is not uniform, a solution can be calculated at each cross section of interest. Figure 3.6 shows the above

<sup>4</sup>This is comparable to plane strain deformation in mechanics.



**Figure 3.6:** Viscous and thermal fields  $\Psi_\phi$ ; (a) analytic layer solution of equation (3.45a), (b) analytic cylindrical tube solution of equation (3.45b); (—)  $|k_\phi\ell| = 100$ , (---)  $|k_\phi\ell| = 30$ , (-.-)  $|k_\phi\ell| = 10$ , (.....)  $|k_\phi\ell| = 3$ .

analytic solutions which depend on  $|k_v\ell|$  and  $|k_h\ell|$ . The dimensionless parameter  $|k_v\ell|$  is named *shear wave number* by Tijdean and Beltman. It is a measure of the amount of viscous effects: a low value means highly viscous, a high value means nearly isentropic acoustics. Likewise, a dimensionless thermal wave number may be defined as  $|k_h\ell|$ . Both wave numbers are of comparable size and depend on the frequency  $\omega$ , on the characteristic cross section length scale  $\ell$  and on the parameters of the medium.

Besides the presented solutions for layers and cylindrical tubes, analytic solutions for rectangular, equilateral triangular and annular tube cross sections are also available; see appendix A. Furthermore, analytic solutions of  $\Psi_\phi$  for impedance-like boundary conditions have been presented by Kozlov [49]. Notice that the solution for no shear force and adiabatic boundary conditions is unity ( $\Psi_\phi = 1$ ) over the entire cross section surface  $\Omega_{cd}$ .

### Lumping of the viscothermal fields

The next important step in the LRF model is to consider only the mean values of all variables over the cross section (lumping). These mean values, expressed by  $\langle \cdot \rangle_{\Omega_{cd}}$  are, comparable to equation (3.27),

$$\langle \mathbf{v}_{pd} \rangle_{\Omega_{cd}} = \frac{-\Upsilon_v \nabla_{pd} \mathbf{p}}{i k_0 Z_0}, \quad \langle T \rangle_{\Omega_{cd}} = \frac{\Upsilon_h \mathbf{p}}{\rho_0 C_p}, \quad \langle \rho \rangle_{\Omega_{cd}} = \frac{\Upsilon'_h}{c_0^2} \mathbf{p}, \quad (3.46a)$$

where

$$\Upsilon'_h \equiv \gamma - (\gamma - 1) \Upsilon_h \quad (3.46b)$$

is the modified mean thermal field. The symbols  $\Upsilon_\nu$  and  $\Upsilon_h$  are the mean values of  $\Psi_\nu$  and  $\Psi_h$ , defined as

$$\Upsilon_\phi \equiv \langle \Psi_\phi \rangle_{\Omega_{cd}} \equiv S_{cd}^{-1} \int_{\Omega_{cd}} \Psi_\phi \, d\Omega_{cd}. \quad (3.47a)$$

The above equation also defines the lumping operator  $\langle \cdot \rangle_{\Omega_{cd}}$ . The analytic expressions of the mean values of the viscous and thermal fields are for layers

$$\Upsilon_\phi = 1 - \frac{\tan(k_\phi \ell / 2)}{k_\phi \ell / 2}, \quad (3.47b)$$

and for cylindrical tubes

$$\Upsilon_\phi = -\frac{J_2(k_\phi \ell)}{J_0(k_\phi \ell)}, \quad (3.47c)$$

where,  $\phi$  is either  $\nu$  or  $h$ . Analytic solutions for rectangular, equilateral triangular, and annular tube cross sections are again listed in appendix A. Clearly, the mean values of the viscous and thermal fields depend on the dimensionless parameter  $k_\phi \ell$  discussed above.

Figure 3.7 shows  $\Upsilon_\phi$  versus  $|k_\phi \ell|$ , for several geometries. In the isentropic acoustic limit (for high  $|k_\phi \ell|$ ), the fields  $\Upsilon_\phi$  converge to the asymptote

$$\Upsilon_\phi = 1 + \frac{2i}{k_\phi \ell} \quad \text{for } |k_\phi \ell| \gg 1 \quad (3.48)$$

for all cross section geometries. For the geometries shown in figure 3.7, this asymptote is accurate for  $|k_\phi \ell| > 10$ . The low  $|k_\phi \ell|$  asymptote is

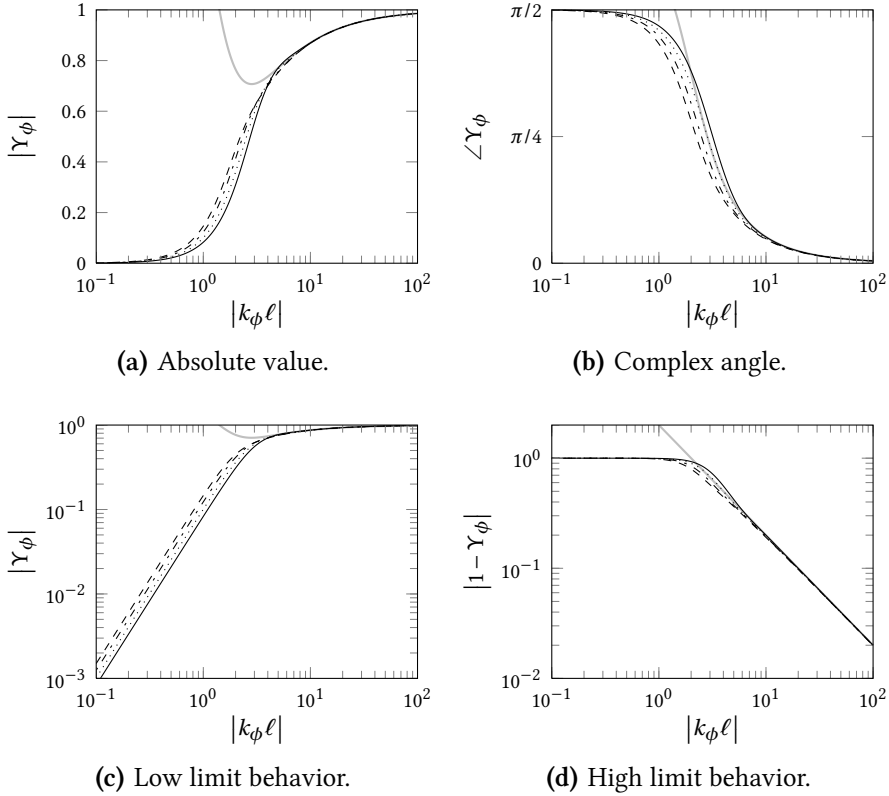
$$\Upsilon_\phi = -K k_\phi^2 \ell^2 \quad \text{for } |k_\phi \ell| \ll 1, \quad (3.49)$$

where  $K$  is a real valued number that depends on the cross section geometry. Cummings [19] has presented a discussion on these asymptotes.

### FEM for the viscothermal fields

For more complicated tube cross section geometries, the solutions of  $\Psi_\phi$  may be calculated with finite elements, see for example [16]. Although this reference does not use the LRF model, the FEM calculation of the viscous and thermal fields is similar. The weak form corresponding to equation (3.42) is

$$\langle \Psi_w, \Psi_\phi \rangle_{\Omega_{cd}} - k_\phi^{-2} \langle \nabla_{cd} \Psi_w, \nabla_{cd} \Psi_\phi \rangle_{\Omega_{cd}} = \langle \Psi_w, 1 \rangle_{\Omega_{cd}} - k_\phi^{-2} \langle \Psi_w, h_\phi \rangle_{\partial\Omega_{cd}}, \quad (3.50)$$



**Figure 3.7:** The mean viscous and thermal fields  $Y_\phi$  as a function of  $|k_\phi \ell|$  (shear wave number or thermal wave number). Sub-figures (c) and (d) show the same data as (a) with a presentation that focuses on the asymptotes for low and high  $|k_\phi \ell|$ . (—) slit / layer, (- · -) circular cross section, (---) triangular cross section, (····) rectangular cross section with aspect ratio 1/6, (—) upper limit asymptote of equation (3.48).

with  $\Psi_w$  the weighing functions and  $\Omega_{cd}$  and  $\partial\Omega_{cd}$  as given in table 3.1. Quadratic Lagrangian shape functions are used for this calculation. The boundary conditions that can be prescribed at  $\partial\Omega_{cd}$  are

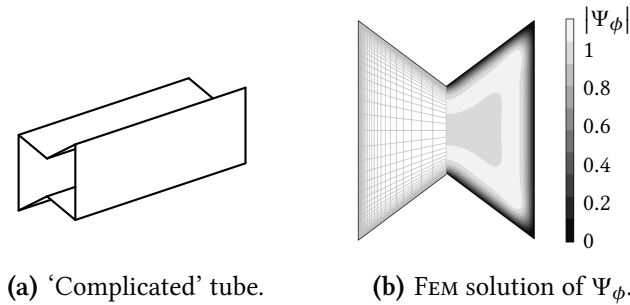
$$\Psi_\phi = 0 \quad (\text{no-slip / isothermal}), \quad (3.51a)$$

$$h_\phi = 0 \quad (\text{no-force / adiabatic}), \quad (3.51b)$$

$$h_\phi = \zeta_\phi^{-1} \Psi_\phi \quad (\text{impedance-like}). \quad (3.51c)$$

The no-force and adiabatic BCs are typically used to model symmetry.

Figure 3.8 shows the field  $\Psi_\phi$  calculated by FEM for a ‘complicated’ tube cross section geometry at the frequency for which  $|k_\phi \ell| = 10$ . Next,  $Y_\phi$  can



**Figure 3.8:** The viscothermal fields for tubes with complicated cross sections can be calculated with FEM; (a) a ‘complicated’ tube (b) the FEM solution of  $\Psi_\phi$  for  $|k_\phi \ell| = 10$  and the used mesh.

be calculated with equation (3.47a). Comprehensibly, the results (not shown in figure 3.7) resemble the curves of the equilateral triangle.

For most cross section geometries, the  $\Upsilon_\phi$ -curves can be fitted by calculating only a few points (that is for a few frequencies). The asymptotes for high and low values of  $|k_\phi \ell|$  are given by equations (3.48) and (3.49). One calculation at very low  $|k_\phi \ell|$  suffices to determine  $K$  in the equation of the asymptote. Additionally, a few points in the mid- $|k_\phi \ell|$  region are needed to fit the transition between the two asymptotes.

### Original derivation

The original derivation is slightly different than presented here. It can be found in Tijdean [68]. Very briefly, it starts with a reduction of the set of PDES (3.10) with the LRF requirements, resulting in

$$\mathbf{v}_{pd} + k_v^{-2} \Delta_{cd} \mathbf{v}_{pd} = \frac{-\nabla_{pd} p}{i\omega \rho_0}, \quad (3.52a)$$

$$T + k_h^{-2} \Delta_{cd} T = \frac{p}{\rho_0 C_p}, \quad (3.52b)$$

$$\nabla \cdot \mathbf{v} / c_0 - i k_0 T / T_0 + i k_0 p / p_0 = 0. \quad (3.52c)$$

Now the solutions of  $T$ ,  $\rho$  and  $\mathbf{v}_{pd}$  in equation (3.27) together with the viscous and thermal fields  $\Psi_\phi$  presented above, are exact solutions of this set of approximate equations if  $p$  is taken uniform over the cross section  $\Omega_{cd}$ .

### 3.3.3 Acoustic pressure

The pressure PDE results from the continuity equation (3.28) after a few steps. First, the equation is integrated over the cross section area. Second, Gauss’



divergence theorem (1.19) is applied to the term containing the cross section velocity. Last, the solution of the propagation velocity (3.46a) is substituted. The final result is

$$\nabla_{pd} \cdot [S_{cd} \Upsilon_v \nabla_{pd} p] + S_{cd} \Upsilon_v k_\ell^2 p = i k_0 Z_0 \vartheta_{cd}, \quad (3.53)$$

with

$$k_\ell^2 \equiv k_0^2 \frac{\Upsilon'_h}{\Upsilon'_v}, \quad (3.54)$$

$$\vartheta_{cd} \equiv \int_{\partial\Omega_{cd}} \mathbf{v}_{cd} \cdot \mathbf{n}_{cd} d\partial\Omega_{cd}, \quad (3.55)$$

where  $k_\ell$  is the LRF wave number in  $[\text{m}^{-1}]$ . The symbol  $\vartheta_{cd}$  denotes the volume flow over the cross section boundary  $\partial\Omega_{cd}$  per unit propagation area or length in  $[\text{m}/\text{s}]$  for layers and  $[\text{m}^2/\text{s}]$  for tubes. Another important quantity is the characteristic LRF impedance  $Z_\ell$ , defined as

$$Z_\ell^2 \equiv \frac{Z_0^2}{\Upsilon'_h \Upsilon'_v}. \quad (3.56)$$

This impedance can be used to rewrite the expression of the velocity in equation (3.46a) in a form that resembles the isentropic acoustic momentum equation (1.11) more closely:

$$\langle \mathbf{v}_{pd} \rangle_{\Omega_{cd}} = \frac{-\nabla_{pd} p}{i k_\ell Z_\ell}. \quad (3.57)$$

Notice that equation (3.53) is similar to Webster's horn equation, discussed in for example Pierce [58]. For uniform cross sections, it reduces to the Helmholtz equation

$$\Delta_{pd} p + k_\ell^2 p = i k_\ell Z_\ell \frac{\vartheta_{cd}}{S_{cd}}. \quad (3.58)$$

Especially if  $\vartheta_{cd} = 0$ , the above equation closely resembles the isentropic acoustic Helmholtz equation (1.9). Different is that the spatial dimensionality is limited to the propagation directions and that the wave number  $k_\ell$  is complex, instead of real valued.

Equation (3.58) may be solved analytically in some cases (uniform tubes) but in general a finite element formulation based on equation (3.53) is advantageous.

### FEM for the pressure field

While the viscothermal fields  $Y_\phi$  on the cross section are typically solved analytically, the pressure field in the propagation coordinates is often solved by FEM; especially if the cross section is not uniform. Therefore, the FEM formulation is based on equation (3.53) in weak form:

$$\begin{aligned} S_{cd} Y_v \left[ k_\ell^2 \langle p_w, p \rangle_{\Omega_{pd}} - \langle \nabla_{pd} p_w, \nabla_{pd} p \rangle_{\Omega_{pd}} \right] \\ = i k_0 Z_0 \left[ \langle p_w, \vartheta_{cd} \rangle_{\Omega_{pd}} + \langle p_w, \vartheta_{pd} \rangle_{\partial\Omega_{pd}} \right], \end{aligned} \quad (3.59)$$

with  $\Omega_{pd}$  and  $\partial\Omega_{pd}$  as given in table 3.1. Quadratic Lagrangian shape functions are used for the pressure.

The term  $\vartheta_{pd}$  results from application of Green's theorem (1.20) and denotes a volume flow. It is defined, using equation (3.46a), as

$$\vartheta_{pd} \equiv S_{cd} \langle \mathbf{v}_{pd} \cdot \mathbf{n}_{pd} \rangle_{\Omega_{cd}}. \quad (3.60)$$

This volume flow has dimension  $[\text{m}^3/\text{s}]$  for tubes and  $[\text{m}^2/\text{s}]$  for layers:  $\vartheta_{pd}$  and  $\vartheta_{cd}$  do not have the same dimensions. This is compensated by their different regions of integration in the weak form.

Fluid structure interaction can be modeled using  $\vartheta_{pd}$  at  $\partial\Omega_{pd}$  and  $\vartheta_{cd}$  at  $\partial\Omega_{cd}$ . Notice that for layers, the integral in  $\vartheta_{cd}$  as described by equation (3.55) is the difference in the velocity at the top of the layer and the bottom of the layer:

$$\vartheta_{cd} = \mathbf{v}_{cd} \Big|_{z=\ell/2} - \mathbf{v}_{cd} \Big|_{z=-\ell/2} \quad (\text{layers}). \quad (3.61)$$

The LRF finite element was previously presented by Beltman [5, 8]. Unfortunately, his weak form contains an error, resulting in a slight violation of the volume conservation for layers or tubes with non-uniform thickness.<sup>5</sup>

### Cross section velocity

In the derivation of the BLI model, everything revolved around an accurate expression for the perpendicular velocity. In the derivation of the LRF model, by contrast, the related cross section velocity  $\mathbf{v}_{cd}$  has only been mentioned to define  $\vartheta_{cd}$ . Nevertheless, all significant viscothermal effects are included. Looking a bit closer, the derivations are not as different as they may seem at first sight. The perpendicular velocity in the boundary layer of the BLI model has been derived from the expressions of the temperature and the

<sup>5</sup>This error can be corrected by multiplying Beltman's weak form by  $B$  in his notation (related to  $Y_v$ ).

shear velocity. Therefore, both the derivation of LRF model and of the BLI model start with the temperature and the shear velocity solutions. These are the important variables that *determine* the perpendicular of cross section velocity.

In the LRF model, an accurate expression of the cross section velocity is not yet derived, because it is not essential for the model. If needed, it may be derived from the continuity equation in the same way as it was done for the BLI model: the temperature and propagation velocity solutions are substituted and the resulting expression is integrated. An example can be found in the appendix of [43]. In any case, the cross section velocity is much smaller than the propagation velocity and the approximation  $\mathbf{v}_{cd} \approx 0$  is valid in that respect. In fact, this has been implicitly used in the derivation of LRF model by assuming a uniform pressure over the cross section.

### 3.3.4 Fluid structure interaction with the LRF model

Like in the BLI model and in isentropic acoustics, the fluid structure interaction with the LRF model only couples the normal velocity and the normal load of the fluid and the structure. The tangential velocity and temperature are uncoupled. Therefore, the fluid structure interaction is a coupling with the pressure LRF calculation (3.59) only; there is no coupling with the calculation of the viscothermal fields.

The fluid structure interaction is a bit more complicated than in the BLI model, because of the lumping over the cross section. The structure can be located at the end of the waveguide  $\partial\Omega_{pd}$  (end of a tube for example) or at the surface of the waveguide  $\partial\Omega_{cd}$  (above or below the layer for example).

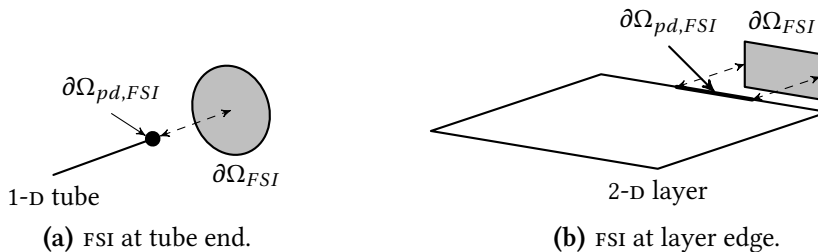
#### Structure at the waveguide end

If the structure is located at the end of the waveguide, see figure 3.9, the coupling involves the boundary conditions of the waveguide. The fluid structure interface  $\partial\Omega_{FSI}$  is typically a surface in the structure model.<sup>6</sup> This surface is coupled to the boundary  $\partial\Omega_{pd,FSI}$  of the LRF model, which is a point for tubes, or an edge for layers. The velocity of the structure is lumped to  $\vartheta_{pd}$  as in equation (3.60) and applied as a natural boundary condition of the LRF weak form (3.59):

$$\begin{aligned} \vartheta_{pd} &= i\omega S_{cd} \langle \mathbf{u} \cdot \mathbf{n}_{pd} \rangle_{\Omega_{cd}}, & (\text{natural fluid BC at } \partial\Omega_{pd,FSI}), \\ \vartheta_{pd} &= S_{cd} \langle \dot{\mathbf{u}} \cdot \mathbf{n}_{pd} \rangle_{\Omega_{cd}}, \end{aligned} \quad (3.62)$$

for displacement or velocity DOFs respectively. Recall that  $\vartheta_{pd}$  is a value in [m<sup>3</sup>/s] for tubes, while for layers it depends on the pd-coordinates along

<sup>6</sup>It can be a line in axi-symmetric models for example.



**Figure 3.9:** Fluid structure interaction with the LRF model: structure at the waveguide end. The FSI interface  $\partial\Omega_{FSI}$  is shown in gray. (a) tube: FSI interface coupled to *boundary point* of 1-D tube; (b) layer: FSI interface coupled to *boundary edge* of 2-D layer.

the boundary and has the dimension  $[\text{m}^2/\text{s}]$ . In both cases it depends on the yet unknown DOFs of the structure. Therefore, the above equation defines  $\mathbf{F}_{s \rightarrow a}$  of equation (1.31) after the weak forms of the fluid and structure are discretized in the standard manner described in section 1.3. In general, the velocity profile at the FSI interface does not match the local velocity of the structure. Only the *volume* velocities over the interface match. The potential errors that are caused by this local velocity mismatch are neglected.

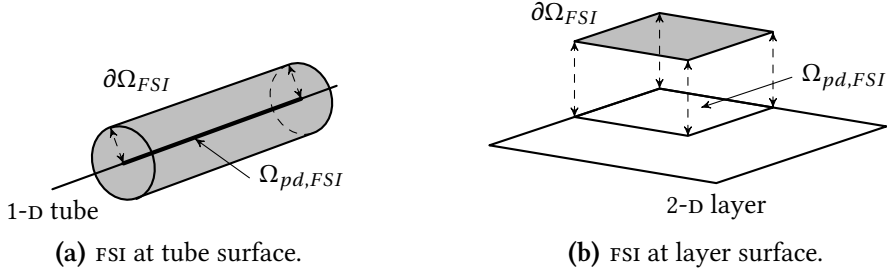
The pressure at  $\partial\Omega_{pd,FSI}$  is applied as a load on the structure. It has a uniform value over the  $cd$ -direction. This means that the load is uniform over the entire surface  $\partial\Omega_{FSI}$  for tubes, while it depends on the  $pd$ -coordinates for layers. This load in normal direction is

$$\mathbf{f}_s = \mathbf{n}_{pd} p \quad (\text{structure load at } \partial\Omega_{FSI}), \quad (3.63)$$

where  $\mathbf{n}_{pd}$  is the normal vector on the boundary pointing away from the fluid. The load depends on the yet unknown pressure DOF(s) of the LRF model and ends up in  $\mathbf{F}_{a \rightarrow s}$  of equation (1.31).

### Structure at the waveguide surface

If the structure is located at the waveguide surface  $\partial\Omega_{cd}$ , the interaction with the LRF model does not involve boundary conditions, but interior source terms; see figure 3.10. The fluid structure interface  $\partial\Omega_{FSI}$  interacts with the interior of the domain on which the pressure is calculated  $\Omega_{pd,FSI}$ , which is a line for the tube and a surface for the layer. The velocity of the



**Figure 3.10:** Fluid structure interaction with the LRF model: structure at the waveguide surface. The FSI interface  $\partial\Omega_{FSI}$  is shown in gray. (a) tube: FSI interface coupled to *interior line* of 1-D tube; (b) layer: FSI interface coupled to *interior surface* of 2-D layer.

structure is lumped to the interior source term  $\vartheta_{cd}$  using equation (3.55):

$$\begin{aligned} \vartheta_{cd} &= i\omega \int_{\partial\Omega_{cd}} \mathbf{u} \cdot \mathbf{n}_{cd} d\partial\Omega_{cd}, \\ \vartheta_{cd} &= \int_{\partial\Omega_{cd}} \dot{\mathbf{u}} \cdot \mathbf{n}_{cd} d\partial\Omega_{cd}, \end{aligned} \quad \begin{array}{l} \text{(fluid source at } \partial\Omega_{pd,FSI}\text{),} \\ \end{array} \quad (3.64)$$

and is included in the weak form (3.59). Recall that  $\vartheta_{cd}$  depends on the  $pd$ -coordinates and has units  $[\text{m}^2/\text{s}]$  for tubes and  $[\text{m}/\text{s}]$  for layers. The lumping for layers is just the summation of the normal velocities above and below the layer, like in equation (3.61). In any case, the source term  $\vartheta_{cd}$  depends on the yet unknown velocity of the structure and ends up in  $\mathbf{F}_{s \rightarrow a}$  of the total system matrix (1.31).

The load of the fluid on the structure is in normal direction and has the magnitude of the local pressure  $p$ . This pressure depends on the  $pd$ -coordinates and is uniform along the cross section boundary  $\partial\Omega_{cd}$ . This can be written as

$$\mathbf{f}_s = \mathbf{n}_{cd} p \quad \text{(structure load at } \partial\Omega_{FSI}\text{),} \quad (3.65)$$

with  $\mathbf{n}_{cd}$  the normal vector at the boundary that points away from the fluid. Because the load depends on the yet unknown fluid pressure  $p$ , the term ends up in  $\mathbf{F}_{a \rightarrow s}$  of the total system matrix (1.31). The exact formulation depends on the structure elements that are used.

### 3.3.5 LRF algorithm

The calculations in the LRF model are given below step-by-step

1. Calculate  $Y_v$  and  $Y_h$ , the mean values of the viscous and thermal fields, on each cross section geometry. This calculation is typically analytical (see appendix A), but optionally by FEM for complicated tube cross sections (equation (3.50)). Use these values to calculate the LRF wave number  $k_\ell$  with equation (3.54).
2. Calculate the pressure field on the propagation geometry, typically by FEM for layers and (smoothly) varying tubes (equation (3.59)). For FEM, the boundary conditions at the waveguide *edge* are the natural normal velocity boundary condition (3.60) involving  $\vartheta_{pd}$  and the essential pressure boundary condition. This calculation can include FSI.
3. If needed, calculate the temperature, density and propagation velocity fields from  $\Psi_v$ ,  $\Psi_h$  (which should be calculated first) and  $p$ , using equation (3.27). The cross section velocity approximately equals zero, but a more accurate expression can be obtained from the continuity equation.

### 3.4 The sequential linear Navier-Stokes model

This section presents the sequential linearized Navier-Stokes model (SLNS). Like in the BLI and LRF models, the fields  $\Psi_h$ ,  $\Psi_v$  and  $p$  are sequentially calculated. Unlike these models, the SLNS model does not require any geometric assumptions. It only uses the approximations from section 3.1. A preliminary version of the SLNS model, in which only the thermal effects are decoupled, is presented in the conference paper [42].

#### 3.4.1 Viscous and thermal fields

The viscothermal fields  $\Psi_v$  and  $\Psi_h$  are calculated with FEM, based on equation (3.24). The weak form of this equation is:

$$\langle \Psi_w, \Psi_\phi \rangle - k_\phi^{-2} \langle \nabla \Psi_w, \nabla \Psi_\phi \rangle = \langle \Psi_w, 1 \rangle - k_\phi^{-2} \langle \Psi_w, h_\phi \rangle_{\partial\Omega}, \quad (3.66)$$

where  $\Psi_w$  are the weighing functions. The dummy variable  $\phi$  can be replaced by  $v$  for the viscous field and by  $h$  for the thermal field. Unlike in the LRF model, equation (3.50), the viscous and thermal fields in the SLNS model are calculated on the complete 3-D geometry.

The boundary conditions for the viscous and thermal fields are:

$$\Psi_\phi = 0 \quad (\text{no-slip / isothermal BC}), \quad (3.67a)$$

$$h_\phi = 0 \quad (\text{no-shear force / adiabatic BC}). \quad (3.67b)$$

For each of the fields  $\Psi_v$  and  $\Psi_h$ , exactly one of the above boundary conditions has to be prescribed at each location on the boundary. The no-slip

and isothermal boundary conditions are essential boundary conditions. Furthermore, the natural no-shear force and adiabatic boundary conditions are approximations, as explained for equation (3.16).

The temperature, velocity and density are given by equation (3.27), with the viscothermal fields from the above calculation and a pressure field that can be calculated with a method that is presented next.

### 3.4.2 Acoustic pressure

The acoustic pressure PDE is derived from the continuity equation (3.28). The weak form of this equation, after application of Green's theorem to the divergence of the velocity, reads

$$k_0^2 \Psi'_h \langle p_w, p \rangle + i k_0 Z_0 \langle \nabla p_w, \mathbf{v} \rangle = i k_0 Z_0 \langle p_w, \mathbf{v} \cdot \mathbf{n} \rangle_{\partial\Omega}. \quad (3.68)$$

The velocity solution of equation (3.27) is substituted into this weak continuity equation, but only at the left-hand side. The velocity term at the right-hand side is used to specify natural velocity boundary conditions. The substitution yields

$$k_0^2 \Psi'_h \langle p_w, p \rangle - \Psi_v \langle \nabla p_w, \nabla p \rangle = i k_0 Z_0 \langle p_w, \mathbf{v} \cdot \mathbf{n} \rangle_{\partial\Omega}. \quad (3.69)$$

The pressure can be prescribed as an essential boundary condition and the velocity or impedance as a natural boundary condition.

This concludes the derivation of the SLNS model. Nevertheless, a few remarks need to be made on the perpendicular velocity.

#### Perpendicular velocity

The perpendicular velocity in equation (3.27) assumed to be proportional to the product of the viscous field and the perpendicular pressure gradient:  $v_\perp \propto \Psi_v \nabla_\perp p$ . This description is inconsistent in one specific case, when both

- The no-slip boundary condition  $\Psi_v = 0$  is prescribed.
- The velocity normal to the boundary is non-zero  $v_n \neq 0$ .

This case is typical for fluid structure interaction problems. If the normal velocity has a finite non-zero value at the boundary where  $\Psi_v$  vanishes then the pressure gradient should locally go to infinity. However, the effect of this inconsistency cannot be local because of the FEM discretization. It is spread out over the region of the shape functions and weighing functions. Nevertheless, the inconsistency could lead to problems, especially if the mesh for the pressure calculation is very *fine* near the concerned boundary. No problems are found regarding the conservation of mass. The inconsistency only matters for the pressure and its gradient. Fortunately, the



**Figure 3.11:** Two extremes of fluid structure interaction problems. In ‘piston’ problems, the viscous effects at the piston can be neglected. In ‘squeeze film’ problems, viscous effects at the moving structure are important and cannot be neglected, but the errors remain small.

pressure (which is used in FSI) is much less affected than the pressure gradient.

The examples that are presented in chapter 4 show that the results of the SLNS model in which inconsistency is neglected may be fully acceptable. Nevertheless, two methods to circumvent or reduce the error are discussed for the cases that require more accuracy

1. Prescribe the slip boundary condition  $\nabla_n \Psi_\nu = 0$ .
2. Use a coarse mesh for the pressure calculation.

The first method circumvents the problem, but it is only applicable if the wave propagates in the direction normal to the vibrating boundary. In this case the viscous effects at this boundary can be neglected anyway; see equation (3.33). Thermal effects can still be taken into account. This type of problem is labeled ‘piston-like’; see figure 3.11(a). The method of using slip bcs is not applicable in the other extreme: a ‘squeeze film’ problem, see figure 3.11(b). Interestingly, the errors remain relatively small in this case if no extra measures are taken, because the normal velocity can be neglected with respect to the tangential velocity; see section 4.3 for an example. Therefore, a rule of thumb is: *use slip-BCs at the FSI boundary in piston-like problems.* This rule is validated in section 4.4.

The second method is effective for all types of problems. Since the acoustic wavelength is much larger than the boundary layer thickness, it does not lead to inaccuracies. Furthermore, it can be recommended to reduce the computational costs. One issue should not be overlooked: the coarse mesh method needs a higher order numerical integration to accurately take the viscothermal fields into account. Its effectiveness in an FSI problem is demonstrated in section 4.4. Using a coarse mesh for the pressure calculation is also beneficial for problems without the normal velocity inconsistency; see section 4.2.3 for an example.

### A weak form without the normal velocity inconsistency

The weak form (3.69) could be changed by using another expression for the normal component (perpendicular component  $v_\perp$  to be more precise) of the



velocity. An accurate expression of this velocity component derived for the BLI model is equation (3.33). This equation reduces to the isentropic acoustic momentum equation (Euler equation)  $v_{\perp} = -\nabla_{\perp} p / (i k_0 Z_0)$  if the first order small terms are neglected. With this expression of the perpendicular velocity, the weak form (3.69) changes to

$$k_0^2 \Psi'_h \langle p_w, p \rangle - \Psi_v \langle \nabla p_w, \nabla p \rangle - (1 - \Psi_v) \langle \nabla_{\perp} p_w, \nabla_{\perp} p \rangle = i k_0 Z_0 \langle p_w, \mathbf{v} \cdot \mathbf{n} \rangle_{\partial\Omega}. \quad (3.70)$$

The research on the SLNS model started with this weak form rather than with equation (3.69). It does not have the inconsistency and works well if boundaries are aligned with a coordinate direction. However, the results were poorer than with the weak form (3.69) in other cases. Small errors even appeared in problems without fluid structure interaction. The weak form (3.70) needs a robust implementation of the perpendicular gradient  $\nabla_{\perp}$ , which has not been found. Therefore, the SLNS model is proposed with the weak form (3.69). Nevertheless, further research could consider both weak forms.

### 3.4.3 Fluid structure interaction with the SLNS model

Fluid structure interaction with the SLNS model resembles that of isentropic acoustics: only the normal velocity and load are coupled. The velocity of the structure is prescribed as a natural boundary condition in equation (3.69) as

$$\begin{aligned} \mathbf{v} \cdot \mathbf{n} &= i\omega u_n, \\ \mathbf{v} \cdot \mathbf{n} &= \dot{u}_n, \end{aligned} \quad (\text{natural fluid BC at } \partial\Omega_{FSI}). \quad (3.71)$$

Either boundary condition defines the sub-matrix  $\mathbf{F}_{s \rightarrow a}$  in equation (1.31).

The normal load on the structure is the pressure  $p$

$$\mathbf{f}_s = p \mathbf{n} \quad (\text{structure load at } \partial\Omega_{FSI}), \quad (3.72)$$

where  $\mathbf{n}$  is the unit vector, normal to the boundary, away from the fluid domain. This equation defines  $\mathbf{F}_{a \rightarrow s}$  in equation (1.31). The above discussion on the normal velocity inconsistency applies to this part of the FSI, because  $p$  can become inaccurate at the boundary.

The tangential velocities and temperature are uncoupled like in the other models in this chapter.

### 3.4.4 SLNS algorithm

The calculations in the SLNS model are given below step-by-step

1. Calculate  $\Psi_v$  and  $\Psi_h$  with FEM, using the weak form (3.66) and the homogeneous boundary conditions (3.67).

2. Calculate the pressure field with FEM, using the weak form (3.69) and the usual acoustic boundary conditions: pressure (essential) or velocity/impedance (natural), possibly including FSI.
3. If needed, calculate the temperature, density and velocity solutions from the viscous, thermal and pressure fields; equation (3.27).

## 3.5 Comparison of the models

Many viscothermal acoustic problems can be modeled with the four models presented in this thesis. This section discusses and summarizes some general differences between these models, with a focus on the new SLNS model. The next chapter validates the models and assesses their performance on several sample problems.

### 3.5.1 Summary: advantages and disadvantages per model

A brief overview of the advantages (✓) and disadvantages (✗) of each presented model is given below.

#### Full linearized Navier-Stokes model

- ✓ Direct FEM implementation of the governing equations, without further approximations.
- ✓ Non-homogeneous viscothermal boundary conditions (like non-zero shear velocity) and body sources (like heat) can be applied straightforwardly.
- ✓ This model can be regarded as the reference model.
- ✗ Computationally very costly, especially in 3-D: 5 coupled fields, fine mesh in the boundary layers.
- ✗ Proper meshing is cumbersome, but important to keep the computational costs as low as possible.<sup>7</sup>

#### Boundary layer impedance model

- ✓ Much like isentropic acoustics: only the boundary conditions are different.

---

<sup>7</sup>Joly [37] presents an interesting adaptive mesh refinement procedure for a (slightly different) viscothermal acoustic finite element.

- ✓ Computationally efficient: the pressure field is the only FEM degree of freedom and a coarse mesh may be used because there are no boundary layers to be meshed. The pressure is calculated twice.<sup>8</sup>
- ✗ Only accurate for problems that are just slightly viscothermal: all characteristic lengths of the geometry should be much larger than the viscothermal boundary layer thickness.
- ✗ Requires the tangential wave number (tangential Laplacian of the pressure field) which introduces an additional source of error if standard  $\mathcal{C}^0$  continuous shape functions are used.<sup>9</sup>

### Low reduced frequency model

- ✓ Computationally very efficient: viscothermal fields are usually solved analytically; the pressure field is modeled as 1-D or 2-D and can be coarsely meshed in FEM.
- ✓ Much research has proven its accuracy and applicability.
- ✓ The pressure calculation is much like an isentropic acoustic calculation. Furthermore, the isentropic acoustic end corrections can be used to effectively reduce some common errors; see Nijhof [55].
- ✗ Only applicable to tubes and layers below the cut-off frequency, with slowly varying cross sections.
- ✗ Non-homogeneous viscothermal boundary conditions or body sources (heat or force) introduce additional fields.

### Sequential linearized Navier-Stokes model

- ✓ Computationally much more efficient than the FLNS model, but less efficient than the BLI and LRF models: three fields (viscous, thermal and pressure) are calculated sequentially, on a 3-D mesh that is fine in the boundary layers.<sup>10</sup>
- ✓ The modeled geometry does not need to satisfy geometric constraints (unlike for the BLI and LRF models).
- ✓ The pressure calculation is much like an isentropic acoustic calculation. Acousto-elastic interaction is also modeled similarly.

---

<sup>8</sup>Nijhof [55] proposes a formulation of the BLI model in which only one pressure calculation is needed.

<sup>9</sup>Cutanda Henríquez viscothermal acoustic BEM model [20] also contains a tangential Laplacian.

<sup>10</sup>The mesh for the viscous and thermal fields should be fine. The pressure can be calculated on the same mesh or on a coarser mesh, provided that the numerical integration takes the viscothermal fields into account, see section 4.2.3.

- ✓ The model consists of three uncoupled Helmholtz equations, which are thoroughly studied in the literature.<sup>11</sup>
- ✗ Non-homogeneous viscothermal boundary conditions or body sources (heat or force) introduce additional fields.
- ✗ No-slip boundaries with non-zero normal velocities are inconsistent and can lead to errors. Fortunately, these errors are typically small. Moreover, two methods to reduce or circumvent the inconsistency have been presented.

### 3.5.2 Discussion: paradigms for the SLNS model

The SLNS model is related to isentropic acoustics and to the other viscothermal acoustic models in this thesis (FLNS, LRF and BLI). Therefore, the SLNS model can be regarded in several ways, each emphasizing the relation to one of these other models:

- The SLNS model is an approximation of the FLNS model, based on the difference between wavelength and boundary layer thickness (equation (3.4) and figure 1.4).
- The LRF model is a lumped SLNS model. This lumping process requires the LRF geometric constraints. Still, the structure of the two models is much alike.
- The SLNS is an isentropic acoustic model in which the thermal effects are accounted for by pressure dependent distributed monopole sources. Likewise, the viscous effects are accounted for by pressure gradient dependent distributed dipole sources.
- The BLI model is an SLNS model in which the effects of the viscous and thermal fields are lumped to the boundary.

---

<sup>11</sup>Only the standard Galerkin method is used in this thesis. The review article of Thompson [67] is recommended as an introduction to more refined FEM formulations.



## Validation and performance analyses

This chapter presents a selection of tests to demonstrate the validity and performance of the four viscothermal acoustic models presented in the previous chapters. These test problems are relatively simple, but illustrative for the strengths and weaknesses of the different models.

Section 4.1 presents models for waveguide geometries. These geometries are accurately described by the LRF model and the performance of the other models is compared to it. A few convergence tests show that the FLNS and SLNS model have a similar performance on identical FEM meshes, provided that the pressure field is sufficiently interpolated.

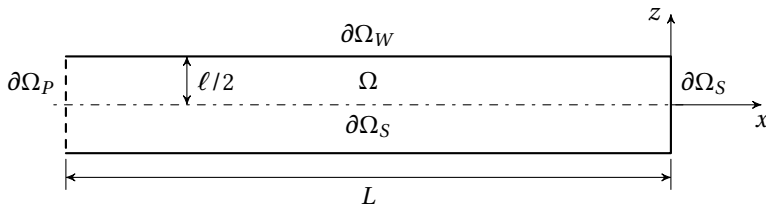
More interesting geometries are modeled in section 4.2: two resonators for an impedance tube setup. In this section, the four viscothermal acoustic models (FLNS, BLI, LRF and SLNS) are compared to measurements. One of the resonators is best modeled with the BLI model and the other with the SLNS model. This section also explores the use of coarser meshes for the pressure calculation in the SLNS model.

Section 4.3 presents an axi-symmetric microphone model. This model includes fluid structure interaction with a membrane. The analytic model listed in Cutanda Henríquez's thesis [20] models the same problem and is reused here as an additional reference. It makes an indirect comparison with Cutanda's BEM model possible.

The SLNS model contains an inconsistency if a non-zero velocity is prescribed at a no-slip boundary. This inconsistency may lead to inaccuracies in the SLNS model. Section 4.4 presents a study of these inaccuracies with fluid structure interaction problems. The proposed methods for improvement are discussed. The chapter ends with a summary of the results.

### 4.1 Waveguides

The first models in this chapter describe a 2-D slit. The LRF model accurately describes these problems, if the thickness of the slit is much smaller than



**Figure 4.1:** The geometry of the slit. Only half the slit is modeled in FEM, because the problem is symmetric.

the acoustic wavelength. There is little need for the other models for such geometries. However, the waveguide problem is well suited to show the convergence of these other models. An important convergence test to validate the FLNS model has already been presented in [43]; see appendix B. Therefore, this section uses a somewhat different approach.

#### 4.1.1 Frequency response of slit near resonance

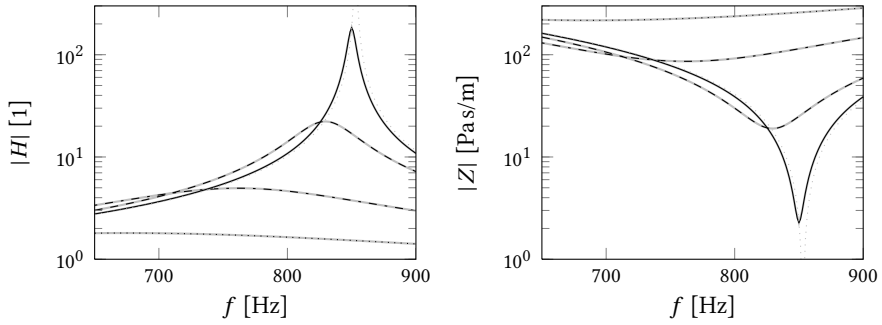
The geometry of the slit is shown in figure 4.1. The slit has a length of  $L = 0.1$  m, is closed at the right end and has a unit pressure source at the left end, see figure 4.1. This figure also shows the coordinate system with the propagation coordinate  $x = [-L, 0]$  and the cross section coordinate  $z = [-\ell/2, \ell/2]$ . The analytic LRF solution of the slit problem is

$$\hat{p} = \frac{\cos(k_\ell x)}{\cos(k_\ell L)}, \quad \hat{v}_x = \frac{\Psi_v / Y_v \sin(k_\ell x)}{i Z_\ell \cos(k_\ell L)}, \quad (4.1)$$

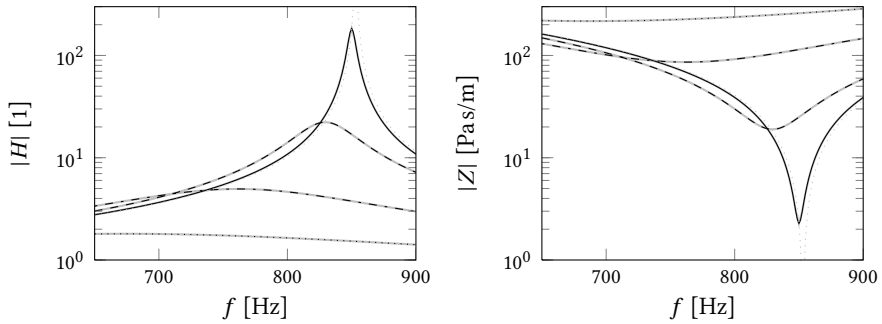
with the layer solutions of the viscothermal fields  $\Psi_v$  (and  $\Psi_h$ ) and the corresponding mean values  $Y_v$  (and  $Y_h$ ) as defined for the layer in equations (3.45a) and (3.47b), and the LRF wave number  $k_\ell$  and characteristic impedance  $Z_\ell$  from equations (3.54) and (3.56). The hat on  $\hat{p}$  and  $\hat{v}_x$  denotes that it is the reference solution.

Only half the geometry is modeled in the finite element models, because the solution is symmetric across the line  $z = 0$ . The boundary conditions for the FLNS model are shown in figure 4.1 and are defined in table 2.2. The corresponding boundary conditions for the SLNS and BLI models are listed in table 4.1, where  $\nabla_n$  denotes the gradient in normal direction.

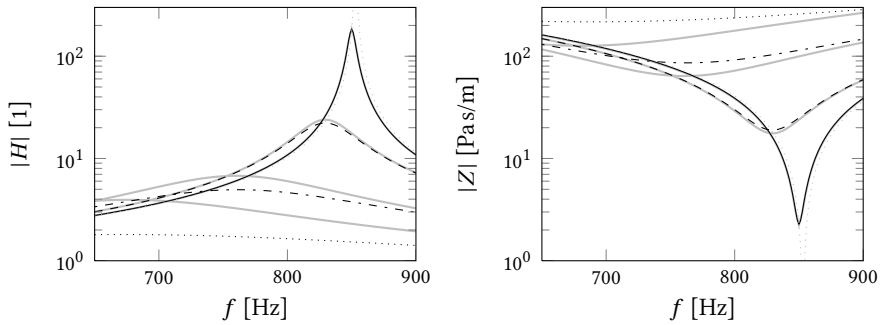
The frequency response curves near the quarter wavelength resonance frequency are shown in figure 4.2 for several slit thicknesses:  $\ell = [1/4, 1/2, 2, 16]$  mm. Two quantities are plotted. The first is the magnitude of the pressure transfer function, defined as the pressure at the closed end of the slit divided by the input pressure (of unity)  $H = p|_{x=0} / p|_{x=-L}$ . The second quantity is the magnitude of the impedance at the open end of the slit



(a) FLNS versus LRF.



(b) SLNS versus LRF.



(c) BLI versus LRF.

**Figure 4.2:** Absolute values of pressure transfer function  $|H|$  and input impedance  $|Z|$ . The LRF model is used as the reference with slit thickness  $\ell$  16 mm (—), 2 mm (---), 0.5 mm (-·-·-), 0.25 mm (·····). The isentropic acoustic solution is also shown (·····). The LRF solutions are compared to (a) the FLNS, (b) the SLNS and (c) the BLI solutions, (— for each). The BLI model underestimates the dissipation if the viscothermal boundary layers become thicker.



FLNS BC	SLNS BCS	BLI BC
$\partial\Omega_W$	$\Psi_\phi=0, \nabla_n p=0$	$v_{wall}=0^*$
$\partial\Omega_S$	$\nabla_n \Psi_\phi=0, \nabla_n p=0$	$\nabla_n p=0$
$\partial\Omega_P$	$\nabla_n \Psi_\phi=0, p=1$	$p=1$

\* in the BC of equation (3.36)

**Table 4.1:** Boundary conditions for the SLNS and BLI models that correspond to the FLNS BCS that are defined in table 2.2.

$\ell$ [mm]	$ k_v \ell $	$ k_h \ell $
16	[262, 308]	[223, 262]
2	[33, 38]	[28, 33]
0.5	[8.2, 9.6]	[7.0, 8.2]
0.25	[4.1, 4.8]	[3.5, 4.1]

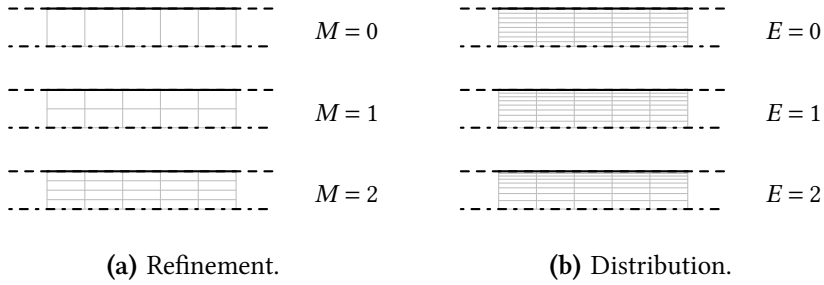
**Table 4.2:** Ranges of the shear wave number  $|k_v \ell|$  and the thermal wave number  $|k_h \ell|$  corresponding to the used frequency range  $f = [650, 900]$  Hz and layer thicknesses.

$Z = p|_{x=-L}/\vartheta|_{p=-L}$ . The LRF results are drawn with black lines. The slit thickness clearly influences the magnitude of the resonance peak and the resonance frequency. The gray lines in the figure represent the results from the FLNS, SLNS and BLI models. Very good agreement to the LRF model is obtained with the FLNS and SLNS models. By contrast, but in line with expectations, the results of the BLI model are only accurate for the larger slit thicknesses. Figure 4.2(c) shows a small error for the tube with  $\ell = 2$  mm near the resonance frequency. Notice that the shear wave number is approximately 30 at the resonance frequency. This means that the BLI model contains a noticeable error even before the boundary layers at opposite boundaries overlap. However, the error is very small further from the resonance frequency.

#### 4.1.2 Convergence of the slit problem

A convergence study for the FLNS and SLNS models is presented for the same slit problem as in the previous sub-section, with  $\ell = 2$  mm and  $f = 835$  Hz, which is near the resonance. The analytic LRF solutions (4.1) are used as the reference in the relative error measures that are defined as

$$e_p = \frac{\|p - \hat{p}\|}{\|\hat{p}\|}, \quad e_{v_x} = \frac{\|v_x - \hat{v}_x\|}{\|\hat{v}_x\|}, \quad (4.2)$$



**Figure 4.3:** Mesh sequences used in the convergence studies: in (a) the number of elements across the half slit is  $2^M$ , in (b) the largest element is a factor  $2^E$  thicker than the smallest element. Only a small part of the slit length is shown.

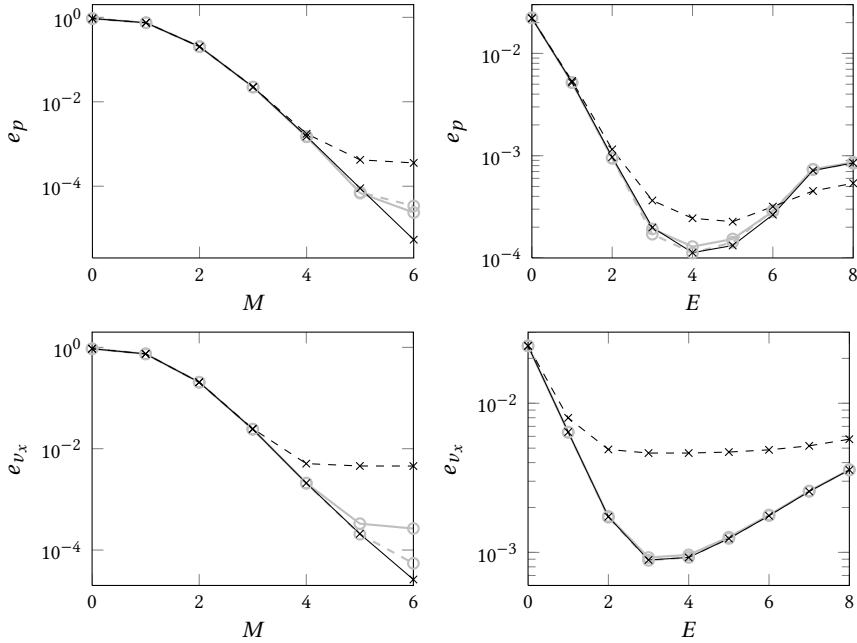
with  $\|\phi\| \equiv \sqrt{\langle \phi, \phi \rangle}$  and  $\langle \phi, \phi \rangle$  as defined in equation (2.24). These error measures quantify the difference with the reference solution (the LRF model here).

The results shown in figure 4.2 have been calculated on a fine FEM mesh. For the convergence test, several mesh cases are used. These are subdivided into two mesh sequences. The first mesh sequence runs with parameter  $M$  from a coarse to a fine mesh, as shown for the first three meshes in figure 4.3(a). The element length remains 1 mm for each mesh in this sequence and the element thickness is  $2^{-M}$  mm. The second mesh sequence has 8 elements over the thickness, but the distribution of the element thicknesses is exponential, not uniform; see figure 4.3(b). The ratio of the thickness of the largest element over the thickness of the smallest element is  $F$ , and the mesh parameter  $E$  defines this ratio as  $F = 2^E$ . The  $z$ -coordinates of the element edges are

$$\tilde{z}_n = \frac{z_n}{\ell/2} = 1 - \frac{1 - F^{\frac{n}{N-1}}}{1 - F^{\frac{N}{N-1}}}, \quad \text{with } n = 0, 1, \dots, N \text{ and } F > 1. \quad (4.3)$$

Here  $N = 8$  for the number of elements. The mesh  $E = 0$  is identical to the mesh  $M = 3$ .

The results for the two mesh sequences and the two error measures are shown in figure 4.4. For  $M \geq 5$ , the SLNS solution better converges to the LRF solution than the FLNS solution does. The reason is that the FLNS model has inlet effects at both the open and the closed end of the slit. These inlet effects are implicitly neglected in the LRF and the SLNS models by using the approximate boundary conditions, see equation 3.16. Furthermore, the inlet effects that are present in the FLNS model are exaggerated because the elements are rather long (1 mm). The influence of the viscous boundary



**Figure 4.4:** Error in the pressure and velocity fields for the slit problem at 835 Hz. The meaning of the mesh parameters  $M$  and  $E$  is shown in figure 4.3. (—) FLNS model with standard BCs; (---) FLNS model with  $v_z = 0$  BCs at  $x = 0$  and  $x = -L$ ; (—) standard SLNS model; (---) SLNS model with bi-linear (instead of bi-quadratic) pressure shape functions.

conditions on the FLNS solution can be easily demonstrated by replacing the zero shear force BC by the zero shear velocity BC at the entrance and the closed end of the slit. In this case, the inlet effects are different (but not absent). The velocity error reduces for these boundary conditions; see figure 4.4. In any case, differences between the FLNS and SLNS solutions are small.

The convergence of the mesh sequence with parameter  $E$  shows that the solution can be improved without adding elements by choosing a distribution with a relatively large number of elements in the boundary layer. However, this should not be exaggerated. There is an optimum near  $E = 4$  ( $F = 16$ ), after which the errors increase; see figure 4.4.

The dashed black line in figure 4.4 shows the convergence for an SLNS model with first order (instead of second order) Lagrangian shape functions for the pressure degrees of freedom. The results show that especially the velocity error is larger in this case. This is understandable, because the velocity solution is reconstructed from the pressure gradient in the SLNS model.

In the convergence study for the FLNS model presented in [43] (appendix B), the elements are refined in both directions (instead of only in the

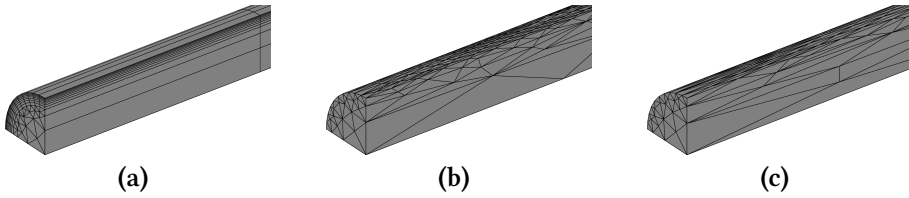
$z$ -direction). In this study, special boundary conditions and body forces and heat sources are used to ensure that the FLNS solution converges to the LRF solution. The convergence rates found in that study conform to the interpolation theory once the number of elements in the boundary layer increases in a subsequent mesh refinement:  $e_{v_x} \propto h^3$ , with  $h$  the characteristic linear size of the finite element. The order of convergence of the pressure degree of freedom is even higher. In figure 4.4, the same convergence rate is obtained by refining only in the  $z$ -direction. Apparently, the mesh is sufficiently fine in the propagation direction.

### 4.1.3 3-D cylindrical tube: element aspect ratio

The above results are all obtained with mapped quadrilateral meshes. However, in many practical problems an unstructured mesh is used. Sometimes it is possible to create a good boundary layer mesh, but not always. Especially in 3-D it can be troublesome to create an adequate boundary layer mesh, such as in figure 2.2. Then, it may be beneficial to use tetrahedral elements with a large aspect ratio. The performance of the SLNS model and two FLNS models with different discretization is tested on a 3-D cylindrical tube problem. The reference solution is again the analytic LRF solution of equation (4.1), but now with the round tube viscothermal field solutions from equations (3.45b) and (3.47c). The frequency is again 835 Hz and the radius of the circular cross section  $\ell = 2$  mm. This problem is axi-symmetrical, but here 3-D models are used. Some advantage of symmetry is used by modeling only a quarter of the tube.

Parts of the three considered meshes are shown in figure 4.5. The boundary layer mesh consist of highly stretched prism and brick elements. The two other meshes are stretched tetrahedral meshes with element aspect ratios of 5 and 10 respectively. This aspect ratio is much smaller than in the boundary layer mesh. The boundary layer mesh has a finer discretization of the boundary layer than the tetrahedral meshes. Therefore, larger errors are expected in the latter.

Table 4.3 shows the results of the Taylor-Hood-like (TH) and Crouzeix-Raviart-like (CR) FLNS FEM formulations and of the SLNS model. For the boundary layer mesh (a), the SLNS model has a lower error than the TH-FLNS model. Different than in the previous study, this difference is not caused by the inlet effects, but by the coarse discretization in the propagation direction (element length  $> 8$  mm). Using a  $v_t = 0$  boundary condition in the FLNS model does not change the error, but halving the element length results in a similar error as for the SLNS model ( $e_p = 3.6 \cdot 10^{-4}$  and  $e_{v_x} = 8.1 \cdot 10^{-4}$ ). Here, the higher order pressure interpolation of the SLNS model is advantageous. Furthermore, the SLNS model is more than 8 times faster to solve than the FLNS model on the same mesh.



**Figure 4.5:** Three meshes: (a) boundary layer mesh; (b) stretched mesh with aspect ratio 5; (c) stretched mesh with aspect ratio 10. Only a small part of the meshes is shown.

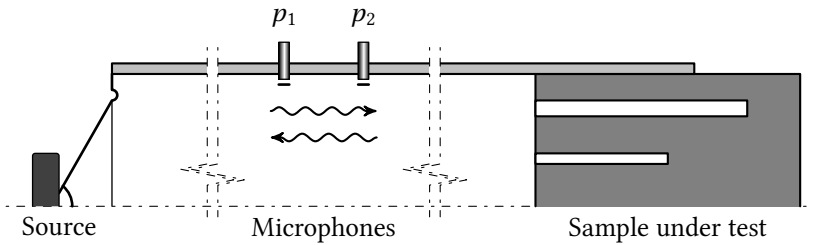
Mesh	Model and FE	# of DOFs	$t_c$ [s]	$e_p$	$e_{v_x}$
(a)	TH FLNS	$44.8 \cdot 10^3$	112	$7.3 \cdot 10^{-4}$	$25 \cdot 10^{-4}$
(a)	SLNS	$(21.7 + 10.8) \cdot 10^3$	7 + 4	$3.4 \cdot 10^{-4}$	$8.3 \cdot 10^{-4}$
(b)	TH FLNS	$114 \cdot 10^3$	55	$5.2 \cdot 10^{-2}$	$5.8 \cdot 10^{-2}$
(b)	CR FLNS	$224 \cdot 10^3$	69	$4.9 \cdot 10^{-2}$	$4.9 \cdot 10^{-2}$
(b)	SLNS	$(55.1 + 27.5) \cdot 10^3$	7 + 4	$5.5 \cdot 10^{-2}$	$5.9 \cdot 10^{-2}$
(c)	TH FLNS	$59.7 \cdot 10^3$	23	$11 \cdot 10^{-2}$	$11 \cdot 10^{-2}$
(c)	CR FLNS	$117 \cdot 10^3$	39	$4.0 \cdot 10^{-2}$	$4.6 \cdot 10^{-2}$
(c)	SLNS	$(28.7 + 14.4) \cdot 10^3$	3 + 2	$5.3 \cdot 10^{-2}$	$5.7 \cdot 10^{-2}$

**Table 4.3:** Errors of several FEM formulations on the meshes of figure 4.5. The Crouzeix-Raviart-like (CR) FLNS element and the SLNS model are more robust in stretched meshes than the Taylor-Hood-like (TH) FLNS element. The number of DOFs and the calculation time per frequency  $t_c$  are listed for comparison.

The errors on the tetrahedral mesh (b) with an element aspect ratio of 5 are similar for each of the entries in table 4.3. If the elements are stretched further to an aspect ratio of 10, mesh (c), the results are different. The TH-FLNS solution deteriorates, while error in the solutions of the other two models even reduces slightly. The SLNS model and the CR-FLNS formulation are more robust for stretched elements than the TH-FLNS formulation. The larger number of pressure degrees of freedom in the CR-FLNS and SLNS models is beneficial. The solving time reduction of the SLNS model versus the FLNS model is not as large as for mesh (a), because the matrix assembly time is relatively large in these smaller models.

## 4.2 Impedance tube samples

The models in the previous section are simple waveguides that have an analytic LRF solution. There is no reason to use finite element models for such



**Figure 4.6:** An impedance tube. The axial symmetry is indicated by the center line. This measurement setup consists of three sections: a source, a measurement section and a sample under test. The tube is drawn with shorter proportions than in reality, as indicated by the break lines.

geometries, other than for the evaluation of the finite elements themselves. By contrast, the problems in this section do not have accurate analytic solutions. Therefore, a numerical method is needed to find an accurate solution. The results of the different viscothermal acoustic FEM models are compared to each other and to measurements.

The measurement setup is an impedance tube. This setup and the used measurement method are presented first. Subsequently, the results of the viscothermal acoustic models for two impedance tube resonators are presented. Furthermore, a faster SLNS model that uses a coarse mesh for the pressure is discussed.

### 4.2.1 Impedance tube setup

The impedance tube setup is drawn in figure 4.6. It is a tube that is narrow with respect to the wavelength, but large compared to the viscous and thermal boundary layer thicknesses. Therefore, the pressure is approximately uniform on each tube cross section, while the viscothermal effects are small. At one end of the tube an acoustic wave is created by a loudspeaker. This wave travels through the tube and interacts with a sample at the other end of the tube. Depending on the sample, part of the incoming acoustic energy is absorbed by viscothermal effects and the rest is reflected back to the loudspeaker. Two microphones placed at a known distance from each other, half way in the tube, are used to measure the pressure. The absorption coefficient can be reconstructed from the measured signals.

The method to calculate the absorption coefficient uses the transfer function between the two microphones. A SIGLAB data acquisition system is used to estimate this transfer function  $H = p_2/p_1$  with standard spectral techniques. MATLAB's function 'resample' is used to slightly smooth the

measurement results. Next, the absorption coefficient can be calculated using:

$$\alpha = 1 - \left| \frac{e^{-ik_0d} - H}{H - e^{ik_0d}} \right|^2, \quad (4.4)$$

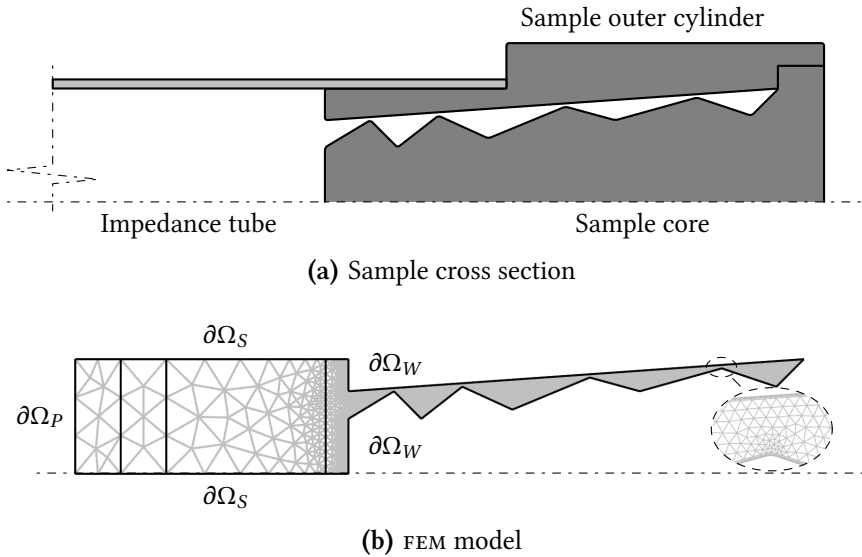
with  $d$  the distance between the two microphones. The absorption coefficient has a value between 0 (no absorption) and 1 (100% absorption) which varies with frequency. Interestingly, in isentropic acoustic models without radiation, the absorption coefficient equals zero everywhere. Viscothermal acoustic models are needed to get a non-zero value of the absorption coefficient. Therefore, the absorption coefficient is well suited to assess the performance of the viscothermal acoustic models. The two samples presented next are rigid acoustic resonators.

### 4.2.2 Jansen's sample

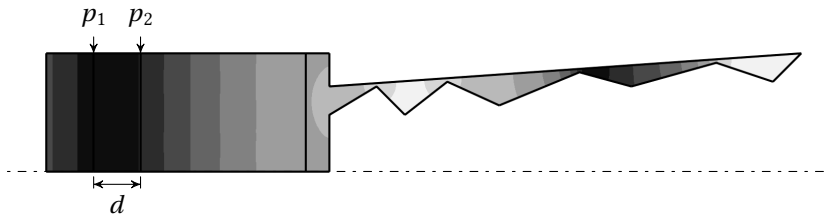
Jansen made a sample for his master's project [35] to demonstrate that the LRF model is inaccurate for waveguides with rapidly varying cross sections. The FLNS model and the SLNS model should not have any problems to handle such geometries. The geometry of Jansen's sample is shown in figure 4.7(a). It is made of two turned parts: the outer cylinder and the core. The sample is modeled with axi-symmetric FEM models. The used geometry, mesh and boundary conditions are shown in figure 4.7(b) and are defined in table 2.2 for the FLNS model. As shown in the figure, the viscothermal effects at the wall of the impedance tube are neglected ( $\partial\Omega_S$  rather than  $\partial\Omega_W$  is used). If these effects were to be taken into account, the mesh needs to be much finer at this wall. Corresponding boundary conditions for the SLNS and BLI models are given in table 4.1. The FEM geometry of the LRF model is the 1-D axial line. The cross section at the axial coordinate is lumped at the corresponding point. The LRF viscothermal fields on the circular (impedance tube) and annular (sample) cross sections are given in appendix A. However, to conform to the other models, the adiabatic slip conditions ( $Y_\nu = 1, Y_h = 1$ ) are used in the impedance tube; not in the sample of course.

After the problem is solved for the frequency range of interest, the absorption coefficient is calculated as a post-processing step. At each frequency, the pressure at two points is used to calculate  $H = p_2/p_1$ ; see figure 4.8. The distance between these points is  $d$  as shown in the figure. Like in the experiments, the absorption coefficient follows from equation (4.4). Figure 4.8 also shows the curved pressure contours in and near the sample, which indicate that the LRF assumptions of uniform pressure on each cross section surface are invalid.

The calculated and measured absorption coefficient curves are shown in figure 4.9. The BLI model underestimates the absorption coefficient. This



**Figure 4.7:** Jansen's sample: (a) schematic drawing of the axi-symmetric cross section; (b) FEM geometry, mesh and boundary conditions.

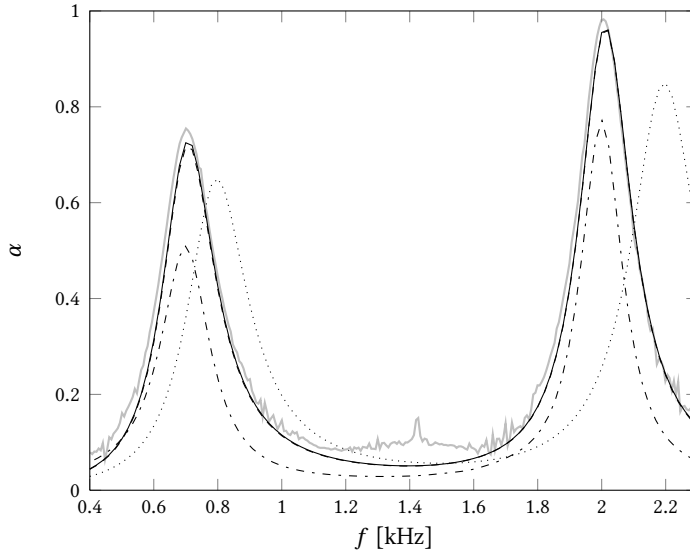


**Figure 4.8:** Pressure magnitude for  $f = 1.7$  kHz. The pressures  $p_1$  and  $p_2$ , at the indicated locations are used to calculate the absorption coefficient. Notice that the pressure contours are curved in and near the resonator.

might have been expected, because the heights of the narrowest passages in the sample are of the same order of magnitude as the boundary layer thicknesses. The LRF model gives worse results. Both the heights and the frequencies of the peaks are erroneous. These errors result from neglecting the momentum in the radial direction, and the viscothermal boundary layer effects in the axial direction. These LRF assumptions are only accurate in waveguides with slowly varying cross sections. The error of neglecting the radial velocity can be compensated for in some cases in isentropic acoustics; see for example [54] for piecewise conical geometries.

The FLNS model's absorption curve closely matches the measured curve in figure 4.9. Furthermore, the results of the SLNS model and the FLNS model





**Figure 4.9:** The absorption coefficient of Jansen’s sample: (—) measurement; (—) FLNS model; (---) SLNS model, partially hidden behind the FLNS curve; (-·-) BLI model; (····) LRF model.

Model	$t_c$ [s]	# of DOFs
FLNS	44	$178 \cdot 10^3$
SLNS	6.8	$(110 + 55) \cdot 10^3$
BLI	0.7	$2 \times 11 \cdot 10^3$
LRF	0.2	254

**Table 4.4:** Calculation time per frequency ( $t_c$ ) and number of DOFs in the different models for Jansen’s sample. The FLNS and SLNS models use the same FEM mesh.

are nearly identical. The same mesh was used for both models. A coarser mesh is used for the BLI model, and a 1-D mesh for the LRF model. Nevertheless, all used meshes are relatively fine: more careful meshing may reduce the computational time without noticeably changing the curves in figure 4.9.

The calculation times per frequency are listed in table 4.4. The SLNS model is approximately six times faster than the FLNS model. This large reduction in computational time did not compromise accuracy. Even higher reductions may be expected for large 3-D problems. Only the FLNS model and the SLNS model can be directly compared, because these use the same mesh. The results of BLI and LRF model can only be compared roughly. Nevertheless, these models clearly have less computational costs.



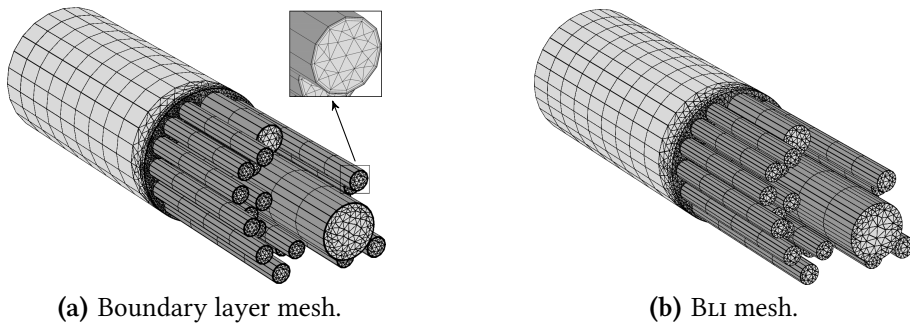
**Figure 4.10:** Photo of Hannink’s sample: twenty tube resonators with different radii and lengths.

Although the LRF model requires the least computational time of the four models, this time is still relatively large. A much lower time may have been expected, because it is a 1-D model with a small number of DOFs. The reason for the relatively long calculation time is that the analytic expression of the annular cross section requires twenty Hankel function evaluations at each integration point; see appendix A. Circular cross sections can be modeled more efficiently.

### 4.2.3 Hannink’s sample

The sample in this subsection has 3-D features that can only be modeled accurately with 3-D models. The sample is created by Hannink [30] as a demonstration of broadband absorption with a limited number (twenty) of tube resonators. These tubes have different radii and lengths, see the photo in figure 4.10. Two different meshes are used in the FEM model: a boundary layer mesh for the FLNS and SLNS models and a coarser mesh for the BLI model, see figure 4.11. Like in the previous sample, the viscous effects are only taken into account on the walls on which these are important. This is especially needed in this large 3-D model, in order to reduce the computational costs. Still, the calculations for this sample do not fit on an average desktop computer: more than 12 GB of RAM is used for the FLNS calculation.

Figure 4.12 shows the pressure magnitude at  $f = 1.667$  kHz, calculated with the BLI model. Some tubes are in resonance depending on the frequency. The absorption coefficient is calculated from the pressure with the same method as described in section 4.2.2. The resulting absorption coefficient curves are shown in figure 4.13. This figure also shows the absorption coefficient curve of a 0-D 2-port network LRF model as described by Van der Eerden [25]. This model does not take the 3-D effects at the tube inlets into account. Instead, the baffled tube end correction has been used in this LRF model: elongation of the tubes with  $\delta_L = \frac{8r}{3\pi}$ . These end corrections are not



**Figure 4.11:** Two meshes are used to model the sample. Viscothermal effects are only modeled at the dark walls. The boundary layer mesh in (a) with 4 layers of thin elements along the dark walls is used for the FLNS and SLNS models. The mesh in (b) does not have these elements and is used in the BLI model.

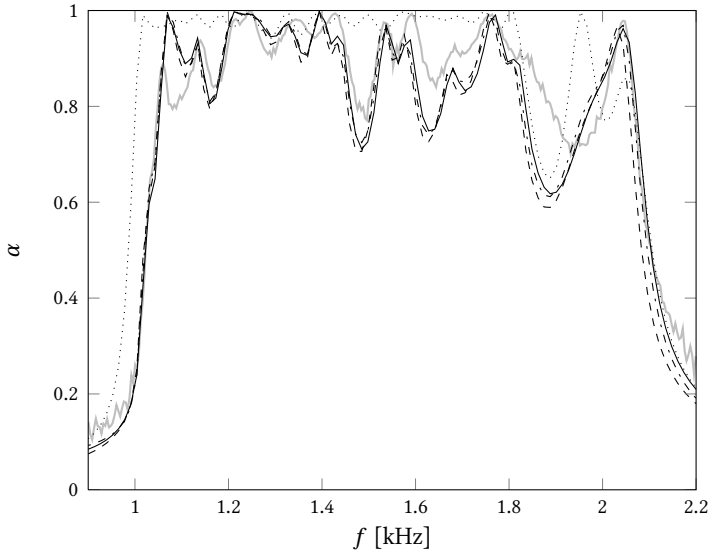


**Figure 4.12:** Pressure magnitude of Hannink's sample for  $f = 1.667$  kHz.

Model	$t_c$ [s]	# of DOFs
FLNS	1926	$584 \cdot 10^3$
SLNS	148	$3 \times 141 \cdot 10^3$
BLI	24	$2 \times 54 \cdot 10^3$
LRF	0.001	22

**Table 4.5:** Calculation time per frequency and number of DOFs for the different models of Hannink's sample. The FLNS and SLNS models use the same FEM mesh.

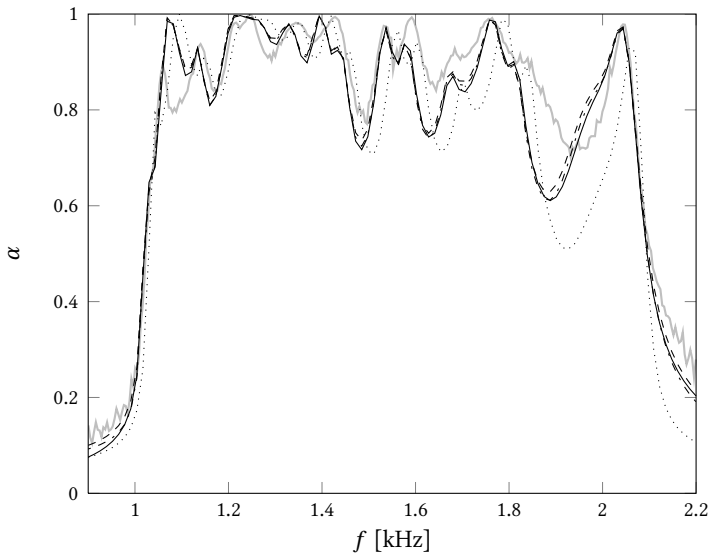
valid in this case, but the results with these end corrections are better than without them; see [41]. Figure 4.13 shows that the LRF model is not very accurate. Nevertheless, the accuracy may be sufficient. The other models show curves that are similar to each other. Moreover, these results agree better with the measured absorption coefficient.



**Figure 4.13:** The absorption coefficient of Hannink’s sample: (—) measurement; (—) FLNS model; (---) SLNS model; (-·-) BLI model; (····) LRF model.

The computational times per frequency and the number of degrees of freedom are listed in table 4.5. This LRF model is very efficient, because it requires just two DOFs per tube (including the impedance tube). Connected tubes share a DOF, resulting in a total of 22 DOFs. If the accuracy of the LRF model is not acceptable, the BLI model is the best choice. In this model, the boundary layers do not need to be meshed, which results in a much smaller number of DOFs and less computational time. The FLNS and SLNS models do require a fine mesh for the boundary layers; both use the same mesh. Notice that the SLNS model is approximately thirteen times more efficient than the FLNS model.

Figure 4.14 shows the results of the BLI model with viscothermal effects on all walls to verify the assumptions made in the previous calculations. Moreover, it contains a number of simulations of another SLNS model. The idea is to make the pressure calculation more efficient by using a coarser mesh (the BLI mesh). This is expected not to increase errors, because the pressure is smooth across the viscothermal boundary layers. The analytic BLI viscothermal field solutions (3.29) are used. Therefore, the calculations of the viscothermal fields are skipped in this ‘coarse SLNS’ model. The pressure field has to be calculated only once, where two calculations are needed in the BLI model. Two results of the coarse SLNS model are shown in figure 4.14. The first model used standard (fourth) order integration. This results in an absorption curve that deviates from the other results; see figure 4.14.



**Figure 4.14:** The absorption coefficient of Hannink’s sample: (—) measurement; (- - -) standard BLI model like in figure 4.13; (- · -) BLI model with an impedance on all walls; (- · -) SLNS model with BLI mesh and  $\Psi_\phi$  fields and higher order numerical integration; (····) SLNS model with BLI mesh and  $\Psi_\phi$  fields and standard order numerical integration.

Model	Integration	$t_c$ [s]	# of DOFs
BLI	standard	24	$2 \times 54 \cdot 10^3$
Coarse SLNS	standard	13	$54 \cdot 10^3$
Coarse SLNS	finer	21	$54 \cdot 10^3$

**Table 4.6:** Calculation time per frequency and number of DOFs for the different models of Hannink’s sample. The modified SLNS model with finer integration is approximately as efficient as the BLI model.

The standard order numerical integration in the assembly of the FEM matrix is incapable to accurately capture the thin boundary layer profiles of the viscothermal fields on this coarse mesh. Therefore, the second model uses a higher (eighth) order integration, while everything else is equal. The figure shows that this model yields a similar absorption curve as the other models. Therefore, it is possible to use a coarse mesh for the pressure calculation, provided that the order of the numerical integration is sufficient to capture the boundary layer profile.

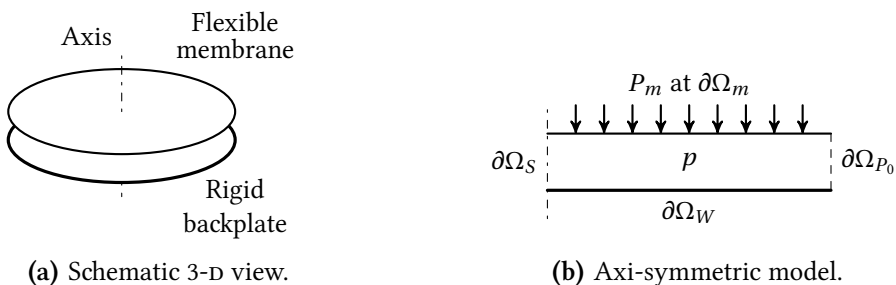
Table 4.6 compares the efficiency of the coarse SLNS models to the BLI model. For standard integration, the SLNS model is almost twice as efficient, because only one pressure calculation is needed in the SLNS model

versus two for the BLI model. Standard integration is insufficient and unfortunately, the higher order of integration consumes almost all the gained computational time. Nevertheless, the fine integration is only required for elements that coincide with the boundary layers. If somehow the order of integration of only the elements in the boundary layer is increased by an appropriate amount, the modified SLNS model may be a more efficient alternative to the BLI model. Moreover, the SLNS model is more generally applicable. In the presented coarse SLNS model, the viscothermal fields are determined by the analytic expression of the BLI model. The numerical FEM calculation can be used if this analytic expression is inaccurate.

### 4.3 Condenser microphone

A condenser microphone is modeled with the viscothermal acoustic finite element models in this section. This problem contains fluid structure interaction with a membrane as the structure. Several variations of this problem are studied in the literature; see for example [20, 45, 50, 59]. All these references model the microphone axi-symmetrically.

Figure 4.15(a) shows the most basic geometry for a condenser microphone: a round flexible membrane and round rigid backplate of the same size enclose a thin air layer of uniform thickness. This 3-D geometry can be modeled as a 2-D axi-symmetric problem, see figure 4.15(b). As indicated in this figure, a pressure release boundary condition is used at the edge  $\partial\Omega_{P_0}$  of the air layer. The other prescribed boundary conditions are the wall and symmetry BCs; see table 2.2. Furthermore, at  $\partial\Omega_m$  a fluid structure interaction boundary condition is used, which is explained later.



**Figure 4.15:** Condenser microphone (a) and axi-symmetric model (b). The air layer between membrane and backplate is much thinner than drawn here. The measured pressure  $P_m$  above the membrane is assumed to be uniform. The boundary conditions are shown in (b) and  $\partial\Omega_m$  is the boundary with the membrane.

### 4.3.1 Membrane model

The membrane, like the acoustics, is modeled with a time harmonic finite element formulation. The displacement of a flexible membrane can be described by a wave equation, see for example [53]. In time harmonic form, this simplifies to

$$\nabla \cdot (\sigma_m \nabla \dot{u}) + \omega^2 \rho_m \dot{u} = i\omega (P_m - p), \quad (4.5)$$

with normal membrane velocity  $\dot{u}$  in [m/s], the membrane mass per unit surface  $\rho_m$  [kg/m<sup>2</sup>], the membrane tension  $\sigma_m$  [N/m], the uniform pressure acting on the upper side of the membrane  $P_m$  [Pa], and the pressure in the air gap between the membrane and the backplate  $p$  [Pa]. The variables  $p_a$ ,  $P_m$  and  $\dot{u}$  are complex magnitudes, or phasors.

For uniform tension, the above equation reduces to the Helmholtz equation with the wave number  $k_m$  [m<sup>-1</sup>] defined as

$$k_m^2 = \frac{\omega^2 \rho_m}{\sigma_m}. \quad (4.6)$$

The weak form of equation (4.5) and of the mentioned Helmholtz equation is

$$\begin{aligned} & -\sigma_m \langle \nabla \dot{u}_w, \nabla \dot{u} \rangle_{\partial\Omega_m} + \sigma_m k_m^2 \langle \dot{u}_w, \dot{u} \rangle_{\partial\Omega_m} \\ & = i\omega \langle \dot{u}_w, P_m - p \rangle_{\partial\Omega_m} - \sigma_m \langle \dot{u}_w, h_m \rangle_{\partial^2\Omega_m}, \end{aligned} \quad (4.7)$$

with  $\partial\Omega_m$  the boundary of the acoustic domain  $\Omega$  on which the membrane is present. The symbol  $\partial^2\Omega_m$  denotes the boundary of the membrane. Furthermore,  $\dot{u}_w$  is the weighing function and  $h_m = \nabla_n \dot{u}$  is the natural boundary condition which can be used to prescribe the angular velocity perturbation of the membrane:  $h_m = 0$  at the center of the membrane ( $r = 0$ ). At the edge of the membrane ( $r = R_m$ ), the essential  $\dot{u} = 0$  boundary condition is prescribed. Quadratic shape functions are used for  $\dot{u}$  (and  $\dot{u}_w$ ) in the finite elements of the membrane.

The weak form of the membrane (4.7) is multiplied by  $-\rho_0$  (quiescent density of air). This makes the coupled finite element formulation complex symmetric if the LRF or SLNS model is used for the acoustics. The involved coupling terms are  $i\omega\rho_0 \langle \dot{u}_w, p \rangle_{\partial\Omega_m}$  in the weak form of the membrane and  $i\omega\rho_0 \langle p_w, \dot{u} \rangle_{\partial\Omega_m}$  in the weak form of the SLNS or LRF model. The problem is not symmetric if the acoustics is modeled by the FLNS model. In that case, the velocity of the membrane is prescribed as an essential boundary condition of the FLNS model. Matching meshes are used on the fluid structure interface as in figure 1.8(a).

Name	Symbol	Value	Unit
Radius of membrane	$R_m$	2	mm
Air layer thickness	$\ell$	18	$\mu\text{m}$
Membrane tension	$\sigma_m$	3128	N/m
Membrane mass per unit surface	$\rho_m$	0.0577	$\text{kg}/\text{m}^2$
Membrane thickness		6.95	$\mu\text{m}$

**Table 4.7:** Parameters for the microphone model, based on the B&K 4938 microphone described by Cutanda Henríquez [20].

### 4.3.2 Results

The signal measured by the microphone is proportional to the membrane deflection, which is caused by the pressure  $P_m$ . Therefore, the microphone sensitivity  $H$  can be defined as the mean deflection of the membrane per unit input pressure:

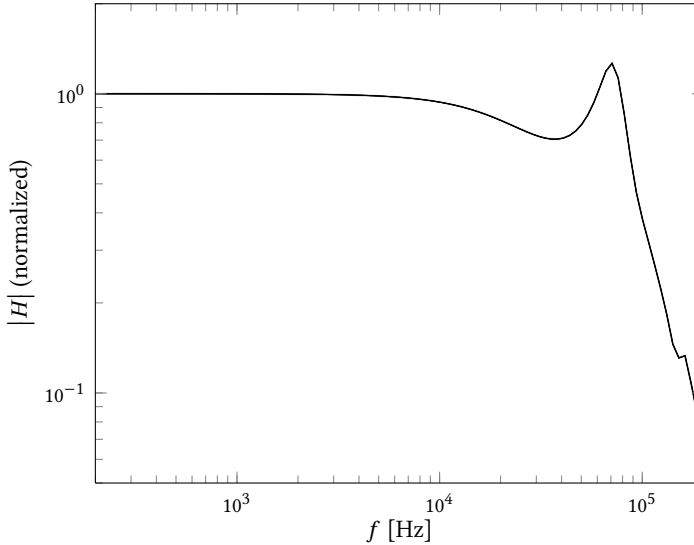
$$H = \left\langle \frac{\dot{u}}{i\omega P_m} \right\rangle_{\partial\Omega_m} = \frac{2}{i\omega P_m R_m^2} \int_0^{R_m} \dot{u} r \, dr, \quad (4.8)$$

with  $R_m$  the radius of the membrane. It can be multiplied with the membrane surface if membranes with different radii are compared. Moreover, if the backplate is not the same size as the membrane, a sensitivity measure may be defined in which the membrane deflection is only integrated over the surface above the backplate. Nevertheless, the sensitivity of equation (4.8) is sufficient for the comparisons in this thesis.

The air parameters in table 2.1 are used in the microphone model. The other parameters are given in table 4.7. These parameters are based on the B&K 4938 microphone model presented by Cutanda Henríquez [20]. In the simple model of figure 4.15(b), the backplate has the same radius as the membrane, but in the real microphone, the backplate is smaller. These differences are not important in the present study in which several models are compared to each other. The MATLAB code of Plantier's analytic model [59], which is listed in the appendix of Cutanda Henríquez' thesis [20] is used as an additional reference. This code is changed to use the air parameters of table 2.1.

The sensitivity as a function of the frequency is calculated with the axi-symmetric FLNS, LRF and SLNS FEM formulations and with the analytic model. The results are normalized on the sensitivity of the analytic model at the lowest frequency and plotted in figure 4.16. The membrane displacement of the analytic model, which is calculated for several discrete values of the radial coordinate, is integrated with the trapezoid rule to obtain the sensitivity. A BLI model is not compared in this figure, because of the shear



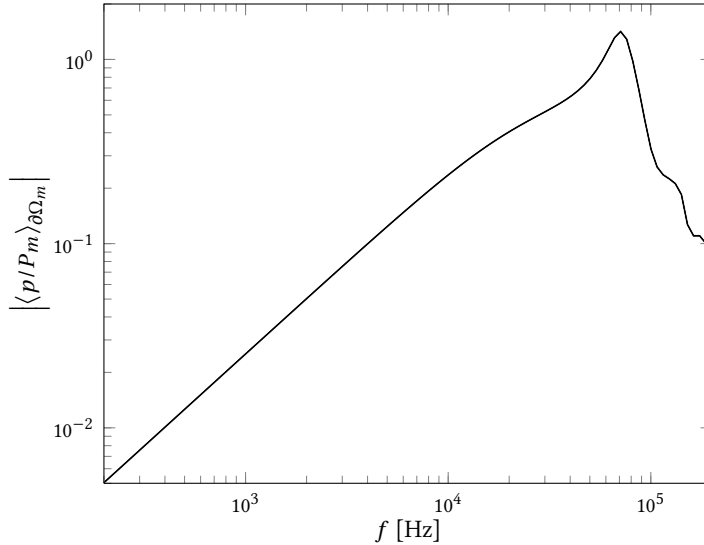


**Figure 4.16:** The normalized sensitivity of the microphone. (—) analytic model, ( $3\times$  —) FLNS, SLNS and LRF models. The difference between the models is smaller than the line thickness at the scale of this plot.

wave number  $|k_\nu \ell| \leq 2$  in the considered frequency range. At such low shear wave numbers, the boundary layers of opposing boundaries overlap, see figure 3.6(a), and the geometric constraints of the BLI model are not valid. The result in figure 4.16 shows that the sensitivity curves calculated by the FLNS, LRF and SLNS models agree perfectly with each other and with the analytic model. These results are better than the results that Cutanda Henríquez presented for his viscothermal acoustic BEM model [20].

The differences between the models is not visible in figure 4.16, despite the inconsistency in the normal velocity in the SLNS model at fluid structure interaction boundaries. A second plot is made to further investigate this error in the SLNS model. In this plot, shown in figure 4.17, the mean pressure on the membrane (at  $\partial\Omega_m$ ) is calculated and compared between the models. These results are also accurate for the SLNS model: the differences are again invisible at the scale of the plot.

The calculation times per frequency  $t_c$  of the different models are listed in table 4.8. The SLNS model is more than two times faster than the FLNS model, and both require less than a second for this simple problem. The difference is relatively small, because the time to assemble the system matrices is included. The LRF model and the analytic model are much faster. In the analytic model, most time is used to evaluate the solution on all grid points.



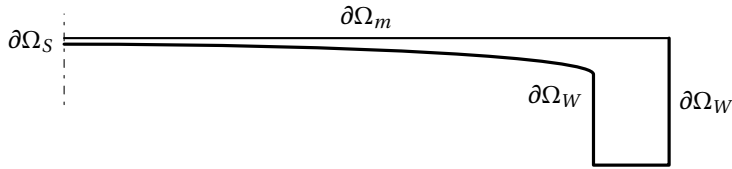
**Figure 4.17:** The mean pressure in the air layer at the membrane per unit  $P_m$ . (—) analytic model, ( $3\times$  —) FLNS, SLNS and LRF models. The difference between the models is not visible at the scale of this plot, although the no-slip FSI boundary condition is used in the SLNS model.

Model	$t_c$ [s]	# of DOFS
FLNS	0.60	7440
SLNS	0.25	4422+2412
LRF	0.01	402
Analytic	0.02	

**Table 4.8:** Calculation times for the microphone models. In the analytic model 5 modes are taken into account and a grid of 101 radial by 15 axial points is used.

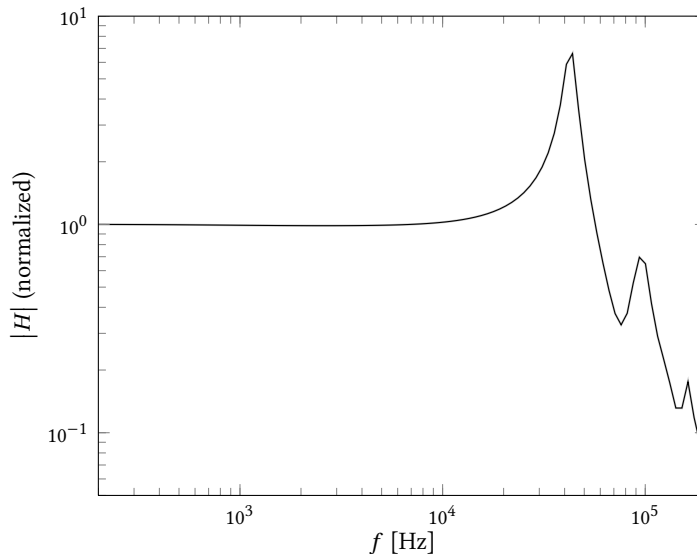
### 4.3.3 Microphone 2

A slightly more complicated microphone geometry is modeled as a demonstration. The backplate is curved (quarter ellipse) and its radius is reduced to 1.75 mm. A small volume is located around the backplate. Figure 4.18 shows the axi-symmetric cross section of this microphone in proportion. The used boundary conditions are given. The membrane has the same properties as in the first microphone, see table 4.7. The thickness of the air layer varies with the radial coordinate, and for  $r > 1.75$  mm the geometry is not a layer anymore. Therefore, it is not straightforward to make an accurate LRF model of microphone 2. For the FLNS and SLNS model, this is not a problem. The solutions of these two models are compared to each other.



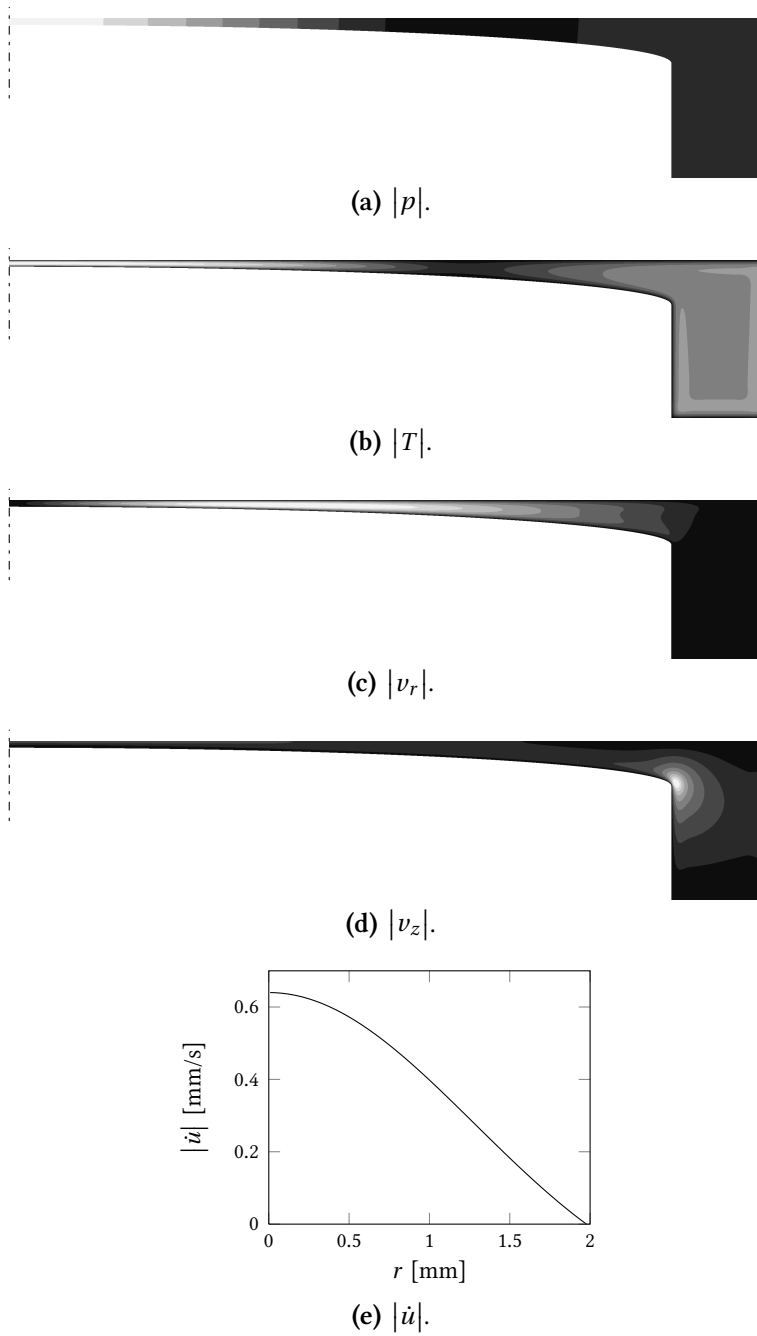
**Figure 4.18:** Microphone 2 has a curved backplate and a small volume near the edge of the membrane. The radius of the membrane is 2 mm. The air gap has a thickness of 18  $\mu\text{m}$  at the axis.

The results of the FEM calculations are shown in figure 4.20. The profiles of the temperature and radial velocity are clearly visible. These fields are a bit more complicated than the LRF-like fields in the first microphone model. The sensitivity curves are calculated with equation (4.8) and plotted in figure 4.19. This figure shows that the SLNS and FLNS again yield almost identical results. The peaks in the figure are membrane resonances that are coupled to the acoustics. The first resonance is only lightly damped by the viscothermal effects.



**Figure 4.19:** The FLNS (—) and SLNS (—) models yield very similar sensitivity curves for microphone 2.

Real microphones may have perforated backplates or other non-axisymmetric features. Such microphones can be modeled by 3-D SLNS and FLNS models. The computational costs of the SLNS model are much smaller than those of the FLNS model, especially in 3-D models; as shown in section 4.2.3.



**Figure 4.20:** Solution of the pressure, temperature, velocity components and the membrane velocity at a frequency of 44 kHz.

The SLNS models of the two microphones that are presented in this section are very accurate, despite the inconsistency in the normal velocity. Low errors for squeeze film types of problems have been anticipated in section 3.4.2. The next section discusses the errors caused by the normal velocity inconsistency in more detail for a piston-type problem.

## 4.4 On fluid structure interaction with the SLNS model

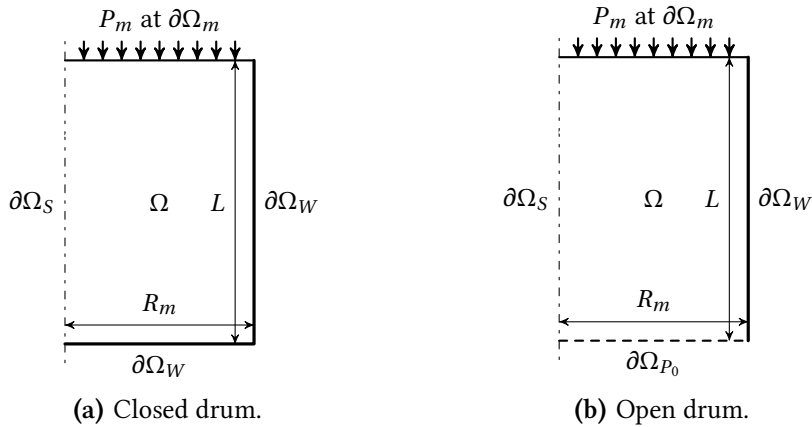
The SLNS model contains an inconsistency if the normal velocity does not vanish on no-slip boundaries, as discussed in section 3.4.2. This case is typical in FSI problems. The errors that are caused by this inconsistency are demonstrated and discussed here. The proposed countermeasures are evaluated as well.

The previous section presented a microphone model with fluid structure interaction. The results did not show significant errors in the SLNS model. This is in line with expectations, because the microphone is a ‘squeeze film’ type of problem. The inconsistency in the normal velocity can lead to larger errors in the other extreme case: the ‘piston-like’ problems, see figure 3.11 for a schematic drawing of these two types of problems.

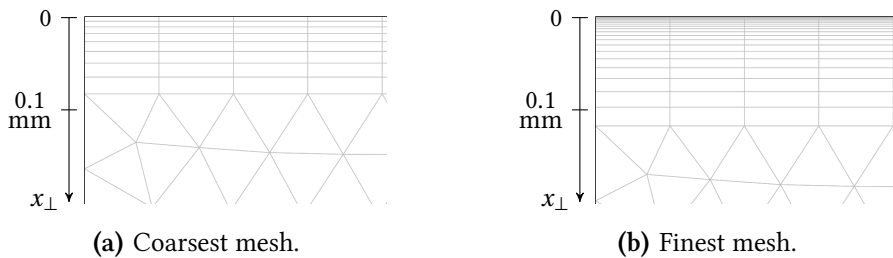
### Piston like problem

Figure 4.21 shows the fluid structure interaction problems that are used to demonstrate the errors in the SLNS model that are related to the inconsistency in the normal velocity. The problems use a comparable model as for the microphone in section 4.3: an axi-symmetric FSI problem with a membrane as the structure. However, the fluid domain has different dimensions with  $R_m = 2$  mm and  $L = 3$  mm. The problems resemble small drums, one with a closed cavity behind the membrane and one in which the boundary opposite to the membrane is open. The drums are excited by the uniform pressure  $P_m = 1$  above the membrane. The details of the model are presented in section 4.3 of the microphone model.

The error in the SLNS model that is caused by the inconsistency depends on the used mesh. Therefore, a mesh sequence is defined with a boundary layer mesh; see figure 4.22 for the coarsest and the finest mesh in this sequence. This figure shows only a small part of the geometry. In each mesh refinement, the existing boundary layer elements are made twice as thin, and four layers of elements are added to keep the total boundary layer mesh thickness approximately the same. The figure also shows the perpendicular coordinate  $x_\perp$  and a reference length of 0.1 mm.



**Figure 4.21:** Axi-symmetric fluid structure interaction problems used to discuss the normal velocity inconsistency in the SLNS model.

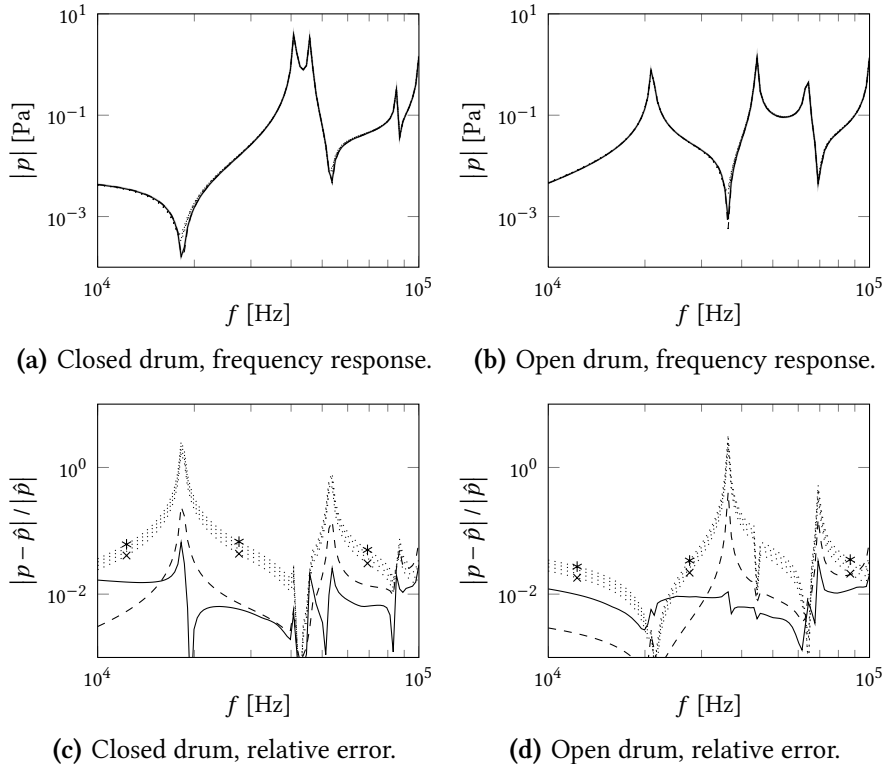


**Figure 4.22:** The coarsest and finest boundary layer mesh used for the SLNS model. Only a small area near the membrane center is shown.

## Results

The pressure at the membrane is an important variable, because it is the load on the structure in FSI problems. Figure 4.23 shows the pressure magnitude at the center of the membrane versus the frequency. The errors are not clearly seen in sub-figures (a) and (b), therefore, the relative errors with respect to the reference model are plotted in sub-figures (c) and (d). This reference model is an FLNS model on the finest mesh. The errors in the standard SLNS models are larger than the errors in the BLI model and the SLNS model that uses the rule of thumb, especially near pressure nodes. The error is larger for fine meshes as anticipated in section 3.4.2. Furthermore, the proposed rule of thumb (to use a slip boundary condition if the model is ‘piston-like’) reduced the error considerably, but not completely.

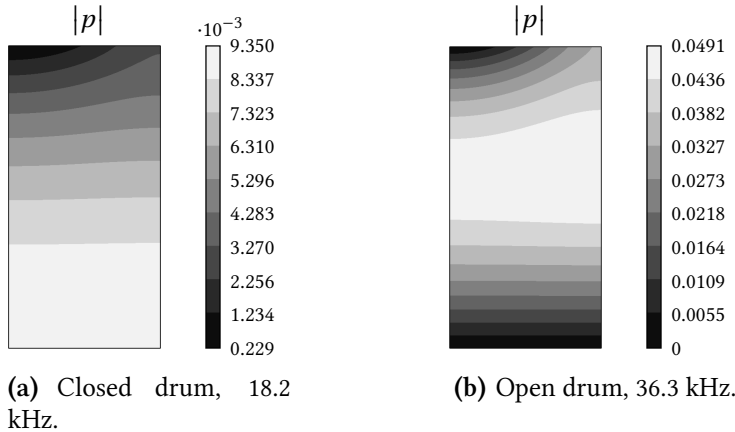
The remainder of the discussion focuses on two solutions: the closed drum at 18.2 kHz and the open drum at 36.3 kHz, which are the frequencies



**Figure 4.23:** Pressure magnitude at the center of the membrane versus the frequency in (a) and (b); normalized difference with the FLNS reference solution  $\hat{p}$  in (c) and (d); (—) FLNS model; (---) BLI model; (4×⋯) SLNS model for four meshes with finest mesh (\*) and coarsest mesh (x); (-·-·) SLNS model with a slip BC at the membrane.

with the largest relative errors. The pressure fields of these solutions are shown in figure 4.24. The frequencies are near the quarter and half wavelength acoustic resonances. Wave propagation is essentially in the axial direction at these resonances, therefore the problem is ‘piston-like’. Nevertheless, the pressure contours are curved near the membrane. Therefore, neglecting the viscosity at  $\partial\Omega_m$ , following the rule of thumb, does lead to a small error, which is confirmed by figure 4.23.

The pressure magnitude at the axis near the membrane is plotted versus the perpendicular coordinate  $x_\perp$  in figure 4.25 for the different models. The FLNS and BLI models yield similar results. Furthermore, the model with the no-slip rule of thumb also yields good results at the membrane, but the error does not disappear further away from the boundary: neglecting the viscosity at the boundary has slightly reduced the total amount of dissipation in the model, because the problem is not completely ‘piston-like’. The



**Figure 4.24:** Pressure field of the SLNS solution on the finest mesh.

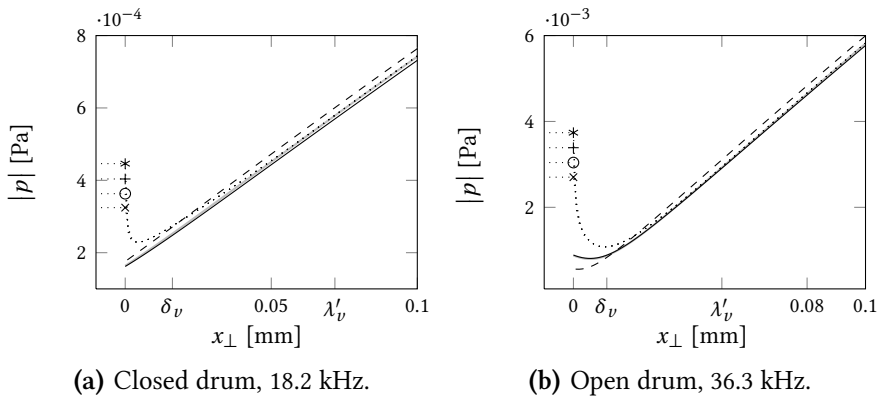
four SLNS solutions are not much different from each other near the membrane. Only directly at the membrane do the pressures differ. For clarity, short horizontal lines and plot marks are drawn in the figures. The finer meshes yield higher errors for the pressure field. The solutions converge to the reference solutions for higher  $x_{\perp}$ . In other words, the errors are local to the boundary layers. The structural problem is hardly affected, because the pressure  $P_m$  at the other side of the membrane is much larger than the pressure  $p$  of the FSI.

The normal velocity inconsistency is introduced in section 3.4.2 by assuming that the normal velocity field converges to the correct solution. This assumption is verified in figure 4.26, which plots the normal velocity at the axis near the membrane for several models. The SLNS solution does converge to the FLNS reference solution if the mesh is refined, but not in a smooth manner. Nevertheless, this explains the errors in the pressure field. The figure also shows that the SLNS model with the slip BC yields a normal velocity that is similar to the velocity in the BLI model.

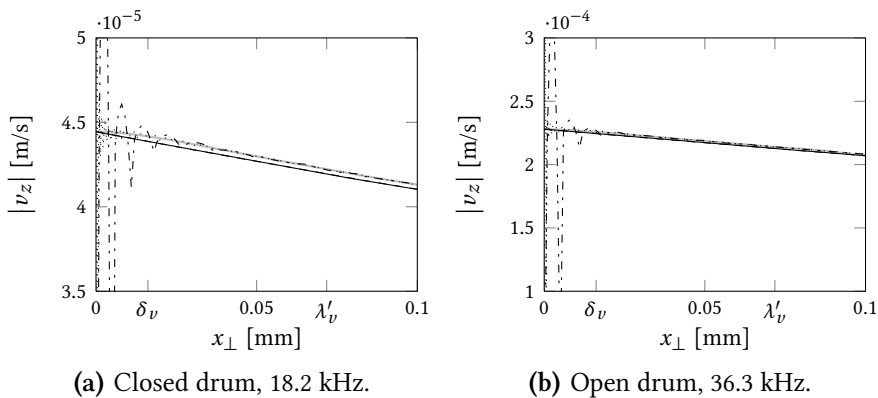
### Coarser pressure mesh

The above results may lead to curiosity about the performance of the SLNS model with a much coarser pressure mesh, like in the models presented in section 4.2.3. This is checked with three other meshes like those in figure 4.22, but with just a single layer of quadrilateral boundary layer elements. The thicknesses of the elements in this layer are 0.05, 0.08 and 0.1 mm for the three meshes. The viscothermal fields of the analytic BLI expression (3.29) are used in these calculations. The resulting pressure magnitude near the membrane axis is plotted in figure 4.27. The errors are clearly

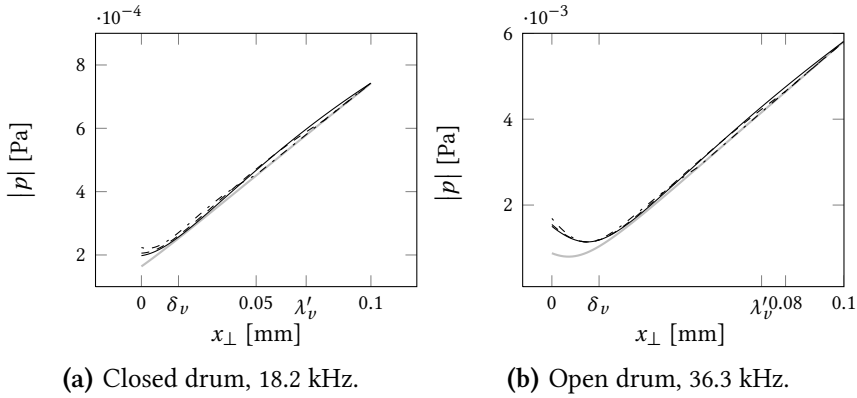




**Figure 4.25:** The pressure magnitude versus the coordinate  $x_{\perp}$ . The FLNS (—) and BLI (---) models yield almost identical results. The error at the membrane is small if the slip rule of thumb is used (-.-), but the error does not disappear at locations away from the membrane. The SLNS models ( $\times$ .....) have no error away from the membrane, but have a large error at the membrane. This error increases for finer meshes: ( $\times$ ) coarsest mesh; ( $\circ$ , $+$ ) finest mesh; ( $\circ$ , $+$ ) in between.



**Figure 4.26:** The normal velocity magnitude versus the coordinate  $x_{\perp}$ . (—) FLNS reference model; (---) BLI model; (-.-) SLNS model with slip BC (hidden below the BLI curve); (.....) SLNS model on coarse mesh; (-.-.-) SLNS model on fine mesh. The SLNS model shows an error near the boundary which is smaller on the finer mesh.



**Figure 4.27:** The pressure magnitude versus the coordinate  $x_{\perp}$  for the SLNS model with a coarse pressure mesh and high order numerical integration: (—) FLNS reference; (---) coarse SLNS with 0.1 mm element thickness; (- - -) coarse SLNS with 0.08 mm element thickness; (· · ·) coarse SLNS with 0.05 mm element thickness. Only the first element shows an error in the pressure magnitude. The errors are much smaller than those in the fine SLNS model in figure 4.25.

smaller than in figure 4.25. Furthermore, the error is only visible in the first element and disappears for larger  $x_{\perp}$ . The order of integration in the pressure calculations is 30, which is higher than necessary to obtain the plotted curves. Thus, the error in the pressure field that is caused by the normal velocity inconsistency can indeed be reduced by using a coarse mesh for the pressure calculation.

## 4.5 Summary

This chapter has demonstrated the four presented viscothermal acoustic models on a collection of sample problems. The most important advantages and disadvantages from the list in section 3.5.1 have been encountered.

The BLI and LRF models are erroneous for applications that do not meet their geometric constraints. Nevertheless, these models are very efficient and therefore highly recommended for applications in which these constraints are satisfied. On the other hand, the FLNS model can be used for any geometry, but it is computationally costly, especially in 3-D.

The SLNS model is a more efficient alternative to the FLNS model. The SLNS model is sufficiently accurate in all presented cases in this chapter, even in the fluid structure interaction problems for which the errors are expected to be larger because of the normal velocity inconsistency. In the squeeze

film problems, the errors were found to be negligible and in the piston-like problems the errors were noticeable but small. Two ideas to reduce this error are demonstrated to be effective. First, a slip boundary condition can be applied to the FSI boundary in piston-like problems. Second, a coarse mesh in the pressure smooths the error and can be applied in any problem. This second method has the added advantage of increasing the efficiency of the model.

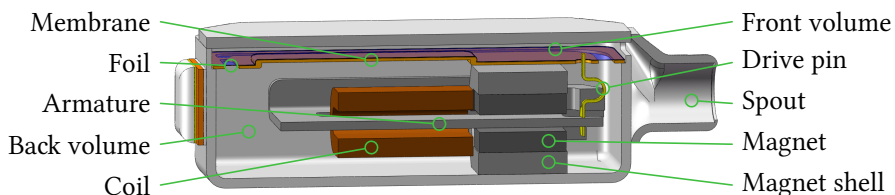
# Miniature loudspeaker

The PhD project, of which this thesis is the report, is a cooperation between SONION and the University of Twente. SONION's goal for this project is to model hearing aid loudspeakers. Such a model is presented in this chapter as an example of how the viscothermal acoustic finite elements can be used in a design environment.

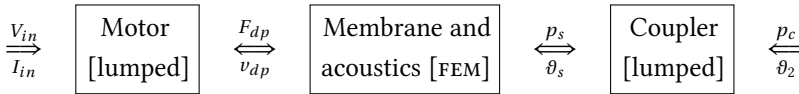
## 5.1 Structure of the model

The hearing aid receiver is a transducer that comprises four physical domains: electric, magnetic, mechanic and acoustic. Figure 1.1 of the receiver cross section is shown again in figure 5.1 for convenience. The important parts are labeled and will be referred to in this chapter.

It is not sensible to put everything in a single coupled FEM model. It is a better idea to model as many parts as possible with lumped models and use a FEM model for only the parts that are studied in detail or the parts that yet do not have accurate lumped models. The model of the receiver in this chapter uses an FSI FEM model for the membrane, the foil and the air in the front volume, the back volume and the spout. This FEM part of the receiver model divides the total receiver model in three parts as shown in figure 5.2:



**Figure 5.1:** Cross section of a hearing aid receiver (reproduction of figure 1.1). Its total length is 8 mm. The important parts are labeled.



**Figure 5.2:** The model of the receiver contains three coupled sub-models. The FEM part models the membrane, the foil, the back volume, the rear volume and the spout. The interface variables are given above and below the arrows.

Domain	Effort variable			Flow variable		
	Name	Symbol	Unit	Name	Symbol	Unit
Electric	Voltage	$V$	V	Current	$I$	A
Magnetic	Mmf*	$\mathfrak{F}$	A	Flux rate	$\dot{\phi}$	Wb/s=V
Mechanic	Force	$F$	N	Velocity	$\dot{u}$	m/s
Acoustic	Pressure	$p$	Pa	Volume flow	$\vartheta$	m <sup>3</sup> /s

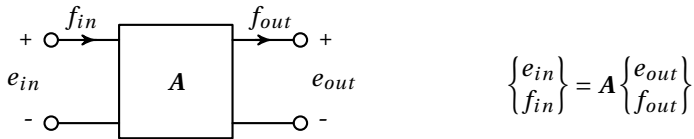
\* magneto-motive force

**Table 5.1:** The effort and flow variables of the receiver’s four physical domains. The product of effort and flow results in power [W] for each domain.

the lumped motor model, the FEM part just described and lumped model of the coupler. This coupler is a measurement tool that is connected to the spout as an acoustic termination of the receiver. It contains a microphone that measures the pressure the receiver can generate in the ear of a user. In other words, the coupler is an ‘ear simulator’.

Figure 5.2 shows the input variables  $V_{in}$  and  $I_{in}$  that denote the electric input voltage and current, the output variables  $p_c$  and  $\vartheta_2$  that denote the pressure and (leak) volume flow at the coupler. Furthermore, the interface variables that are used to couple the sub-models to each other are  $F_{dp}$ ,  $v_{dp}$ ,  $p_s$ ,  $\vartheta_s$  which denote the force and velocity at the connection between drive pin and membrane, and the pressure and volume flow at the end of the spout respectively. The given pairs of variables all contain one ‘effort variable’ and one ‘flow variable’. Table 5.1 lists the pairs of variables for the four physical domains. All pairs have the property that the product of the effort and the flow variables has the unit of power [W]. This is a convenient property for comparing the different physical domains.

The sub-models of the receiver can be assembled in two ways. The first method is to include the lumped models in the FEM model. This approach is recommended for studying the effect of the parameters in the FEM model. The second method is to lump the FEM model and then couple it to the other lumped models. The advantage of this second method is that the parameters



**Figure 5.3:** Schematic representation of a transmission matrix two-port model. The symbols  $e$  and  $f$  denote effort and flow variables respectively. The transmission matrix  $\mathbf{A}$  can be frequency dependent.

in the lumped part of the model can be studied without recalculation of the FEM part of the model. Both methods are used in this chapter.

The lumped model can be put in several forms. Here, the transmission matrix form is used, which has the advantage that sub-models can be easily assembled to form larger models. For example, the complete receiver model contains three sub-models, each with its own transmission matrix: the transmission matrix model of the complete receiver is

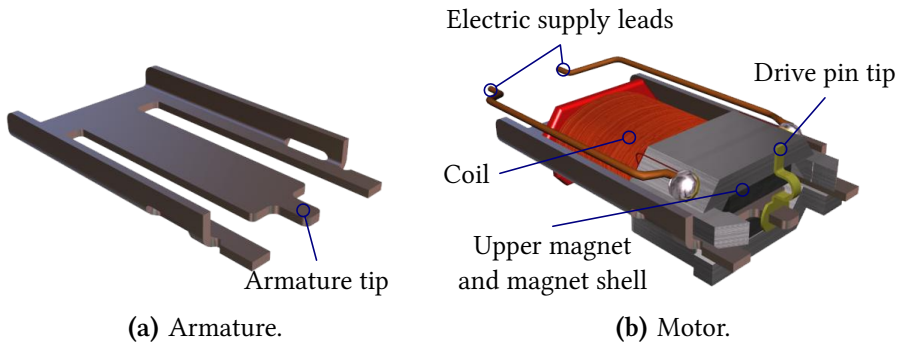
$$\begin{Bmatrix} V_{in} \\ I_{in} \end{Bmatrix} = \mathbf{A}_{receiver} \begin{Bmatrix} p_c \\ \vartheta_2 \end{Bmatrix}, \quad \mathbf{A}_{receiver} = \mathbf{A}_{motor} \mathbf{A}_{FEM} \mathbf{A}_{coupler}, \quad (5.1)$$

in which  $\mathbf{A}_{motor}$ ,  $\mathbf{A}_{FEM}$  and  $\mathbf{A}_{coupler}$  are the transmission matrix sub-models of the motor, the FEM part (lumped of course) and the coupler.

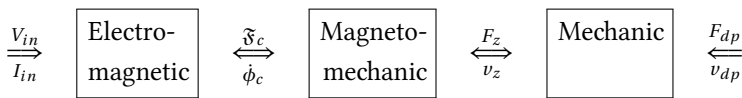
Transmission matrix models have the structure that is shown in figure 5.3. The 2-by-2 transmission matrix  $\mathbf{A}$  is frequency dependent: each matrix entry can be thought of as a transfer function. The collection of tables of Schmid [63] is useful to derive ‘two-port models’, of which the transmission matrix models are a sub-class. The next sections present the three sub-models  $\mathbf{A}_{motor}$ ,  $\mathbf{A}_{FEM}$  and  $\mathbf{A}_{coupler}$ .

## 5.2 Motor model

The lumped model of the motor is presented first. This motor operates according to the balanced armature principle in which an armature is placed in a gap between two equally poled permanent magnets (opposite poles facing the armature). The armature is attracted by each of these magnets, but its stiffness keeps it centered in the gap. Figure 5.4(a) shows the armature and figure 5.4(b) shows it with the other motor components. An electric current through the coil induces a magneto-motive force in the armature. As a result, the armature is attracted stronger by one permanent magnet and weaker by the other, resulting in a nett force. This force bends the armature and pushes a membrane that is connected to it by the drive pin. However,



**Figure 5.4:** The balanced armature motor of the receiver consists of an armature with several electric and magnetic parts.



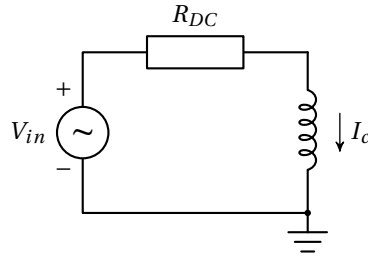
**Figure 5.5:** The sub-models of the motor model with the interface variables. The electro-magnetic part contains the coil, the magneto-mechanic part contains the permanent magnets, magnet shells and the magnetic properties of the armature, and the mechanic part contains the mechanic properties of the armature and the drive pin.

the lumped model of the motor stops at the drive pin tip and the membrane is a part of the FEM model presented later.

The lumped sub-model of the balanced armature motor contains several sub-models itself; see figure 5.5. The interface variables  $\mathfrak{F}_c$ ,  $\dot{\phi}_c$ ,  $F_z$  and  $v_z$  are the magneto-motive force and the flux rate that are generated by the coil and the effective force and velocity at the armature that are generated by the magnetic circuit respectively. The complete motor model is assembled after the sub-models are presented.

### 5.2.1 Electro-magnetic coupling

The electric circuit of the receiver consists of a single component: the coil. An ideal voltage source is assumed to supply the power to the coil. In a lumped electric circuit, the coil's resistance can be modeled as a ideal series resistor and the electro-magnetic properties as an ideal coil, as shown in figure 5.6. The resistor's two-port equation is a combination of Ohm's law



**Figure 5.6:** Schematic of the lumped electrical domain of the 3100 hearing aid receiver. The coil is not modeled as an inductance, but couples the electrical domain to the magnetic domain.

and Kirchhoff's laws:

$$\begin{Bmatrix} V_{in} \\ I_{in} \end{Bmatrix} = \begin{bmatrix} 1 & R_{DC} \\ 0 & 1 \end{bmatrix} \begin{Bmatrix} V_c \\ I_c \end{Bmatrix}, \quad (5.2)$$

with  $V_c$  and  $I_c$  the electric voltage over and current through the coil and  $R_{DC}$  the value of the resistor.

Coils are often modeled as inductances in an electric circuit, implicitly converting all magnetic effects to the electric domain. Here, the magnetic domain and the electromagnetic coupling are explicitly modeled. The induced magneto-motive force is proportional to the current through the coil, multiplied by the number of turns of the coil. Vice versa, the magnetic flux rate induces a voltage in the coil. The transmission matrix of this electro-magnetic coupling is

$$\begin{Bmatrix} V_c \\ I_c \end{Bmatrix} = \begin{bmatrix} 0 & n_c \\ n_c^{-1} & 0 \end{bmatrix} \begin{Bmatrix} \mathfrak{F}_c \\ \dot{\phi}_c \end{Bmatrix}, \quad (5.3)$$

with  $n_c$  the number of turns of the coil and  $\mathfrak{F}_c$  and  $\dot{\phi}_c$  the induced magneto-motive force and flux rate in the armature.

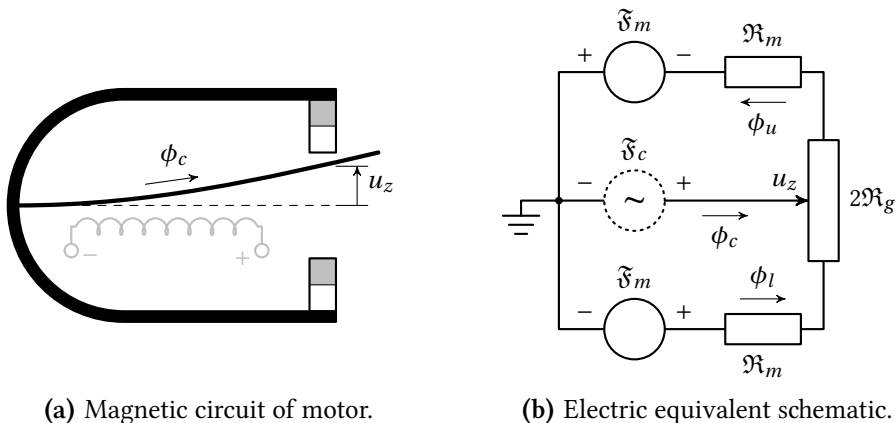
The total electro-magnetic system can now be described by the multiplication of the transmission matrices of the sub-systems:

$$\begin{Bmatrix} V_{in} \\ I_{in} \end{Bmatrix} = \mathbf{A}_{e,m} \begin{Bmatrix} \mathfrak{F}_c \\ \dot{\phi}_c \end{Bmatrix}, \quad \mathbf{A}_{e,m} = \begin{bmatrix} 1 & R_{DC} \\ 0 & 1 \end{bmatrix} \begin{bmatrix} 0 & n_c \\ n_c^{-1} & 0 \end{bmatrix}. \quad (5.4)$$

### 5.2.2 Magneto-mechanic coupling

The magnetic circuit is a bit more complicated than the electric circuit. Furthermore, the physics of the magnetic domain are less well known than those of the electric and mechanic domains. Therefore, the equations of the





(a) Magnetic circuit of motor.

(b) Electric equivalent schematic.

**Figure 5.7:** The magnetic circuit of a balanced armature motor and its electric equivalent schematic. The armature deflection  $u_z$  and the magnetic flux from the coil  $\phi_c$  are shown in both sub-figures. The  $\mathfrak{F}_c$  source is not ideal, but satisfies the equation derived above.

magnetic circuit are derived first and are written in transmission matrix form later.

The magnetic circuit is shown in figure 5.7(a). The 3-D shape of the magnet shells is simplified to a 2-D C-shape in the circuit. The two permanent magnets are drawn in gray and white to indicate the polarity. The armature is magnetized by the electric coil as modeled above. This results in a magneto-motive force  $\mathfrak{F}_c$  and a mechanical force  $F_m$  at the end of the armature. As a result the armature bends toward one of the permanent magnets, with the deflection at the magnet center denoted as  $u_z$ . For clarity, the air gap thickness and the armature deflection are exaggerated in the figure.

The only type of magnetic component used in the circuit is a reluctance, denoted by  $\mathfrak{R}$  (not to be confused with the real value operator  $\Re$  in the previous chapters). It satisfies a law that resembles Ohm's law of an electric resistance:

$$\mathfrak{F} = \mathfrak{R}\phi. \quad (5.5)$$

Therefore, it is possible to represent the magnetic circuit by an equivalent electric circuit, see figure 5.7(b). In this analogy, the magneto-motive forces are represented by voltages, the magnetic fluxes by electric currents and the magnetic reluctances by electric resistances. However, realize that magnetic reluctances *store* magnetic energy rather than dissipate it, unlike electric resistances.<sup>1</sup>

<sup>1</sup>The analogy would be energy consistent if current would be set equivalent to flux rate  $\dot{\phi}$  (instead of the flux  $\phi$ ), and the magnetic reluctance equivalent to a capacitance (with  $C \propto \mathfrak{R}^{-1}$ ).

In figure 5.7(b), the permanent magnets are modeled as an ideal  $\mathfrak{F}$ -source with a series reluctance. The space between the permanent magnets is divided into two air gaps, each with reluctance  $\mathfrak{R}_0$  if the armature is in the middle position. When the armature deflects, one air gap narrows and the other widens, and the corresponding reluctances change proportionally. This is indicated by a potentiometer in the electric schematic (drawn with the armature in the middle position). The reluctances of the magnet shells and the armature are neglected with respect to the other reluctances. The magneto-motive force from the coil  $\mathfrak{F}_c$  is not modeled as an ideal source, but satisfies the electro-magnetic equation (5.4).

The equations of the magnetic circuit can be derived from the electrical circuit in figure 5.7(b). The equations are easier to express with the reluctances at one side of the centered armature ( $\mathfrak{R}_0$ ) and of the armature displacement ( $\mathfrak{R}_z$ )

$$\mathfrak{R}_0 = \mathfrak{R}_m + \mathfrak{R}_g, \quad \mathfrak{R}_z = \mathfrak{R}_g u_z / h_0, \quad (5.6)$$

with  $h_0$  the thickness of each air gap if the armature is in the middle position.

Kirchoff's laws and equation (5.5) can be combined to express the flux  $\phi_c$  as a function of the armature displacement (in  $\mathfrak{R}_z$ ) and the magneto-motive force from the coil  $\mathfrak{F}_c$ :

$$\phi_c = \frac{2\mathfrak{R}_0\tilde{\mathfrak{F}}_c + 2\mathfrak{R}_z\tilde{\mathfrak{F}}_m}{\mathfrak{R}_0^2 - \mathfrak{R}_z^2}. \quad (5.7)$$

An expression for the armature magneto-motive force follows from rewriting the above equation:

$$\tilde{\mathfrak{F}}_c = \frac{\mathfrak{R}_0^2 - \mathfrak{R}_z^2}{\mathfrak{R}_0} \frac{\phi_c}{2} - \frac{\mathfrak{R}_z}{\mathfrak{R}_0} \tilde{\mathfrak{F}}_m. \quad (5.8)$$

This nonlinear equation can be linearized under the typical operating conditions of the receiver

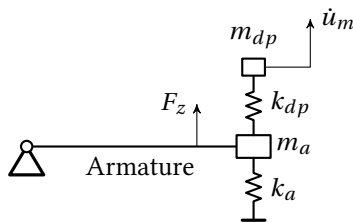
$$\mathfrak{R}_z \ll \mathfrak{R}_0, \quad \tilde{\mathfrak{F}}_c \ll \tilde{\mathfrak{F}}_m, \quad u_z \ll h_0. \quad (5.9)$$

The linearized relation of the armature magneto-motive force now reads

$$\tilde{\mathfrak{F}}_c = \frac{\mathfrak{R}_0}{2} \phi_c - \eta_m u_z. \quad (5.10)$$

with the magnetic coupling constant

$$\eta_m = \frac{\mathfrak{R}_g \tilde{\mathfrak{F}}_m}{\mathfrak{R}_0 h_0}. \quad (5.11)$$



**Figure 5.8:** Schematic of the lumped mechanical system. The armature is approximated as a hinged rigid bar. The armature's mass and stiffness are lumped to the tip. The mass and stiffness of the drive pin are included in the mechanical model.

This constant can also be used to express the mechanical force  $F_z$  as a function of the magnetic flux:

$$F_z = \eta_m \phi_c, \quad (5.12)$$

which is the linear relation valid around  $u_z = 0$ .

Equations (5.10) and (5.12) can be combined in the matrix equation

$$\begin{Bmatrix} \mathfrak{F}_c \\ \phi_c \end{Bmatrix} = \begin{bmatrix} \frac{\mathfrak{X}_0}{2\eta_m} & -\eta_m \\ \eta_m^{-1} & 0 \end{bmatrix} \begin{Bmatrix} F_z \\ u_z \end{Bmatrix}. \quad (5.13)$$

Notice that the magnetic system has a negative stiffness: for  $\mathfrak{F}_c = 0$ , the displacement  $u_z$  and the force  $F_z$  have the same sign. This negative stiffness is compensated for by the positive mechanical bending stiffness of the armature, which is added later.

The above matrix equation can be rewritten in the preferred effort and flow variables of table 5.1, which yields the magneto mechanic transfer matrix

$$\begin{Bmatrix} \mathfrak{F}_c \\ \dot{\phi}_c \end{Bmatrix} = \mathbf{A}_{m,M} \begin{Bmatrix} F_z \\ \dot{u}_z \end{Bmatrix}, \quad \mathbf{A}_{m,M} = \begin{bmatrix} \frac{\mathfrak{X}_0}{2\eta_m} & \frac{-\eta_m}{i\omega} \\ \frac{i\omega}{\eta_m} & 0 \end{bmatrix}. \quad (5.14)$$

### 5.2.3 Mechanical model

The schematic of the lumped mechanical model is shown in figure 5.8. The armature is approximated as a hinged rigid bar with its equivalent stiffness  $k_a$  and mass  $m_a$  lumped to the tip; see figure 5.8. The drive force from the magnetic circuit acts not at the tip of the armature, but at a location that corresponds to the center of the permanent magnets. The drive pin at the tip of the armature is modeled as a lumped mass and stiffness.

Without considering the drive pin stiffness and mass, the transmission matrix of the drive force and velocity at the armature's location near the

magnet center to the effective force and velocity at the armature tip is

$$\begin{Bmatrix} F_z \\ \dot{u}_z \end{Bmatrix} = \begin{bmatrix} T_m & 0 \\ 0 & T_m^{-1} \end{bmatrix} \begin{bmatrix} 1 & \frac{k_a}{i\omega} + i\omega m_a \\ 0 & 1 \end{bmatrix} \begin{Bmatrix} F_t \\ \dot{u}_t \end{Bmatrix}, \quad (5.15)$$

where  $T_m > 1$  is the transmission ratio that relates the force and velocity to their equivalent values at the tip. The stiffness and mass of the armature reduce the force  $F_t$  that is available to drive the membrane through the drive pin.

The drive pin can be added to the model with the transmission matrix

$$\begin{Bmatrix} F_t \\ \dot{u}_t \end{Bmatrix} = \begin{bmatrix} 1 & 0 \\ \frac{i\omega}{k_{dp}} & 1 \end{bmatrix} \begin{bmatrix} 1 & i\omega m_{dp} \\ 0 & 1 \end{bmatrix} \begin{Bmatrix} F_{dp} \\ \dot{u}_{dp} \end{Bmatrix}. \quad (5.16)$$

The transmission matrix that takes the drive pin stiffness into account is different than the matrix for the armature stiffness, because the drive pin stiffness  $k_{dp}$  is in series while the armature stiffness  $k_a$  is parallel.

The transmission matrix model of the mechanical part of the motor can be assembled as

$$\begin{Bmatrix} F_a \\ \dot{u}_a \end{Bmatrix} = \mathbf{A}_M \begin{Bmatrix} F_{dp} \\ \dot{u}_{dp} \end{Bmatrix},$$

$$\mathbf{A}_M = \begin{bmatrix} T_m & 0 \\ 0 & T_m^{-1} \end{bmatrix} \begin{bmatrix} 1 & \frac{k_a}{i\omega} + i\omega m_a \\ 0 & 1 \end{bmatrix} \begin{bmatrix} 1 & 0 \\ \frac{i\omega}{k_{dp}} & 1 \end{bmatrix} \begin{bmatrix} 1 & i\omega m_{dp} \\ 0 & 1 \end{bmatrix}. \quad (5.17)$$

#### 5.2.4 Complete motor model

The complete balanced armature motor model is simply the chain of the sub-models of equations (5.4), (5.14) and (5.17):

$$\begin{Bmatrix} V_{in} \\ i_{in} \end{Bmatrix} = \mathbf{A}_{motor} \begin{Bmatrix} F_{dp} \\ \dot{u}_{dp} \end{Bmatrix}, \quad \mathbf{A}_{motor} = \mathbf{A}_{e,m} \mathbf{A}_{m,M} \mathbf{A}_M. \quad (5.18)$$

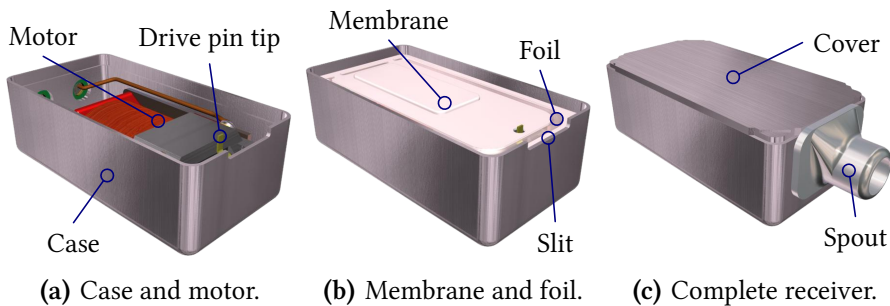
Table 5.2 lists the parameters of the lumped motor model. The values of these parameters are not listed for confidentiality. This motor model has the drive pin force and velocity as outputs. It is coupled to the FEM model of the membrane and the acoustic volumes which has these variables as inputs.

### 5.3 Finite element model

The FEM part of the receiver model describes the membrane and the air in the back volume, front volume and spout. These ‘parts’ are labeled in figure 5.1, but this figure does not show the geometry of the membrane clearly.

Parameter	Symbol	Unit
DC resistance of coil	$R_{DC}$	$\Omega$
Number of coil windings	$n_c$	1
Total reluctance at one side of the armature	$\mathfrak{R}_0$	$\text{H}^{-1}$
Magneto-mechanical coupling coefficient	$\eta_m$	$\text{N/Wb}$
Transformation ratio	$T_m$	1
Equivalent stiffness at tip	$k_a$	$\text{N/m}$
Drive pin stiffness	$k_{dp}$	$\text{N/m}$
Equivalent mass at tip	$m_a$	$\text{kg}$
Half of drive pin mass	$m_{dp}$	$\text{kg}$

**Table 5.2:** Parameters for the lumped balanced armature motor model. The values are confidential and are therefore not listed.



**Figure 5.9:** The back volume and front volume are located on both sides of the membrane. The back volume is the air in the case that surrounds the motor (a). It is sealed off by the membrane and the foil (b). The front volume is the small layer of air above the membrane (b) and is sealed off by the cover of the case (c). The spout (c) and the front volume are connected by the slit (b).

Figure 5.9 shows the parts from another view point. The back volume of the receiver is the air that surrounds the motor. It is enclosed by the case of the receiver and the membrane. The front volume of the receiver is located on the other side of the membrane. It is enclosed by the membrane, the case and the cover of the case. The profile in the membrane that is shown in figure 5.9(b) increases its stiffness. By contrast, the foil that surrounds the membrane has a profile to allow the membrane to move up and down easily. Furthermore, the foil provides an airtight seal between the front volume and the back volume. The front volume is a layer with a non-uniform thickness because of the shape of the membrane and the foil. A small slit, shown in figure 5.9(b), connects the front volume to the spout.

Because of symmetry, the geometry for the FEM model is half the geometry of the front volume, the slit and the spout. The FEM geometry is shown in figure 5.10, but upside-down in comparison with figure 5.9 so that the membrane side is visible. The thickness of the front volume is 0.3 mm, which corresponds to a shear wave number range of  $|k_v \ell| = [2.1, 21]$  for the frequency range  $f = [10^2, 10^4]$  Hz. The air is modeled with the SLNS model and the used mesh is shown in figure 5.10(a). The membrane and the foil are modeled by COMSOL's shell elements on the boundary of the fluid domain; see figures 5.10(c) and 5.10(d) for the geometries of these structures. The membrane shape is such that a flexible hinge is formed at one side. The drive pin force  $F_{dp}$  and velocity  $v_{dp}$  are applied and evaluated at the other side of the membrane at the semicircle patch in the figure. The variables at the output of the FEM model are the pressure  $p_s$  and volume flow  $\vartheta_s$  at the end of the spout, shown in figure 5.10(b).

The finite element model contains fluid structure interaction between the shell elements and the SLNS elements in the front volume as described in section 3.4.3. Besides the FSI with the front volume, there is an interaction with the back volume. This volume is not modeled with finite elements, but is included by means of a lumped model that calculates the pressure from the mean normal structure (membrane and foil) displacement. This pressure is applied as a uniform normal load at the structure. The lumped model of a volume is derived later and results in equation (5.22).

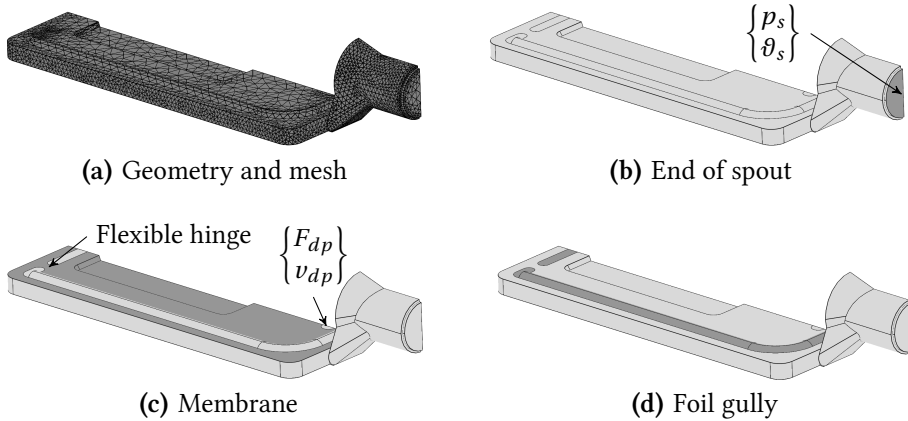
### 5.3.1 Lumping the FEM model to a transmission matrix

The FEM model of the membrane, the volumes and the spout has to be coupled to the lumped models of the motor and the coupler that is described later. As mentioned, there are two methods: the lumped models can be included in the FEM model, or the FEM model can be lumped. The implementation of the first method depends on the used FEM software. The second method is explained here. The entire FEM calculation is lumped to the two-port transmission matrix

$$\begin{Bmatrix} F_{dp} \\ v_{dp} \end{Bmatrix} = \mathbf{A}_{FEM} \begin{Bmatrix} p_s \\ \vartheta_s \end{Bmatrix}, \quad \mathbf{A}_{FEM} = \begin{bmatrix} a_{11} & a_{12} \\ a_{21} & a_{22} \end{bmatrix}. \quad (5.19)$$

The four frequency dependent entries in the matrix can be estimated from two FEM calculations:

- Calculation 1: Unity input force ( $F_{dp} = 1$ ) and zero volume velocity at the spout ( $\vartheta_s = 0$ ).
- Calculation 2: Unity input force ( $F_{dp} = 1$ ) and zero pressure at the spout ( $p_s = 0$ ).



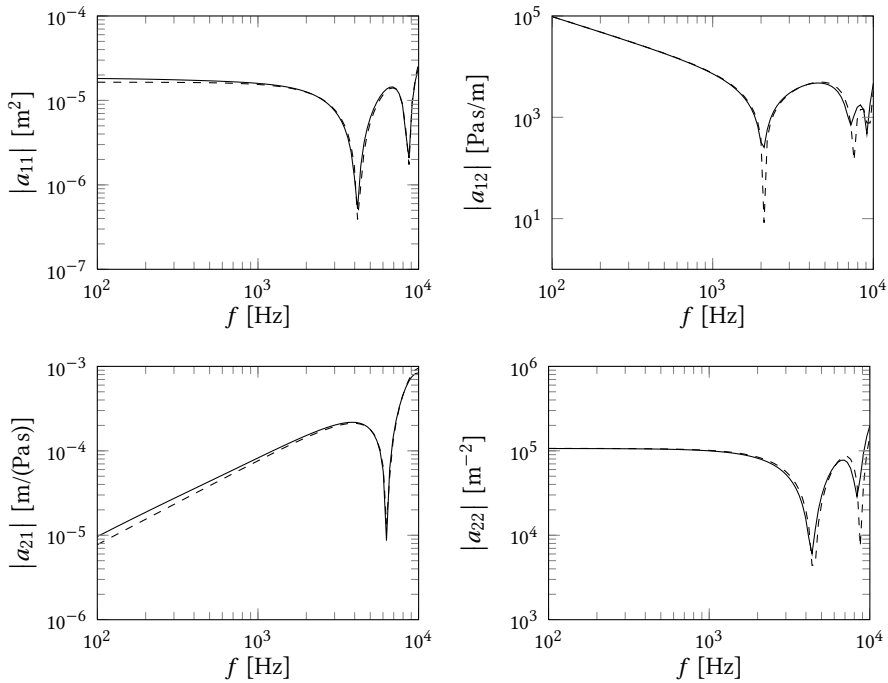
**Figure 5.10:** Finite element model of the front volume and the spout (half the geometry and upside-down). Figures (c) and (d) show the membrane and the foil gully with a darker color. The interface variables for the lumped parts of the model are the pressure and the volume flow ( $p_s$ ,  $\vartheta_s$ ) at the end of the spout, and the force and velocity at the drive pin tip ( $F_{dp}$ ,  $v_{dp}$ ), located at the marked semicircle patch.

The interface variables that are used in the coupling are mean values at the interface. The pressure at the spout is assumed to be uniform and likewise, the distributed force at the drive pin area is assumed to be uniform. Calculation 1 yields the matrix entries  $a_{11} = 1/p_s$  and  $a_{21} = v_{dp}/p_s$ , and likewise, calculation 2 yields the matrix entries  $a_{12} = 1/\vartheta_s$  and  $a_{22} = v_{dp}/\vartheta_s$ .

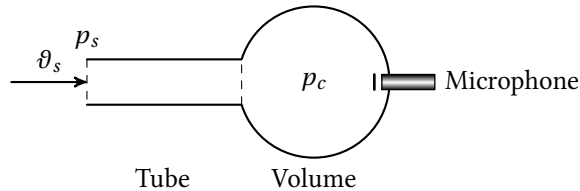
The transmission matrix  $A_{FEM}$  that results from the FEM calculations is shown in figure 5.11. Another calculation without viscothermal effects (SLNS model with  $\Psi_v = \Psi_h = 0$ ) is shown for comparison. The figure shows that the viscothermal effects do not change the curves much, although the front volume is narrow (0.3 mm). An explanation is that the length of the front volume is much smaller than the wavelength. Nevertheless, the viscothermal effects are already noticeable and increase if the front volume is narrowed further. The modeled receiver is one of SONION's larger types. Thus, more viscothermal damping can be expected in models of smaller (newer) receivers.

## 5.4 Coupler model

The performance of a receiver can be measured with a coupler. This tool resembles a Helmholtz resonator with a 2 cc volume in which the pressure is measured by a microphone; see figure 5.12. The compliance of a 2 cc volume corresponds to the compliance of a typical ear canal with eardrum. The



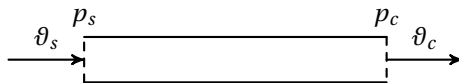
**Figure 5.11:** The components of the transmission matrix  $A_{FEM}$  (—). The results of an isentropic acoustic calculation (---) are added for comparison. Viscothermal damping does not influence the curves much in this calculation.



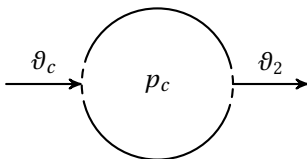
**Figure 5.12:** Schematic drawing of a coupler. It is a measurement tool in the form of a Helmholtz resonator. The measured pressure  $p_c$  is such that it corresponds to the pressure in the ear canal of a user. The specification of the tube depends on the type of hearing aid.

specification of the tube of the coupler depends on the use of the receiver: a behind-the-ear hearing aid has a longer tube than an in-the-ear hearing aid for example. A tube with an inner radius of 0.5 mm and a length of 10 mm is used here.





**Figure 5.13:** Schematic of a tube 2-port. In general, the velocity depends on the location in the tube, thus here  $\vartheta_s \neq \vartheta_c$ , unlike in some other lumped (short) tube models.



**Figure 5.14:** Schematic of an acoustic volume 2-port. Another component can be coupled to the volume with  $\vartheta_2$ , but for the coupler  $\vartheta_2 = 0$ .

### 5.4.1 Tube

A two-port of a uniform tube is defined by using the variables shown in figure 5.13. For tubes that are very short compared to the wavelength, the velocity can be approximated as uniform over the length ( $\vartheta_s = \vartheta_c$ ). However, for longer tubes, or higher frequencies, a different approach is needed. Then, the transmission matrix can be obtained from the analytic solutions of the acoustic model (LRF model), resulting in

$$\begin{Bmatrix} p_s \\ \vartheta_s \end{Bmatrix} = \mathbf{A}_{tube} \begin{Bmatrix} p_c \\ \vartheta_c \end{Bmatrix}, \quad \mathbf{A}_{tube} = \begin{bmatrix} \cos(k_\ell L) & -\frac{Z_\ell}{iS} \sin(k_\ell L) \\ \frac{iS}{Z_\ell} \sin(k_\ell L) & \cos(k_\ell L) \end{bmatrix}, \quad (5.20)$$

with  $L$  in [m] the length of the tube and  $S$  in [m<sup>2</sup>] the surface area of the tube cross section. The above transmission matrix is comparable to the results of Van der Eerden [25]. The difference is that he used admittance matrices instead of transmission matrices. Rules for conversion between these descriptions are listed in [63]. The LRF wave number  $k_\ell$  and characteristic impedance  $Z_\ell$  depend on the tube cross section radius, the frequency and the air parameters; see section 3.3.

### 5.4.2 Volume

The pressure is assumed to be uniform in a lumped acoustic volume; see figure 5.14. The governing equation follows from integrating the continuity equation (3.28) over the volume and the applying Gauss' theorem (1.19) to the divergence of the velocity:

$$\vartheta_{out} = -\frac{ik_0}{Z_0} p \int_{\Omega} \Psi'_h d\Omega, \quad (5.21)$$

where  $\vartheta_{out} = \vartheta_2 - \vartheta_c$  is the nett outward volume velocity in [m<sup>3</sup>/s]. If thermal effects are neglected,  $\Psi'_h = 1$  and the integral equals the volume  $V_0$  in [m<sup>3</sup>]. The two-port transmission matrix equation of the isentropic acoustic volume is

$$\begin{Bmatrix} p_c \\ \vartheta_c \end{Bmatrix} = \mathbf{A}_{volume} \begin{Bmatrix} p_2 \\ \vartheta_2 \end{Bmatrix}, \quad \mathbf{A}_{volume} = \begin{bmatrix} 1 & 0 \\ \frac{ik_0 V_0}{Z_0} & 1 \end{bmatrix}. \quad (5.22)$$

Here,  $\vartheta_2$  (and  $p_2$ ) can be used to connect another component. Figure 5.12 shows a microphone at this location which has a non-zero compliance in general. However, the 2 cc value of the volume already accounts for the microphone compliance. Therefore, the volume flow  $\vartheta_2 = 0$  in the coupler model.

### 5.4.3 Complete coupler

The complete coupler is the series connection of the tube and the volume:

$$\begin{Bmatrix} p_s \\ \vartheta_s \end{Bmatrix} = \mathbf{A}_{coupler} \begin{Bmatrix} p_c \\ 0 \end{Bmatrix}, \quad \mathbf{A}_{coupler} = \mathbf{A}_{tube} \mathbf{A}_{volume}. \quad (5.23)$$

The termination with zero volume flow in the above equation is in fact the prescription of the boundary condition  $\vartheta_2 = 0$ . Furthermore,  $p_2 = p_c$  in the lumped volume by definition. The required parameter values are listed in table 5.3.

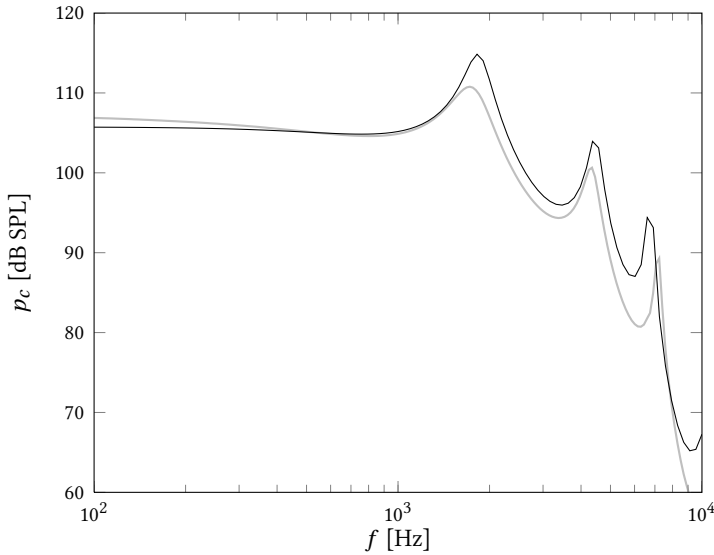
Parameter	Symbol	Value	Unit
Tube radius	$\ell$	$0.5 \cdot 10^{-3}$	m
Tube length	$L$	$10 \cdot 10^{-3}$	m
Coupler volume	$V_0$	$2 \cdot 10^{-6}$	m <sup>3</sup>

Table 5.3: Parameter values for the coupler model.

## 5.5 Results of the complete receiver model

The complete receiver model is described by equation (5.1) in which all sub-models have been presented. The model needs two boundary conditions. The boundary condition at the coupler is  $\vartheta_2 = 0$  as discussed above and the other boundary condition is the electric input which is prescribed as  $V_{in} = 0.11$  V.

The pressure in the coupler  $p_c$  that is calculated by the model is compared to the measured value in figure 5.15. The model and measurement



**Figure 5.15:** Pressure in the coupler for an input voltage  $V_{in} = 0.11$  V: (—) result of the model; (---) measured response.

match well. The model parameters supplied by SONION are for the receiver type, not for the specific specimen that is used in the measurement. Therefore, the results may be improved by validating all model parameters, but this course of action is not pursued here. Since a model of the receiver is now available, it is interesting to visualize the effect of changing several model parameters on the response of the receiver.

Figure 5.16 shows the effect of several motor parameters on the response of the model. These responses are calculated with the original two-port matrix of the FEM part of the model. Therefore, no additional FEM calculations are needed to yield these curves. The calculation time is less than a second for each parameter change. The figure shows that the electric and magnetic parameters ( $R_{DC}$ ,  $n_c$  and  $h_0$ ) mainly influence the response at frequencies below the first resonance peak at 1.8 kHz. The drive pin stiffness  $k_{dp}$  is too high to have a large influence in the shown frequency range. It only influences the third resonance at 6.6 kHz. The armature stiffness influences the response at all frequencies near and below the second resonance peak at 4.4 kHz, while the armature mass  $m_a$  influences the response at all frequencies near and above this resonance.

Figure 5.17 shows how the curves change with several parameters of the FEM model. These parameter studies are much more time consuming to perform than the previous studies, because the coupled FEM calculation has to be redone. Instead of creating a new transmission matrix which requires two

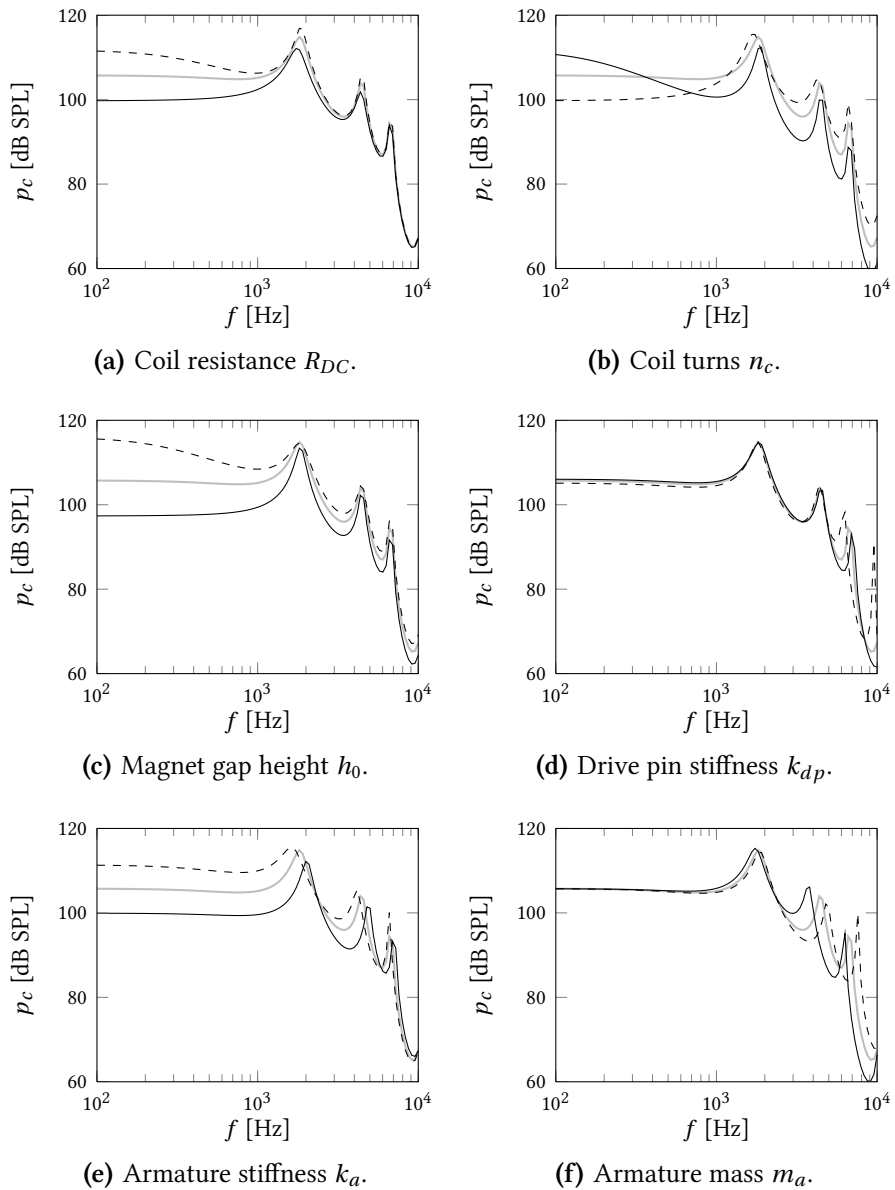
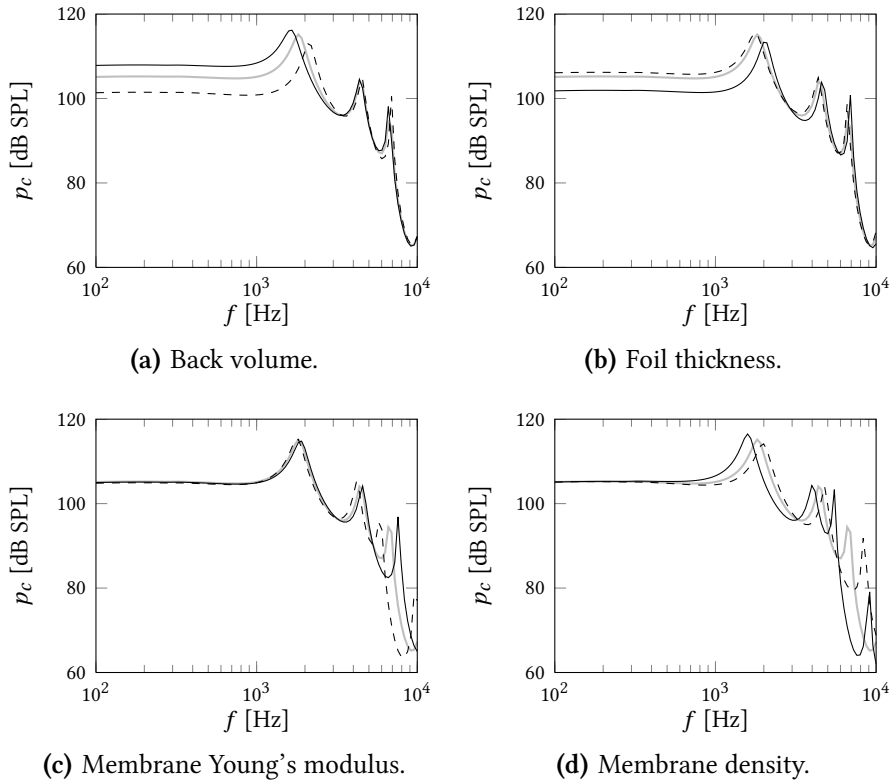


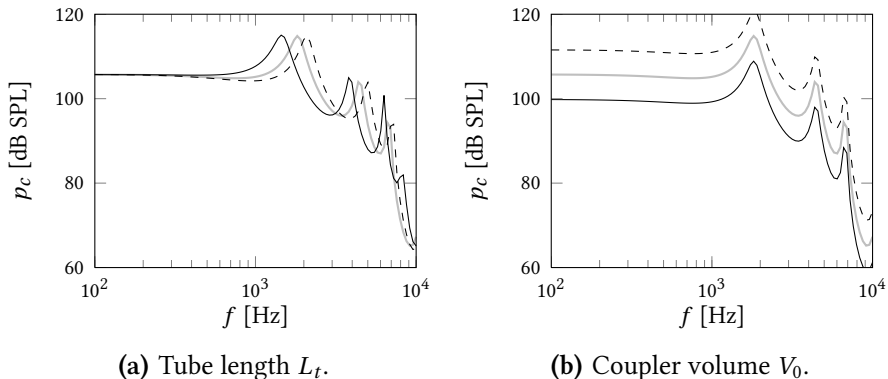
Figure 5.16: Effects of perturbing several motor model parameters: (—) unperturbed model; (---) doubled value; (· · ·) halved value.



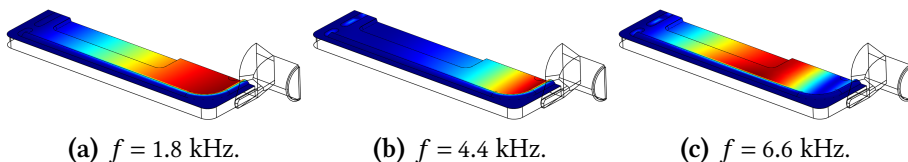
**Figure 5.17:** Effects of perturbing several FEM model parameters: (—) unperturbed model; (---) doubled value; (-.-) halved value.

calculations per curve, the lumped motor and coupler models are included into the FEM model. Therefore, a single FEM calculation per curve suffices, but this calculation is only valid for the used set of model parameters. The figure shows that the back volume has a similar, but smaller, influence on the low frequency response as the armature stiffness. However, the back volume hardly influences the second resonance peak at 4.4 kHz, unlike the armature stiffness. The change of the curves with the foil thickness is unsymmetric: doubling the thickness shows a low frequency decrease of the response, but halving the thickness does not have much influence on the curve at all. Apparently, the contribution of the foil to the total stiffness of the model is insignificant at its nominal thickness. The Young's modulus of the membrane especially influences the third resonance peak at 6.6 kHz. The membrane density has an even larger influence on this peak, but also influences the two other peaks.

The influence of changing the model parameters of the coupler on the response is shown in figure 5.18. The tube length  $L_t$  has an influence that



**Figure 5.18:** Effects of perturbing several coupler model parameters: (—) unperturbed model; (---) doubled value; (-.-) halved value.



**Figure 5.19:** Magnitude of the deflection of the membrane and foil at the three resonance peaks.

is comparable to the other mass-influencing parameters. However, the tube length has a relatively large influence on the first resonance peak at 1.8 kHz. The curves for different coupler volumes  $V_0$  shows that the receiver is effectively an acoustic volume source. The termination volume determines the pressure that this volume source can generate.

An explanation of the resonance peaks follows from the above parameter studies. The first two peaks (1.8 and 4.4 kHz) are coupled mechanic acoustic resonances that are influenced by the tube length, the membrane density and the armature stiffness. Furthermore, the first peak is sensitive to the back volume and the second peak to the armature mass. The third peak is a membrane resonance that is influenced by the density and Young's modulus of the membrane. This resonance is also influenced by the drive pin stiffness and the armature mass. Figure 5.19 shows the deflection amplitude of the structure at the three resonance peaks. The drive pin deflection is relatively small at the third resonance peak and large at the first two peaks.

## 5.6 Summary

This chapter has demonstrated how the viscothermal acoustic models can be used in a design environment. A hearing aid receiver, including coupler, has been modeled. The viscothermal acoustic air is modeled by the SLNS model (FEM part) and the LRF model (coupler part).

Only the front volume, spout, and membrane are modeled with a coupled FEM model and the other parts with efficient lumped models. By using this approach it is possible to do parameter studies efficiently. The costly FEM calculation has to be redone only if one of the parameters in the FEM part of the model is changed; not if parameters in the lumped parts are changed. Several parameter studies are presented. These studies show that the acoustic and mechanic parts are tightly coupled at the first two resonances of the receiver.

The response of the original model matches the measured response. Nevertheless, it may be possible to improve the model if all parts of the model were to be thoroughly validated with measurements.

# Conclusions and discussion

## 6.1 Conclusions

The goal of the PhD project that resulted in this thesis was to create efficient viscothermal acoustic models for arbitrary geometries that may include fluid structure interaction and can be used in a design environment. Four models are presented and compared to each other and to measurements: the full linear Navier-Stokes (FLNS) model, the boundary layer impedance (BLI) model, the low reduced frequency (LRF) model and the sequential linear Navier-Stokes (SLNS) model. Each model contains both the viscous and the thermal effects on the acoustic wave propagation. Furthermore, the models are formulated in the time harmonic form (frequency domain). This section is used to compare the results to the goal of the project. Table 6.1 summarizes these conclusions. The models are more thoroughly compared to each other in section 3.5.

Only the FLNS and SLNS models can be used to model *arbitrary geometries*. Non-homogeneous viscous (shear velocity/force) and thermal (temperature/heat flux) boundary conditions can be prescribed in the FLNS model, but not in the SLNS model. It is possible to extend the SLNS model, but this increases the complexity and the computational costs of the model. Non-homogeneous acoustic (pressure/normal velocity) boundary conditions can be prescribed in both models. The BLI and LRF models are not applicable to arbitrary geometries. The BLI model is suited for relatively large geometries in which all characteristic lengths are larger than the boundary layer thickness. The LRF model is applicable to waveguides (tubes and layers) below the cutoff frequency. A uniform pressure at each waveguide cross section is assumed in the LRF model, like in comparable isentropic acoustic models.

A large difference is observed in the *efficiency* of the models. The equations of the FLNS model have been scaled such that a complex symmetric FEM system matrix results. Although this reduces the computational costs,



Model	Arbitrary geometries	Efficiency	FSI
FLNS	yes	costly	full coupling
SLNS	yes	intermediate	only pressure and normal velocity
BLI	no: all lengths much larger than the boundary layer thickness	efficient	only pressure and normal velocity
LRF	no: waveguides below the cutoff frequency	efficient	only pressure and normal velocity

**Table 6.1:** Comparison of the models for the aspects of suitability for arbitrary geometries, efficiency and fluid structure interaction. All four models are presented in a form that can be used in a design environment. Therefore, this aspect is not included in the table.

the FLNS model is still the least efficient model of this thesis. The limits of a contemporary desktop computer are easily exceeded in 3-D FLNS models. Fortunately, 2-D models require much less computational resources such that the FLNS model can be a good alternative to the other models in 2-D. The BLI and especially the LRF model are the most efficient models in this thesis. Both have computational costs in the order of isentropic acoustic models; with reduced spatial dimensionality for the LRF model.<sup>1</sup> The SLNS model fills the gap between the costly FLNS model and the efficient LRF and BLI models.

All four models can be used in *fluid structure interaction* problems. However, in the SLNS, BLI and LRF models only the velocity in normal direction and the pressure are coupled to the structure. The FLNS model can be used if the shear velocity and forces, and the temperature and heat flow should be coupled to the structure as well. The FLNS model has the disadvantage that essential boundary conditions are involved in the fluid structure interaction. This requires either a reinterpolation (not covered in this thesis) or matching fluid and structure meshes (limiting the choice of structural finite elements). Theoretically, the SLNS model has a potential problem in fluid structure interaction because of the inconsistency in the normal velocity boundary condition. Fortunately, the errors caused by this inconsistency are acceptable in many cases and can be circumvented or reduced in many other cases. No practical limitations to fluid structure interaction with the SLNS model have been encountered.

<sup>1</sup>The calculation of the pressure field has a reduced spatial dimensionality in the LRF model. The viscous and thermal waves are typically calculated analytically. The computational cost increases if these waves must be calculated by FEM.

The applicability in a *design environment* cannot be measured unambiguously. Chapter 5 is an example of how the viscothermal acoustic models can be applied in practice. That chapter presented a model of a hearing aid receiver which agrees well with the measurements. Several parameter studies are carried out efficiently with the model. Another aspect of applicability besides efficiency is the *ease of use*. All four models have been implemented in the finite element software COMSOL. This increases the ease of use, because all preprocessing and postprocessing features of this software can be used. Furthermore, the viscothermal acoustic models can be easily coupled to COMSOL's predefined structural models. Together, the four presented models in this thesis can be used to model many viscothermal acoustic problems effectively.

## 6.2 Discussion

This section discusses the possibilities for further research on the viscothermal acoustic models in this thesis. The discussion is divided into two parts: extensions of the models and improvements of the models.

### 6.2.1 Extending the models

As mentioned, the SLNS model and the LRF model can be extended to include non-homogeneous viscothermal boundary conditions. Hannink [29] presented an LRF model with such an extension. Furthermore, Nijhof [55] presents the LRF model in a very general setting that includes inhomogeneous terms for both the boundary conditions and the PDES. The SLNS model can be extended along similar lines.

One important limitation of all models in this thesis is that the linear acoustic assumptions should be satisfied. Without these assumptions, the already high computational costs of the models would increase dramatically. Inevitably, the linear models have a limited applicability. Given a linear solution of any of the viscothermal acoustic models, the magnitudes of the non-linear terms in the original Navier-Stokes equations can be calculated to check the consistency of the linear assumptions for the modeled problem. Perhaps an estimator can be created from these terms which quantifies the overall model accuracy. In many problems (certainly in hearing aid receivers) a linear overall response is aimed for. It would be beneficial if the user of the model is warned by such an estimator that the model is invalid for input signals larger than a certain value.

Another direction to extend the models in this thesis is the inclusion of mean flow and static temperature gradients. Applications are thermoacoustic engines and mufflers in car exhausts for example. These topics are

studied in for example [1, 2, 13, 24, 33, 48, 56, 57, 66], using models that resemble the LRF model. Similar extensions may be formulated for the FLNS and SLNS models such that problems with mean flow and static temperature gradients can be modeled for arbitrary geometries.

## 6.2.2 Improving the models

The models in this thesis use fairly standard finite element methods. The performance of the models may be improved upon if more sophisticated methods are developed. Several ideas are discussed here.

The FLNS model uses a mixed formulation to prevent locking, as demonstrated in section 2.2.2. Mixed methods are not the only means to prevent locking. For some problems other than viscothermal acoustics, stabilizing terms are added to the standard weak form. These ‘stabilized methods’ potentially result in a good convergence with less degrees of freedom. In viscothermal acoustics, the formulation of Joly [38, 36, 37], which does not include the pressure field, could be a good basis for such stabilized methods. The referenced publications do not mention the use of a stabilization term and may still suffer from mild locking.

The other ideas in this discussion concern the SLNS model. The SLNS model has an inconsistency in the normal velocity boundary condition. Although this inconsistency did not limit the applicability of the SLNS model in practice, the model would be more elegant without the inconsistency. Further research might succeed in finding such an SLNS model, possibly based on the weak form of equation (3.70).

The calculation of the pressure field in the SLNS model can use a much coarser mesh than the calculation of the viscous and thermal fields. However, the pressure field depends on the viscothermal fields. Therefore, the numerical integration method for the assembly of the system matrix of the pressure problem must be accurate enough to account for the small boundary layers of the viscothermal fields. Unfortunately, the gain that is obtained from using a coarse mesh is partially wasted by increasing the order of the numerical integration, as has been shown in section 4.2.3. The method would be more efficient with a smart numerical integration method that increases the order of integration only for the elements in the boundary layer and not for the elements in the bulk.

The above idea could be taken further with adaptive mesh refinement. If the initial mesh of the SLNS problem is the coarse pressure mesh, the viscous and thermal fields can be calculated by using an adaptive mesh refinement procedure that refines the mesh in the boundary layer. The subsequent pressure calculation can use the shape functions that are defined on the coarse initial mesh and the numerical integration scheme that is based on the refined mesh of the viscothermal fields.

Possibly an even more efficient implementation can be created by using both FEM and BEM (boundary element method) for the SLNS model. The viscous and thermal fields can be modeled efficiently in BEM in which only the boundary has to be discretized. This results in a smaller number of degrees of freedom. Furthermore, the system matrix is not full as in acoustic BEM problems, but sparse. This sparsity results from the Green's function that vanishes exponentially with distance for the diffusion-like viscous and thermal fields. The pressure field can be calculated with FEM on a coarse mesh. This calculation would benefit from a smart numerical integration method as described above. The clear drawback of this procedure is that the used software would need to contain both a FEM and a BEM framework.



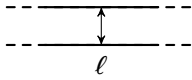
# Appendices



## Viscothermal fields for the LRF model: analytic solutions

Only the results for isothermal / no-slip boundary conditions are shown. The presented equations (excluding those for the ring) are based on the results of Stinson [64, 65] and Kozlov [49].

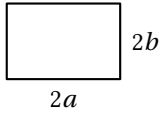
### Slit (Layer)



$$z = [-\ell/2, \ell/2], \quad S_{cd} = \ell,$$

$$\Psi_\phi = 1 - \frac{\cos(k_\phi z)}{\cos(k_\phi \ell/2)}, \quad \Upsilon_\phi = 1 - \frac{\tan(k_\phi \ell/2)}{k_\phi \ell/2}.$$

### Rectangle



$$x = [-a, a], \quad y = [-b, b],$$

$$\ell = \frac{2ab}{a+b}, \quad S_{cd} = 4ab,$$

$$m' = (m + 1/2)\pi,$$

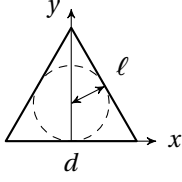
$$\alpha_m = \sqrt{k_\phi^2 - \left(\frac{m'}{a}\right)^2}, \quad \beta_m = \sqrt{k_\phi^2 - \left(\frac{m'}{b}\right)^2},$$

$$\Psi_\phi = k_\phi^2 \sum_{m=0}^{\infty} \frac{-1^m}{m'} \left[ \frac{\cos\left(\frac{m'x}{a}\right)}{\alpha_{\phi m}^2} \left(1 - \frac{\cos(\alpha_{\phi m} y)}{\cos(\alpha_{\phi m} b)}\right) + \frac{\cos\left(\frac{m'y}{b}\right)}{\beta_{\phi m}^2} \left(1 - \frac{\cos(\beta_{\phi m} x)}{\cos(\beta_{\phi m} a)}\right) \right],$$

$$\Upsilon_\phi = k_\phi^2 \sum_{m=0}^{\infty} \left[ (\alpha_{\phi m} m')^{-2} \left(1 - \frac{\tan(\alpha_{\phi m} b)}{\alpha_{\phi m} b}\right) + (\beta_{\phi m} m')^{-2} \left(1 - \frac{\tan(\beta_{\phi m} a)}{\beta_{\phi m} a}\right) \right].$$



## Equilateral triangle

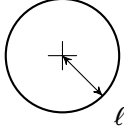


$$\ell = \frac{d}{2\sqrt{3}}, \quad S_{cd} = 3\sqrt{3}\ell^2,$$

$$\Psi_\phi = 1 - \frac{\sin\left(k_\phi \frac{3\ell-2y}{2}\right) + \sin\left(k_\phi \frac{y-\sqrt{3}x}{2}\right) + \sin\left(k_\phi \frac{y+\sqrt{3}x}{2}\right)}{\sin\left(\frac{3}{2}k_\phi\ell\right)},$$

$$\Upsilon_\phi = 1 - 3 \frac{\tan\left(\frac{3}{2}k_\phi\ell\right) - \frac{3}{2}k_\phi\ell}{\left(\frac{3}{2}k_\phi\ell\right)^2 \tan\left(\frac{3}{2}k_\phi\ell\right)}.$$

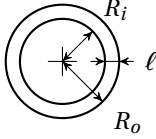
## Circle



$$r = [0, \ell], \quad S_{cd} = \pi\ell^2,$$

$$\Psi_\phi = 1 - \frac{J_0(k_\phi r)}{J_0(k_\phi\ell)}, \quad \Upsilon_\phi = -\frac{J_2(k_\phi\ell)}{J_0(k_\phi\ell)}.$$

## Ring



$$S_{cd} = S_o - S_i, \quad S_o = \pi R_o^2, \quad S_i = \pi R_i^2,$$

$$r = [R_i, R_o], \quad \ell = R_o - R_i,$$

$$\alpha_\phi = \frac{1 - \frac{H_0^{(2)}(k_\phi R_o)}{H_0^{(2)}(k_\phi R_i)}}{1 - \frac{H_0^{(1)}(k_\phi R_i)}{H_0^{(1)}(k_\phi R_o)} \frac{H_0^{(2)}(k_\phi R_o)}{H_0^{(2)}(k_\phi R_i)}}, \quad \beta_\phi = \frac{1 - \frac{H_0^{(1)}(k_\phi R_i)}{H_0^{(1)}(k_\phi R_o)}}{1 - \frac{H_0^{(1)}(k_\phi R_i)}{H_0^{(1)}(k_\phi R_o)} \frac{H_0^{(2)}(k_\phi R_o)}{H_0^{(2)}(k_\phi R_i)}}$$

$$\Psi_\phi = 1 - \alpha_\phi \frac{H_0^{(1)}(k_\phi r)}{H_0^{(1)}(k_\phi R_o)} - \beta_\phi \frac{H_0^{(2)}(k_\phi r)}{H_0^{(2)}(k_\phi R_i)},$$

$$\Upsilon_\phi = \frac{S_i}{S_{cd}} \left[ \alpha_\phi \frac{H_2^{(1)}(k_\phi R_i)}{H_0^{(1)}(k_\phi R_o)} + \beta_\phi \frac{H_2^{(2)}(k_\phi R_i)}{H_0^{(2)}(k_\phi R_i)} \right] - \frac{S_o}{S_{cd}} \left[ \alpha_\phi \frac{H_2^{(1)}(k_\phi R_o)}{H_0^{(1)}(k_\phi R_o)} + \beta_\phi \frac{H_2^{(2)}(k_\phi R_o)}{H_0^{(2)}(k_\phi R_i)} \right].$$

The use of (MATLAB's) scaled Hankel functions is recommended to improve numerical robustness.<sup>1</sup> Furthermore, an approximation as slit is accurate if  $\ell \ll R_i$ .

<sup>1</sup>In ratios of Hankel functions with different arguments (using both  $R_i$  and  $R_o$ ), the unequal scaling of numerator and denominator can be compensated by multiplying the ratio with  $e^{ik_\phi(R_i-R_o)}$ .

## Paper: Performance of Several Viscothermal Acoustic Finite Elements

Copy of the paper [43] published in Acta Acustica united with Acustica. This paper presents convergence tests on several FLNS FEM formulations that satisfy the inf-sup condition. Furthermore, the effect of the discretization of the temperature field on the order of convergence is demonstrated.

# Performance of Several Viscothermal Acoustic Finite Elements

W. R. Kampinga, Y. H. Wijnant, A. de Boer

University of Twente, Department of Applied Mechanics, Drienerlolaan 5, 7500 AE Enschede, The Netherlands.  
W.R.Kampinga@ctw.utwente.nl

## Summary

Viscothermal acoustics can be described by the linearized Navier Stokes equations. Besides inertia and compressibility, these equations take the heat conductivity and the viscosity of the medium (air) into account. These ‘viscothermal’ effects are significant in, for example, miniature acoustic transducers and MEMS devices. A finite element for viscothermal acoustics, which can be used to model such devices, is presented. The particular set of equations used in the model of viscothermal acoustics leads to a complex symmetric finite element system matrix. Several different FEM discretizations are studied on a 2D thin gap problem. These discretizations are known, in the context of the Stokes equation, as the Taylor Hood quadrilateral and triangle elements, the Crouzeix Raviart element and the MINI element. All elements are implemented in the FEM software COMSOL. The elements with quadratic velocity and temperature shape functions show the best orders of convergence.

PACS no. 43.20.-f

## 1. Introduction

The standard model for isentropic acoustics is the wave equation or the Helmholtz equation. The (dissipative) viscothermal effects, being heat conduction and viscous friction, are neglected in this model. Unfortunately, this simplification is not allowed in many cases. Particularly in small geometries, these effects cannot be neglected. Examples of such applications are small acoustic transducers used in hearing aids and mobile telephones, and vibrating micro electro-mechanical systems (MEMS). A finite element that can model the behavior of air in these devices is presented in this paper.

Viscothermal acoustic models consist of a linearized set of the Navier Stokes equations. Solving these models generally requires much more computational effort than solving isentropic acoustic problems. However, under certain geometric constraints, the equations can be simplified considerably. The literature presents models for gaps (layers) and tubes that are hardly more costly to solve than isentropic acoustic problems; see for example [1, 2, 3], based on [4]. In these models, the gap thickness or the tube cross section dimensions should be smaller than the acoustic wavelength. Another family of models for which the required computational effort is reduced, is only valid for large domains, relative to the viscous and thermal boundary layer thicknesses, with smooth boundaries; see [5]. This model is based on the finite acoustic impedance of a rigid boundary due to viscothermal effects, see also for example [6, 7].

In contrast, no geometric restrictions are imposed on the finite element in this paper. However, this advantage does lead to an increase in computational effort to solve the model. The finite element in this paper has not only the pressure, but also the temperature and the velocity vector as degrees of freedom. Furthermore the FE mesh needs to be much finer to resolve the boundary layer. Therefore, the finite element in this paper is mainly intended to model applications for which the simplified models mentioned above can not be used.

Several viscothermal acoustic models without geometric restrictions have already been presented in the literature; see Cutanda [8] (based on Karra [9] and Bruneau [6]) for BEM and Malinen [10] for FEM. Cheng [11] presented an acoustic finite element including viscous friction, but without heat conduction. Furthermore, users of the FEM software COMSOL can request an implementation of a finite element for viscothermal acoustics. All these finite elements use a mixed formulation to accurately account for near incompressibility. Joly [12] presents a method for viscothermal acoustics without explicitly mentioning a mixed method. Instead, similarity to standard elastodynamic and diffusion equations is emphasized, which also may be solved by a mixed method.

The finite elements used in this paper resemble COMSOL’s unofficial implementation. However, a differently scaled entropy equation (for the thermal effects) is used. This has the advantage of resulting in a complex symmetric (although not Hermitian) FEM system matrix, which can be solved with reduced computational costs.

Besides the specific formulation, several combinations of shape functions can be chosen for the viscothermal finite element. For example, Malinen [10] uses bi-linear

shape functions with added bubble functions for the velocity field, and Cheng [11] uses bi-quadratic shape functions for the velocities and linear discontinuous shape functions for the pressure. This paper shows the effect of the shape functions on the order of convergence on a simple 2D problem.

The paper starts with a presentation of the linearized Navier Stokes equations for viscothermal acoustics in section 2. Next, a weak formulation of this set of equations and seven different finite element discretizations of it are presented in section 3. In section 4, the convergence of these finite elements are studied on a simple 2D problem. Finally, the results are discussed in section 5. The viscothermal finite elements are implemented in the ‘PDE application mode’ of the FEM software COMSOL; see [13].

## 2. Model of viscothermal acoustics

After introducing the notation of this paper, a set of linearized Navier Stokes equations which describes viscothermal acoustics is presented. Next, a material model for air is explained. Then the Navier Stokes equations are rewritten in a form with velocities, temperature and pressure as the degrees of freedom. This section ends with a discussion of the boundary conditions for viscothermal acoustics.

### 2.1. Notation

Similar to normal acoustics, the equations of viscothermal acoustics can be formulated in time harmonic form, in which the degrees of freedom are the complex valued perturbation amplitudes of the variables. For example, the pressure can be written as

$$\check{p} = p_0 + \Re(p e^{i\omega t}), \quad (1)$$

with  $i$  the imaginary unit,  $\omega$  the angular frequency and  $t$  the time. The operator  $\Re$  takes the real part of its argument. Moreover,  $\check{p}$  is the (real valued) absolute pressure,  $p_0$  is the (real valued) mean pressure, and  $p$  is the complex valued pressure perturbation amplitude (or phasor) that is used as a degree of freedom in the model. Similar definitions hold for the other degrees of freedom; temperature  $T$ , density  $\rho$ , velocity vector  $\mathbf{v}$ , entropy  $s$  and enthalpy  $H$ . The mean velocity  $\mathbf{v}_0$  is assumed to be zero.

### 2.2. Linearized time harmonic Navier Stokes equations

Viscothermal wave propagation can be described by the linearized Navier Stokes equations; see for example [14, 7]. For the linearization, small perturbations are assumed, for example

$$\left| p/p_0 \right| \ll 1. \quad (2)$$

Similar relations are valid for the other degrees of freedom. The exception is the velocity vector, whose magnitude is small compared to the (isentropic) speed of sound, rather than the mean velocity (which is assumed to be

zero). It is also assumed that the non-linear convective derivatives of the Navier Stokes equations can be replaced by the linear time derivatives. Both assumptions are also made in the derivation of the wave equation for isentropic acoustics.

Using the notation from section 2.1, the linearized time harmonic Navier Stokes equations for viscothermal acoustics can be written as

$$i\omega\rho_0\mathbf{v} = \nabla \cdot \boldsymbol{\sigma} + \mathbf{f}, \quad (3a)$$

$$i\omega\rho_0 T_0 s = -\nabla \cdot \mathbf{q} + Q, \quad (3b)$$

$$i\omega\rho/\rho_0 = -\nabla \cdot \mathbf{v}. \quad (3c)$$

The symbols  $\mathbf{q}$  and  $\boldsymbol{\sigma}$  denote the heat flow perturbation and the total stress tensor;  $\mathbf{f}$  and  $Q$  are the body force (per unit volume) and the heat source. The symbol  $\nabla$  denotes the divergence operator ( $\nabla$  is the gradient operator).

Equation (3a) is the *momentum balance* and relates momentum change to the applied forces (per unit volume). Equation (3b) is the *entropy balance* and relates the entropy change to the applied heat. Equation (3c) is the *mass balance* or *continuity equation* and relates density change to mass inflow.

Interestingly, in the limit where the angular frequency  $\omega$  goes to zero, the set of equations reduces to the incompressible Stokes equations. In this case, the entropy equation decouples. Based on this observation, the viscothermal acoustic equation could be regarded as the Stokes equation with added inertia and compressibility terms.

The set of equations also contains the isentropic acoustic limit, for which  $s = 0$ . This requires zero heat transfer and zero viscous stresses; or  $\kappa = 0$ ,  $Q = 0$ ,  $\mu = 0$  and  $\lambda = 0$ .<sup>1</sup> Under these constraints, the system of equations reduces to the acoustic Helmholtz equation if the remaining terms of the momentum equation and the entropy equation are substituted into the continuity equation. The viscothermal equations can therefore be regarded as isothermal acoustics with added viscous and heat conduction terms. This is of course where the name ‘viscothermal acoustics’ originates from.

### 2.3. Material model

The set of equation (3) is not complete: it does not contain a material model. A Newton Fourier ideal gas model is accurate for air in viscothermal acoustics in many cases; see for example [14, 7].

A *Newtonian fluid* model is used to express the total stress tensor as function of the velocity vector and the pressure:

$$\boldsymbol{\sigma} = \tau - p\mathbf{I}, \quad (4a)$$

$$\tau = \lambda(\nabla \cdot \mathbf{v})\mathbf{I} + 2\mu\boldsymbol{\epsilon}, \quad (4b)$$

$$\boldsymbol{\epsilon} = \frac{1}{2}(\nabla\mathbf{v} + (\nabla\mathbf{v})^T). \quad (4c)$$

<sup>1</sup> The last two constraints cannot be deduced from equation (3b). They originate from the *nonlinear* entropy equation, which contains a term that accounts for viscous heating. This term is quadratic in the velocities and therefore very small compared to the other terms under viscothermal conditions. Therefore, this viscous heating term has been neglected in the linearization.

Here  $\tau$  is the viscous stress tensor,  $\mathbf{I}$  is the identity tensor,  $\varepsilon$  is the symmetric part of the velocity gradient, and  $\mu$  and  $\lambda$  are the dynamic viscosity and the second viscosity respectively.

The heat flow can be expressed as function of the temperature gradient by *Fourier's law* of heat conduction:

$$\mathbf{q} = -\kappa \nabla T, \quad (5)$$

where  $\kappa$  is the heat conduction coefficient.

Finally, the assumptions of an *ideal gas* are made, which results in the thermal and caloric equations of state:

$$\frac{\rho}{\rho_0} = \frac{p}{p_0} - \frac{T}{T_0}, \quad (6a)$$

$$H = C_p T, \quad (6b)$$

where  $H$  is the enthalpy perturbation and  $C_p$  is the specific heat at constant pressure. Equation (6a) is the linearized version of the well known ideal gas law  $\check{p} = \check{\rho} R_0 \check{T}$  with  $R_0$  the specific gas constant.

#### 2.4. Final PDE formulation

An additional identity is needed to rewrite the entropy in the preferred degrees of freedom ( $\mathbf{v}$ ,  $T$  and  $p$ ). This equation is known as the Gibbs relation:  $\check{T} d\check{s} = d\check{H} - \check{\rho}^{-1} d\check{p}$ . Linearization yields

$$\rho_0 T_0 s = \rho_0 H - p. \quad (7)$$

The equations (4–7) can be substituted in the set of equations (3) to put it in a form with the velocity, temperature and pressure as the degrees of freedom,

$$i\omega \rho_0 \mathbf{v} - \nabla \cdot \boldsymbol{\sigma} = \mathbf{f}, \quad (8a)$$

$$i\omega \rho_0 C_p T + \nabla \cdot \mathbf{q} - i\omega p = Q, \quad (8b)$$

$$\nabla \cdot \mathbf{v} - i\omega \frac{T}{T_0} + i\omega \frac{p}{\rho_0} = 0. \quad (8c)$$

The divergence terms are also a function of the chosen degrees of freedom,

$$\nabla \cdot \boldsymbol{\sigma} = (\lambda + \mu) \nabla (\nabla \cdot \mathbf{v}) + \mu \Delta \mathbf{v} - \nabla p, \quad (8d)$$

$$\nabla \cdot \mathbf{q} = -\kappa \Delta T, \quad (8e)$$

where  $\Delta$  is the Laplace operator.

#### 2.5. Boundary conditions

A total of four boundary conditions (BCs) must be prescribed on each location of the boundary: three mechanical BCs and one thermal BC. The mechanical BCs are velocity

$$\mathbf{v} = \mathbf{g}_v, \quad (9)$$

or stress

$$\boldsymbol{\sigma} \cdot \mathbf{n} = (\lambda (\nabla \cdot \mathbf{v}) \mathbf{I} + 2\mu \boldsymbol{\varepsilon} - p \mathbf{I}) \cdot \mathbf{n} = \mathbf{h}_v, \quad (10)$$

where the symbol  $\mathbf{n}$  is the normal unit vector on the boundary,  $\mathbf{g}_v$  is the prescribed velocity data and  $\mathbf{h}_v$  the prescribed stress data. Often, the mechanical BCs are decomposed into the directions normal and tangential to the boundary.

On each boundary location and in each direction either a velocity, or a stress must be prescribed. The thermal BCs are temperature (Dirichlet)

$$T = g_T, \quad (11)$$

or heat flux (Neumann)

$$\mathbf{q} \cdot \mathbf{n} = -\kappa (\nabla T) \cdot \mathbf{n} = h_T. \quad (12)$$

Likewise, on each boundary location either a temperature, or a heat flux must be prescribed.

Typically, viscous effects are a result of zero tangential velocity BCs, and thermal effects of zero temperature perturbation (isothermal) BCs. Frequently used BCs include the *wall* BC with  $\mathbf{g}_v = \mathbf{0}$  and  $g_T = 0$ ; and the *symmetry* BC with  $\mathbf{g}_v \cdot \mathbf{n} = 0$ ,  $\mathbf{h}_v \cdot \mathbf{t}_1 = 0$ ,  $\mathbf{h}_v \cdot \mathbf{t}_2 = 0$  and  $h_T = 0$ . Where  $\mathbf{t}_1$  and  $\mathbf{t}_2$  are the unit vectors tangential to the boundary.

Notice that the expression for the normal stress ( $\boldsymbol{\sigma} \mathbf{n}$ ) is usually dominated by the pressure. Therefore, a prescribed normal stress is similar to a prescribed acoustic pressure. Furthermore, an acoustic impedance boundary condition can be prescribed as a normal stress as function of the normal velocity:  $\mathbf{h}_v \cdot \mathbf{n} = Z \mathbf{v} \cdot \mathbf{n}$ , where  $Z$  is the impedance. Notice that the isentropic acoustic model inherently satisfies the zero tangential (shear) stress and zero heat flux. Interestingly, if zero tangential stress and zero heat flux would be prescribed on *all* boundaries in a viscothermal acoustical model, it would yield similar results as the isentropic acoustic model.

In the finite element context, it would be straightforward to apply the Dirichlet (velocity and temperature) BCs as essential BCs and the Neumann (stress and heat flux) BCs as natural BCs. The set of equations (8) already shows the divergence of the stress tensor and divergence of the heat flow vector. These terms can lead to the preferred natural BCs; see the next section.

### 3. Finite element formulations

The set of equations (8) is the basis for the finite element. This is called a *mixed formulation*, because the pressure variable  $p$  can be removed (without increasing the order of the differential equations) but is not. Removing the pressure seems advantageous because it reduces the number of equations and degrees of freedom, but it may cause problems related to the (near) incompressibility; see [15]. Malinen [10] uses a scaled density variable instead of the pressure to tackle the same problem in his mixed finite element for viscothermal acoustics. Notice that the density fields also show boundary layers, which may be a disadvantage since this field is discretized with lower order shape functions.

First, the weak form for the viscothermal finite element is derived from the set of linearized Navier Stokes equations. The complex symmetry of the weak form is pointed out. Next, several stable discretizations of this weak form are presented.

### 3.1. Weak form

The weak form is obtained by using a Galerkin approach: the equations in (8) are multiplied by the weighing functions  $\mathbf{v}_w$ ,  $T_w$  and  $p_w$  respectively, and integrated over the domain  $\Omega$ . Next, Green's formula is applied to the terms containing second order derivatives, namely  $\nabla \cdot \sigma$  and  $\nabla \cdot \mathbf{q}$ . Last, the entropy equation is divided by  $T_0$  to obtain a symmetric weak form. The resulting equations are

$$a(\mathbf{v}_w, \mathbf{v}) - \langle \nabla \cdot \mathbf{v}_w, p \rangle = \langle \mathbf{v}_w, \mathbf{f} \rangle + \langle \mathbf{v}_w, \mathbf{h}_v \rangle_{\partial\Omega}, \quad (13a)$$

$$c(T_w, T) + \frac{i\omega}{T_0} \langle T_w, p \rangle = -\frac{1}{T_0} \langle T_w, Q \rangle + \frac{1}{T_0} \langle T_w, h_T \rangle_{\partial\Omega}, \quad (13b)$$

$$e(p_w, p) - \langle p_w, \nabla \cdot \mathbf{v} \rangle + \frac{i\omega}{T_0} \langle p_w, T \rangle = 0, \quad (13c)$$

with

$$a(\mathbf{v}_w, \mathbf{v}) = i\omega\rho_0 \langle \mathbf{v}_w, \mathbf{v} \rangle + 2\mu \langle \varepsilon_w, \varepsilon \rangle + \lambda \langle \nabla \cdot \mathbf{v}_w, \nabla \cdot \mathbf{v} \rangle, \quad (13d)$$

$$c(T_w, T) = -\frac{i\omega\rho_0 C_p}{T_0} \langle T_w, T \rangle \quad (13e)$$

$$-\frac{\kappa}{T_0} \langle \nabla T_w, \nabla T \rangle, \quad (13f)$$

$$e(p_w, p) = -\frac{i\omega}{\rho_0} \langle p_w, p \rangle, \quad (13g)$$

where  $\varepsilon_w$  is defined by equation (4c) in which  $\mathbf{v}$  is replaced by  $\mathbf{v}_w$ . Equation (13) uses the inner products over the domain  $\Omega$  and its boundary  $\partial\Omega$ , which are given by

$$\langle \mathbf{v}_w, \mathbf{v} \rangle = \int_{\Omega} \overline{\mathbf{v}_w} \cdot \mathbf{v} \, d\Omega, \quad (14)$$

$$\langle \mathbf{v}_w, \mathbf{h}_v \rangle_{\partial\Omega} = \int_{\partial\Omega} \overline{\mathbf{v}_w} \cdot \mathbf{h}_v \, d\Omega, \quad (15)$$

and similar for other arguments. The bar over  $\mathbf{v}_w$  denotes complex conjugation. Notice that all complex conjugations in equation (13) are taken over the real valued weighing functions. The complex conjugation is only included for the definition of a real valued norm that is used later (equation 18). For tensors, the dot products in equations (14) and (15) are replaced by the double dot product.

As usual in a Galerkin approach, the weighing functions will use the same function basis as their corresponding degrees of freedom; for example,  $p$  and  $p_w$  have the same function basis. All used bases consist of real valued functions only. Therefore, the weak form of equation (13) already shows that the resulting FEM system matrix will be complex symmetric (not Hermitian). The system matrix becomes complex only because of the  $i\omega$  terms in equation (13). In matrix notation, the discretized FEM version of equation (13) reads

$$\begin{bmatrix} \mathbf{A} & \mathbf{0} & \mathbf{B} \\ \mathbf{0} & \mathbf{C} & \mathbf{D} \\ \mathbf{B}^T & \mathbf{D}^T & \mathbf{E} \end{bmatrix} \begin{Bmatrix} \vec{\mathbf{v}} \\ \vec{T} \\ \vec{p} \end{Bmatrix} = \begin{Bmatrix} \vec{\mathbf{f}} \\ \vec{Q} \\ \mathbf{0} \end{Bmatrix}, \quad (16)$$

where  $\vec{\mathbf{v}}$ ,  $\vec{T}$  and  $\vec{p}$  are the vectors of nodal values of the FE model. The sub-matrices  $\mathbf{A}$ ,  $\mathbf{C}$  and  $\mathbf{E}$  correspond to  $a$ ,  $c$  and  $e$  defined by equation (13). The sub-matrices  $\mathbf{B}$  and  $\mathbf{D}$  stem from the terms in the weak form that contain  $\langle \nabla \cdot \mathbf{v}_w, p \rangle$  and  $\langle T_w, p \rangle$ ; and the transposed of these sub-matrices stem from the terms that contain  $\langle p_w, \nabla \cdot \mathbf{v} \rangle$  and  $\langle p_w, T \rangle$ . The right hand side of equation (16) corresponds to the right hand sides of equation (13) and contains the body forces, the heat sources and the natural boundary conditions. If these terms are prescribed as a function of the DOFs, they will contribute to the system matrix. This can be the case for impedance boundary conditions. Usually, this contribution is complex symmetric. Therefore, usually the system matrix is complex symmetric. Some solvers, see [13], can use this symmetry to reduce the solving time and memory requirements; see section 4.3 for an indication of these reductions.

### 3.2. FEM discretizations

The weak form of equation (13) can be discretized by using the usual FEM shape functions to interpolate the degrees of freedom. Similar to FEM discretizations of the incompressible Stokes equations, only certain combinations of the velocity and the pressure shape function spaces are stable. For example, if the same shape functions are chosen for these DOFs, the element is unstable. This problem, related to the incompressibility, has been extensively analyzed in the literature, especially on the Stokes equations. For example, Gunzburger [15] describes solutions to this problem. Comparable mixed formulations can be used in isentropic acoustics (using a displacement/pressure based formulation); see [16].

For viscothermal acoustics, which can be regarded as nearly incompressible, the same problem occurs. In this paper, four conforming discretizations of  $\mathbf{v}$  and  $p$  that are stable for the Stokes equations (they satisfy the inf-sup condition) will be used to discretize equation (13). Table I summarizes these four discretizations: the Taylor Hood triangle element and the Taylor Hood quadrilateral element [17], the Crouzeix Raviart element [18] and the MINI element of Arnold, Brezzi and Fortin [19]. The original publications are indicated, but an overview of all these elements and many more in the context of the (Navier-)Stokes equations can be found in many textbooks and papers, for example [15, 20, 21]. The symbols  $\triangle$  and  $\square$  denote a triangular and a quadrilateral shape. The symbols  $P_1$ ,  $P_2$ ,  $Q_1$  and  $Q_2$  indicate piecewise linear, quadratic, bilinear and biquadratic  $C^0$  continuous FEM shape functions respectively. These shape functions are all from the family of Lagrangian shape functions. The symbol  $P_{-1}$  denotes piecewise linear pressure shape functions that are discontinuous over the element boundaries. Finally, the superscript plus sign as in  $P_1^+$  indicates that the function space is enriched by cubic bubble functions. This paper only shows a 2D case, but all elements have 3D equivalents which are stable for the Stokes equations.

In comparison, Malinen [10] uses a quadrilateral element that is related to the MINI element; see also [22].

Table I. Discretizations that are stable for the mixed Stokes equations.

Stokes element	shape	$\mathbf{v}, \mathbf{v}_w$	$p, p_w$	$T, T_w$
Taylor Hood	$\triangle$	$P_2$	$P_1$	$P_2$
Taylor Hood	$\square$	$Q_2$	$Q_1$	$Q_2$
Crouzeix Raviart	$\triangle$	$P_2^+$	$P_{-1}$	$P_2$
MINI	$\triangle$	$P_1^+$	$P_1$	$P_1$

This element uses alternative bubble functions that COMSOL does not provide. Cheng [11] uses a 3D brick element with  $Q_2$  velocity shape functions and  $P_{-1}$  pressure shape functions, and no temperature shape functions. COMSOL does not provide  $P_{-1}$  shape functions on brick (or quadrilateral) elements.

There are no indications that the discretization of the temperature DOF is critical for the stability of the element; the temperature field even decouples in the limit  $\omega \rightarrow 0$ . Since the temperature and velocity boundary layer are similar in shape and size, it seems advantageous to use the same order of shape functions for the temperature as for the velocity components, as indicated in table I. Besides these shape functions, lower order shape functions for  $T$  are also tested in the next section.

### 4. Results

The finite element is intended to model engineering problems with arbitrarily shaped geometries. Especially for geometries with one or more characteristic dimensions that are of comparable size as the boundary layers. In other cases, Bossart’s model [5] might be a computationally less costly alternative to the finite element presented in this paper.

For the evaluation of the elements, a problem with a known solution is used: the thin gap. After introduction of this problem, the performance of the elements with different discretizations are compared. Last, the benefits of the complex symmetry of the FEM matrix are demonstrated.

#### 4.1. The thin gap problem

The considered problem is a thin 2D gap that is closed at the left hand side ( $v_x = 0$ ) and has a pressure source at the right hand side ( $p = 1$ ); see Figure 1. Viscous and thermal boundary layers form along the walls of the gap (drawn with thick lines). The thickness is  $h_0 = 0.25$  mm and the length is  $L = 2$  mm.

The gap is very thin compared to the acoustic wavelength. Therefore, it can be accurately described by the low reduced frequency (LRF) model for layers; see [2]. This model describes the viscous and thermal effects in the gap thickness, or  $z$ -direction and the dissipative wave propagation in  $x$ -direction. The LRF model is accurate for the velocity in propagation direction, the pressure and the temperature DOFs. This *accurate* solution can be made to satisfy equations (8) *exactly* by letting these solutions define the velocity in cross section direction  $v_z$ , the heat source

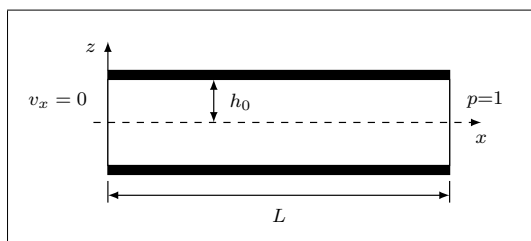


Figure 1. The gap geometry with LRF boundary conditions, dimensions, symmetry line and coordinate directions.

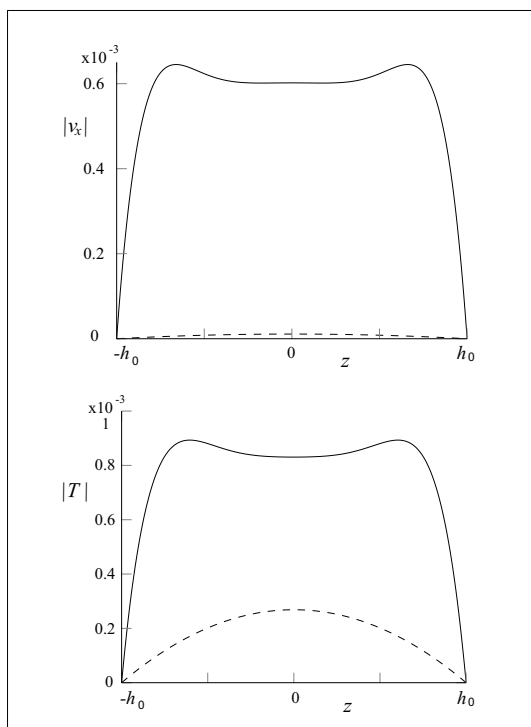


Figure 2. Velocity and temperature solutions at  $x = L$ , for  $f = 10$  kHz (—) and  $f = 100$  Hz (---).

$Q$  and the body forces  $\mathbf{f}$ ; see the appendix. Although the effects of  $Q$  and  $\mathbf{f}$  on the solution are very small, the exact solution is used to compare the convergence behavior of the four FEM discretizations described in the previous section and the alternatives with lower order temperature discretization.

A frequency range of 10 Hz to 10 kHz is used in the tests. Only the upper half of the layer is modeled in the FE model. A symmetry boundary condition is applied at the symmetry line. Furthermore, essential velocity and temperature boundary conditions that are defined by the exact solution are applied on the remaining three boundaries.

Figure 2 shows the solutions of the temperature and the velocity in  $x$ -direction, at  $x = L$ , for  $f = 100$  Hz and  $f = 10$  kHz, obtained with the LRF model. Clearly, the viscothermal effects are prevalent even for the upper limit of

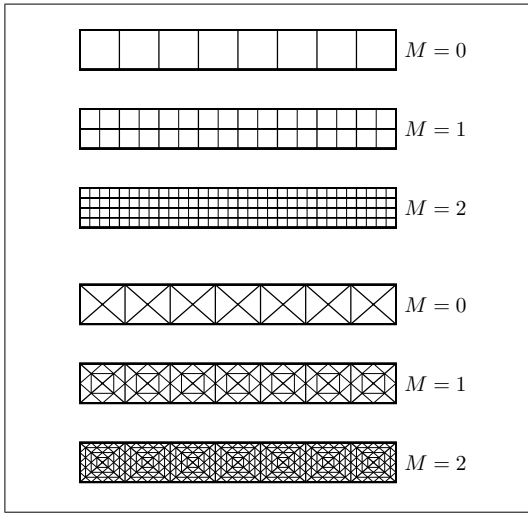


Figure 3. Quadrilateral and triangular mesh sequences. In each refinement, the element size is halved and the surface area divided by four. Notice that for each value of  $M$ , the triangular mesh contains more degrees of freedom than the corresponding rectangular mesh.

the chosen frequency range. This frequency range is chosen, because within this range the model of Bossart [5] loses accuracy and the viscothermal finite element gains accuracy; see the next section. Furthermore, the stability problems related to incompressibility, if present, are expected to occur at low frequencies.

#### 4.2. Convergence

The convergence of the finite element is tested by investigating the error for a sequence of meshes. In a subsequent mesh refinement, each element is divided in four elements, halving the element size  $h_e$ . Figure 3 shows the first three mesh cases. The higher mesh cases follow the same pattern.

A relative error measure is used in this section, defined by

$$e_p = \frac{\|p - \hat{p}\|}{\|\hat{p}\|} \quad (17)$$

for the pressure and similarly for the other degrees of freedom. In this equation the hat, as in  $\hat{p}$ , denotes the exact solution. The used norm is the  $L^2$  norm:

$$\|\hat{p}\| = \sqrt{\langle \hat{p}, \hat{p} \rangle}. \quad (18)$$

These norms and error measures are real valued because of the complex conjugation in the inner product, defined by equation (14).

The finite element errors are shown in Figures 4 to 6. Comparable elements are plotted in the same figures. Clearly the lowest errors are obtained with the quadrilateral elements in Figure 4. For these elements, the errors in

all variables drop to very low values at low frequencies. Furthermore, these elements show the largest error reduction for each mesh refinement; that is the largest order of convergence.

The dotted line in these figures is the result from a FEM implementation of the model of Bossart. The parameter  $k_w$  (see [5]) is manually set to the accurate value  $k_w = k = \omega/c_0$ , to show the best case scenario for this model. The figure shows the anticipated increase in the errors  $e_{v_x}$  and  $e_T$  for lower frequencies. Despite the high error in the velocity and temperature of this model at low frequencies, the error in the pressure  $e_p$  remains very low and reduces for lower frequencies. This is not surprising because the modeled gap is very short compared to the wavelength. Therefore the pressure is almost uniform and becomes more uniform for lower frequencies (larger wavelengths). For the high frequency range the errors in the velocity and temperature of Bossart's model are competitive with those of the viscothermal finite element.

The figures show a reduction of the error with each mesh refinement. The distances between the lines in the figures indicate the orders of convergence. For the *Taylor Hood* and *Crouzeix Raviart* elements listed in table I, the orders of convergence, calculated from Figure 4, are

$$e_{v_x} \propto h_e^3, \quad e_T \propto h_e^3, \quad e_p \propto h_e^4;$$

with  $h_e$  the element size in [m]. If the (bi)quadratic shape functions for the *temperature* are replaced by (bi)linear *shape functions*, the orders of convergence, calculated from Figure 5, are

$$e_{v_x} \propto h_e^3, \quad e_T \propto h_e^2, \quad e_p \propto h_e^2;$$

and for the *mini element*, also listed in table I, the orders of convergence, calculated from Figure 6, are

$$e_{v_x} \propto h_e^2, \quad e_T \propto h_e^2, \quad e_p \propto h_e^2.$$

The order of convergence is one order higher than the order of the used shape functions, as expected from interpolation theory. The only exception, in positive sense, is the pressure degree of freedom in Figure 4, which is the additional DOF in the mixed formulation. Its order of convergence is 4 for these elements with quadratic velocity and temperature shape functions.

In most figures, the error is proportional to frequency:  $e \propto f$ . However, for elements with linear shape functions, the frequency dependence vanishes below 300 Hz: the lines become horizontal. Below this frequency, the temperature and velocity profiles become parabolic, see Figure 2. Therefore quadratic shape functions become exact in the low frequency limit.

The error in the velocity for the *triangular* elements with quadratic shape functions also becomes frequency independent, but at a frequency of 10 Hz. The *quadrilateral Taylor Hood* element does not show this behavior. The effect is not further investigated, because the lowest frequency is already an extremely viscous case. Moreover,



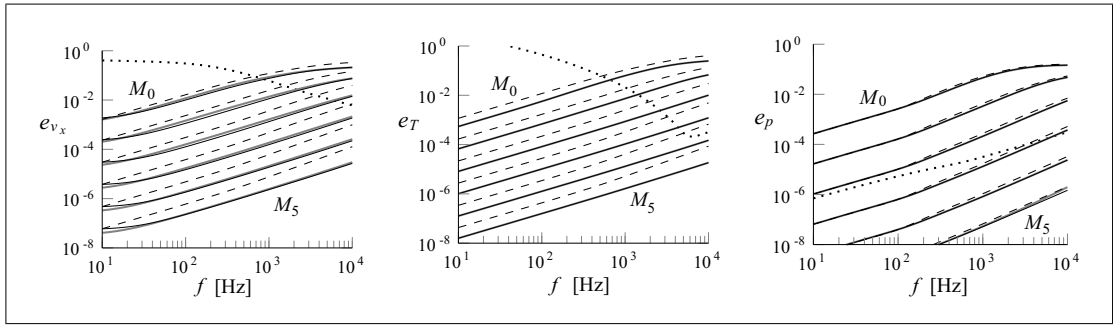


Figure 4. Performance of the Taylor hood quadrilateral (---), triangle (—) and the Crouzeix Raviart element (thick grey line, mostly hidden below —) for mesh cases  $M = 0$  to  $M = 5$ , from top to bottom. Especially the order of convergence of the pressure is high. The error of Bossart’s model is shown in comparison (···).

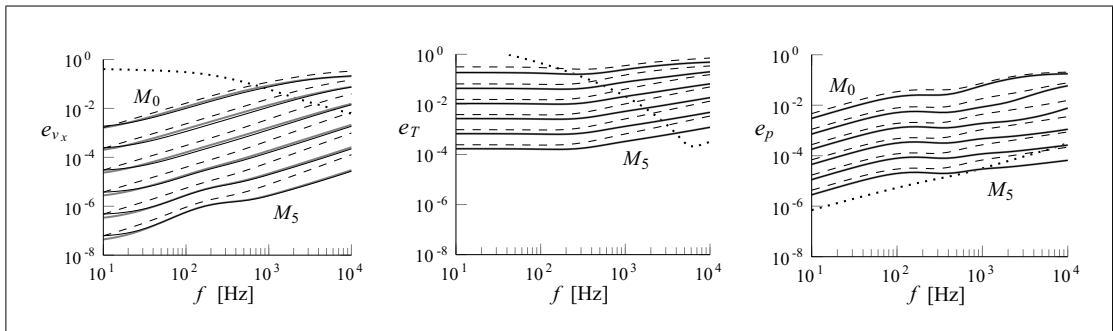


Figure 5. Performance of the Taylor hood quadrilateral with bilinear temperature (---), triangle with linear temperature (—) and the Crouzeix Raviart (thick grey line, mostly hidden below —) element with linear temperature for mesh cases  $M = 0$  to  $M = 5$ , from top to bottom. The linear temperature discretization affects not only the temperature error, but also the pressure error. The error of Bossart’s model is shown in comparison (···).

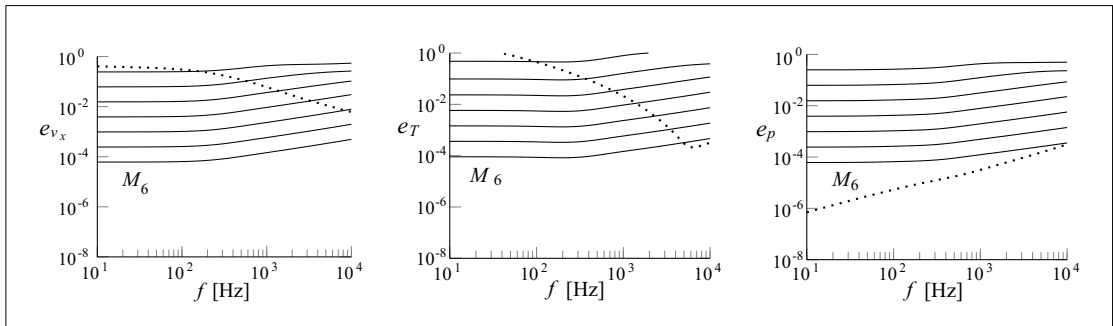


Figure 6. Performance of the mini element for mesh cases  $M = 0$  to  $M = 6$ , from top to bottom. The errors in the different variables are comparable, especially at low frequencies. The error of Bossart’s model is shown in comparison (···).

the order of convergence is not reduced and the error is already very low.

In conclusion, the Taylor Hood and Crouzeix Raviart elements with quadratic velocity and temperature variables are the best of the reviewed elements. The order of convergence of the pressure is two orders better than for the other elements. Furthermore, they behave better at the low frequency range where the velocity and temperature profiles become parabolic.

### 4.3. Benefits of complex symmetry

In section 3, the complex symmetry of the finite element formulation was presented as an advantage with respect to computational costs. Since the computational cost depends on many parameters, such as mesh, element and solver, the above claim is not thoroughly investigated. However, Table II does give an idea of the differences between the calculation times with a symmetrical system ma-

Table II. The benefits of a complex symmetric FEM system matrix: faster solving and lower memory usage.

Element	Mesh	Solver	$t$ symm	$t$ unsymm
TH $\triangle$	4	PARDISO	35 [s]	45 [s]
TH $\square$	5	PARDISO	139 [s]	fails
CR	4	SPOOLES	96 [s]	129 [s]
MINI	4	SPOOLES	28 [s]	71 [s]

trix and an unsymmetrical system matrix. The only difference between the symmetrical and unsymmetrical formulation is that in the latter, the entropy equation (13b) is re-multiplied by  $T_0$ .

The solvers PARDISO and SPOOLES are *direct* solvers which can benefit from the complex symmetry and are included in the FEM software COMSOL. The time listed in Table II is the total solving time for ten frequencies between 10 Hz and 10 kHz and includes assembly as well as factorization of the system matrix. One calculation failed because of insufficient system memory. Clearly, the complex symmetric formulation results in a reduction of both the solving time and the required system memory, although the amount of this reduction varies.

## 5. Conclusions

This paper shows that viscothermal wave propagation, based on the linearized Navier Stokes equations, can be described by finite elements with *complex symmetric* FEM system matrices. Some solvers can use the complex symmetry, resulting in reduced solving time and reduced memory requirements.

Several FEM discretizations, which are stable for the Stokes equations, have been tested. These discretizations also yield stable viscothermal acoustic finite elements. The best performance is obtained with the Taylor Hood and Crouzeix Raviart elements with *quadratic temperature shape functions*.

## Appendix: Analytical solution based on the LRF model

The exact solution used in the paper is derived in this appendix. It is based on the LRF model, see [1] for tubes and [2, 3] for both tubes and layers. The coordinates of the problem in Figure 1 are  $x = [0, L]$  and  $z = [-h_0, h_0]$ . In the context of the LRF model, the  $x$  coordinate is the propagation direction and the  $z$  coordinate is the cross section direction. First some variables and functions need to be defined.

Define the wave numbers (not to be confused with the entropy  $s$ ):

$$s_\mu = h_0 \sqrt{\frac{\rho_0 \omega}{\mu}}, \quad s_\kappa = h_0 \sqrt{\frac{\rho_0 C_p \omega}{\kappa}}, \quad (A1)$$

$$k_r = \frac{\omega h_0}{c_0}, \quad k = \frac{\omega}{c_0}.$$

These wave numbers are dimensionless, except for  $k$ . The LRF model is only valid if

$$\frac{k_r}{s_\mu} \ll 1, \quad (A2)$$

$$\frac{k_r}{s_\kappa} \ll 1, \quad (A3)$$

$$k_r \ll 1. \quad (A4)$$

The LRF equations can be partially solved in the cross section direction. For layer geometries, this results in the  $z$  dependent functions

$$A(z) = \frac{\cosh(s_\mu \frac{z}{h_0} \sqrt{i})}{\cosh(s_\mu \sqrt{i})} - 1,$$

$$B(z) = \frac{\sinh(s_\mu \frac{z}{h_0} \sqrt{i})}{s_\mu \sqrt{i} \cosh(s_\mu \sqrt{i})} - \frac{z}{h_0},$$

$$\tilde{B}(z) = \frac{\sinh(s_\mu \frac{z}{h_0} \sqrt{i})}{s_\mu \sqrt{i} \cosh(s_\mu \sqrt{i})}, \quad (A5)$$

$$C(z) = \frac{\cosh(s_\kappa \frac{z}{h_0} \sqrt{i})}{\cosh(s_\kappa \sqrt{i})} - 1,$$

$$D(z) = \frac{\sinh(s_\kappa \frac{z}{h_0} \sqrt{i})}{s_\kappa \sqrt{i} \cosh(s_\kappa \sqrt{i})} - \frac{z}{h_0},$$

$$\tilde{D}(z) = \frac{\sinh(s_\kappa \frac{z}{h_0} \sqrt{i})}{s_\kappa \sqrt{i} \cosh(s_\kappa \sqrt{i})},$$

where  $B$  is the dimensionless integral of  $A$ , and  $D$  that of  $C$ , defined by  $(1/h_0) \int_0^z \dots dz$ . Furthermore,  $\partial A / \partial z = i s_\mu^2 / h_0 \tilde{B}$  and, likewise,  $\partial C / \partial z = i s_\kappa^2 / h_0 \tilde{D}$ . These functions are used to formulate the solutions.

The pressure is constant in the cross section direction. In the propagation direction, it should satisfy the Helmholtz equation

$$\frac{\partial^2 p}{\partial x^2} - k^2 \Gamma^2 p = 0. \quad (A6)$$

The symbol  $\Gamma$  in this equation denotes the propagation constant. It is a complex valued correction of the acoustic wave number, defined by

$$\Gamma = \sqrt{\frac{\gamma}{nB(h_0)}},$$

$$n = \left(1 + \frac{R_0}{C_p} D(h_0)\right)^{-1}. \quad (A7)$$

With boundary conditions  $v_x = 0 \rightarrow \partial p / \partial x = 0$  at  $x = 0$  and  $p = 1$  at  $x = L$ , the LRF pressure solution is

$$p(x) = \frac{\cosh(\Gamma k x)}{\cosh(\Gamma k L)}. \quad (A8)$$

The velocity and temperature fields are defined as function of the pressure field.

$$v_x(x, z) = -\frac{iA(z)}{k\rho_0 c_0} \frac{\partial p(x)}{\partial x}$$

$$= -\frac{\tanh(\Gamma k x) A(z)}{\rho_0 c_0} i\Gamma p, \quad (A9)$$

$$T(x, z) = -\frac{C(z)}{\rho_0 C_p} p(x). \quad (A10)$$

The velocity in cross section direction can be determined from the continuity equation (8c):

$$\frac{\partial v_z}{\partial z} = -\frac{\partial v_x}{\partial x} + \frac{i\omega}{T_0}T - \frac{i\omega}{\rho_0}p \quad (\text{A11})$$

$$= \left( \frac{\Gamma^2}{\gamma}A(z) - \frac{R_0}{C_p}C(z) - 1 \right) \frac{i\omega}{\rho_0}p. \quad (\text{A12})$$

Integration using  $v_z = 0$  at  $z = 0$ , from symmetry considerations, yields

$$v_z = \left( \frac{\Gamma^2}{\gamma}B(z) - \frac{R_0}{C_p}D(z) - \frac{z}{h_0} \right) \frac{\gamma k_r}{\rho_0 c_0} i p. \quad (\text{A13})$$

thus  $v_z$  is small compared to  $p$  and  $v_x$ , according to equation (A2). The volumetric heat source can be calculated from the entropy equation (8b):

$$Q = i\omega\rho_0 C_p T - \kappa\Delta T - i\omega p = \frac{k_r^2}{s_k^2} \Gamma^2 C(z) \omega p, \quad (\text{A14})$$

which is very small compared to the term  $i\omega p$ , according to equation (A2).

The body force in propagation direction can be determined from the momentum equation (8a) in this direction:

$$f_x = i\omega\rho_0 v_x - (\nabla \cdot \sigma)_x \quad (\text{A15})$$

$$= \left( \frac{\lambda + \mu}{\mu} \left( \frac{\gamma R_0}{C_p} C(z) + \gamma \right) + \Gamma^2 A(z) \right) i \frac{k_r^2}{s_\mu^2} \frac{\partial p}{\partial x}.$$

This is small compared to  $\frac{\partial p}{\partial x}$ , present in  $(\nabla \cdot \sigma)_x$  in the momentum equation; again according to equation (A2).

Finally, the body force in  $z$  direction can also be calculated from the momentum equation (8a), but now in  $z$  direction:

$$f_z = i\omega\rho_0 v_z - (\nabla \cdot \sigma)_z$$

$$= \left( 1 + i\Gamma^2 \frac{k_r^2}{s_\mu^2} \right) i\omega\rho_0 v_z \quad (\text{A16})$$

$$+ \left( \Gamma^2 \tilde{B}(z) - \frac{\lambda + 2\mu}{\mu} \frac{\gamma R_0}{C_p} \frac{s_k^2}{s_\mu^2} \tilde{D}(z) \right) k_r k p.$$

This body force has a larger magnitude than  $f_x$ , but it is still small and does not influence the solutions of  $v_x$ ,  $T$  and  $p$  significantly. It does have a small but noticeable effect on  $v_z$ . Nevertheless, this velocity has a small magnitude itself and is not a very interesting degree of freedom of the model for most applications of the LRF model.

The exact solution used in section 4 is defined by equations (A8–A10, A13–A16).

The difference in the error that result from a calculation with and without the terms  $f$  and  $Q$  are small. For Taylor Hood quadrilaterals mesh case  $M = 4$  (see section 4) the difference is the largest, but still small, for the pressure field; see Figure A1.

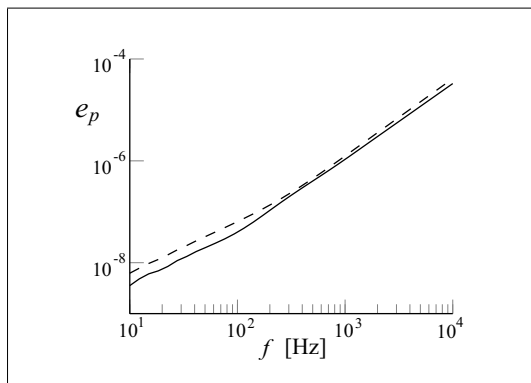


Figure A1. Error of the pressure field with (—) and without (---)  $f$  and  $Q$ ; mesh case  $M = 4$ , Taylor Hood quadrilateral.

## Acknowledgements

*Sonion* is gratefully acknowledged by the authors for financing this research.

We also like to thank M. J. J. Nijhof for our fruitful discussions on viscothermal acoustic finite elements.

## References

- [1] H. Tijdeman: On the propagation of sound waves in cylindrical tubes. *Journal of Sound and Vibration* **39** (1975) 1–33.
- [2] W. M. Beltman: Viscothermal wave propagation including acousto-elastic interaction. Dissertation. University of Twente, Enschede, 1998.
- [3] W. M. Beltman: Viscothermal wave propagation including acousto-elastic interaction, part I: Theory. *Journal of Sound and Vibration* **227** (1999) 555–586.
- [4] C. Zwicker, C. Kosten: *Sound absorbing materials*. Elsevier, 1949.
- [5] R. Bossart, N. Joly, M. Bruneau: Hybrid numerical and analytical solutions for acoustic boundary problems in thermo-viscous fluids. *Journal of Sound and Vibration* **263** (2003) 69–84.
- [6] M. Bruneau, P. Herzog, J. Kergomard, J. D. Polack: General formulation of the dispersion equation in bounded visco-thermal fluid, and application to some simple geometries. *Wave Motion* **11** (1989) 441–451.
- [7] A. Pierce: *Acoustics: An introduction to its physical principles and applications*. Acoustical Society of America, 1991.
- [8] V. Cutanda Henriquez: Numerical transducer modeling. Dissertation. Technical University of Denmark, DTU, Lyngby, 2002.
- [9] C. Karra, M. Ben Tahar: An integral equation formulation for boundary element analysis of propagation in viscothermal fluids. *The Journal of the Acoustical Society of America* **102** (1997) 1311–1318.
- [10] M. Malinen, M. Lyly, P. Råback, A. Kärkkäinen, L. Kärkkäinen: A finite element method for the modeling of thermo-viscous effects in acoustics. *Proceedings of ECCOMAS, Jyväskylä, Finland, 2004*.
- [11] L. Cheng, R. D. White, K. Gosh: Three-dimensional viscous finite element formulation for acoustic fluid-structure

- interaction. *Computer Methods in Applied Mechanics and Engineering* **197** (2008) 4160–4172.
- [12] N. Joly, M. Bruneau, R. Bossart: Coupled equations for particle velocity and temperature variation as the fundamental formulation of linear acoustics in thermo-viscous fluids at rest. *Acta Acustica united with Acustica* **92** (2006) 202–209.
- [13] Comsol Multiphysics user's guide. 3.5 ed. 2008.
- [14] P. Morse, K. Ingard: *Theoretical acoustics*. McGraw-Hill, 1968.
- [15] M. D. Gunzburger: *Finite element methods for viscous incompressible flows*. Academic Press, 1989.
- [16] X. Wang, K.-J. Bathe: Displacement/pressure based mixed finite element formulations for acoustic fluid-structure interaction problems. *International Journal for Numerical Methods in Engineering* **40** (1997) 2001–2017.
- [17] C. Taylor, P. Hood: A numerical solution of the Navier-Stokes equations using the finite element technique. *Computers and Fluids* **1** (1973) 73–100.
- [18] M. Crouzeix, P. Raviart: Conforming and nonconforming finite element methods for solving the stationary Stokes equations I. *Revue Française d'Automatique, Informatique et Recherche Opérationnelle* **7** (1973) 33–76.
- [19] D. N. Arnold, F. Brezzi, M. Fortin: A stable finite element for the Stokes equations. *Calcolo* **21** (1984) 337–344.
- [20] K.-J. Bathe: *Finite element procedures*. Prentice Hall, 1996.
- [21] M. Fortin: Finite element solution of the Navier-Stokes equations. *Acta Numerica* **2** (1993) 239–284.
- [22] W. Bai: The quadrilateral 'mini' finite element for the Stokes problem. *Computer Methods in Applied Mechanics and Engineering* **143** (1997) 41–47.



# Comsol script: FLNS microphone model

```

% COMSOL Multiphysics Model M-file
% Generated by COMSOL 3.5 (COMSOL 3.5.0.494, $Date: 2008/09/19 16:09:48 $)
% Edited by W.R. Kampinga

flclear fem

% COMSOL version
clear vrsn
vrsn.name = 'COMSOL 3.5';
vrsn.ext = '';
vrsn.major = 0;
vrsn.build = 494;
vrsn.rcs = '$Name: $';
vrsn.date = '$Date: 2008/09/19 16:09:48 $';
fem.version = vrsn;

% Constants
fem.const = {'freq','160e3','Pm','1', ...
    'sma','3128','rho0','8300*6.95e-6', ...
    'km','omega*sqrt(rho0/sma)','T0','294.30000', ...
    'p0','101500.00','rho0','1.2254935', ...
    'c0','341.20058','mu','1.8294e-005', ...
    'kappa','0.0251808','Cp','gg/(gg-1)*p0/(rho0*T0)', ...
    'gg','rho0*c0^2/p0','omega','2*pi*freq', ...
    'Pr','mu*Cp/kappa','lda','(0.6-2/3)*mu', ...
    'pref','20e-6','Z0','rho0*c0', ...
    'k0','omega/c0','kv','sqrt(-i*omega*rho0/mu)', ...
    'kh','sqrt(-i*omega*rho0*Cp/kappa)'};

% Geometry
clear draw
g11=rect2('0.0020','18E-6','base','corner','pos',{'0','0'},'rot','0');
draw.s.objs = {g11};
draw.s.name = {'R1'};
draw.s.tags = {'g11'};
fem.draw = draw;
fem.geom = geomcsg(fem);

% Create mapped quad mesh
fem.mesh=meshmap(fem, ...
    'edgegroups',{'[2],[4],[3],[1]}', ...
    'edgelen',{1,[0 0.08 0.31 0.69 0.92 1],2,[0:0.01:1], ...
    3,[0:0.01:1],4,[0 0.08 0.31 0.69 0.92 1]}, ...
    'hauto',4);

% (Default values are not included)

% Application mode 1: viscothermal acoustics
clear appl
appl.mode.class = 'FlPDEW';
appl.dim = {'vr','vz','T','p','vr_t','vz_t','T_t','p_t'};
appl.sdim = {'r','z','theta'}; % cylinder coordinates
appl.name = 'vtacoaxi';
appl.shape = {'shlag(2,'vr'),'shlag(2,'vz'),'shlag(2,'T'),'shlag(1,'p)'};
appl.gporder = {4,2};

```

```

appl.cporder = {2,1};
appl.assignsuffix = '_vtacoaxi';
clear bnd
bnd.constrf = {'test(-vr)','test(-vr)';'test(-vz)';'test(-T)'};0,'test(-vr*nr-vz*nz)', ...
'test(-vz*tz-vr*tr)',{'test(u-vz)';'test(-vr)';'test(-T)'};
bnd.name = {'axis','isoth. wall','P','isentropic wall','P0 normal flow','vmemb'};
bnd.constr = {'-vr',{'-vr';'-vz';'-T'};0,'-vr*nr-vz*nz','-vz*tz-vr*tr',{'u-vz'; ...
'-vr';'-T'};};
bnd.weak = {0,0,'P*r*(test(vz)*nz+test(vz)*nr)',0,0,0};
bnd.ind = [1,2,6,5];
appl.bnd = bnd;
clear equ
equ.cporder = {{1;1;1;2}};
equ.bndgporder = {{1;1;1;2}};
equ.dweak = 0;
equ.gporder = {{1;1;1;2}};
equ.name = 'vtacoaxi';
equ.weak = {{{['i*omega*rho0*r*(vr*test(vr)+vz*test(vz))+' ...
'2*mu*(r*vrr*test(vrr)+vr/r*test(vr)+r*vzz*test(vzz))+mu*r*(vrr+vzr)*(test(vrz)+test(vzr))+' ...
'lda*(vrr+vr/r+vzz)*(r*test(vrr)+test(vr)+r*test(vzz))']; ...
'-i*omega*rho0*Cp/T0*r*T*test(T)-kappa/T0*r*(Tz*test(Tz)+Tr*test(Tr))']; ...
['-i*omega/p0*r*p*test(p)-(r*vrr+vr+r*vzz)*test(p)-p*(r*test(vrr)+test(vr)+*test(vzz))+' ...
'i*omega/T0*r*(T*test(p)+p*test(T))']}}]; % axi-symmetric weak form of FLNS model
equ.ind = [1];
appl.equ = equ;
fem.appl{1} = appl;

% Application mode 2: membrane
clear appl
appl.mode.class = 'FLPDEWBoundary';
appl.sdim = {'r','z','theta'};
appl.name = 'membrane';
appl.sshape = 2;
appl.assignsuffix = '_membrane';
clear prop
clear weakconstr
weakconstr.value = 'off';
weakconstr.dim = {'lm9','lm10'};
prop.weakconstr = weakconstr;
appl.prop = prop;
clear pnt
pnt.constrf = {0,'test(-u)'};
pnt.constr = {0,'-u'};
pnt.ind = [1,1,1,2];
appl.pnt = pnt;
clear bnd
bnd.name = {'','membrane'};
bnd.usage = {0,1};
% axi-symmetric weak form membrane model:
bnd.weak = ['-sma*uTz*r*test(uTz)-sma*uTr*r*test(uTr)+sma*km^2*r*u*test(u)-' ...
'(Pm-p+lda*(vrr+vr/r+vzz)+2*mu*vzz)*(i*omega)*r*test(u)']; % for membrane at z=const surface
bnd.ind = [1,1,2,1];
appl.bnd = bnd;
fem.appl{2} = appl;
fem.sdim = {'r','z'};
fem.frame = {'ref'};
fem.border = 1;

% Coupling variable elements
clear elemcpl
% Integration coupling variables
clear elem
elem.elem = 'elcplscalar';
elem.g = {'1'};
src = cell(1,1);
clear bnd
bnd.expr = {{{,'u/(i*omega)*r'}}};
bnd.ipoints = {{{,'4'}}};
bnd.frame = {{{,'ref'}}};
bnd.ind = {{'1','2','4'},{'3'}};
src{1} = {{},bnd,{};
elem.src = src;
geomdim = cell(1,1);
geomdim{1} = {};
elem.geomdim = geomdim;
elem.var = {'U'}; % related to sensitivity: U=(H*Rm^2)/2
elem.global = {'1'};
elem.maxvars = {};
elemcpl{1} = elem;
fem.elemcpl = elemcpl;

```

```

% Descriptions
clear descr
descr.const= {'kv','viscous wave number [1/m]', ...
  'freq','frequency [Hz]','p0','quiescent pressure [Pa]', ...
  'Pm','pressure outside the mic [Pa]','kappa','dynamic viscosity [W/(m*K)]', ...
  'mu','dynamic viscosity [Pa*s]','k0','isentropic acoustic wave number [1/m]', ...
  'omega','angular frequency [rad/s]','T0','quiescent temperature [K]', ...
  'km','membrane wave number [1/m]','lda','second viscosity [Pa*s]', ...
  'Z0','characteristic isentropic impedance [Pa/(m/s)]','kh','thermal wave number [1/m]', ...
  'sma','membrane tension [N/m]','Pr','Prandtl number [1]', ...
  'Cp','specific heat at constant pressure [W/(m*K)]','rhom','membrane density [kg/m^2]', ...
  'c0','speed of sound [m/s]','gg','ratio of specific heats [1]', ...
  'rho0','quiescent density [kg/m^3]','pref','reference pressure [Pa]'};
fem.descr = descr;

% ODE Settings
clear ode
clear units;
units.basesystem = 'SI';
ode.units = units;
fem.ode=ode;

% Multiphysics
fem=multiphysics(fem);

% Extend mesh
fem.xmesh=meshextend(fem);

% Solve problem
fem.sol=femstatic(fem, ...
  'u',0, ...
  'solfile','on', ...
  'solcomp',{'T','u','vz','p','vr'}, ...
  'outcomp',{'T','u','vz','p','vr'}, ...
  'blocksize','auto', ...
  'pname','freq', ...
  'plist',[2*logspace(2,5,3)], ... % only 3 frequencies for faster opening (was 101)
  'oldcomp',{'', ...
  'linsolver','pardiso');

% Save current fem structure for restart purposes
fem0=fem;

% Plot solution
postplot(fem, ...
  'tridata','abs(p)', ...
  'trimap','jet(1024)', ...
  'solnum','end');

```





# Nomenclature

Latin variables			
$c_0$	Speed of sound	[m/s]	Eq. (2.9)
$C_p$	Specific heat at constant pressure	[J/(kgK)]	Eq. (2.7)
$C_v$	Specific heat at constant volume	[J/(kgK)]	Eq. (2.11)
$e$	Euler's number	[1]	
$\mathfrak{F}$	Magneto-motive force	[A]	Eq. (5.5)
$H$	Specific enthalpy phasor	[J/kg]	Eq. (2.7)
$k_0$	Isentropic acoustic wave number	[m <sup>-1</sup> ]	Eq. (3.1)
$k_h$	Thermal wave number	[m <sup>-1</sup> ]	Eq. (3.1)
$k_\ell$	Modified acoustic wave number (LRF)	[m <sup>-1</sup> ]	Eq. (3.54)
$k_m$	Membrane wave number	[m <sup>-1</sup> ]	Eq. (4.6)
$k_\nu$	Viscous wave number	[m <sup>-1</sup> ]	Eq. (3.1)
$k_\parallel$	Tangential acoustic wave number (BLI)	[m <sup>-1</sup> ]	Eq. (3.37)
$\tilde{k}_h$	Dimensionless thermal wave number	[1]	Eq. (3.2)
$\tilde{k}_\nu$	Dimensionless viscous wave number	[1]	Eq. (3.2)
$\ell$	Characteristic length of LRF cross section	[m]	Eq. (3.40)
$N_{pr}$	Prandtl number	[1]	Eq. (1.15)
$\mathbf{n}$	Outward normal vector on boundary	[1]	
$p$	Pressure phasor	[Pa]	
$p_0$	Quiescent pressure	[Pa]	
$\check{p}$	Total pressure	[Pa]	
$\bar{p}$	Dimensionless pressure phasor	[1]	Eq. (3.2)
$\mathbf{q}$	Heat flow phasor	[W/m <sup>2</sup> ]	Eq. (2.5)
$R_0$	Specific gas constant	[J/(kgK)]	Eq. (2.8)
$\mathfrak{R}$	Magnetic reluctance	[H <sup>-1</sup> ]	Eq. (5.5)
$S_{cd}$	Cross section area of $\Omega_{cd}$ (LRF)	[m], [m <sup>2</sup> ]	
$\check{s}$	Total specific entropy	[J/(kgK)]	
$s$	Specific entropy phasor	[J/(kgK)]	
$T$	Temperature phasor	[K]	
$T_0$	Quiescent temperature	[K]	
$\check{T}$	Total temperature	[K]	
$\bar{T}$	Dimensionless temperature phasor	[1]	Eq. (3.2)
$t$	Time	[s]	Eq. (1.1)
$t_c$	Computational time per frequency	[s]	

$\mathbf{t}$	Tangential vector on boundary	[1]	
$\mathbf{v}$	Velocity vector phasor	[m/s]	
$\check{\mathbf{v}}$	Total velocity vector	[m/s]	
$\tilde{\mathbf{v}}$	Dimensionless velocity vector phasor	[1]	Eq. (3.2)
$Z_0$	Characteristic isentropic impedance	[Pa s/m]	Eq. (1.10)
$Z_\ell$	Characteristic LRF impedance	[Pa s/m]	Eq. (3.56)
Greek variables			
$\gamma$	Ratio of specific heats	[1]	Eq. (2.10)
$\delta_h$	Thermal boundary layer thickness	[m]	Eq. (1.14)
$\delta_v$	Viscous boundary layer thickness	[m]	Eq. (1.14)
$\varepsilon$	Symmetric part of the velocity gradient	[s <sup>-1</sup> ]	Eq. (2.1)
$\zeta_{\text{BLI}}$	Dimensionless impedance (BLI)	[1]	Eq. (3.36b)
$\eta$	Bulk viscosity	[Pa s]	Eq. (2.2)
$\theta$	Angle of incidence	[rad]	Fig. 3.4(a)
$\vartheta$	Acoustic volume flow	[m <sup>3</sup> /s]	
$\vartheta_{cd}$	Acoustic volume flow over $\partial\Omega_{cd}$ (LRF)	[m/s], [m <sup>2</sup> /s]	Eq. (3.55)
$\vartheta_{pd}$	Acoustic volume flow over $\partial\Omega_{pd}$ (LRF)	[m <sup>2</sup> /s], [m <sup>3</sup> /s]	Eq. (3.60)
$\kappa$	Heat conduction coefficient	[W/(K m)]	Eq. (2.5)
$\lambda$	Second viscosity	[Pa s]	Eq. (2.1)
$\lambda_0$	Acoustic wavelength	[m]	Eq. (1.14)
$\lambda_h$	Thermal wavelength	[m]	Eq. (1.14)
$\lambda'_h$	Alt. thermal boundary layer thickness	[m]	Eq. (1.14)
$\lambda_v$	Viscous wavelength	[m]	Eq. (1.14)
$\lambda'_v$	Alt. viscous boundary layer thickness	[m]	Eq. (1.14)
$\mu$	Dynamic viscosity	[Pa s]	Eq. (2.1)
$\rho$	Density phasor	[kg/m <sup>3</sup> ]	
$\rho_m$	Membrane mass per surface	Sec. 4.3.1	
$\rho_0$	Quiescent density	[kg/m <sup>3</sup> ]	
$\check{\rho}$	Total density	[kg/m <sup>3</sup> ]	
$\tilde{\rho}$	Dimensionless density phasor	[1]	Eq. (3.2)
$\sigma$	Stress tensor phasor	[N/m <sup>2</sup> ]	Eq. (2.1)
$\sigma_m$	Membrane tension	[N/m]	Sec. 4.3.1
$\tau$	Viscous stress tensor phasor	[N/m <sup>2</sup> ]	Eq. (2.1)
$Y_h$	Lumped thermal field	[1]	Eq. (3.47a)
$Y'_h$	Lumped modified thermal field	[1]	Eq. (3.46b)
$Y_v$	Lumped of viscous field	[1]	Eq. (3.47a)
$\check{\Phi}$	Viscous heating	[W/m <sup>3</sup> ]	
$\phi$	Dummy variable	[•]	
$\phi$	Magnetic flux (Chapter 5)	[Wb]	Eq. (5.5)
$\dot{\phi}$	Magnetic flux rate (Chapter 5)	[Wb/s]	
$\Psi_h$	Thermal field	[1]	Sec. 3.1.4
$\Psi'_h$	Modified thermal	[1]	Sec. 3.1.4
$\Psi_v$	Viscous field	[1]	Sec. 3.1.4
$\tilde{\xi}$	Dimensionless viscosity group	[1]	Eq. (3.2)
$\omega$	Angular frequency	[rad/s]	Eq. (1.1)
$\Omega$	Domain		
$\partial\Omega$	Boundary of $\Omega$		Eq. (2.12)

$\Omega_{cd}$	Cross section domain (LRF)	Tab. 3.1
$\partial\Omega_{cd}$	Boundary of cross section domain (LRF)	Tab. 3.1
$\Omega_{pd}$	Propagation domain (LRF)	Tab. 3.1
$\partial\Omega_{pd}$	Boundary of propagation domain (LRF)	Tab. 3.1
$\partial\Omega_m$	Boundary with a membrane	
$\partial^2\Omega_m$	Boundary of the membrane	

---

Operators and functions

---

J	Bessel function of the first kind	
H	Hankel function	
$\frac{D\phi}{Dt}$	Material derivative	
$\Im(\phi)$	Imaginary part	
$\Re(\phi)$	Real part	
$\phi^T$	Transpose	
$\bar{\phi}$	Complex conjugate	
$\nabla\phi$	Gradient	
$\nabla_n\phi$	Gradient normal to boundary	
$\nabla_t\phi$	Gradient tangential to boundary	
$\nabla_{\parallel}\phi$	Tangential gradient	Fig. 3.3
$\nabla_{\perp}\phi$	Perpendicular gradient	Fig. 3.3
$\tilde{\nabla}\phi$	Dimensionless gradient	Eq. (3.2)
$\nabla \cdot \phi$	Divergence	
$\tilde{\nabla} \cdot \phi$	Dimensionless divergence	Eq. (3.2)
$\Delta\phi$	Laplacian	
$\tilde{\Delta}\phi$	Dimensionless Laplacian	Eq. (3.2)
$\langle\phi, \phi\rangle$	Hermitian inner product	Eq. (2.24)
$\langle\phi\rangle$	Mean value	Eq. (3.47a)
$ \phi $	Absolute value	
$\angle\phi$	Complex angle	
$\phi_w$	Weighing function	

---

Abbreviations

---

BC	Boundary condition
BEM	Boundary element method
BLI	Boundary layer impedance (model)
DOF	Degree of freedom
FEM	Finite element method
FLNS	Full linear Navier-Stokes (model)
FSI	Fluid structure interaction
LRF	Low reduced frequency (model)
PDE	Partial differential equation
SLNS	Sequential linear Navier-Stokes (model)

---



# Bibliography

- [1] R. J. Astley & A. Cummings. Wave propagation in catalytic converters: formulation of the problem and finite element to solution scheme. *Journal of Sound and Vibration*, 188(5):635–657, 1995.
- [2] S. Backhaus & G. W. Swift. A thermoacoustic-stirling heat engine: Detailed study. *The Journal of the Acoustical Society of America*, 107(6):3148–3166, 2000.
- [3] K.-J. Bathe. *Finite element procedures*. Prentice Hall, 1996.
- [4] R. E. Beatty, Jr. Boundary layer attenuation of higher order modes in rectangular and circular tubes. *The Journal of the Acoustical Society of America*, 22(6):850–854, 1950.
- [5] W. M. Beltman. *Viscothermal wave propagation including acousto-elastic interaction*. Ph.D. thesis, University of Twente, Enschede, The Netherlands, 1998.
- [6] W. M. Beltman. Viscothermal wave propagation including acousto-elastic interaction, part I: theory. *Journal of Sound and Vibration*, 227(3):555–586, 1999.
- [7] W. M. Beltman. Viscothermal wave propagation including acousto-elastic interaction, part II: applications. *Journal of Sound and Vibration*, 227(3):587–609, 1999.
- [8] W. M. Beltman, P. J. M. van der Hoogt, R. M. E. J. Spiering & H. Tijdeman. Implementation and experimental validation of a new viscothermal acoustic finite element for acousto-elastic problems. *Journal of Sound and Vibration*, 216(1):159–178, 1998.
- [9] M. van Blijderveen. *The dynamical behaviour of a hearing aid receiver membrane*. Master's thesis, University of Twente, Enschede, The Netherlands, 2006.
- [10] R. Bossart, N. Joly & M. Bruneau. Hybrid numerical and analytical solutions for acoustic boundary problems in thermo-viscous fluids. *Journal of Sound and Vibration*, 263(1):69–84, 2003.

- [11] C. Bosschaart. *Optimizing the acoustic performance of a hearing aid receiver*. Master's thesis, University of Twente, Enschede, The Netherlands, 2006. Confidential.
- [12] M. Bruneau, P. Herzog, J. Kergomard & J. D. Polack. General formulation of the dispersion equation in bounded visco-thermal fluid, and application to some simple geometries. *Wave Motion*, 11(5):441–451, 1989.
- [13] P. H. Ceperley. A pistonless stirling engine—the traveling wave heat engine. *The Journal of the Acoustical Society of America*, 66(5):1508–1513, 1979.
- [14] L. Cheng, R. D. White & K. Grosh. Three-dimensional viscous finite element formulation for acoustic fluid-structure interaction. *Computer Methods in Applied Mechanics and Engineering*, 197(49-50):4160–4172, 2008.
- [15] *COMSOL Multiphysics user's guide*, 3.5 edition, 2008.
- [16] A. Craggs & J. G. Hildebrandt. Effective densities and resistivities for acoustic propagation in narrow tubes. *Journal of Sound and Vibration*, 92(3):321–331, 1984.
- [17] L. Cremer. Über die akustische Grenzschicht vor starren Wänden. *Archiv der elektrischen Übertragung*, 2:136–139, 1948.
- [18] M. Crouzeix & P. A. Raviart. Conforming and nonconforming finite element methods for solving the stationary Stokes equations I. *Revue Française d'Automatique, Informatique et Recherche Opérationnelle*, 7(R-3):33–76, 1973.
- [19] A. Cummings. Sound propagation in narrow tubes of arbitrary cross-section. *Journal of Sound and Vibration*, 162(1):27–42, 1993.
- [20] V. Cutanda Henríquez. *Numerical transducer modeling*. Ph.D. thesis, Technical University of Denmark (DTU), Lyngby, Denmark, 2002.
- [21] R. T. DeHoff. *Thermodynamics in Materials Science*. McGraw-Hill, 1993.
- [22] E. Dokumaci. An integral equation formulation for boundary element analysis of acoustic radiation problems in viscous fluids. *Journal of Sound and Vibration*, 147(2):335–348, 1991.
- [23] E. Dokumaci. Prediction of the effects of entropy fluctuations on sound radiation from vibrating bodies using an integral equation approach. *Journal of Sound and Vibration*, 186(5):805–819, 1995.
- [24] E. Dokumaci. An approximate dispersion equation for sound waves in a narrow pipe with ambient gradients. *Journal of Sound and Vibration*, 240(4):637–646, 2001.
- [25] F. J. M. van der Eerden. *Noise reduction with coupled prismatic tubes*. Ph.D. thesis, University of Twente, Enschede, The Netherlands, 2000.
- [26] M. Fortin. Finite element solution of the Navier-Stokes equations. *Acta Numerica*, 2:239–284, 1993.

- [27] R. E. Graves & B. M. Argrow. Bulk viscosity: past to present. *Journal of Thermophysics and Heat Transfer*, 13(3):337–342, 1999.
- [28] M. D. Gunzburger. *Finite element methods for viscous incompressible flows*. Academic Press, 1989.
- [29] M. H. C. Hannink. *Acoustic resonators for the reduction of sound radiation and transmission*. Ph.D. thesis, University of Twente, Enschede, The Netherlands, 2007.
- [30] M. H. C. Hannink, Y. H. Wijnant & A. de Boer. Optimized sound absorbing trim panels for the reduction of aircraft cabin noise. In *Proceedings of ICSV 11*. St. Petersburg, Russia, 2004.
- [31] T. J. R. Hughes. *The finite element method — Linear static and dynamic finite element analysis*. Dover Publications, 2000.
- [32] T. J. R. Hughes, A. Reali & G. Sangalli. Duality and unified analysis of discrete approximations in structural dynamics and wave propagation: Comparison of p-method finite elements with k-method NURBS. *Computer Methods in Applied Mechanics and Engineering*, 197(49-50):4104–4124, 2008.
- [33] J.-G. Ih, C.-M. Park & H.-J. Kim. A model for sound propagation in capillary ducts with mean flow. *Journal of Sound and Vibration*, 190(2):163–175, 1996.
- [34] H. Inayat Hussain. *Thermoviscous effects in acoustic radiation problems*. Ph.D. thesis, l’Institut National des Sciences Appliquées de Lyon, Lyon, France, 2009.
- [35] J. F. J. Jansen. *Viscous and thermal behavior of acoustic wave propagation*. Master’s thesis, University of Twente, Enschede, The Netherlands, 2009.
- [36] N. Joly. Finite element modeling of thermoviscous acoustics in closed cavities. In *Proceedings of Acoustics 08*. Paris, France, 2008.
- [37] N. Joly. Finite element modeling of thermoviscous acoustics on adapted anisotropic meshes: Implementation of the particle velocity and temperature variation formulation. *Acta Acustica united with Acustica*, 96(1):102–114(13), 2010.
- [38] N. Joly, M. Bruneau & R. Bossart. Coupled equations for particle velocity and temperature variation as the fundamental formulation of linear acoustics in thermo-viscous fluids at rest. *Acta Acustica united with Acustica*, 92(2):202–209, 2006.
- [39] W. R. Kampinga, C. Bosschaart, Y. H. Wijnant & A. de Boer. The coupling of a hearing aid loudspeaker membrane to visco-thermal air layers. In *Proceedings of ICSV 14*. Cairns, Australia, 2007.
- [40] W. R. Kampinga, Y. H. Wijnant & A. de Boer. Viscothermal wave propagation in a circular layer with a partially open and partially closed boundary. In *Proceedings of ISMA*. Leuven, Belgium, 2006.



- [41] W. R. Kampinga, Y. H. Wijnant & A. de Boer. A finite element for viscothermal wave propagation. In *Proceedings of ISMA*. Leuven, Belgium, 2008.
- [42] W. R. Kampinga, Y. H. Wijnant & A. de Boer. A two step viscothermal acoustic FE method. In *Proceedings of ICSV 16*. Kraków, Poland, 2009.
- [43] W. R. Kampinga, Y. H. Wijnant & A. de Boer. Performance of several viscothermal acoustic finite elements. *Acta Acustica united with Acustica*, 96(1):115–124(10), 2010. See Appendix B.
- [44] S. M. Karim & L. Rosenhead. The second coefficient of viscosity of liquids and gases. *Reviews of Modern Physics*, 24(2):108–116, 1952.
- [45] C. Karra & M. Ben Tahar. An integral equation formulation for boundary element analysis of propagation in viscothermal fluids. *The Journal of the Acoustical Society of America*, 102(3):1311–1318, 1997.
- [46] C. Karra & M. Ben Tahar. Effects of entropic wave in vibroacoustic problem using boundary element analysis. *Flow, Turbulence and Combustion*, 74(1):49–66, 2005.
- [47] G. Kirchhoff. Ueber den Einfluss der Wärmeleitung in einem Gase auf die Schallbewegung. *Annalen der Physik und Chemie*, 210(6):117–193, 1868.
- [48] M. Knutsson & M. Åbom. Sound propagation in narrow tubes including effects of viscothermal and turbulent damping with application to charge air coolers. *Journal of Sound and Vibration*, 320(1-2):289–321, 2009.
- [49] V. F. Kozlov, A. V. Fedorov & N. D. Malmuth. Acoustic properties of rarefied gases inside pores of simple geometries. *Journal of the Acoustical Society of America*, 117(6):3402–3412, 2005.
- [50] T. Le Van Suu, S. Durand & M. Bruneau. Fluid layer trapped between a plane, circular membrane and an axisymmetrically curved, smooth backing wall: Analytical model of the dynamic behaviour. *Acta Acustica united with Acustica*, 94(3):474–482, 2008.
- [51] M. Malinen, M. Lyly, P. Råback, A. Kärkkäinen & L. Kärkkäinen. A finite element method for the modeling of thermo-viscous effects in acoustics. In *Proceedings of ECCOMAS*. Jyväskylä, Finland, 2004.
- [52] F. P. Mechel. Revision of the Kirchhoff-Rayleigh-theory of sound propagation in visco-thermal air. part I: Basic equations and capillary modes. *Acta Acustica united with Acustica*, 93(4):507–534, 2007.
- [53] P. M. Morse & K. U. Ingard. *Theoretical acoustics*. McGraw-Hill, 1968.
- [54] C. J. Nederveen & J.-P. Dalmont. Corrections to the plane-wave approximation in rapidly flaring horns. *Acta Acustica united with Acustica*, 94(3):461–473, 2008.
- [55] M. J. J. Nijhof. *Viscothermal wave propagation*. Ph.D. thesis, University of Twente, Enschede, The Netherlands, 2010. To be published.

- [56] K. S. Peat. A first approximation to the effects of mean flow on sound propagation through cylindrical capillary tubes. *Journal of Sound and Vibration*, 175(4):475–489, 1994.
- [57] K. S. Peat & R. Kirby. Acoustic wave motion along a narrow cylindrical duct in the presence of an axial mean flow and temperature gradient. *The Journal of the Acoustical Society of America*, 107(4):1859–1867, 2000.
- [58] A. D. Pierce. *Acoustics: An Introduction to Its Physical Principles and Applications*. Acoustical Society of America, 1991.
- [59] G. Plantier & M. Bruneau. Heat conduction effects on the acoustic response of a membrane separated by a very thin air film from a backing electrode. *Journal d'acoustique*, 3:243–250, 1990.
- [60] K. Rasmussen. Calculation methods for the physical properties of air used in the calibration of microphones. Technical Report PL-11b, Technical University of Denmark (DTU), Lyngby, Denmark, 1997.
- [61] K. Rathnam. Influence of velocity slip and temperature jump in rarefied gas acoustic oscillations in cylindrical tubes. *Journal of Sound and Vibration*, 103(3):448–452, 1985.
- [62] K. Rathnam & M. M. Oberai. Acoustic wave propagation in cylindrical tubes containing slightly rarefied gas. *Journal of Sound and Vibration*, 60(3):379–388, 1978.
- [63] H. Schmid. Tables: two-port matrices. Technical report, Eidgenössische Technische Hochschule, Zürich, Switzerland, 2000.
- [64] M. R. Stinson. The propagation of plane sound waves in narrow and wide circular tubes, and generalization to uniform tubes of arbitrary cross-sectional shape. *Journal of the Acoustical Society of America*, 89(2):550–558, 1991.
- [65] M. R. Stinson & Y. Champoux. Propagation of sound and the assignment of shape factors in model porous materials having simple pore geometries. *Journal of the Acoustical Society of America*, 91(2):685–695, 1992.
- [66] G. W. Swift. Thermoacoustic engines. *The Journal of the Acoustical Society of America*, 84(4):1145–1180, 1988.
- [67] L. L. Thompson. A review of finite-element methods for time-harmonic acoustics. *Journal of the Acoustical Society of America*, 119(3):1315–1330, 2006.
- [68] H. Tijdeman. On the propagation of sound waves in cylindrical tubes. *Journal of Sound and Vibration*, 39(1):1–33, 1975.
- [69] C. Truesdell. History of classical mechanics — part I, to 1800. *Die Naturwissenschaften*, 63(2):53–62, 1976.
- [70] C. Truesdell. History of classical mechanics — part II, the 19th and 20th centuries. *Die Naturwissenschaften*, 63(3):119–130, 1976.

- [71] X. Wang & K.-J. Bathe. Displacement/pressure based mixed finite element formulations for acoustic fluid-structure interaction problems. *International Journal for Numerical Methods in Engineering*, 40(11):2001–2017, 1997.
- [72] C. Zwikker & C. Kosten. *Sound Absorbing Materials*. Elsevier, 1949.